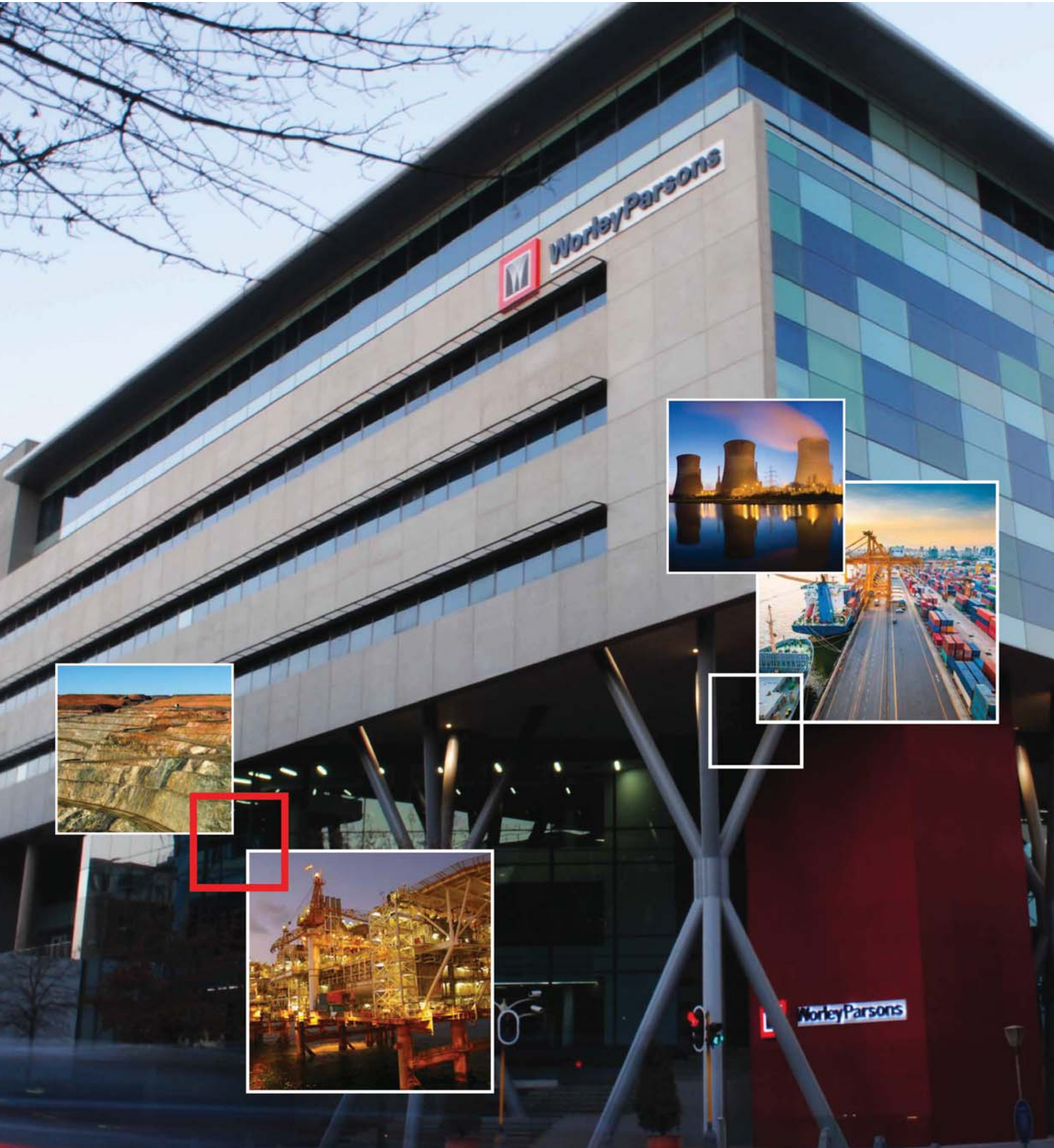




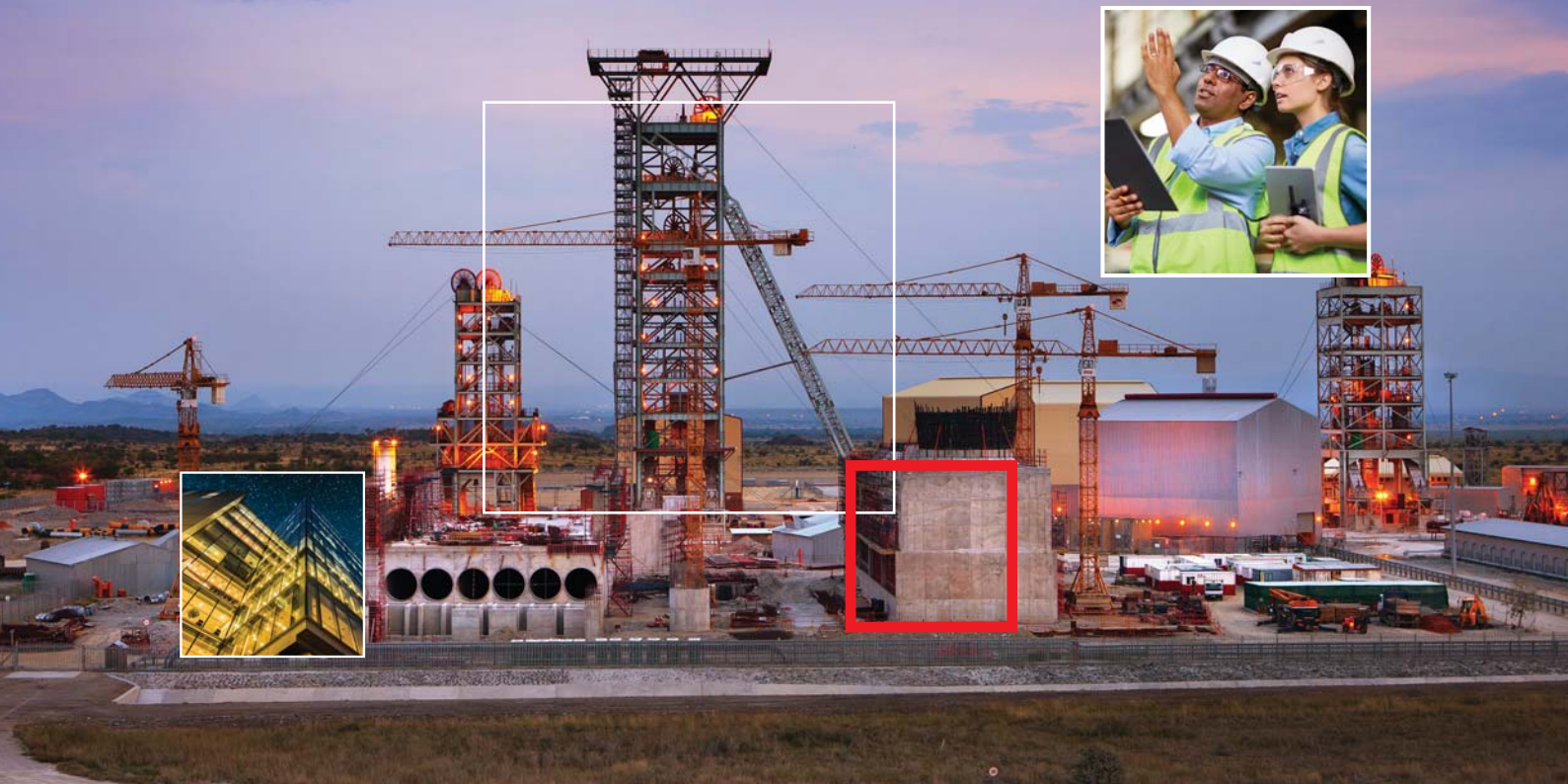
SAIMM

JOURNAL OF THE SOUTHERN AFRICAN INSTITUTE OF MINING AND METALLURGY

VOLUME 118 NO. 2 FEBRUARY 2018



Realising possibilities from **mine to market.**



Resource
Evaluation



Mine
Planning



Mining & Mine
Development



Materials
Handling



Mineral
Processing



Tailings & Waste
Management



Smelting
& Refining



Transport
to Market



Environment
& Approvals



Non-Process
Infrastructure

WorleyParsons adds value through our full scope of services from pit to port including studies, mine planning, impact assessments, permitting and approvals, project management, construction management and global procurement.

Our Mining Centre of Excellence in Johannesburg has niche expertise in underground and open cast mining and provides quality project development and engineering solutions for small to large projects across all areas of base metals, the coal supply chain, chemicals, ferrous metals, alumina, aluminium and iron ore.

Supported by the WorleyParsons global group, we pride ourselves on customising solutions for local environments and committing to our customers' goals.



WorleyParsons

resources & energy

www.worleyparsons.com

wprsainfo@worleyparsons.com



We strive to offer you the lowest cost of ownership

Weir Minerals is a leading designer and manufacturer of mine dewatering solutions, slurry pumps, hydrocyclones, valves, screens, centrifuges, crushers, feeders, washers, conveyers, rubber lining, hoses and wear-resistant linings for the global mining and minerals processing, sand and aggregate, and power and general industrial sectors.

For more information contact us on +27 11 9292600

WEIR

Minerals

www.minerals.weir

www.weirafriicastore.com

OFFICE BEARERS AND COUNCIL FOR THE 2017/2018 SESSION

Honorary President

Mxolis Donald Mbuyisa Mgojo
President, Chamber of Mines of South Africa

Honorary Vice-Presidents

Mosebenzi Joseph Zwane
Minister of Mineral Resources, South Africa

Rob Davies

Minister of Trade and Industry, South Africa

Naledi Pandor

Minister of Science and Technology, South Africa

President

S. Ndlovu

President Elect

A.S. Macfarlane

Senior Vice-President

M.I. Mthenjane

Junior Vice-President

Z. Botha

Immediate Past President

C. Musingwini

Honorary Treasurer

J.L. Porter

Ordinary Members on Council

V.G. Duke

I.J. Geldenhuys

M.F. Handley

W.C. Joughin

E. Matinde

M. Motuku

D.D. Munro

G. Njowa

S.M. Rupprecht

A.G. Smith

M.H. Solomon

D. Tudor

D.J. van Niekerk

A.T. van Zyl

Past Presidents Serving on Council

N.A. Barcza

R.D. Beck

J.R. Dixon

M. Dworzanowski

H.E. James

R.T. Jones

G.V.R. Landman

R.G.B. Pickering

S.J. Ramokgopa

M.H. Rogers

D.A.J. Ross-Watt

G.L. Smith

W.H. van Niekerk

R.P.H. Willis

G.R. Lane–TPC Mining Chairperson

Z. Botha–TPC Metallurgy Chairperson

A.S. Nhleko–YPC Vice-Chairperson

K.M. Letsoalo–YPC Vice-Chairperson

Branch Chairpersons

Botswana

L.E. Dimbungu

DRC

S. Maleba

Johannesburg

J.A. Luckmann

Namibia

N.M. Namate

Northern Cape

W.J. Mans

Pretoria

R.J. Mostert

Western Cape

R.D. Beck

Zambia

D. Muma

Zimbabwe

S. Matutu

Zululand

C.W. Mienie

Corresponding Members of Council

Australia: I.J. Corrans, R.J. Dippenaar, A. Croll,
C. Workman-Davies

Austria: H. Wagner

Botswana: S.D. Williams

United Kingdom: J.J.L. Cilliers, N.A. Barcza

USA: J.M.M. Rendu, P.C. Pistorius

PAST PRESIDENTS

*Deceased

* W. Bettel (1894–1895)

* A.F. Crosse (1895–1896)

* W.R. Feldtmann (1896–1897)

* C. Butters (1897–1898)

* J. Loevy (1898–1899)

* J.R. Williams (1899–1903)

* S.H. Pearce (1903–1904)

* W.A. Caldecott (1904–1905)

* W. Cullen (1905–1906)

* E.H. Johnson (1906–1907)

* J. Yates (1907–1908)

* R.G. Bevington (1908–1909)

* A. McA. Johnston (1909–1910)

* J. Moir (1910–1911)

* C.B. Saner (1911–1912)

* W.R. Dowling (1912–1913)

* A. Richardson (1913–1914)

* G.H. Stanley (1914–1915)

* J.E. Thomas (1915–1916)

* J.A. Wilkinson (1916–1917)

* G. Hildick-Smith (1917–1918)

* H.S. Meyer (1918–1919)

* J. Gray (1919–1920)

* J. Chilton (1920–1921)

* F. Wartenweiler (1921–1922)

* G.A. Watermeyer (1922–1923)

* F.W. Watson (1923–1924)

* C.J. Gray (1924–1925)

* H.A. White (1925–1926)

* H.R. Adam (1926–1927)

* Sir Robert Kotze (1927–1928)

* J.A. Woodburn (1928–1929)

* H. Pirow (1929–1930)

* J. Henderson (1930–1931)

* A. King (1931–1932)

* V. Nimmo-Dewar (1932–1933)

* P.N. Lategan (1933–1934)

* E.C. Ranson (1934–1935)

* R.A. Flugge-De-Smidt

(1935–1936)

* T.K. Prentice (1936–1937)

* R.S.G. Stokes (1937–1938)

* P.E. Hall (1938–1939)

* E.H.A. Joseph (1939–1940)

* J.H. Dobson (1940–1941)

* Theo Meyer (1941–1942)

* John V. Muller (1942–1943)

* C. Biccard Jeppe (1943–1944)

* P.J. Louis Bok (1944–1945)

* J.T. McIntyre (1945–1946)

* M. Falcon (1946–1947)

* A. Clemens (1947–1948)

* F.G. Hill (1948–1949)

* O.A.E. Jackson (1949–1950)

* W.E. Gooday (1950–1951)

* C.J. Irving (1951–1952)

* D.D. Stitt (1952–1953)

* M.C.G. Meyer (1953–1954)

* L.A. Bushell (1954–1955)

* H. Britten (1955–1956)

* Wm. Bleloch (1956–1957)

* H. Simon (1957–1958)

* M. Barcza (1958–1959)

* R.J. Adamson (1959–1960)

* W.S. Findlay (1960–1961)

* D.G. Maxwell (1961–1962)

* J. de V. Lambrechts (1962–1963)

* J.F. Reid (1963–1964)

* D.M. Jamieson (1964–1965)

* H.E. Cross (1965–1966)

* D. Gordon Jones (1966–1967)

* P. Lambooy (1967–1968)

* R.C.J. Goode (1968–1969)

* J.K.E. Douglas (1969–1970)

* V.C. Robinson (1970–1971)

* D.D. Howat (1971–1972)

* J.P. Hugo (1972–1973)

* P.W.J. van Rensburg

(1973–1974)

* R.P. Plewman (1974–1975)

* R.E. Robinson (1975–1976)

* M.D.G. Salamon (1976–1977)

* P.A. Von Wielligh (1977–1978)

* M.G. Atmore (1978–1979)

* D.A. Viljoen (1979–1980)

* P.R. Jochens (1980–1981)

* G.Y. Nisbet (1981–1982)

A.N. Brown (1982–1983)

* R.P. King (1983–1984)

J.D. Austin (1984–1985)

H.E. James (1985–1986)

H. Wagner (1986–1987)

* B.C. Alberts (1987–1988)

C.E. Fivaz (1988–1989)

O.K.H. Steffen (1989–1990)

* H.G. Mosenthal (1990–1991)

R.D. Beck (1991–1992)

* J.P. Hoffman (1992–1993)

* H. Scott-Russell (1993–1994)

J.A. Cruise (1994–1995)

D.A.J. Ross-Watt (1995–1996)

N.A. Barcza (1996–1997)

* R.P. Mohring (1997–1998)

J.R. Dixon (1998–1999)

M.H. Rogers (1999–2000)

L.A. Cramer (2000–2001)

* A.A.B. Douglas (2001–2002)

S.J. Ramokgopa (2002–2003)

T.R. Stacey (2003–2004)

F.M.G. Egerton (2004–2005)

W.H. van Niekerk (2005–2006)

R.P.H. Willis (2006–2007)

R.G.B. Pickering (2007–2008)

A.M. Garbers-Craig (2008–2009)

J.C. Ngoma (2009–2010)

G.V.R. Landman (2010–2011)

J.N. van der Merwe (2011–2012)

G.L. Smith (2012–2013)

M. Dworzanowski (2013–2014)

J.L. Porter (2014–2015)

R.T. Jones (2015–2016)

C. Musingwini (2016–2017)

Honorary Legal Advisers

Scop Incorporated

Auditors

Genesis Chartered Accountants

Secretaries

The Southern African Institute of Mining and Metallurgy

Fifth Floor, Chamber of Mines Building

5 Hollard Street, Johannesburg 2001 • P.O. Box 61127, Marshalltown 2107

Telephone (011) 834-1273/7 • Fax (011) 838-5923 or (011) 833-8156

E-mail: journal@saimm.co.za

Editorial Board

R.D. Beck
P. den Hoed
M. Dworzanowski
B. Genc
M.F. Handley
R.T. Jones
W.C. Joughin
J.A. Luckmann
C. Musingwini
S. Ndlovu
J.H. Potgieter
T.R. Stacey
M. Tlala

Editorial Consultant

D. Tudor

Typeset and Published by

The Southern African Institute of Mining and Metallurgy
P.O. Box 61127
Marshalltown 2107
Telephone (011) 834-1273/7
Fax (011) 838-5923
E-mail: journal@saimm.co.za

Printed by

Camera Press, Johannesburg

Advertising Representative

Barbara Spence
Avenue Advertising
Telephone (011) 463-7940
E-mail: barbara@avenue.co.za
ISSN 2225-6253 (print)
ISSN 2411-9717 (online)



Directory of Open Access Journals



THE INSTITUTE, AS A BODY, IS NOT RESPONSIBLE FOR THE STATEMENTS AND OPINIONS ADVANCED IN ANY OF ITS PUBLICATIONS.

Copyright © 2018 by The Southern African Institute of Mining and Metallurgy. All rights reserved. Multiple copying of the contents of this publication or parts thereof without permission is in breach of copyright, but permission is hereby given for the copying of titles and abstracts of papers and names of authors. Permission to copy illustrations and short extracts from the text of individual contributions is usually given upon written application to the Institute, provided that the source (and where appropriate, the copyright) is acknowledged. Apart from any fair dealing for the purposes of review or criticism under **The Copyright Act no. 98, 1978, Section 12**, of the Republic of South Africa, a single copy of an article may be supplied by a library for the purposes of research or private study. No part of this publication may be reproduced, stored in a retrieval system, or transmitted in any form or by any means without the prior permission of the publishers. **Multiple copying of the contents of the publication without permission is always illegal.**

U.S. Copyright Law applicable to users in the U.S.A.

The appearance of the statement of copyright at the bottom of the first page of an article appearing in this journal indicates that the copyright holder consents to the making of copies of the article for personal or internal use. This consent is given on condition that the copier pays the stated fee for each copy of a paper beyond that permitted by Section 107 or 108 of the U.S. Copyright Law. The fee is to be paid through the Copyright Clearance Center, Inc., Operations Center, P.O. Box 765, Schenectady, New York 12301, U.S.A. This consent does not extend to other kinds of copying, such as copying for general distribution, for advertising or promotional purposes, for creating new collective works, or for resale.



SAIMM

JOURNAL OF THE SOUTHERN AFRICAN INSTITUTE OF MINING AND METALLURGY

VOLUME 118 NO. 2 FEBRUARY 2018

Contents

Journal Comment

by D. Groot v

President's Corner: Education for careers that do not yet exist

by S. Ndlovu vii

Book review: Production, Safety and Teamwork in a Deep-level Mining Workplace

by J. McLuskie vi

Discussion on the paper: Effect of frother and depressant interaction on flotation of Great Dyke PGM ore

by J.M.W. Mackenzie 192

URANIUM 2017 INTERNATIONAL CONFERENCE

Uranium recovery from high-chloride sulphate leach solutions: A cost trade-off study of using treated water vs. saline water as make-up water

by E.L. Forner, S.J. Archer, V.E. Coetzee, K. Soldenhoff, and J. Quinn 95

The opportunity to utilize high-salinity water was evaluated using two uranium solvent-extraction (SX) recovery options. A high-level techno-financial trade-off study revealed that a flow sheet incorporating a high-salinity water source is an economical option under certain conditions.

Uranium circuit development for a West African polymetallic deposit

by A.J. du Toit, and S.J. Archer 103

Process flow sheet development work that was conducted in 2013 on a polymetallic deposit located in West Africa is presented. The work established that copper and silver were associated with the sulphides and could be separated by means of flotation. The results of a trade-off study to evaluate alkali and acid processing routes for the recovery of uranium are presented.

Optimization of the Rössing countercurrent decantation circuit for high-calc ore

by C.J. Anderson, S.L. Rabie, and N.K. Jansen van Rensburg 109

High-calc ore was found to be associated with poor settling performance in the countercurrent decantation CCD circuit. Thickener feed density and process control were identified as key areas for optimizing performance. Results of certain modifications to the thickener feedwell and the new automated control system are currently being evaluated at Rössing.

Polythionate formation during uranium recovery from sulphide flotation concentrate

by V. Yahorava and V. Bazhko 119

Uranium recovery by resin-in-pulp (RIP) from sulphide-bearing material has been found to be adversely affected by polythionate formation due to partial oxidation of sulphide minerals. This study was undertaken to identify whether polythionates are formed during the ore preparation, leaching, or ion exchange recovery steps. A number of practical measures were identified that could prompt the development of mitigation strategies to reduce or avoid the formation of polythionates on commercial plants.

Behaviour and fate of uranium in a high-level nuclear waste processing system

by J. Addai-Mensah and H. Musiyarira 125

Some of the tactical investigations into uranium behaviour and interactions with sodium aluminosilicate phases in the processing of high-level nuclear waste at the US Department of Energy's Savannah River tank farm operations are reported. Some reasons for evaporator fouling and major criticality concerns were identified.

International Advisory Board

R. Dimitrakopoulos, *McGill University, Canada*
D. Dreisinger, *University of British Columbia, Canada*
E. Esterhuizen, *NIOSH Research Organization, USA*
H. Mitri, *McGill University, Canada*
M.J. Nicol, *Murdoch University, Australia*
E. Topal, *Curtin University, Australia*





Contents (continued)

PAPERS OF GENERAL INTEREST

- 3D analysis of longwall face stability in thick coal seams**
by G. Song and Y.P. Chugh 131
The mining of two adjacent longwall faces was simulated using 3D nonlinear analysis to better understand the stress distribution around excavations and development of failed zones on an active longwall face.
- Production of metallurgical-grade silicon from Egyptian quartz**
by H.H.M. Ali, M.H. El-Sadek, M.B. Morsi, K.A. El-Barawy, and R.M. Abou-Shahba 143
A number of parameters that affect the production of metallurgical-grade silicon (MG-Si) in a semi-pilot submerged arc furnace were investigated. A maximum silicon recovery of about 75% with a product purity of about 97% silicon was achieved under the optimum experimental conditions.
- Prevention of spontaneous combustion in coal drifts using a lining material: a case study of the Tuncbilek Omerler underground mine, Turkey**
by M.V. Ozdogan, G. Turan, D. Karakus, A.H. Onur G. Konak, and E. Yalcin 149
A lining material for coating the coal surface in order to prevent coal fires was designed under laboratory conditions. It was found that a 7–8 mm thick application of a cement plus fly ash plus water mixture formed an air-impermeable layer and maintained its structure in underground mine environment.
- Modelling coal pillar stability from mine survey plans in a geographic information system**
by M. Mathey 157
A practical method for analysing the individual stability of large numbers of pillars in bord-and-pillar workings based on mine survey plans is outlined. The proposed pillar stability model is applied to real mining situations, including a case of pillar collapse, so as to verify the validity of the technique.
- Integration of commodity price uncertainty in long-term open pit mine production planning by using an imperialist competitive algorithm**
by M. Mokhtarian Asl and J. Sattarvand 165
This paper describes a new stochastic optimization procedure based on the imperialist competitive algorithm (ICA) for long-term production planning of open pit mines under conditions of commodity price or market uncertainty. The proposed approach was tested on a real-world copper mine, and the results showed that ICA could be efficiently applied to stochastic production planning of a real mine.
- Accounting for a spatial trend in fine-scale ground-penetrating radar data: a comparative case study**
by Y. Dagasan, O. Erten, and E. Topal 173
The performance of universal kriging, intrinsic random function of order k , and ordinary kriging methods was compared on densely sampled ground penetrating radar (GPR) data to assist in delineation of the ore and waste contact within a laterite-type bauxite deposit. The results show that all three algorithms produced satisfactory and similar results.
- Towards safer mining: scientific measurement approaches that could be applied for imaging and locating the buried container lamp-room at Lily mine**
by I. Hussain, F.T. Cawood, and S. Ali 185
Academic and research entities at the University of the Witwatersrand were asked for suggestions as to how to locate the buried container lamp-room. Based on the responses and a literature search, a preliminary conceptual study was undertaken to identify which technologies were likely to be successful.

Journal Comment



Discussions involving the 92nd element in the periodic table, uranium, tend to elicit mixed reactions. Although uranium plays a key role in the production of medical isotopes, it has the dark side of being the power in highly destructive nuclear weaponry. Strong positive and negative viewpoints emerge when nuclear reactors and their wastes are considered. Fortunately, the Uranium 2017 International Conference that took place in Swakopmund, Namibia (11 to 15 September 2017) did not generate quite such strongly opposed views.

The conference, with the theme *Extraction and Applications of Uranium – Present and Future*, brought together professionals in the uranium industry. A broad range of topics was discussed, ranging from mining to some of the applications of uranium, and included safety, as well as post-operations closure and remediation issues. Innovations in the extraction and applications of uranium are constantly being made, and the conference provided a platform for the discussion of advances and for generating new ideas.

We were fortunate in being able to organize the conference in cooperation with the International Atomic Energy Agency (IAEA), the Namibia University of Science and Technology (NUST), the Namibian Uranium Institute, and the Canadian Institute for Mining, Metallurgy and Petroleum (CIM). The IAEA sponsored two delegates from the region. Generous support was received from our sponsors Protea Chemicals Namibia, CiDRA Minerals Processing, AECI Mining & Chemical Services, AEL Mining Services, DRA Projects SA, IMP Automation SA, Naminsol Namibia, Bannerman Resources, Langer Heinrich Uranium, Rössing Uranium, MEI Media, ALTA Metallurgical Services, Lanxess Ltd, Puro-lite Ltd, and SNF Floerger SA.

The conference started with a day where delegates could choose between a short course on *Uranium Ore Processing* led by the well-known Alan Taylor (ALTA Metallurgical Services), or a technical visit. The visit *Viewing the geology of the alaskite mineralisation in the lower Swakop River* was led by Professor Judith Kinnaird and Paul Nex (Wits University), and included a visit to the Bannerman Resources demonstration plant. The day ended with a well-attended cocktail function. The next two days (Tuesday and Wednesday) were full days, with a combined plenary session for keynote lectures each day, followed by two parallel sessions. The last two days offered further technical visits to Rössing Uranium Ltd and to the Langer Heinrich uranium plant.

Swakopmund is a holiday town, in an interesting position: it lies between the shore of the Atlantic Ocean on the western side and the fascinating Namib Desert on the east. Its German origins are still very visible, dating from the early 20th century. For instance, the conference venue was the original Swakopmund railway station.

The conference dinner was held on the Tuesday evening, with the Namib desert providing an interesting and unusual setting. A caravan of 4x4 vehicles took us along the Swakop river to our venue. Fortunately, the cold desert air was mitigated by good company, food, patio heaters, blankets, and fun entertainment.

Attendance was good, with more than a hundred delegates, of which 15 were from the UK, Australia and Europe. Participation from the local uranium mines was disappointing, but understandable due to the extremely tight financial environment they are currently operating in.

Opening addresses were presented by the Namibian Deputy Minister for Mines and Energy, the Hon. Kornelia Shilunga, Professor Selo Ndlovu (SAIMM President), Mr Hilifa Mbako (Namibian Uranium Association Chairman) and Professor Tjama Tjivikua (NUST Vice Chancellor). Four well-received keynote lectures were delivered:

- *Remaining uranium resources: where and how much?* Dr Martin Fairclough, IAEA
- *Uranium in Namibia – past, present and future.* Mr Werner Duvenhage, Rössing Uranium Ltd
- *The Namibian Uranium Association, the environment, and sustainable development.* Dr Gabi Schneider, Namibian Uranium Institute
- *Will fission Mo-99 production be seriously impacted through other efforts to diversify the supply of Mo-99?* Dr Jan-Rijn Zeevaart, NECSA.

In addition, 40 technical papers and 5 poster papers rounded out the technical content of the conference.

This edition of the *Journal* carries a vignette of selected contributions from the conference. These focus mainly on metallurgical processing – as did the conference – without neglecting the broader issues such as the safe containment of nuclear waste. While the processes for leaching (alkaline or acidic), concentration and purification, and recovery are well established, challenges still abound, as may be seen from these papers. Complex mineralization, as well as process water, often present considerable impediments to the processing circuits. Several conference papers discussed the possibilities of using saline waters, and even seawater. The high chloride levels impact on the separation processes and on plant equipment, and the papers discuss a number of innovations to meet these challenges. Other topics include improved on-line measurements for plant control and the optimization of plant equipment.

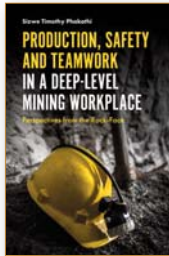
At present uranium mining is under pressure due to low prices and processing challenges. However, if this conference was a stethoscope gauging the health of the uranium industry, it indicated a still strongly beating heart.



The exhibition area at the conference

D. Groot

Book review: Production, Safety and Teamwork in a Deep-level Mining Workplace



In almost any industry, the day-to-day experiences of workers directly shape production processes. Those experiences are of fundamental importance to a range of managerial concerns, including organizational behaviour and human resource management, organizational safety and risk management, production systems, work relationships, and change management. Yet they are too often overlooked by the executives and managers who design management strategies.

In this book, Sizwe Phakathi, Head of Safety and Sustainable Development at the Chamber of Mines, addresses such issues head-on, providing insights into the underlying social, human, managerial, and organizational processes that shape workers' orientations towards reorganization of work, production, safety, teamwork, and work relationships. Through an in-depth study of a deep-level mining workplace, Phakathi brings to the fore the realities of how work processes shape the actions of frontline teams, production supervisors, and managers. He points out how these realities trigger the informal work practice of making a plan, which is an indispensable organizational tactic for production, safety, teamwork, and work relationships in the mining workplace. In the process, he highlights frontline miners' perspectives of managing, balancing and coping with the competing demands of physically challenging work, production, safety, and team dynamics while at the rock-face.

This book will help practitioners, policy-makers, and researchers to understand the factors influencing work processes, production, safety, teamwork, and work relationships, not only in a mining workplace but more generally as well. The insights it provides into the importance of day-to-day working experiences will help them to improve organizational, employee, and team performance.

The book can be purchased through Emerald Book Store at a 30% discount until April.
<http://books.emeraldinsight.com/page/detail/Production-Safety-and-Teamwork-in-a-DeepLevel-Mining-Workplace/?k=9781787145641>

James McLuskie, one-time operations director of Western Deep Levels Ltd and Elandsrand Gold Mining Co Ltd, has provided a brief review and critique of this book.

Before I left deep-level mining in 1995 I had reached the conclusion that training based on "do as I say" and rote learning of standards was not sufficient. We needed to add risk assessment and evaluation of alternatives based on experience. In many ways standards should be a guideline. Of course, the government could never accept this and so you have the situation of *planisa* (making a plan) by frontline teams and collusion by supervisors and managers.

I agree that strict adherence to standards is not always possible, or desirable. *Planisa* is a must. Standard practices or standard operating procedures assume standard conditions. Conditions underground in a deep-level mine are seldom, if ever, standard. What is needed is a set of basic skills applied to a range of situations that change---just like a successful sports team.

Regarding organizational culture, I agree that the old culture of top-down authoritarianism was neither healthy nor effective and that teamwork and mutual respect were vital. I thought that I had tried over a period of 5 years to change the organizational culture from the old to a new one. I do not believe I even scratched the surface in my attempts, despite having a great deal of positional power. Culture change requires top-down drive but it also requires acceptance, belief and ability at all levels. The story in the book of the different results obtained by two different shift bosses is a telling one. Individuals do make differences and some styles are difficult, if not impossible to change. I have had personal experience of this.

It was illuminating for me in the book that despite all the talk of cost pressure, the one shift boss was always able to get the required timber and other supplies on time. So, is there a shortage of money or of organization? There is much emphasis placed on shortage of tools and equipment because of cost pressure. In my day, cost pressure was felt more at top and senior management level: If you got your production safely you were fine and costs were secondary.

Self-directed Work Teams [SDWT] is an old idea and one that in itself indicates how long it takes to change culture. Nevertheless it is still a good idea and the chapter on SDWT was a good one. It is a pity, however, that in the training course the issue of 'planisa' and the condonement of departure from standards was not tackled.

In conclusion the book discussed many valid issues, the most important being the identified need to depart from standards in order to achieve organizational and personal goals. The same applies in any team sport. Having identified the issues the author spends very little time proposing solutions. There were many references to management being at fault but they were too generalized to be of much help. However, the concluding chapter pulls together key issues raised in the book and does propose some solutions and indeed that there are many valid issues.

J. McLuskie



Education for careers that do not yet exist



Universities have opened their doors for the new academic year, welcoming both the old and the new students. Every year there is an increase in demand for university places as young people look into acquiring a tertiary education as a means of securing and empowering their future. Following the newly announced free education dispensation by the South African government, university placements promise to be much more highly competitive as more students are expected to take advantage of this dispensation to gain the academic skills that will form the foundation for their careers.

The importance of higher education cannot be overemphasized. Countries look to universities for the capacity and skills that drive local economies, lead effective governments, support civil society, and at the same time guide very important decisions, which affect entire societies. University education is expected to enable individuals to expand their knowledge, express their thoughts and ideas clearly, gain higher level skills, increase their understanding of the world and their community, and thus contribute meaningfully to the development of the country's economy. But, most importantly, the resultant graduates should be dynamic and easily adapt to the changing needs of the industry that they will serve. This aspect has become more significant and relevant when considering the modern-day technological developments and industrial changes.

The advent of big-data technologies, the Industrial Internet of Things or the fourth industrial revolution, prompts the question of whether the graduates currently being produced in the engineering fields, including our very own area of mining and metallurgical engineering, are geared for the changes that are inevitable in the industry that they will serve. Technological innovations and disruptors, for example robotics, self-driven cars and virtual assistants, are emerging at such a rapid pace that some of the mining and metallurgical career roles we know today will inevitably become obsolete, while new jobs that currently do not yet exist will be created. The challenge then becomes the preparation for, and the development of skills for, career roles that will exist only in the future.

Although predicting future trends and industries in engineering and technology is a challenging task, an attempt to articulate a vision of future technological trends is essential so that we can produce graduates who can seamlessly transition to the future world. Thus, the approach to teaching and learning as applied in the past needs to change as it cannot be expected to fully satisfy the needs of mines of the future. There is a need to restructure and enhance the education systems in order to bring both the real modern-day and the possible futuristic virtual world into the classroom. Immersing the students in virtual learning environments can help to bridge the gap between the abstract university learning experience and what will be expected or required for the future. The sheer pace of technological advances can make digital competency difficult to teach; however, the idea is not to turn engineers into data scientists, but instead to equip them with sufficient knowledge and skills in the relevant areas to enable them to function meaningfully in their primary roles in the new technology-based environment.

The change in the learning approach should not only apply to university education but should also be considered for the graduate learner programmes in the mining sector. While the mining and metallurgical industry is evolving and changing, graduate learner programmes have remained virtually the same. Graduate learners need to be trained on systems that will enable them to offer a meaningful contribution in the new environments. It is, therefore, heartening to see that the SAIMM Young Professionals Council (YPC) is taking a lead in this. The YPC is working on developing a new graduate learner programme that is in line with the current technological industry revolutions. Such initiatives are meaningful, noteworthy steps towards embracing the developments and changes in the mining sector.

Clearly, both the institutes of learning and the mining industry need to realize that it's not a case of 'business as usual' any more. A whole new level of system thinking is required to ensure that the industry is not blindsided by the future.

S. Ndlovu
President, SAIMM

Application of Multiple Point Statistics to Mineral Resource Estimation—School

OBJECTIVES

The course is aimed at providing geostatistics practitioners and mineral resource evaluators with newly developed skills, knowledge and competency for application in the evaluation and classification of Mineral Resources. The development of these skills is seen as being of strategic importance.

To increase the knowledge and competency amongst technical staff of the application of Multiple Point Statistics in Mineral Resources estimation and evaluation.

23–26 April 2018

**School of Mining Engineering at the
University of the Witwatersrand**

Lecturers:

Prof. Philippe Renard and Prof. Julian Straubhaar



Philippe Renard, Prof. Dr. Eng., (born 1967), Professor of Hydrogeology at the University of Neuchatel, Switzerland (2006-present), PhD from École des Mines de Paris in 1996 (honours), Lecturer in hydrogeology at the Swiss Federal Institute of Technology Zurich (ETHZ) from 1997 to 2001. Water supply engineer in Kankan, Guinea for the French ministry of Cooperation from 1992 to 1993. His research focuses on groundwater hydraulics in

porous and fractured rocks, upscaling techniques, and innovative geostatistical methods for uncertainty quantification. He has been working on the regional modeling of saltwater intrusions in Cyprus and Tunisia. He has participated to numerous international projects such as the evaluation of the groundwater resources in the north-west of the Sahara (Mauritania) for the world bank. He was editor of Hydrogeology Journal, president of the geoENVia association and is currently a member of the leadership team of the Groundwater Committee of the International Association of Hydraulic Research (IAHR). He is the author of more than 100 scientific articles in international journals and covering a wide range of topics. His current research is focused on the development of multiple-point statistics methods as well as pseudo genetic approaches for heterogeneity modeling, uncertainty quantification and inverse groundwater modeling.

Julien Straubhaar, Prof. Dr., born in 1979, senior researcher in the stochastic hydrogeology group of the University of Neuchâtel. He holds a PhD in applied mathematics (University of Neuchâtel, 2007), with a focus on numerical methods for partial differential equations and in particular preconditioners for linear equations. His current research mainly deals with geostatistics and inverse methods. He is author of more than 20 scientific papers published in international journals and he has been a reviewer for several scientific journals. Over the last ten years, he has been heavily involved in the development of parallel multiple-point statistics algorithms, in particular Impala and Deesse softwares, which are available in professional products.



WHO SHOULD ATTEND

The course content will be of interest to:

- Geostatisticians
- Geologists
- Surveyors
- Samplers
- MRM practitioners
- Mineral resource technicians.

For further information contact:

Head of Conferencing: Camielah Jardine, SAIMM · P O Box 61127, Marshalltown 2107
Tel: (011) 834-1273/7 · Fax: (011) 833-8156 or (011) 838-5923
E-mail: camielah@saimm.co.za · Website: <http://www.saimm.co.za>



Uranium recovery from high-chloride sulphate leach solutions: A cost trade-off study of using treated water vs. saline water as make-up water

by E.L. Forner*, S.J. Archer*, V.E. Coetzee*, K. Soldenhoff†, and J. Quinn†

Synopsis

A well-established technology for uranium recovery comprises sulphuric acid leaching, followed by solvent extraction (SX) with tertiary amines such as Alamine 336. The inherent challenge with uranium processing in arid mining regions, such as Namibia and Australia, is that good quality water sources are in short supply. Supplying water through a desalination facility is a costly solution, and the use of high-salinity water, for example, seawater or saline bore water, could provide an alternative option. However, the presence of chlorides above 3 g/L in the pregnant leach solution hinders uranium loading on the conventional tertiary amine solvent extraction organic. In this paper, the opportunity to utilize high-salinity water (20 g/L Cl⁻) as make-up water in the plant is evaluated using two uranium solvent-extraction (SX) recovery options: Option 1 employs a large seawater reverse-osmosis treatment plant for the supply of fresh water throughout the process, together with Alamine 336 organic for SX; option 2 uses saline water for the front-end water requirements, with the chloride-tolerant Cyanex 272 organic for purification and a smaller reverse osmosis plant for fresh water supply downstream of SX. The main focus is the selection of materials of construction as well as the capital and operating expenditure differentials for water treatment and front-end unit operations. A high-level techno-financial trade-off study using cost differentials revealed that a flow sheet incorporating a high-salinity water source is an economical option when mild steel rubber-lined platework and super-duplex SAF2507 steel mechanicals are used.

Keywords

uranium recovery, solvent extraction, chloride tolerance, high-salinity.

Introduction and literature review

There is an inherent challenge associated with mining in arid regions, such as Namibia and Australia, in identifying a clean source of water for use in the processing plant. Alternative sources such as borehole water or seawater tend to have a high salt content. The presence of chloride, in particular, is problematic because of its deleterious impact on uranium solvent extraction with conventional long-chain tertiary amine reagents such as Alamine 336 (Morais and Ladeira, 2008; Soldenhoff *et al.*, 2000).

Research has been ongoing to identify solvent extraction (SX) processes that are chloride-tolerant. Different reagents have been proposed, including:

- ▶ Mixed reagents, di-(2-ethylhexyl)phosphoric acid and tertiary amine (DEHPA/Alamine 336) (Quinn,

Wilkins, and Soldenhoff,; Soldenhoff *et al.*, 2000, 2005)

- ▶ Solvating reagent, based on phosphine oxide blends (Dudley and Sumner, 2014)
- ▶ Single reagent, bis(2,4,4-trimethylpentyl)phosphoric acid (Cyanex 272) (Soldenhoff and Quinn, 2015).

The DEHPA/Alamine 336 process has been applied at industrial scale (Ballestrin *et al.*, 2014). Sodium carbonate is used for stripping. Challenges associated with this process include crud formation due to iron carry-over to the strip circuit, solvent loss, and third-phase formation (Ballestrin *et al.*, 2014; Quinn, Wilkins, and Soldenhoff, 2013). Sulphuric acid stripping has been tested with this reagent mix, but the concentration of acid required is significantly greater than that used in conventional strong-acid strip circuits using tertiary amines (Soldenhoff *et al.*, 2005).

The application of phosphine oxide-type reagents, such as tri-octyl phosphine oxide (TOPO), has also been reported. These reagents are not amenable to sulphuric acid stripping, and ammonium sulphate has been suggested (Dudley and Sumner, 2014).

A study on the application of Cyanex 272 in this context has shown that high uranium loadings can be achieved at chloride concentrations commensurate with those found in seawater. Furthermore, the solvent is selective for uranium over ferric and can be stripped with 4 M H₂SO₄ (Quinn and Soldenhoff, 2015). A comparative study examining these options with respect to uranium loading, selectivity over ferric ion, response to strong acid stripping, and

* DRA Projects, South Africa.

† ANSTO Minerals, South Africa.

© The Southern African Institute of Mining and Metallurgy, 2018. ISSN 2225-6253. This paper was first presented at the Uranium 2017 International Conference, 12–13 September 2017, Swakopmund Hotel, Swakopmund, Namibia..

Uranium recovery from high chloride sulphate leach solutions

requirement for phase modifier showed that Cyanex 272 performed best against these process-relevant criteria (Soldenhoff and Quinn, 2015).

The presence of chloride has wide-ranging implications for the overall hydrometallurgical flow sheet, apart from its impact on the SX process. The broader implications of operating in a high chloride environment have not previously been considered in detail. In this paper, we examine the relative merits of using a conventional SX process for uranium based on tertiary amines, coupled with a water treatment plant to remove chloride, as opposed to using a chloride-tolerant SX process based on Cyanex 272 coupled with high-salinity process water. The relative merits of these two approaches are compared with reference to the implications for the capital and operating expenditure (CAPEX and OPEX).

Comparison of flow sheets

Two uranium SX recovery circuits were modelled and compared. The differences in the overall flow sheets are presented in Figure 1 and Figure 2.

1. Option 1 (conventional uranium SX with treated water) – employs a large seawater reverse osmosis (SWRO) treatment plant for the supply of fresh water throughout the entire process, together with the use of standard Alamine 336 organic in the SX unit operation.
2. Option 2 (chloride-tolerant uranium SX with saline water) – uses saline/seawater as the water source for the front-end unit operations, together with Cyanex 272 organic for extraction of uranium. Key unit operations downstream of SX still necessitate a SWRO for the supply of treated water, although on a significantly smaller scale. The RO water treatment plant could have been even smaller, essentially just for product washing as SX stripping can be done with seawater and H_2SO_4 . However, the nanofiltration

circuit would need to be tested for acid recovery in high-chloride solutions. In this option, a chloride concentration in the process water in the order of 20 g/L Cl^- was modelled, similar to that in seawater. It was assumed that there is no chloride contribution from the ore. Peroxide precipitation was modelled for both flow sheets to facilitate comparison of the two flowsheets on the same basis.

One of the main factors affecting the selection of the unit operation for uranium purification is the uranium tenor of the pregnant leach solution (PLS). An ore head grade of 650 ppm U_3O_8 , typical of areas such as Namibia, was used for this trade-off. After leaching, with a uranium recovery of about 89%, the PLS typically contains 0.52 g/L U_3O_8 . According to Brown and Haydon (1979), SX is economically favoured over ion exchange (IX) at PLS tenors greater than 0.9 g/L U_3O_8 , whereas IX is more economical below 0.35 g/L U_3O_8 . Additionally, at higher uranium concentrations, SX is beneficial after countercurrent decantation (CCD) (van Tonder and Kotze, 2007). Accordingly, the overflow from the CCD in the two flow sheets is recycled to leach to build the PLS uranium tenor in order to warrant the use of SX instead of IX, and the overflow from the post-leach thickener proceeds to SX at a higher tenor of 0.83 g/L U_3O_8 .

In this paper, we traded off the materials of construction (MoC) for two treated water options (1a and 1b) and two seawater options (2a and 2b), shown in Figure 3. Option 1a considered mild steel rubber-lined (MSRL) platework and represented the basis of comparison. Option 2a considered the equivalent materials of construction for circuits containing high chlorides (20 g/L Cl^-). The other two options (1b and 2b) offered more corrosion-resistant MoC for mechanical equipment and platework.

CAPEX differentials

Materials selection and corrosion resistance

Materials selection for high-saline applications with soluble

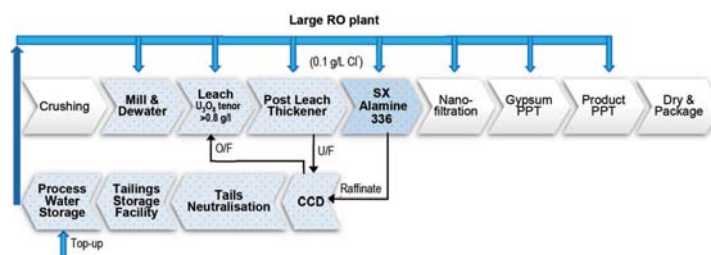


Figure 1—Option 1 (treated water) flow sheet highlighting costed differential unit operations

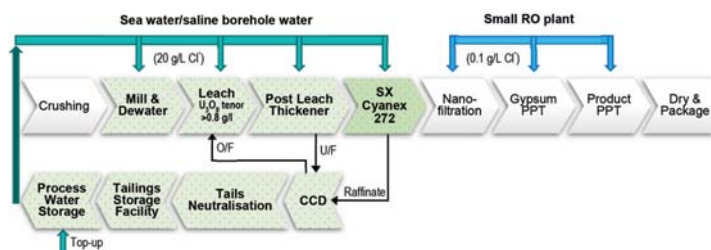


Figure 2—Option 2 (seawater) flow sheet highlighting costed differential unit operations

Uranium recovery from high chloride sulphate leach solutions

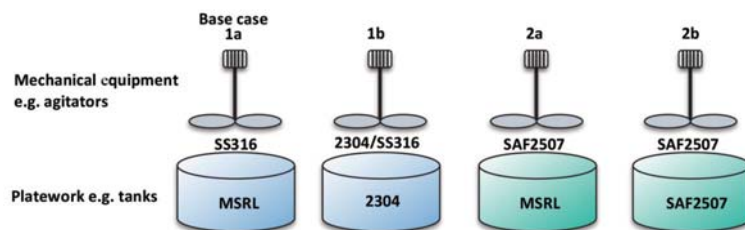


Figure 3—Four options evaluated in terms of capital expenditure (CAPEX) and operating expenditure (OPEX)

salts/sulphates depends on many factors, including salt concentration, acid concentration/pH, materials composition, compatibility, and strength, processing characteristics (abrasion), as well as cost and availability. Newer high-alloy stainless and duplex steels, which were unavailable a few decades ago, are now commonplace as MoC.

Soluble salts, particularly chlorides and sulphates, initiate and accelerate corrosion of steel, becoming deeply embedded within the iron corrosion products. Furthermore, when selecting linings for carbon- or mild steel tanks, cognisance needs to be taken of operating conditions. In this section, the factors influencing material selection are reviewed. The benefits and limitations associated with common steels and tank linings implemented in modern-day hydrometallurgical applications are also discussed.

- **Pitting resistance equivalent number (PREN)**—PREN is a theoretical way of comparing and ranking the pitting corrosion resistance of various types of stainless steels, based on their contents of chrome, nickel, and molybdenum. Steels with PREN less than 32 are generally not considered corrosion-resistant in seawater. According to the empirical relationship (Equation [1]), the pitting resistance of stainless steel alloys increases as the contents of these three alloying elements are raised. The typical compositions of some stainless steels incorporated in this study are given in Table I, which also provides data on their mechanical properties (Goldswain and Rogers, 2017a), PREN, and critical pitting temperature (CPT).

$$\text{PREN} = \% \text{Cr} + 3.3 \times \% \text{Mo} + 16 \times \% \text{Ni} \quad [1]$$

- **Critical pitting temperature (CPT)**—There is no single measure of corrosion resistance and PREN alone cannot be used to predict whether a particular grade will be suitable for a given application where pitting

corrosion may be a hazard. Hence, an additional means of ranking steels is used, namely the CPT, which uses an electrochemical method, ASTM G150, in 1 M NaCl. In this test, the temperature is determined when pitting starts to develop (Outokumpu, 2013).

- **Steel mechanical strength**—Duplex stainless steels have roughly twice the yield strength of their counterpart austenitic grades. This allows equipment designers to use thinner gauge material for vessel construction, resulting in large savings in the manufacturing phase. The tank walls can be significantly thinner, yet safe in use (Goldswain and Rogers, 2017b).
- **Rubber linings and epoxy coatings are subject to certain limitations in their application:**
 - Contaminants, such as soluble salts on a steel surface, can prevent bonding during application and establish osmotic driving forces promoting water permeation and blistering of rubber lining
 - Organic coatings like natural rubber dissolve and swell in the presence of the organic solvents used in SX circuits; therefore, no rubber-lined platework is used in SX
 - Organic coatings and solvents are also susceptible to thermal degradation. The uranium circuit is therefore designed for temperatures less than 40°C.

Materials selection and costs

Each data point shown in Figure 4 represents the cost ranking of a fabricated tank, at a specific size/volume, in a selected material, relative to a 9 m³ mild steel tank. Fabrication implies the cost of material and the cost of labour has been accounted for. Typically, the fabricated cost is twice the material cost (Goldswain and Rogers, 2017b).

Table I

Comparative material compositions (mass %), PREN, CPT corrosion resistance (°C), and mechanical strength (0.2% proof MPa) for duplex and austenitic steels (Outokumpu, 2013)

MoC	Type	C (%)	N (%)	Cr (%)	Ni (%)	Mo (%)	Other	PREN -	CPT (°C)	Yield strength (P _{0.2} MPa)
MS epoxy	Ferritic	0.25					99Fe	N/A		250
MSRL	Ferritic	0.25					99Fe	N/A		250
SS316L	Austenitic	0.02		17.2	10.1	2.1		24–25.2	21	220
LDX2101	Lean duplex	0.03	0.22	21.5	1.5	0.3	5MnCu	26	20	450
2304	Lean duplex	0.02	0.1	23	4.8	0.3	Cu	26	28	400
SS904L	Austenitic	0.01		20	25	4.3	1.5Cu	34	65	220
2205	Duplex	0.02	0.17	22	5.7	3.1		35	55	460
SAF2507	Super-duplex	0.02	0.27	25	7.0	4.0		43	88	530

Uranium recovery from high chloride sulphate leach solutions

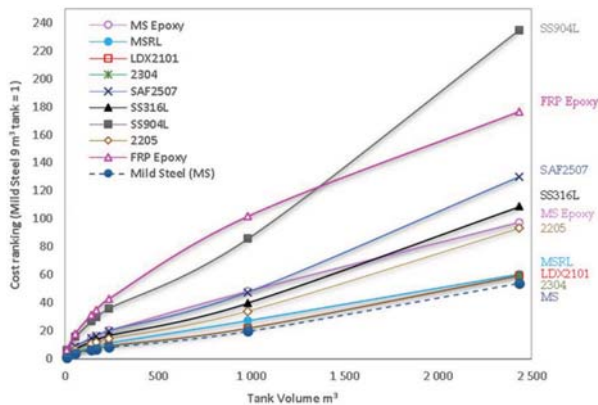


Figure 4—Rankings of fabricated tank costs for various platework materials of construction and tank sizes compared to a 9 m³ mild steel tank

Material quantities were estimated using DRA's bill of quantities. Tank platework material quantities were then factored based on the storage tank shell thickness tool provided by Outokumpu (2015). The tool is based on API650 and EN14015 standards, which allowed us to estimate the material consumption for the cylindrical shell of a tank and to compare how steel grade affects material consumption and cost. We also considered the cost differentials of shop- and site-fabricated tanks.

Materials of construction differentials

In this paper, we traded off MoC for two treated water options (1a and 1b) and two seawater options (2a and 2b), shown in Table II. Option 1a considered mild steel rubber-lined (MSRL) platework and represented the basis of comparison. Option 2a considered the equivalent materials of construction for circuits containing high chlorides (20 g/L Cl⁻). The other two options (1b and 2b) offered more corrosion-resistant MoC for mechanical equipment and platework. Mechanical equipment included agitators and thickener rake mechanisms. Platework included tank and thickener shells. These parameters were applied only to the wetted unit operations of the front-end circuit shown in Figure 1.

For all options, the mill and thickener platework was mild steel with rubber liners/lining. DRA has implemented mills/scrubbers with rubber liners and anodic protection in high-chloride seawater applications. Two such projects

include De Beers' diamond-mining vessels operating off the Namibian coast, involving preferential Kawasaki ball mills as well as the mill installed on the *Ya Toivo*.

- *Options 1a and 2a*—Rubber linings and epoxy vinyl ester coatings exhibit excellent compatibility with dilute sulphuric acid (up to 5 g/L H₂SO₄) that will be present in the leach and CCD areas. Rubber lining and epoxy coating are also highly resistance to chlorides in option 2a, if correctly applied to the tank surfaces. Mild steel/epoxy coating is more costly than mild steel/rubber lining. Consequently, we used rubber as the lining for the mild steel options (1a and 2a).
- *Option 1b*—This option represented 'standard' materials of construction for a conventional uranium processing circuit where chlorides are not of concern. Historically, SS316 has been a 'safe' material to specify for use on hydrometallurgical plants, although there has been a move to duplex in recent years. The PREN number for SS316 is 24, compared with 26 for LDX2101® and 2304. In terms of corrosion resistance, the 'good/better/best' basis would be SS316/LDX2101®/2304. Lean duplex steel 2304 has a CPT of about 28°C, while LDX2101® has a CPT of around 20°C.
- *Option 2b*—In dilute sulphuric acid contaminated with chloride ions:
 - Super-duplex steel SAF2507 has better corrosion resistance than SS904L, which is a highly alloyed austenitic steel grade specially designed to resist sulphuric acid (shown in Table I by a higher PREN and CPT, 88°C for SAF2507 versus 65°C for SS904L)
 - The material cost of SS904L is approximately double that of SAF2507
 - Thinner gauge material (less material) is used with SAF2507 than SS904L due to the higher mechanical strength of SAF2507 (shown in Table I by the 0.2% proof yield strength).

For these reasons, SAF2507 was selected as the 'high-specification' material (option 2b) for seawater.

Solvent extraction circuit differentials

The main differentials affecting CAPEX were due to SX circuit size and are summarized in Table III. The equipment size

Table II

Materials of construction differentials for two treated-water and two seawater flowsheet options

Unit operation	Treated water large RO Alamine SX Base case 1a	Treated water large RO Alamine SX 1b	Seawater small RO Cyanex SX 2a	Seawater small RO Cyanex SX 2b
Mill, feed chute, trommel screen materials and liners	MS rubber liners	MS rubber liners	MS rubber liners	MS rubber liners
Thickener materials	MSRL	MSRL	MSRL	MSRL
Thickener rake mechanism	SS316L	2304	SAF2507	SAF2507
Tank materials	MSRL	2304	MSRL	SAF2507
Agitator materials	SS316L	SS316L	SAF2507	SAF2507
SX mixing tank/settler	SS316L	SS316L	SS316L	SAF2507
SX agitator materials	SS316L	SS316L	SAF2507	SAF2507

Uranium recovery from high chloride sulphate leach solutions

Table III

Key solvent extraction circuit differentials for treated water and seawater flow sheet options

SX circuit differentials	Extract	Scrub	Strip	Regen
Option 1 - treated water with Alamine 336 SX stages	4	3	4	1
Area of settler (m ²)	153	26	26	26
Volume of mixing tanks (m ³)	23	13	13	13
Option 2 - seawater with Cyanex 272 SX stages	3	2	5	0
Area of settler (m ²)	153	12	12	12
Volume of mixing tanks (m ³)	23	7	7	7
Is there a differential between the two circuits? Yes ✓, No x				
No. of equipment	✓	✓	✓	✓
Equipment size	x	✓	✓	✓
Material of construction	✓	✓	✓	✓

Table IV

Differential design parameters affecting operating costs for treated water and seawater flow sheets

	Treated water with Alamine 336 SX	Seawater with Cyanex 272 SX
Common design parameters		
PLS feed flow (m ³ /h)	382	382
U ₃ O ₈ PLS concentration (mg/L)	834	834
Differential design parameters		
SWRO plant capacity (nominal) (m ³ /h)	200	80
Treated water chloride concentration (mg/L)	100	100
PLS chloride concentration (g/L)	0	20
SX organic loading (g/L U ₃ O ₈)	4.8	10.7
SX extractant volume fraction (%v/v)	4.5	3.5
SX phase modifier volume fraction (%v/v)	2.25	-
SX diluent volume fraction (%v/v)	93.3	96.5
SX scrub liquor concentration (g/L H ₂ SO ₄)	10	50
SX strip liquor concentration (g/L H ₂ SO ₄)	435	411
SX regeneration Na ₂ CO ₃ (g/L)	100	No regen.
SX regeneration NaOH (g/L)	50	No regen.

throughout the rest of the uranium circuit was the same for both flow sheets.

The SX equipment for the scrubbing and stripping sections of the treated water option (Alamine 336 organic) was approximately double the size of that in the seawater option (Cyanex 272 organic). The sizes of the extraction circuits for the two flow sheets were the same. For the seawater-Cyanex 272 option, chlorides will be present in the extraction and scrubbing sections of the SX circuit, in the PLS, and the entrained aqueous within the loaded organic. The acidic raffinate containing chlorides is returned to CCD as wash liquor and eventually to leach to build up uranium tenor. The scrub liquor is recycled to the first SX stage. The scrubbed organic, free of chlorides, proceeds to stripping. Mass balance modelling showed that chloride transfer to the stripping circuit is negligible due to the flow rate of the scrub liquor and assumed PLS entrainment concentration. Furthermore, the already low concentrations of chlorides will be further diluted to trace amounts before entering nanofiltration. For simplicity, it was assumed that materials of construction are the same throughout each SX circuit.

OPEX differentials

The main differentials affecting OPEX can be attributed to the SX circuit size, number of unit operations, organic loadings,

and reagent requirements for scrubbing, stripping and regeneration. OPEX is also affected by the desalination plant size. Design parameters affecting OPEX are summarized in Table IV.

Techno-financial evaluation

Overall basis of comparison

Analysis was done on a bare-bones basis, in real terms, and excludes the effects of taxes, interest, financing terms, or any cost escalation. The costs shown are not to be regarded as definitive, but rather differential costs relative to the base-case option 1a. Any costs considered to be common between the various options were excluded from the analysis. The technical basis for comparison of the system economics is provided in Table V.

CAPEX costing and assumptions

The CAPEX estimate was based on the following:

- Differences in the major mechanical equipment
- The use of typical process design parameters (PDP) for compiling the mass balances that were then used to size major equipment
- Mechanical equipment costs were determined from recently executed studies, DRA's internal database, and selected vendor quotes (Heyns, 2017; Pryor, 2017)

Uranium recovery from high chloride sulphate leach solutions

Table V

Economic basis of comparison for all flow sheet options

Process design parameter	Value
Run-of-mine head grade	650 ppm U ₃ O ₈
Uranium production	5 million lb/a U ₃ O ₈
Operating hours per annum	7509 h
Life-of-mine and discount percentage	15 years at 10% discount

- Internal DRA factors were applied to the two SX circuit mechanical costs for civils, structural (supply and erection), platework (supply and erection), mechanical erection, piping (supply and installation), electrical, control and instrumentation (supply and installation), transport, project services, preliminary and general costs
- For the smaller SWRO plant, it was assumed that two SWRO skids, each capable of producing 55 m³/h (at average water temperature), would be required. In winter, at low water temperature, the two skids would produce >100 m³/h and in summer would be able to produce more than the required amount (80 m³/h, nominal)
- For the large SWRO plant, it was assumed that three SWRO skids, each capable of producing 83 m³/h (at average water temperature), would be required. In winter, at low water temperature, the three skids would produce >220 m³/h and in summer would be able to produce more than the required amount (200 m³/h, nominal)
- Piping was excluded as a differential as it was assumed to be high-density polyethylene (HDPE)
- Pump costing was excluded as a differential. It was assumed that slurry pumps in both flow sheets would have high-chrome metal impellers and liners and solution pumps would have ethylene propylene diene monomer (EPDM) rubber impellers and liners.

OPEX costing and assumptions

Reagents

Reagent costs were obtained from DRA's recently updated

reagent database. Reagent consumptions were based on test work (ANSTO test work in the case of SX) and were determined using high-level mass balances. Reagent consumptions for the RO plants were based on estimates.

Power

Power consumption and labour costs for the RO plants were provided by Prentec (Pryor, 2017). The power estimate included seawater abstraction into the product water tank. The estimate assumed that desalination would be at the coast and excluded delivery to the mine. Power for the SX circuit was estimated from equipment sizing. Power for the rest of the uranium processing plant is not a differential and was therefore not included.

Maintenance

Maintenance costs are factored for mechanical replacement cost, platework and rubber lining maintenance, and valve maintenance. Piping maintenance was excluded.

Consumables

Grinding media for milling for option 1 is forged steel balls and for option 2 the media is of the high-chrome variety. Grinding media consumption was assumed the same, with costs of materials of construction varying. Membrane life for the SWRO plants was five years. Mill liners were excluded as a consumable cost.

Financial analysis

The CAPEX and OPEX cost estimates are summarized in the bar charts shown in Figures 5a and 5b. The bars show the estimated costs for a 75% confidence range, as well as the maximum and minimum ranges expected. OPEX estimates are annual expected costs.

The OPEX estimates in Figure 5a were based on upside and downside supply cost. The main factors affecting OPEX included:

- SX strip liquor acid consumption: the two flow sheets use different amounts of acid for stripping uranium. Option 1 requires more acid. Acid supply costs are based on US\$109 per ton, with an upside of US\$60 per ton and downside of US\$140 per ton (based on feedback from numerous reputable reagent suppliers).
- SX diluents contribute a noteworthy portion to the OPEX cost in both options.

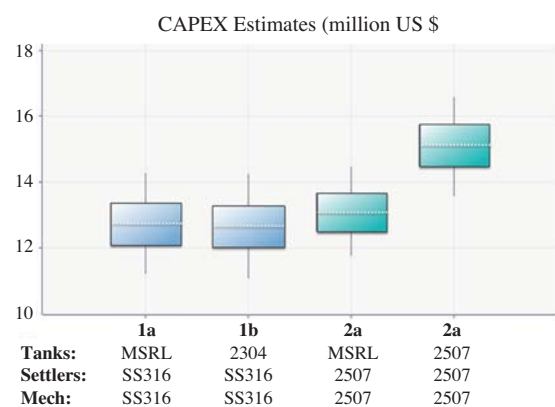
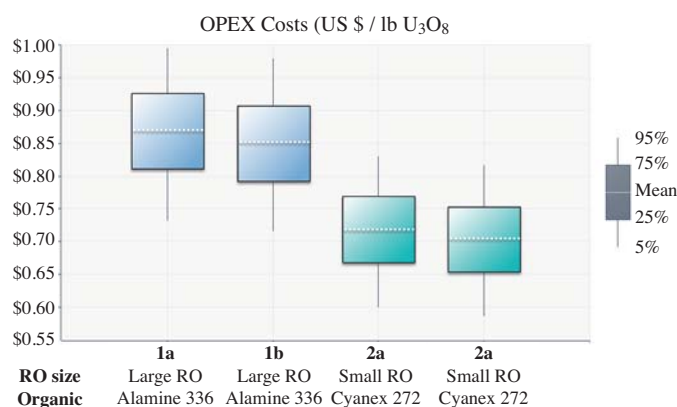


Figure 5—(a) OPEX cost estimates (\$ per pound U₃O₈) and (b) CAPEX cost estimates (\$ million)

Uranium recovery from high chloride sulphate leach solutions

- SX regeneration agents, sodium carbonate (Na₂CO₃) and sodium hydroxide (NaOH), contribute to a higher baseline OPEX for option 1. Option 2 has no organic regeneration step in SX. The Na₂CO₃ cost is based on US\$594 per ton, with a range from US\$416 to US\$772 per ton.
- Power usage for a large RO plant increases the OPEX in option 1.

The box-plot graph shown in Figure 6 shows the differential net present cost (NPC) for each option relative to the base case.

Figure 6 demonstrates that all options relative to the base case will return improved cash flows over a 15 year life-of-mine, despite the higher capital expenditure required. The flow sheet options that consider the use of seawater, namely options 2a and 2b, provide the highest cost savings over a 15-year life-of-mine. The expected life-of-mine economic benefit is calculated to be between US\$0.5 million and US\$4.5 million. Option 1b is expected to provide some cost benefit when compared with the base-case option 1a, mainly because of reduced platework maintenance costs. There is, however, a moderate likelihood of breaking even with the base-case option, in terms of life-of-mine cost savings.

Sensitivity analysis

Tornado charts, indicating the major uncertainty contributors, for options 1b, 2a, and 2b relative to the base-case option 1a are shown in Figure 7, Figure 8, and Figure 9, respectively.

In Figure 7, the greatest uncertainty lies in the platework maintenance cost for the option 1b differential NPC. In option 1a, it is the cost of maintaining MSRL platework compared with maintaining SS316/2304 platework in option 1b.

For option 2a in Figure 8, the greatest uncertainty lies in the super-duplex stainless steel mechanical cost (rake mechanism). The power cost of the RO plants, SX diluents, and acid supply costs are significant contributors to economic uncertainty. Nonetheless, even at the extremities of these supply costs, this option using seawater is expected to return economic benefits to the project.

For option 2b in Figure 9, the greatest uncertainty lies in the super-duplex stainless steel mechanical and platework costs. At the downside of the SAF2507 supply cost estimate, the use of high-alloy materials, for a high-chloride circuit is not expected to return economic benefits.

Conclusions and recommendations

The aim of this trade-off study was to propose a hypersaline-tolerant uranium processing flow sheet through the use of an alternative uranium SX organic, Cyanex 272, and to determine whether this is an economically viable option.

A stochastic approach was used to quantify the differentials in expenditure between uranium processing with SWRO-treated water and seawater. Together with a basic high-level evaluation of the CAPEX and OPEX requirements, a comparison of the economics revealed that a flow sheet incorporating a hypersaline water source is an economical option when MSRL platework and super-duplex SAF2507 mechanicals are used. Nevertheless, the concentration of U₃O₈ in the PLS plays key part in the selection of the process route and the SX purification route.

Chlorides in combination with sulphate salts and acidic solutions are not well understood in industry. Engineering design companies should open a dialogue with steel suppliers and vendors to find suitable MoC for these corrosive

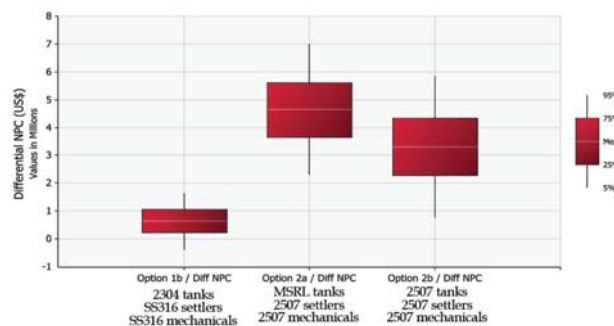


Figure 6—Differential net present cost (NPC) of the various options relative to option 1 (15-year LoM, 10% discount)

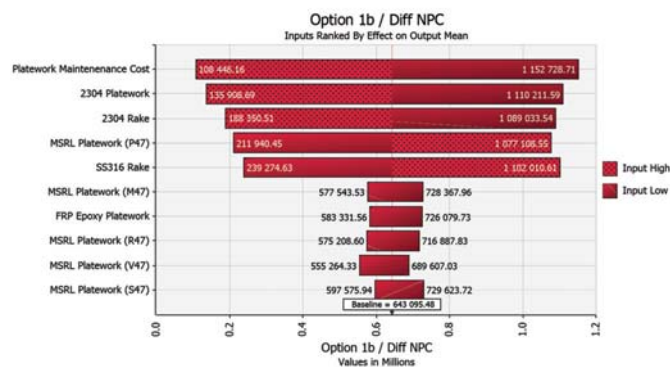


Figure 7—Tornado plot of differential NPC of options relative to option 1b (15-year LoM, 10% discount)

Uranium recovery from high chloride sulphate leach solutions

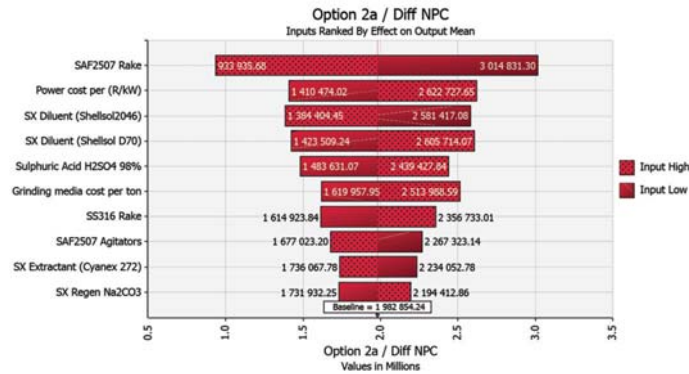


Figure 8—Tornado plot of differential NPC of option 2a relative to option 1 (15-year LoM, 10% discount)

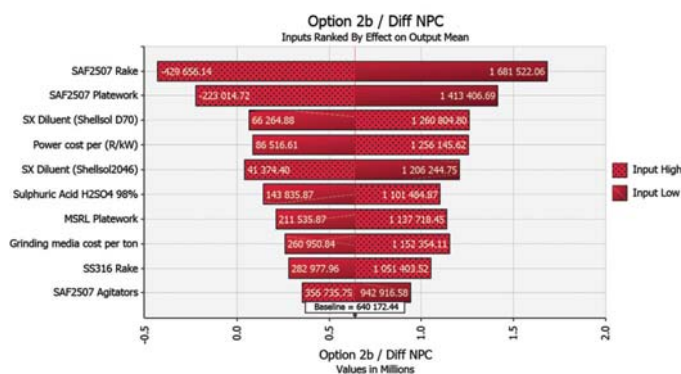


Figure 9—Tornado plot of differential NPC of option 2b relative to option 1 (15-year LoM, 10% discount)

applications, which are becoming more commonplace as orebody grades decline and clean water sources become scarce.

Acknowledgements

Our thanks to ANSTO for their valued input, professional research, and comments on the process design parameters for the chloride-tolerant uranium SX technology. Prentec and Mixtec are thanked for providing comprehensive costing.

References

- BALLESTRIN, S., LOW, R., REYNAUD, G., and CRANE, P. 2014. Honeymoon mine Australia: Commissioning and operation of the process plant using a novel solvent extraction reagent mixture in a high chloride environment. *Proceedings of ALTA 2014 Uranium-REE. ALTA Metallurgical Services*, Australia. pp. 291–308.
- BROWN, A.J. and HAYDON, B.C. 1979. Comparison of liquid and resin ion-exchange processes for the purification and concentration of uraniferous solutions. *CIM Bulletin*, vol. 72, no. 805. pp. 141–149.
- DUDLEY, K.A. and SUMNER, R.J. 2014. Solvent extraction process. International patent WO2014040136. BHP Billiton Olympic Dam Corporation Pty Ltd.
- GOLDSWAIN, B. and ROGERS, T. 2017a. Stainless steel for engineers. Consulting Engineers South Africa, CESA-614-11/2017. pp. 1–32.
- GOLDSWAIN, B. and ROGERS, T. 2017b. Costs and materials of construction for corrosive applications. Interviewed by Eleanore Forner. [meeting] DRA Global, Sunninghill, South Africa, 23 May 2017.
- Heyns, T. 2017. Budget quote on agitator motors, blades and shafts in selected materials of construction. Mixtec, Germiston, South Africa.
- MORAIS, C.A. and LADEIRA, A.C. 2008. The influence of competitive species on uranium recovery using resin and solvent extraction techniques. *Proceedings of the Sixth International Symposium of Hydrometallurgy*. Young, C.A., Taylor, P.R., and Anderson G.G. (eds.). Society for Mining, Metallurgy & Exploration, Inc., Littleton, CO. pp. 292 - 296.
- OUTOKUMPU. 2013. Duplex stainless steels. https://www.outokumpu.com/SiteCollectionDocuments/Duplex_Stainless_Brochure.pdf [accessed 22 January 2017].
- OUTOKUMPU. 2015. Storage tank shell thickness calculation. <http://steelfinder.outokumpu.com/storage-tank/> [accessed 16 May 2017].
- PRYOR, M. 2017. Budget estimates of two seawater reverse osmosis plants. Process Manager, Prentec, Kempton Park, South Africa.
- QUINN, J.E., WILKINS, D., and SOLDENHOFF, K.H. 2013. Solvent extraction of uranium from saline leach liquors using DEHPA/Alamine 336 mixed reagent. *Hydrometallurgy*, vol. 134–135, no. 0. pp. 74–79.
- QUINN, J.E. and SOLDENHOFF, K.H. 2015. Process for uranium recovery using Cyanex 271. *Hydrometallurgy*, vol. 152. pp. 7–12.
- SOLDENHOFF, K., WILKINS, D., SHAMIEH, M., and RING, R. 2000. Solvent extraction of uranium in the presence of chloride. *Proceedings of the International Symposium on the Process Metallurgy of Uranium: 30th Annual Hydrometallurgical Meeting*. Ozberk, E. and Oliver, A.J. (eds). Canadian Institute of Mining, Metallurgy and Petroleum, Montreal, Canada. pp. 339–351.
- SOLDENHOFF, K., WILKINS, D., SHAMIEH, M., and MANIS, A. 2005. Mini-plant testing of uranium solvent extraction process for acid leach liquors containing chloride. *Proceedings of the 17th International Solvent Extraction Conference*, Beijing, China. Hara, T. (ed.). Taylor & Francis/Balkema, The Netherlands.
- VAN TONDER, D. and KOTZE, M. 2007. Uranium recovery from acid leach liquors: IX or SX? *Proceedings of the Alta 2007 Uranium Conference*. ALTA Metallurgical Services, Melbourne, Australia. p. 226. ◆



Uranium circuit development for a West African polymetallic deposit

by A.J. du Toit, and S.J. Archer

Synopsis

This article presents the process flow sheet development conducted in 2013 on a polymetallic deposit located in West Africa. The mineralization, consisting of uranium and to a lesser extent silver and copper, posed challenges due to the presence of high levels of both carbonates (acid consumers) and sulphides (alkali consumers). It was established that copper and silver were associated with the sulphides and could be separated by means of flotation. Thus a trade-off study was conducted to evaluate both alkali and acid processing routes for the recovery of uranium. The following two flow sheets were investigated:

1. Acid leaching of the run-of-mine (ROM) ore, followed by sulphide flotation of leach tails for the recovery of silver and copper from the concentrate
2. Sulphide flotation of the ROM ore for silver and copper recovery, followed by alkali leaching of the float tails for uranium recovery.

The trade-off study showed a differential operating cost saving of between 10% and 40%, within a 90% confidence level, in favour of the alkali-based flow sheet, which was selected for further evaluation and optimization.

Further flow sheet development was also conducted to determine the following:

- Alkali addition and minimizing water requirements
- Processing of flotation concentrates to produce saleable silver and copper by products.

Keywords

uranium, process development, polymetallic ore, alkali leaching, acid leaching.

Introduction

DRA developed a uranium circuit for a polymetallic deposit in West Africa during an internal economic study. The deposit lies within a well-established gold mining region and contains significant uranium, silver, and copper mineralization, with an approximate head grade of 0.145% U₃O₈, 116 ppm Ag, and 0.217% Cu. The dominant uranium-bearing mineral was identified as uraninite, typically in association with quartz, chlorite, or muscovite. Coffinite, which is often found in association with uraninite, quartz, muscovite, chamosite, and other sulphides were also present. A small portion of brannerite was observed to be associated with muscovite. Copper is mainly present as sulphide minerals, typically chalcopyrite, and silver as argentite (Ag₂S), but also as tennantite (Cu,Ag,Zn,Fe)₁₂As₄S₁₃ and in its native form. The gangue matrix

consists mainly of quartz, muscovite, chlorites, carbonates, and feldspars.

A six-week process concept study was initially executed during the second quarter of 2011. An atmospheric acid leach flow sheet was selected as the basis for the concept study, and comprised the following unit operations:

- Ore receiving
- Crushing
- Ball milling
- Primary atmospheric acid leach
- Resin-in-pulp (RIP)
- Froth flotation
- Solvent extraction (SX)
- Sodium diuranate (SDU) precipitation
- Drying and packaging
- Consideration of the potential sale of the flotation concentrate (not included in the concept study operating cost (OPEX) estimate).

Following the completion of the concept study, it was concluded that the high sulphuric acid consumption in the atmospheric leach circuit had a dramatic effect on the plant OPEX and subsequently affected the overall project economics negatively. The abnormally high acid consumption ranged from 65 kg/t to 100 kg/t ROM material. Typical North American operations consume 18 kg to 50 kg sulphuric acid per ton of ore (Meritt, 1971). The high acid consumption was attributed to the carbonate content of the ore. Uranium leach extractions of 85% to 88% were initially observed. Scoping an alkali leaching route of the ore resulted in high reagent (carbonate) consumption rates, but at significantly higher uranium leach extractions (90.5% to 91.6%). The high carbonate consumption for the scoping alkali tests was ascribed to the sulphide content of the ore.

* DRA Projects, South Africa.

© The Southern African Institute of Mining and Metallurgy, 2018. ISSN 2225-6253. This paper was first presented at the Uranium 2017 International Conference, 12–13 September 2017, Swakopmund Hotel, Swakopmund, Namibia..

Uranium circuit development for a West African polymetallic deposit

Golder Associates Inc. conducted a feasibility assessment on the potential for *in situ* recovery (ISR) of uranium. It was determined that the host formation did not have sufficient permeability to enable lixiviant to percolate through the ore zone. The International Atomic Energy Agency (IAEA), in its technical document on acid leaching of uranium ores, defines hydraulic permeability below 1 m/d as very low and unfavourable for uranium recovery by the ISR process (IAEA, 2001). The test results indicated permeability of several orders of magnitude below this limit, which confirmed that the ISR method was not feasible for this orebody.

Various comminution test work evaluations were conducted. Bond rod mill and Bond ball mill work indices (BRWi and BBWi) were used to calculate comminution energy requirements based on various top sizes. BRWi, when compared to BBWi, indicated a relative degree of ore competency. The JK drop weight test was used to determine rock breakage parameters. Parameters derived from the test work, together with operating parameters, were used to predict autogenous or semi-autogenous milling behaviour, and to confirm crushing and milling parameters employed in the comminution circuit design. The results indicated that the deposit material could be characterized as medium to moderately hard. The unconfined compressive strength values for various samples evaluated ranged widely (60 MPa to 140 MPa) but were generally high, also indicating competent ore.

The presence of native silver nuggets was identified during the flotation piloting test work. Variability was observed in the silver department, analyses, and reported recoveries. However, mineralogical analyses showed that all floatable silver species were recovered, notwithstanding the analytical variability due to the presence of the silver nuggets. Furthermore, it was determined that gravity concentration would not be a viable option for separating and upgrading the silver nuggets after milling. The flotation test work on milled ore (P_{80} of 75 μm) resulted in typical copper and silver recoveries of between 90% and 92% into mass pulls of approximately 3.5% to 6.3%.

Although crushing, milling, and flotation observations have been provided above as background information, the main focus of the article will be on the following items:

- Acid *versus* alkali process route trade-off
- Alkali circuit configuration trade-off:
 - Leach/RIP
 - Leach/countercurrent decantation (CCD)/ion exchange (IX)
 - Leach/CCD/evaporation or membrane technology
 - Leach/filtration/evaporation or membrane technology
 - Leach/RIP/CCD
- Optimization of the CCD circuit
- Flotation concentrate processing issues and options:
 - Radionuclide removal from concentrate
 - Uranium, copper, and silver recovery from sulphide concentrate:
 - Uranium recycled to alkali circuit
 - Ag-jarosite formation:
 - Lime boil application
 - Sulphur flotation.

A 2013 financial base date was used for all the financial data used and reported in this article.

Acid versus alkali process route trade-off

Broadly, two leaching strategies exist for uranium extraction: sulphuric acid leaching or carbonate (alkali) leaching. An alkali leach is generally more selective than acid leaching and is particularly useful for high-lime and carbonate-containing ore that would consume excessive amounts of acid (Merrit, 1971). The ore from the deposit contains high levels of carbonate (acid consumers), as well as sulphides (alkali consumers). It is possible to separate sulphides from other mineral phases using froth flotation, which could result in a substantial reduction in the overall operating costs. As a result, two flow sheet options were identified for the recovery of uranium and secondary products from the milled ore:

- Acid leaching of ROM ore for uranium recovery, followed by flotation of the leach tailings and recovery of silver and copper from the flotation concentrate
- Flotation of ROM ore for silver and copper (sulphide) recovery, followed by alkali leaching of the flotation tailings for uranium recovery. This option follows a similar processing theme as the Canadian Beaverlodge operation (Feasby, 1980).

Prior to commencing with the internal economic study, the DRA process team was requested to undertake a high-level desktop trade-off evaluation, with the objective of assessing whether either of the two processing options could provide a significant operating cost saving, and could be selected for further investigations or test work. The selection of one option on this basis would simplify the test work requirements, engineering focus, and subsequent cost and timing for completion of the internal economic study.

From the alkali/acid trade-off study there appeared to be enough motivation, despite the levels of test work and engineering completed at the time, to proceed with the second option (the alkali-based flow sheet).

The trade-off methodology that was applied included the following:

- Development of a concept techno-financial model (based on limited engineering and test data available at the time)
- Use of 2013 reagent and transport costs
- Following a stochastic modelling approach
- Considering only differential incremental OPEX values
- Assuming the capital cost (CAPEX) differential to be insignificant relative to the larger project capital layout
- Excluding common areas, as well as the concentrate processing area.

Block flow diagrams of the two processing options are shown in Figure 1. The trade-off study did not consider secondary metal (silver and copper) recovery, since this is common to both flow sheet options and would not necessarily impact on the acid or alkali circuit selection.

Since the focus of the trade-off was on establishing operating cost differentials, no definitive cash flow evaluations were conducted for either option. CAPEX differentials were not considered at this stage, as the differential CAPEX is expected to be small in comparison to the larger project capital.

Due to the process variability and subsequent uncertainty in reagent consumption rates, supply costs, and status of process engineering (preliminary mass and energy balances),

Uranium circuit development for a West African polymetallic deposit

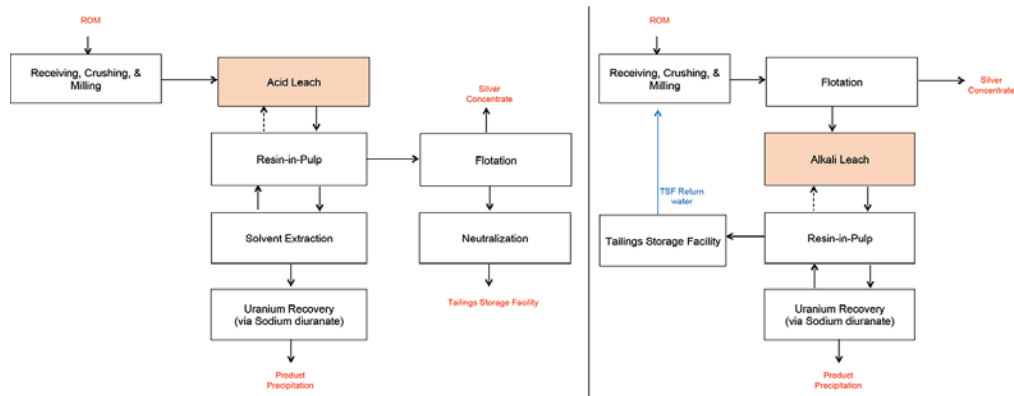


Figure 1 – Block flow diagrams: acid versus alkali process options

a stochastic approach was used to assess the differential in operating costs between the two processing routes. This was done by using the Monte Carlo simulation technique, which seeks to assess the collective risk of all parameter uncertainties simultaneously, rather than using a single-variable sensitivity analysis approach.

In the simulation, the key uncertain operating cost drivers were represented using ranges of possible values, or probability distributions, derived from metallurgical test work, preliminary high-level mass and energy balances, as well as engineering experience. This provided a framework for risk analysis, quantification, and the testing of alternatives. The Monte Carlo simulation output probability distribution, shown in Figure 2, indicates the potential operating cost saving should an alkali leach flow sheet be adopted. Based on the assumptions and preliminary test work results, the likely saving is expected to be between 10% and 40% (90% confidence level) compared to an equivalent acid leach flow sheet. The alkali-based flow sheet was, therefore, selected for further study.

Alkali circuit configuration trade-off

One of the major uncertainty risk items identified for the alkali-based circuit was the effect of overall plant solution and salt balance, taking into account the climatic conditions (rainfall). An alkali circuit configuration review was required

to optimize the use of reagents and maximize the possible recycling of unreacted reagents. Therefore, an alkali circuit configuration trade-off study was initiated based on engineering experience, and also considering various key process drivers (Lunt *et al.*, 2007). The following five configurations were evaluated:

- Leach – RIP
- Leach – countercurrent decantation (CCD) – ion exchange (IX)
- Leach – CCD – evaporation/reverse osmosis (RO)
- Leach – filtration – evaporation/RO
- Leach – RIP – CCD.

The alkali circuit configuration trade-off was based on the following:

- Optimizing the solution and salt balances
- Excluding the CAPEX from the analysis
- Using high-level mass balances and test work assumptions
- Reagent/alkali requirements.

The overall alkali requirements and technology status dictated the final configuration selection. The results are shown in Table I.

A leach-CCD-IX configuration was selected as natural evaporation is not feasible in the high-rainfall areas of the West African region, and forced evaporation will be too cost-

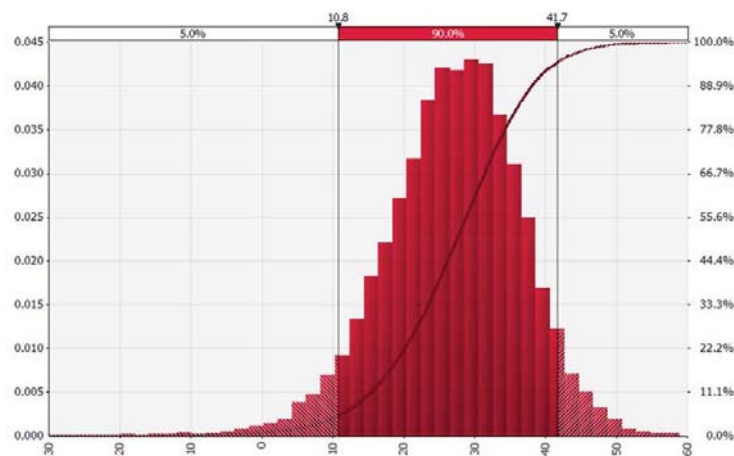


Figure 2 – Acid-alkali trade-off: differential OPEX (alkali leach OPEX saving relative to acid leach)

Uranium circuit development for a West African polymetallic deposit

Table 1
Alkali configuration trade-off evaluation

Circuit configuration	Alkali requirements	Technology status	Circuit selected
Leach-RIP	Baseline	Proven	No
Leach-CCD-IX	40% to 80% reduction	Proven	Yes
Leach-CCD-evaporation/RO	> 80% reduction	RO not proven	No
Leach-filter-evaporation/RO	> 80% reduction	RO not proven	No
Leach-RIP-CCD	40% to 80% reduction	Proven	Alternative

intensive. RO can be incorporated in an alkali circuit for upgrading uranium, although it is not proven on a commercial scale. Another African uranium producer is currently piloting the concept of using membrane technology for reagent recovery (Peacock *et al.*, 2016). The CCD-IX configuration was selected in preference to the RIP-CCD configuration as the IX step provides the flexibility to be replaced by RO.

Optimization of the CCD circuit

The post-alkali leach slurry is washed, while solid-liquid separation is facilitated, using a two-phase CCD system. The first phase uses barren solution from the previous IX unit operation to wash the uranium; and the second phase involves two stages of washing to balance the salts in the circuit by using fresh water as the washing solution. Initially, a high washing efficiency (approx. 99.8%) was targeted for the uranium washing and a seven-stage system was incorporated in the design circuit, resulting in a calculated underflow uranium content of approximately 3–6 ppm U₃O₈. Subsequently, it was identified that the tailings treatment facility will incorporate a lining, and a high-level economic evaluation was conducted to determine the economical cut-off between uranium recovery and number of CCD stages. The overall washing efficiencies are shown in Figure 3.

The results of the economic evaluation are shown in Figure 4 and, based on the expected life-of-mine, it was identified that five stages of uranium washing will be sufficient for an economically viable solution.

Flotation concentrate processing issues and options

It was identified during the initial concept study that the sale of the valuable metals in the concentrate as a secondary product would play a pivotal role in the economic evaluation of the project. Flotation test work and piloting showed that the concentrate contained radioactive components. Subsequently, radionuclide removal and concentrate processing test work ensued to determine the most value-adding processing option.

Radionuclide removal from concentrate

Generally, a radioactivity level of less than 1 Bq/g is required for a non-radioactive transport and trade agreement. The concentrate, prior to uranium removal, is in secular equilibrium as was observed by similar activities of radionuclides in each decay chain. The secular equilibrium was distributed by sulphuric acid leaching. This removed uranium as well as thorium successfully; however, radium,

lead, polonium, and protactinium remained. Further radionuclide removal options were evaluated at the following batch leach conditions:

- 1M HCl with 6 hours' residence time at 60°C and a solids content of 20% w/w
- Acidified NaCl (2M NaCl) in 10 g/L HCl with 6 hours' residence time at 60°C and a solids content of 20% w/w
- 1M HCl with 6 hours' residence time at 6°C and a solids content of 20% w/w, together with a complexing agent (such as EDTA).

The HCl leaches resulted in some components still exceeding the 2 Bq/g activity. Subsequent thermal treatment (2 hours at 750°C under negative atmosphere) was able to reduce most of the radionuclides. However, this technique

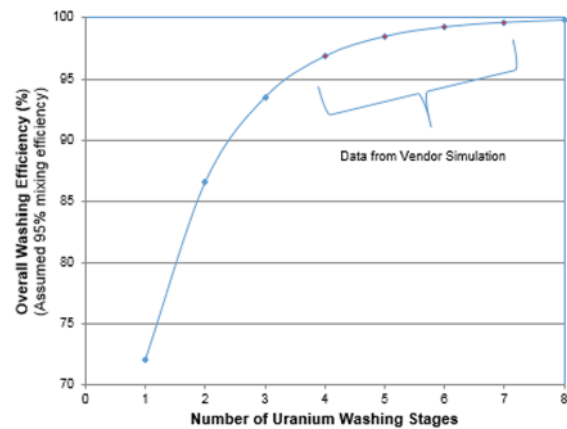


Figure 3—Washing efficiencies per number of uranium wash stages (mixing efficiency of 95%)

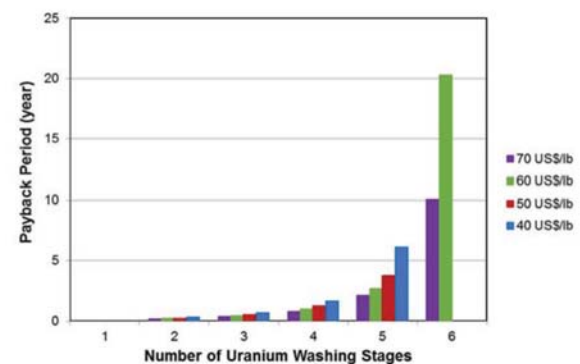


Figure 4—Payback period for each additional CCD washing stage shown for various uranium prices

Uranium circuit development for a West African polymetallic deposit

was unable to reduce the polonium activity below a level of 2 Bq/g. The polonium activity remained at or above 2 Bq/g regardless of the initial value. Although this corresponds to the removal of a significant portion of the polonium, the level still exceeded the 1 Bq/g target.

After leaching to remove uranium, the copper/silver concentrate would still be classified as radioactive and would, therefore, almost certainly require processing to remove radionuclides in order to be saleable as a non-radioactive material. Although there is an opportunity to sell the partially cleaned flotation concentrate, based on the test results, the decision was taken to pursue the production of a final metal by-product.

Uranium, copper, and silver recovery from sulphide concentrate

The recovery of silver from the flotation concentrate proved to be more challenging than initially anticipated. Although some of the uranium phases are associated with sulphide minerals, it was observed that the uranium deportment followed the mass distribution. Since the silver/copper flotation concentrate also contains approximately 20% of the feed uranium, it is necessary to acid leach the concentrate to recover this uranium. The pregnant solution containing the copper and uranium will be processed for copper recovery and the uranium will be precipitated as a magnesium diuranate and recycled to the alkali leach circuit.

During the atmospheric acid leach of the concentrate, it was observed that a silver jarosite species ($\text{AgFe}_3(\text{SO}_4)_2(\text{OH})_6$) formed, which was not amenable to cyanide leaching. Subsequently, five processing options were identified for laboratory evaluation at ANSTO Minerals. However, test work ensued only with the first three options as they were deemed the most likely to succeed. The last two options were not evaluated due to the hazardous nature associated with the practical operability of the processes, as well as the remote location of the deposit. The options identified included the following:

- ▶ Pressure oxidative (POx) leaching, with or without lime boils, followed by cyanide leaching
- ▶ Oxidative atmospheric leaching, with or without lime boils, possible sulphur flotation, followed by cyanide leaching
- ▶ Concentrate roasting, weak acid leaching, neutralization, followed by cyanide leaching
- ▶ Chloride oxidative leach, silver cementation, and copper recovery
- ▶ Ammonia oxidative leach, followed by copper/silver precipitation.

Although it was aimed to thermally decompose the argento-jarosite species at a high temperature, (Frost *et al.*, 2005), the initial concentrate roast option did not yield good silver recoveries. It was suspected that additional refractory silver species formed under the high-temperature roasting conditions. Technical solutions (the first two process options identified) were found to recover the silver successfully; however, when a silver-jarosite species formed, aggressive conditions were required for its destruction. Both uranium and copper can be readily leached, with high extractions (> 95%), under the following oxidative acid leach conditions (both atmospheric and pressure):

- ▶ Atmospheric conditions: 80°C to 90°C, 12 to 24 hours, and an oxidative-reductive potential of approximately 450 mV (Ag/AgCl)
- ▶ POx conditions: 180°C to 220°C with a 2- to 6-hour residence time.

Some silver was partially oxidized to a refractory form (almost certainly argento-jarosite) under atmospheric oxidative leaching conditions. The subsequent cyanide leach efficiency can be improved using an alkali pretreatment technique (*e.g.* lime boil) (Kasani *et al.*, 2008). However, significant amounts of alkali reagent would be required for high silver recoveries. It was observed that sulphides oxidized to elemental sulphur during low/ambient temperature atmospheric leaches. It is likely that the elemental sulphur would consume lime during the lime boil stage, producing calcium polysulphides. Standard lime boil tests were conducted at 90°C, at a pH of 9.5 to 10.5, for residence times from 6 hours. The standard lime boil tests resulted in high silver extraction during cyanide leaching (approx. 97%), but the lime consumptions were high, rendering the option economically unfeasible. Lime boils were conducted in a high-shear multiple impeller system to simulate an attrition effect and showed lower lime consumption with good subsequent silver recoveries, but were significantly more energy-intensive. It was observed that the target lime boil pH can vary, thereby varying the subsequent silver recovery and affecting the total reagent consumption.

Leach residues from the test work were sent for further flotation tests in an attempt to float residual elemental sulphur prior to lime boiling and cyanide leaching. Unfortunately, approximately 24% of the silver reported to the concentrate stream, while a substantial amount of sulphur still reported to the flotation tails and rendered the sulphur flotation option to reduce lime boil reagent consumption unsuccessful.

The addition of sodium compounds to the high-temperature oxidative leaches was found to improve the subsequent silver leach extraction due to the preferential formation of sodium jarosites. A high-level techno-financial model indicated that a cyanide leach silver recovery of 75% to 85% should be targeted, as higher recoveries were value-destructive (see Figure 5). Figure 6 shows the increase in the overall OPEX as higher silver recoveries are targeted.

Both oxidative atmospheric and POx leaching yielded similar recoveries. However, POx was not considered for further evaluation due to the operational complexity of the process. Therefore, an oxidative atmospheric leach process was selected for processing the ore flotation concentrate. A process block flow diagram is shown in Figure 7.

Conclusions and recommendation

It was found that a sulphide flotation circuit, followed by alkali leaching of the flotation tails, will provide the best value for this deposit. Furthermore, owing to the low uranium price, recovery of copper and silver by-products was targeted to provide by-product credits to make the financial case more attractive. However, difficulties were encountered with the silver flotation due to the presence of native silver nuggets, and a refractory silver species was formed during acidic leaching of the concentrate that rendered the silver not

Uranium circuit development for a West African polymetallic deposit

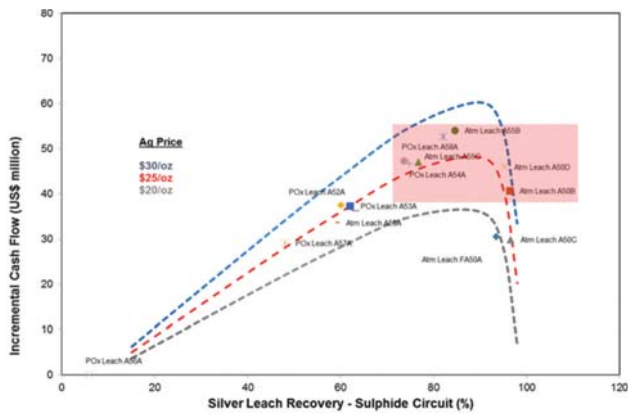


Figure 5—Potential value addition as function of targeted silver recovery

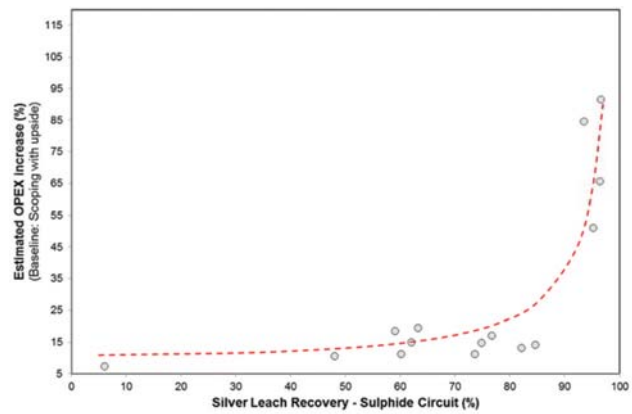


Figure 6—Relationship between OPEX increase and increasing silver recoveries

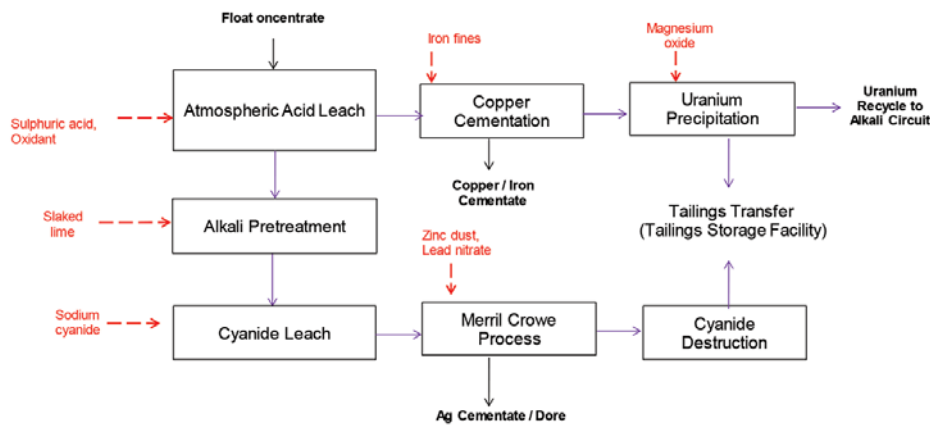


Figure 7—Block flow diagram for concentrate processing

amenable to direct cyanide leaching and silver recovery. The refractory silver species is thought to be an argento-jarosite compound, since the leachability improved with the addition of sodium compounds to the leach; this was probably due to the preferential formation of a sodium jarosite phase. Furthermore, it was found that the possible argento-jarosite phase can be destroyed by incorporating an alkali pretreatment unit operation before cyanide leaching. The subsequent silver recovery was found to be dependent on the targeted pH of the alkali pretreatment unit operation. This in turn impacted on the alkali consumption of the pretreatment step. It was, therefore, concluded that a silver recovery of between 75% and 85% should be targeted as higher recoveries became value-destructive due to the increase in alkali consumption. The deposit has changed ownership a few times over the last couple of years, and it is suggested that the next level of engineering study be conducted should the uranium price and outlook improve.

Acknowledgements

This article is published with the permission of the deposit owner and DRA Projects. The authors would like to thank the DRA process team for their valuable input and peer reviewing

of the article. The majority of the test work was conducted at ANSTO Minerals, with some test work also executed by MetCon, SGS Perth, and SGS South Africa.

References

FEASBY, D.G. 1980. Eldorado's Beaverlodge Operation. *Canadian Mining Journal*, June 1980. pp. 75–149.

FROST, R.L., WILLS, R.A., WEIER, M.L., and MARTENS, W. 2005. Thermal decomposition of synthetic argentojarosite Implications for silver production in medieval times. *Thermochimica Acta*, vol. 437, no. 1-2. pp. 30–33.

IAEA. 2001. Manual of acid in situ leach uranium mining technology. IAEA-TECDOC-1239. International Atomic Energy Agency, Vienna, Austria. August 2001,

KASAINI, H., KASONGO, K., NAUDE, N., and KATABUA, J. 2008. Enhanced leachability of gold and silver in cyanide media: Effect of alkaline pretreatment of jarosite minerals. *Minerals Engineering*, vol. 21, no. 15. pp. 1075–1082.

LUNT, D., BOSHOF, P., BOYLETT, M., and EL-ANSARY, Z. 2007. Uranium extraction: the key process drivers. *Journal of the Southern African Institute of Mining and Metallurgy*, vol. 107. pp. 419–426.

MERRITT, R.C. 1971. The Extractive Metallurgy of Uranium: Processing Operations. Colorado School of Mines Research.

PEACOCK, M., MCDUGALL, S., BOSHOF, P., BUTCHER D., FORD M., DONEGAN S., and BUKUNKWE D. 2016. Paladin Energy Ltd – Nano-filtration technology for reagent recovery. *Proceedings of ALTA 2016 Uranium-REE Proceedings*. ALTA Metallurgical Services, Melbourne, Australia. pp. 264–274. ♦



Optimization of the Rössing countercurrent decantation circuit for high-calc ore

by C.J. Anderson*, S.L. Rabiet†, and N.K. Jansen van Rensburg‡

The Rössing Uranium countercurrent decantation (CCD) circuit is scheduled to process ore with a high calc index from 2017 to 2021. This material was found to be associated with poor settling performance in the CCD circuit. In order to quantify the root causes of the poor performance, bench-scale test work was conducted on the thickener feed. Thickener feed density and process control were identified as key areas for optimizing performance. Two alternative feedwell designs were developed; a simple shelf design and a forced dilution design. An automated control system was also devised to improve the consistency of underflow densities and overflow clarity. These modifications are currently being phased in at Rössing, with the process control upgrades and the feedwell on the terminal thickener being prioritized.

Keywords

countercurrent decantation, optimization, process control thickener, feedwell design.

Introduction

Rössing Uranium Limited (RUL) operates one of the largest open pit uranium mining and leaching operations in the world. As part of the mine plan, the existing plant will be required to process ore with a high calc index (CI) from 2017–2021. The calc index is a measure of the acid-consuming gangue minerals in the feed, such as calcite and amphibole. Currently, calcite and dolomite account for approximately 50% of the gangue acid consumption and amphibole for approximately 26%. The remainder is due to minor acid-consuming minerals such as biotite, chlorite, apatite, pyrrhotite, goethite, and titanomagnetite. This high-CI material increases acid consumption in the leach and results in increased fines in the countercurrent decantation (CCD) circuit. This material has been associated with poor thickener overflow clarity, high solids reporting to the continuous ion exchange (CIX) circuit, and poor underflow densities in the terminal thickener. In severe cases, the plant is forced to run only three of the four mills during high-calc periods, to prevent excessive sliming in the CCD circuit.

In order to mitigate the effects of this high-calc material, Rössing undertook a study to investigate the necessary plant modifications to process high-calc material. This paper focuses on the modifications to the CCD circuit. Test work was undertaken in April 2016 to

determine the settling characteristics of the high-calc material and identify which modifications would lead to the most cost-effective improvements in performance with high-calc ore.

Review of current CCD circuit

Rössing currently operates a seven-stage CCD circuit, consisting of 2×42.7 m clarifiers, 4×42.7 m EIMCO thickeners, and 4×68.5 m Dorr Oliver thickeners (both brand names are now the property of FLSmidth). A schematic of the circuit is given in Figure 1.

The thickeners were originally installed in 1977 and are designed as high-rate thickeners, operating with flocculent addition to the thickener feed launders. Despite the addition of flocculent, the thickeners operate with fairly low solids fluxes (0.08 t/h/m² on the 42.7 m thickeners and 0.12 t/h/m² on the 68.5 m thickeners). Thickener 7 was decommissioned for the past few years but came back online in Q2 2017.

Thickener design

The thickeners (Figure 2) are relatively shallow compared to most modern thickeners and have heavy truss rake structures. Slurry is introduced on launders which feed directly into the centre of the feedwells. The feedwells are annular in shape and direct flow downwards from the point of entry. The feed is diluted by overflow from the preceding CCD stage via another launder situated above the slurry launder. Flocculent is introduced via troughs onto the launders and most of the flocculation occurs on the feed launder before the material enters the feedwell.

* Hatch Africa, Johannesburg, South Africa.

† Vietti Slurrytec, Johannesburg, South Africa.

‡ Rio Tinto, Melbourne, Australia.

© The Southern African Institute of Mining and Metallurgy, 2018. ISSN 2225-6253. This paper was first presented at the Uranium 2017 International Conference, 12–13 September 2017, Swakopmund Hotel, Swakopmund, Namibia.)

Optimization of the Rössing countercurrent decantation circuit for high-calc ore

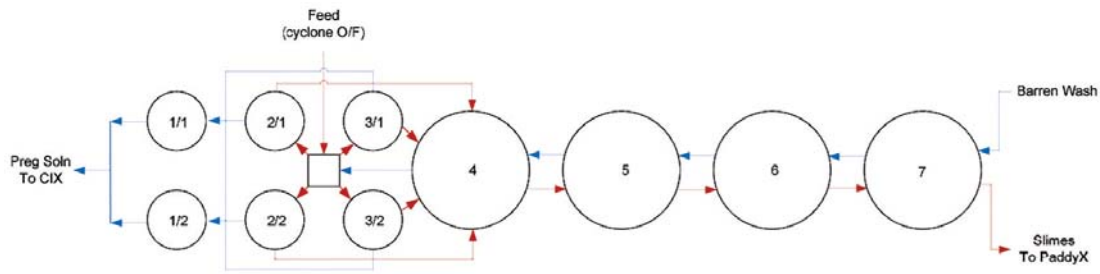


Figure 1—Schematic of the countercurrent decantation circuit at Rössing Uranium



Figure 2—Internal structure of thickener 4



Figure 3—Process control measurements on CCD circuit

Process control

Process control (Figure 3) is a fairly manual style of operation, where operators take hourly samples of the thickener underflow for density and thickener overflow for clarity, using a clarity wedge. The mud bed interface is measured at the thickener perimeter using a graduated dipstick. This information is combined with the thickener rake torque measurement from the SCADA and interpreted using a set of control rules recommended by the flocculent vendor. The underflow pump speed and flocculent dose are adjusted by the control room operator so as to maintain a target underflow density, mud bed height, rake torque, and overflow clarity.

Test work methodology

In order to assess the circuit changes required, it was necessary to gather data from the plant when operating with both normal-calc ore and high-calc ore. To achieve this, a team from Hatch and Vietti Slurrytec visited Rössing from 7–13 April 2016. Rössing arranged for both normal and high-calc material to be campaigned through the plant during the test work. For these tests, the low-calc sample had a calc index of approximately 8 kg/t and the high-calc a calc index of approximately 16 kg/t.

Samples were taken of the CCD circuit feed. The test work included both static and dynamic settling tests aimed at identifying the optimal thickening conditions for high-calc

Optimization of the Rössing countercurrent decantation circuit for high-calc ore

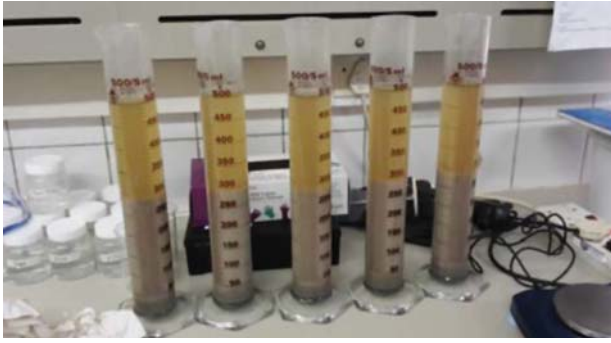


Figure 4—Static sedimentation tests

ore. In addition, SCADA data was collected from site, coinciding with normal and high-calc conditions, to assess the change in plant performance as a result of the feed material.

Static sedimentation tests

Test work was performed using a series of 500 ml measuring flasks as shown in Figure 4. The static sedimentation tests included:

- Flocculent type screening
- Optimization of the feed slurry solids concentration
- Optimization of flocculent demand
- Static settling rate.

Bench-top dynamic settling tests

The dynamic thickening tests were designed to determine:

- The optimum thickening area required for a specific process mass flow (t/h)
- The mud bed accumulation and consolidation properties under dynamic batch operating conditions, on which a suitable control philosophy for a thickener can be based.

The tests were conducted in a 100 mm diameter bench-top dynamic thickener test rig, simulating high-rate (no pickets on the rake) thickening conditions. The dynamic tests included:

- Solids flux tests
- 24 h mud bed consolidation tests.



Figure 5—100 mm bench-top dynamic thickening test rig used

Note that the underflow densities obtained during the bench-top dynamic thickening tests are based on a 100–200 mm mud bed height and therefore essentially exclude the effect of extended mud bed height and residence time on the consolidation behaviour of the material. In order to fully assess the maximum underflow density achievable by full-scale thickening, further mud bed consolidation test work at a semi-pilot scale would be required.

Results

Particle size distribution

The particle size distribution of the CCD feed was measured during the survey. As expected, the high-calc material has a finer size distribution than normal material (Figure 6). This is most likely due to the softer ore components such as calcite affecting the grind in the mills, as well as increased leaching of the gangue minerals in the leach circuit.

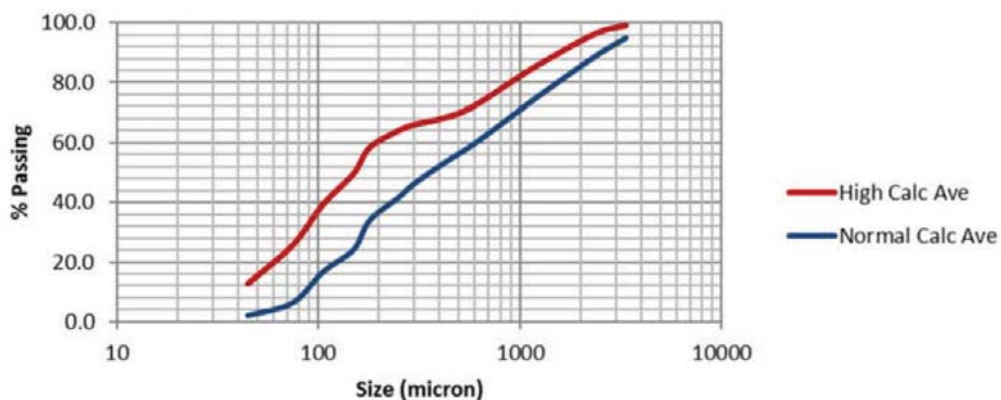


Figure 6—Average particle size distributions of normal and high-calc material during the survey

Optimization of the Rössing countercurrent decantation circuit for high-calc ore

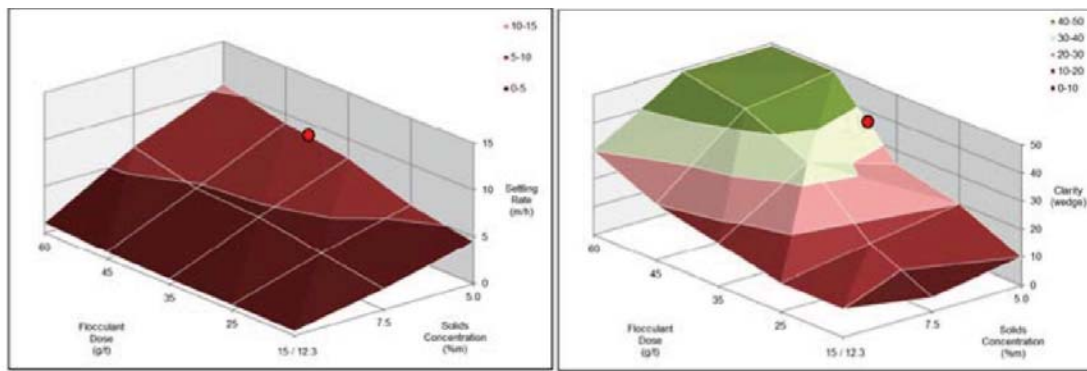


Figure 7 – Settling rate and overflow clarity at various flocculent dosages and feed concentrations for high-calc ore

Static sedimentation tests

Static sedimentation tests considered a range of flocculent dosages and feed densities and evaluated their impact on both settling rate and overflow clarity. Results of the high-calc ore settling tests are shown in Figure 7.

Figure 7 shows that although thickener performance is affected by flocculent dosage, the dominant factor in determining settling rate and clarity for high-calc ore is the feed solids concentration. At the current feed solids concentration of 12.3% (m/m) to the smaller 42.7 m thickeners, flocculent dosage has little impact on the settling rate and must be increased to 60 g/t of CCD feed to achieve the target clarity of 30.

In contrast, a decrease in the feed solids concentration to 5% m/m resulted in an order-of-magnitude increase in the settling rate. However, a flocculent dosage of more than 35 g/t was still required to achieve the target clarity of 30.

The recommended plant conditions based on the static sedimentation tests are summarized in Table I. Although a feed concentration of 5% m/m solids was tested in the static sedimentation tests, a value of 6% m/m was considered more practical for the dynamic thickening tests.

Dynamic sedimentation tests

The effect of optimizing flocculent and feed concentration conditions was assessed in a series of dynamic settling tests. In these tests, the solids flux was varied to determine the capacity limitations of the thickeners. In the current operation, the small thickeners operate at a solids flux of 0.08 t/h/m² and the large thickeners at 0.12 t/h/m².

The low-calc sample was tested at the current plant feed concentration and flocculent dosage (refer Table I). The high-calc sample was tested at both the current plant conditions and at the recommended optimized conditions.

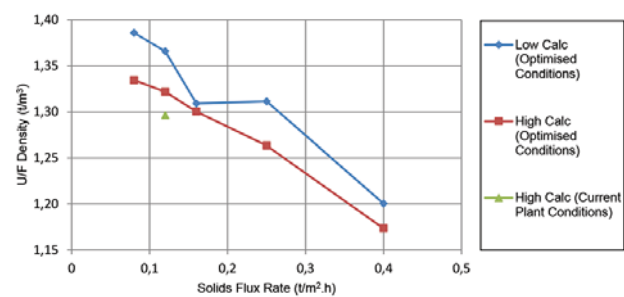


Figure 8—Effect of high-calc material on underflow density

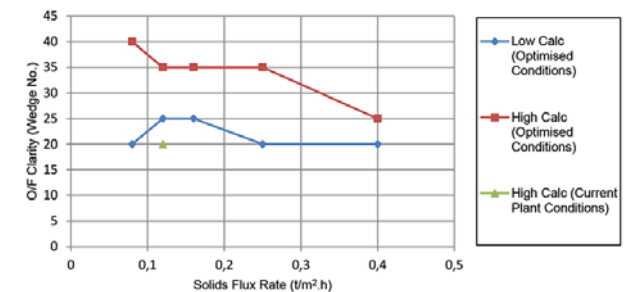


Figure 9—Effect of high-calc material on overflow clarity

Figures 8 and 9 show that at current plant conditions, the high-calc material results in a lower underflow density and overflow clarity than normal-calc material.

Should the plant conditions be optimized as recommended in Table I, a higher underflow density and overflow clarity can be achieved for high-calc material than with current plant conditions.

Table I		
Optimum thickener conditions based on static sedimentation test work		
Operating conditions	Current practice for normal calc (42.7 m) thickeners	Optimum for high-calc
Feed solids concentration (in feedwell)	12% m/m	6% m/m
Flocculent dosage	30 g/t CCD feed	45 g/t CCD feed

Optimization of the Rössing countercurrent decantation circuit for high-calc ore

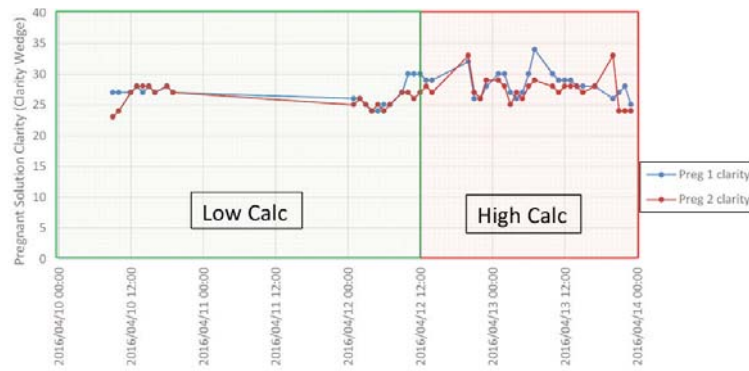


Figure 10—Pregnant solution clarity

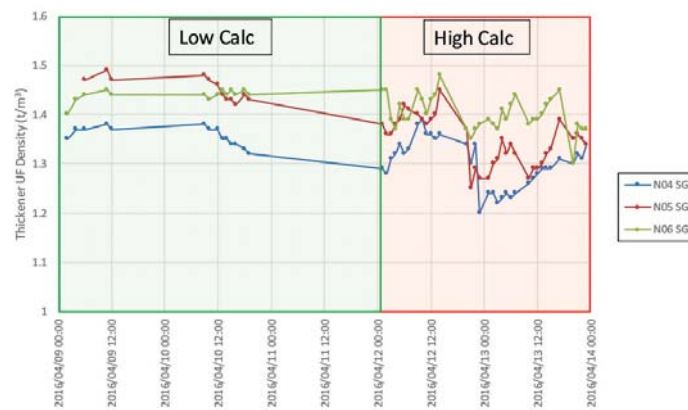


Figure 11—Thickener underflow density in large thickeners

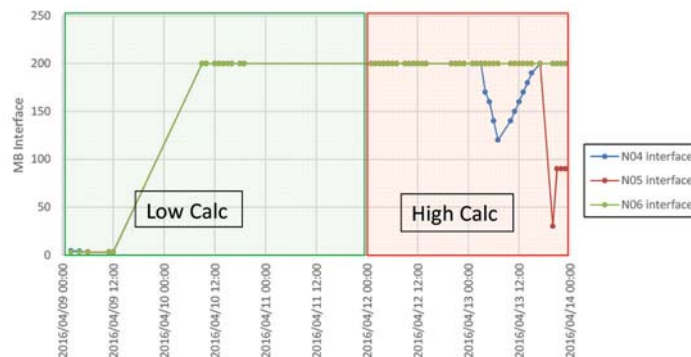


Figure 12—Interface measurements in the large thickeners

SCADA data

The thickener overflow clarity during the plant campaign is shown in Figure 10. The solution clarity was relatively stable, between 24 and 28 for the normal-calc run. Interestingly, this improved to between 25 and 34 for the high-calc run, but was still mostly below the target clarity of 30.

This agrees with the data in Figure 7, which shows that the clarity target of 30 is very difficult to achieve at this feed density unless flocculent dosages are increased to approximately 60 g/t. Currently, the flocculent dosage is maintained at approximately 30 g/t. Further dilution of the feed would be required to improve clarity levels should the flocculent dosage not be substantially increased.

The underflow densities in the large thickeners were found to decrease for high-calc material. Significantly, the final target density target of 1.45–1.48 could not be achieved in the terminal thickener (thickener 6). This would have implications both for the overall plant water balance and the uranium recovery, as more water and dissolved uranium would report to the slimes dam under high-calc conditions. Based on wash efficiency calculations, it is estimated that a decrease in underflow density in the terminal thickener from 1.45 to 1.39 would result in a 1.0% loss in recovery, due to increased soluble losses.

It is interesting to note that the underflow densities were fairly erratic for the high-calc period, indicating difficulty in

Optimization of the Rössing countercurrent decantation circuit for high-calc ore

maintaining stable conditions using the current control philosophy.

Figure 12 shows that despite the considerable variability in underflow density and overflow clarity during the campaign, the interface measurements were virtually unchanged at 200 cm in the large thickeners. This indicates that the interface measurement is fairly unreliable for diagnosing the thickener performance. This could be due to the interface measurement being taken from the side of the thickener, far away from the underflow withdraw point in the centre, where the interface may be more variable.

It was noted during the campaign that the feedwells appeared to create 'pluming' on the opposite end of the feed trough, due to the slurry being directed downward into the feedwell instead of tangentially (Figure 13). It is speculated that these flow patterns may be eroding the bed near the feedwell, whereas the bed level at the sides of the thickener is largely unaffected.

Computational fluid dynamics analysis

A computational fluid dynamics (CFD) model was developed for the existing launder and feedwell using Star CCM+ v11 for mesh generation, solution, and post-processing. The CFD model was able to simulate the flow velocities, flow distribution, strain rate, residence time *etc.*, as well as the location of the ensuing free surface between the flowing slurry and the air. The CFD models applied to this problem used a highly refined mesh with a volume of fluid (VOF)



Figure 13—Problematic flow patterns resulting from thickener feedwell arrangement

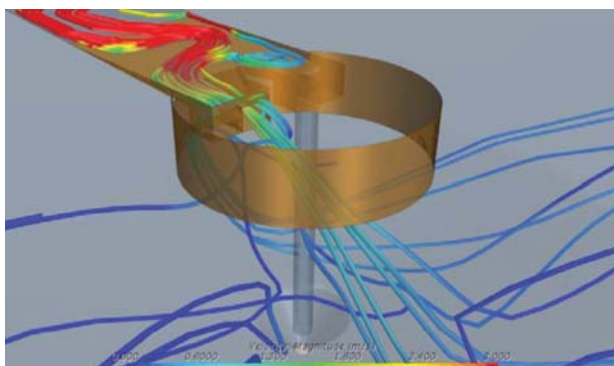


Figure 14—Flow patterns resulting from deflector plates at end of launder

model to resolve the slurry-air interface solved with a Reynolds Averaged Navier-Stokes (RANS) solver to time-average the turbulent flows in the launder, the flow control vanes, and the feedwell.

Using this tool, the flow patterns in the existing feedwells were further investigated and the mode of discharge into the thickener feedwell was modelled. Flow was found to be directed diagonally downwards by the deflector plates at the end of the launder (Figure 14).

These downward flow patterns are consistent with pluming, which has been observed on the surface of the thickener (refer Figure 13). The flow patterns are also associated with short-circuiting of particles out of the feedwell, and poor mixing of the flocculent.

Summary of findings

Based on the bench-scale test work, the SCADA data, and the CFD modelling, the key issues affecting the thickener performance appeared to be the feedwell design and the process control methodology. Static sedimentation tests showed that the current feed concentrations of 10–12% m/m were associated with poor settling rates and poor overflow clarity for both normal and high-calc conditions. A reduction to 6% m/m (in the feedwell) was likely to produce a substantial improvement in settling rates and overflow clarity for both material types. This is confirmed by site experience, where the plant must run on three mills instead of four when processing high-calc ore, as this dilutes the feed to the CCD circuit, reduces the solids flux rate, and improves settling performance.

The underflow density and overflow clarity were generally found to be highly variable for high-calc ore using the current process control methodology. Tighter control of these parameters would prevent short periods of low underflow density and poor clarity, and thereby improve the average underflow density and overflow clarity.

Recommended circuit modifications

Alternative feedwell design

In order to address these issues, modification of the feedwells was investigated. A key aim was to promote a tangential flow pattern within the feedwell to dissipate slurry momentum and promote better mixing of the flocculent with the solids, in line with the recommendations from the literature (Fawell *et al.*, 2009). To achieve this, flow needed to be introduced tangentially into the feedwell, and a shelf was included to create an upper zone for mixing and a lower zone for aggregate growth. The resulting tangential flow pattern increased the slurry residence time in the feedwell and created a volume of improved shear conditions for flocculation.

Following an on-site investigation, it was decided to keep with the existing feed launders rather than replace them with a pipe-fed arrangement. This was partly due to the cost considerations (demolition costs, additional piping, and engineering) and partly because the feed launders were already known to result in significant flocculation of the feed. Furthermore, due to the brownfield environment, it was necessary to minimize the downtime for installing the feedwell modifications.

Optimization of the Rössing countercurrent decantation circuit for high-calc ore

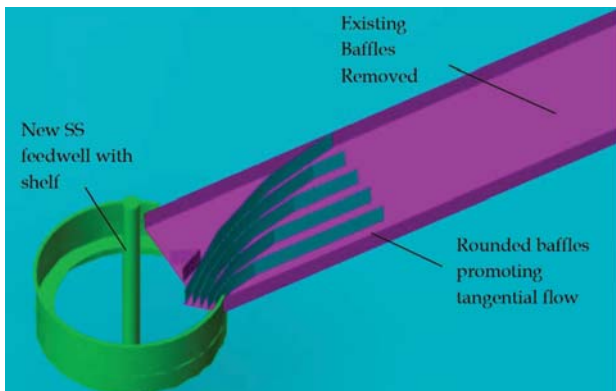


Figure 15—Proposed feedwell modifications

The baffles on the launders were removed in order to promote a more quiescent flow. Rounded stainless steel baffles were welded to direct flow tangentially into the feedwell. The existing fibre-reinforced plastic (FRP) feedwell was replaced with a new stainless steel rubber-lined feedwell with shelf to improve slurry retention time (Figure 15). This concept was tested in the CFD environment (Figure 16) and was found to produce good tangential flow with substantially improved slurry retention time and reduced short-circuiting of slurry out of the feedwell.

The tangential flow patterns produced by the feedwell modifications were found to result in high pressure gradients on the edge of the feedwells. This situation makes the addition of autodilution slots extremely challenging, as a simple opening in the feedwell will not result in liquid flowing into the feedwell to dilute the slurry. When autodilution slots were added to the feedwell, these regions of high pressure

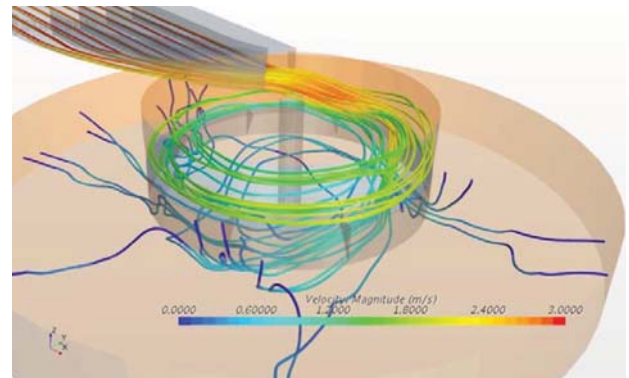


Figure 16—Modified 'shelf' feedwell design

forced slurry out of the feedwell, rather than into the feedwell to dilute the incoming slurry. Various permutations of the autodilution slots were tested; however, the high pressure gradient due to tangential flow meant that liquid was found to consistently flow out of the feedwell, rather than in.

Due to the difficulties in achieving autodilution using the modified feedwell design, Hatch engaged with various vendors to determine whether an alternative, forced dilution system could be implemented. The replacement option was focused on the larger 68.5 m thickeners, as these thickeners receive a higher feed concentration of 27.3% m/m solids, compared to 12.3% m/m solids on the smaller thickeners.

Several of the vendors engaged were not able to make their existing designs fit into the Dorr Oliver and EIMCO thickeners due to the low wall height and truss rake design of these thickeners. This led to tenders for quotations for

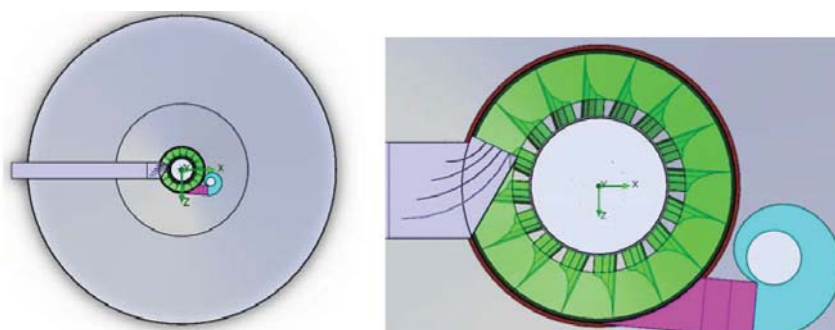


Figure 17—Top view of Radflow feedwell and ETAQ dilution pump retrofit

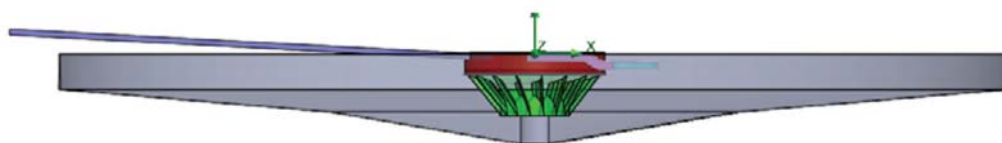


Figure 18—Front view of Radflow feedwell and ETAQ dilution pump retrofit

Optimization of the Rössing countercurrent decantation circuit for high-calc ore

complete replacement of the rake, heightening of the walls, and replacement of the feedwell. The costs were similar to those for total replacement of the thickeners. This was deemed too expensive for the project and was discarded as an option.

One vendor (Roytec) applied a more fit-for-purpose approach of adjusting their feedwell design to match the existing thickener constraints, and proposed a design based on their Radflow™ feedwell with ETAQ™ dilution pump (Figures 17 and 18).

As with the modified feedwell design, the design utilizes the existing launder rather than incorporating a pipe feed arrangement. This was done to minimize the cost and complexity of the thickener modification.

The feedwell is designed in two parts, with the upper section fixed to the central torque cage and the lower vanes mounted on the rake. A 600 mm clearance has been provided to allow for lifting of the rake.

The design incorporates a 1.4 m ETAQ dilution pump (shown in Figure 17 in light blue), which pumps up to 4500 m³/h of dilution water into the feedwell. This is substantially greater than what the current recycle pumps on the large thickeners can deliver (852 m³/h). These current pumps are limited by the NPSH and cannot be further upgraded.

Table II compares the feedwell dilution with the current (external) dilution pumps and the proposed ETAQ (internal) dilution pumps. Note that the feed densities for the large thickeners in Table II are higher than the feed density for the

smaller thickeners (refer Table I), since these thickeners are located further down the CCD train and are fed by the underflow of the preceding stage.

The use of internal dilution pumps will enable a substantial reduction in the feed solids concentration from 27.3% to 9.4% solids. Further increasing the feed dilution to 6% m/m was found to be impractical for the large thickeners, due to the limitations of the large custom retrofit feedwell size required to support such large volumes of dilution water. However, it is believed that the reduction to 9.4% m/m will substantially improve the settling rate and overflow clarity, and reduce flocculent consumption, as per the trend demonstrated in the settling test work (refer Figure 7).

In addition to the higher dilution within the feedwell, the Radflow feedwell incorporates custom-designed vanes, which effectively break the tangential component of the flow as it exits the feedwell. This prevents the vigorous flow within the feedwell from disturbing the bed below.

The Radflow design was found to provide high flow (approx. 2 m/s) and shear within the feedwell (Figure 19), with significant energy dissipation through the vanes below the feedwell. The vanes effectively stop the tangential component of flow as slurry exits the feedwell and project the slurry out radially, at sufficiently low velocity to allow effective settling.

Process control enhancements

Based on the SCADA data obtained during the high-calc plant trial, the following weaknesses were identified in the current control philosophy:

- Variation of underflow pump speed is not coupled with variation of the flocculent dosage to the downstream thickener, often resulting in under- or overdosing of flocculent
- Manual sampling can only be done at hourly intervals, leading to slow reaction times to process upsets
- Inaccuracy of Marcy scale density data due to sampling and measurement errors
- Bed interface measurement taken at perimeter of thickeners, where changes in the bed characteristics are less apparent.

Scenario	Recycle flow rate (m ³ /h)	Solids in feedwell (% m/m)
No dilution pump	0	49.0%
External dilution (current)	852	27.3%
Internal dilution	4500	9.4%

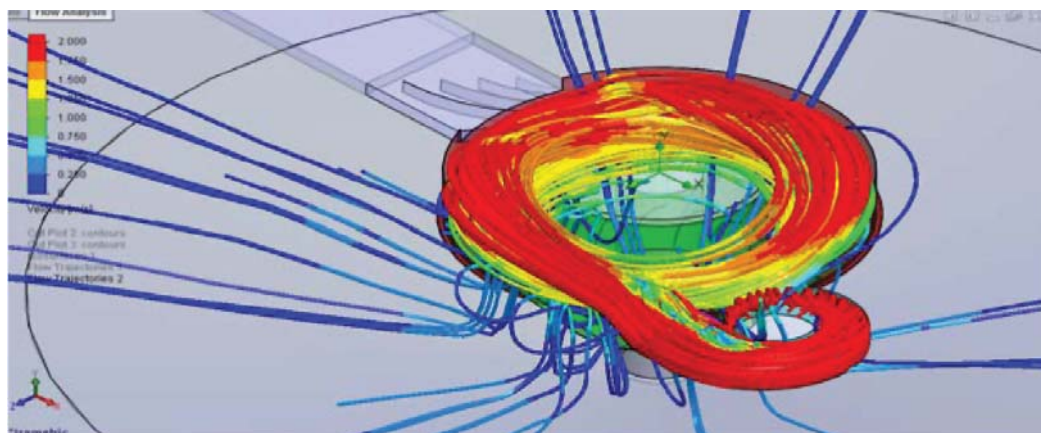


Figure 19—Isometric view of flow trajectories in the Radflow feedwell

Optimization of the Rössing countercurrent decantation circuit for high-calc ore

These weaknesses tend to result in high variability of underflow densities, sub-optimal flocculent dosing, below-target overflow clarity, and reduced washing efficiency. In particular, the washing efficiency is strongly affected by the density in the terminal thickener, as this thickener determines the water losses to the tailings dam.

In order to improve the overall CCD performance, it is proposed that the thickener control philosophy be automated by installing density probes on the underflow of each thickener and two mud bed interface indicators on the final two thickeners in the train (thickeners 6 and 7).

It is recommended that a total of eight density probes be installed on the CCD circuit; (two per large thickener, as each thickener has two underflow lines). These density meters will be calibrated and wired back to the SCADA system. A density set-point will be set in each thickener and the speed of the underflow pump will be varied to hold the set-point. Thickener torque will also be monitored and the pump speed will increase should the specified torque limit be exceeded.

The density measurement and pump speed will be combined and used as the measured variable for varying the flocculent dosing to the subsequent thickening stage. This means that as the mass of solids reporting to the downstream thickener increases, the flocculent dose will increase accordingly. This improvement will effectively remove the need for manual sampling for underflow density, although overflow clarity will still be monitored and used to adjust the flocculent set-point in terms of grams per ton.

A mud bed level probe will be installed on the terminal thickener (thickener 7) to monitor the mud bed interface to the desired set-point. The intention is to maintain a consistently high mud level in order to maximize the mud bed residence time and consolidation. This is particularly important on the terminal thickener as it will allow the thickener to target the maximum possible underflow density, regardless of the material processed (high-calc vs. low-calc).

The mass of slimes pumped to the tailings dam is critical, since this slimes material is mixed with the coarse sands material in the Paddy X tailings system and provides a suspension medium for pumping. Should insufficient slimes be available, the integrity of the tailings pumping system is put at risk. For this reason, it was important to include a mud bed interface indicator on thickener 6 as well as thickener 7 to maintain a high level of slimes inventory. At times when thickener 7 is bypassed, thickener 6 will run as the terminal thickener and must provide the maximum underflow density to ensure good wash efficiency is maintained.

Conclusion

The Rössing Uranium CCD circuit has come under increasing pressure in recent years due to the addition of high-calc ore to the circuit. This material was found to be associated with poor overflow clarities and reduced underflow densities.

In order to quantify the reasons for poor performance, bench-scale test work on the thickener feed was undertaken. This test work suggested that good thickener performance could still be obtained for high-calc ore provided conditions were optimized. Key areas identified for optimization were the feed density and process control.

Two alternative feedwell designs were developed to improve settling performance: one simple shelf design, and one Radflow™ design with an internal pump for forced dilution. It was recommended that the shelf design be implemented on the smaller thickeners where feed dilution is less important. The forced dilution feedwells are recommended for implementation on the larger thickeners, which are supplied with a higher feed concentration.

An automated control system was also devised, comprising eight density meters and two mud bed interface indicators. This will improve the consistency of underflow densities and allow the flocculent to be controlled automatically based on the feed from the preceding stage.

These changes are currently being phased in at Rössing, with the first feedwell planned for the terminal thickener (thickener 7) and the process control upgrades planned for the large thickeners.

Acknowledgements

The authors gratefully acknowledge the support of Rössing Uranium in allowing us to present this paper. In particular, the inputs of Mr Rudolf Shipapo, Mr Messag Kamati, and Ms Leilanie Feris are gratefully acknowledged. The authors would also like to thank Vietti Slurrytec, who assisted with the test work and analysis. Duane Baker and Jennifer Woloshyn of the Hatch Special Engineering and Design Group are acknowledged for their CFD analysis of the existing feedwell, as well as the testing of the modified 'shelf' feedwell concept. The inputs from Roytec in developing the forced dilution feedwell design are also gratefully acknowledged, in particular Alex Krassnokutski, who tested the Radflow design, both in the CFD environment and using various scale models.

References

- FAWELL, P.D., FARROW, J.B., HEATH, A.R., NGUYEN, T.V., OWEN, A.T., PATERSON, D., RUDMAN, M., SCALES, P.J., SIMIC, K., STEPHENS, D.W., SWIFT, J.D., and USHER, S.P. 2009. 20 years of AMIRA P266 'Improving Thickener Technology' – How has it changed the understanding of thickener performance? *Paste 2009: Proceedings of the 12th International Seminar on Paste and Thickened Tailings*, Viña del Mar, Chile, 21-24 April 2009. Australian Centre for Geomechanics, Nedlands, Western Australia. pp. 21-24.
- KRASSNOKUTSKI, A. 2012a. Radflow™ – The next generation feedwell. *Paste 2012: Proceedings of the 15th International Seminar on Paste and Thickened Tailings*, Sun City, Pilanesberg, South Africa, 16-19 April 2012. Australian Centre for Geomechanics, Nedlands, Western Australia. pp. 121-128.
- KRASSNOKUTSKI A., 2012b. Development of the next generation thickener featuring the Radflow™ feedwell technology. *Proceedings of Procemin 2012*, Santiago, Chile. Doll, A., Kracht, W., and Kuyvenhoven, R. (eds). Gecamin Ltda, Santiago.
- TRIGLAVCANIN, R.A. 2008. The heart of thickener performance. *Paste 2008: Proceedings of the Eleventh International Seminar on Paste and Thickened Tailings*, Kasane, Botswana, 5-8 May 2008. Fourie, A., Jewell, R., Slatter, P., and Paterson, A. (eds.). Australian Centre for Geomechanics, Nedlands, Western Australia. pp. 63-81. ◆

Realising possibilities from mine to market.



WorleyParsons adds value through our full scope of services from pit to port including studies, mine planning, impact assessments, permitting and approvals, project management, construction management and global procurement.

Our Mining Centre of Excellence in Johannesburg has niche expertise in underground and open cast mining and provides quality project development and engineering solutions for small to large projects across all areas of base metals, the coal supply chain, chemicals, ferrous metals, alumina, aluminium and iron ore.

Supported by the WorleyParsons global group, we pride ourselves on customising solutions for local environments and committing to our customers' goals.



www.worleyparsons.com wprsainfo@worleyparsons.com



>> 6-7 June 2018
>> Johannesburg, South Africa

Whatever terminology you wish to use, it is obvious is that the world of work is changing rapidly.

The Mining Industry, along the Mining Value Chain, has to be a part of this in order to remain competitive, and to reach its ambition of Zero Harm.

Mining businesses in Africa need to join this journey, to stay alive, or be left behind. This event is a showcase and learning experience for everyone people associated with the Mining Industry, to learn about Global Best Practices, to network with global leaders in mining and other businesses, and to do so in an exciting and interactive format that we have never used before.

Be prepared to be **BLOWN AWAY** and to come away excited, informed and modernized!

FOURTH INDUSTRIAL DIGITAL REVOLUTION REVOLUTION Mining Value Chain

Mining **DON'T MISS THE BOAT!**

THE DIGITAL TRANSFORMATION JOURNEY



Contact: Conference Co-ordinator, Yolanda Ndimande · Tel: +27 11 834-1273/7
Fax: +27 11 833-8156 or +27 11 838-5923
E-mail: yolanda@saimm.co.za
Website: <http://www.saimm.co.za>



Polythionate formation during uranium recovery from sulphide flotation concentrate

by V. Yahorava and V. Bazhko

Synopsis

Uranium recovery by resin-in-pulp (RIP) from sulphide-bearing material was found to be adversely affected by polythionate formation due to partial oxidation of sulphide minerals. Polythionates are loaded more selectively by the conventional strong-base resins used at uranium plants.

A study was undertaken to identify whether polythionates are formed during upstream processing, leaching, or ion exchange recovery steps. It was found that polythionate formation could be minimized by shortening of the leach time, optimizing oxidant and acid addition, minimizing delay between leaching and RIP, and maintaining the neutralization and adsorption retention times as short as possible.

These insights could prompt the development of mitigation strategies on commercial plants to reduce or avoid the formation of polythionates and the adverse impact it has on uranium recovery.

Keywords

uranium recovery, resin-in-pulp, polythionate formation.

Introduction

South Africa has approximately 320 000 ha of surface area covered by gold tailing dumps containing 0.2–0.4 g/t gold and up to 0.7% sulphides as well as around 100 g/t uranium. During the boom in uranium prices around 2007, the re-processing of dumps at gold mines for both gold and uranium recovery became economically attractive. A number of flow sheets were developed, all of which included flotation of a sulphide concentrate followed by uranium leaching and removal via ion exchange prior to gold recovery (Fleming, Brown, and Botha, 2010; van Rensburg and Mashaba, 2016).

The flotation concentrates generated through re-processing of gold dumps typically contain 100 to 900 mg/kg uranium oxide (U_3O_8) (van Rensburg and Mashaba, 2016; van Tonder and Kotze, 2007; Fleming, Brown, and Botha, 2010). RIP technology is often considered for the recovery of uranium from the low-grade slurries (<900 mg/L U_3O_8) due to the cost benefit associated with elimination of the solid/liquid separation step.

In recent years a number of cases have been observed in the Mintek laboratories where unexpectedly low uranium loadings onto the resin were achieved during RIP tests.

In all cases the material treated contained sulphide minerals at various concentrations (1.5% up to 35% S^{2-}). Preliminary investigations revealed that the formation of polythionates in the sulphide-bearing pulp and their co-loading onto strong-base resin adversely influenced uranium adsorption.

This paper presents three case studies where this phenomenon was observed, as well as an evaluation of the conditions conducive to polythionate formation and mitigation strategies that have been identified for preventing/minimizing the inhibition of uranium loading.

Experimental

Parameters of the experiments such as temperature, pH, addition of oxidant, type of resin and others were chosen according to the preferences of a specific client.

Uranium leach procedure

Air-dried solids were slurried using either Rand Water Board or mine process water to achieve a slurry specific gravity of 1.45 (in case 1) or 50% (m/m) solids (in cases 2 and 3). Leaching was performed at pH 1.5 for 24 hours with pH control by manual addition of 800 g/L sulphuric acid (pH and Eh were controlled every hour for the first 8 hours). Temperature was either controlled at 50–60°C (cases 2, 3, and 4) or left at ambient (case 1). The pH and Eh were measured and recorded hourly. Manganese dioxide (MnO_2) was added as oxidant to maintain the Eh at 450 mV (vs. Ag/AgCl) as required.

* Mintek, Randburg, South Africa.

© The Southern African Institute of Mining and Metallurgy, 2018. ISSN 2225-6253. This paper was first presented at the Uranium 2017 International Conference, 12–13 September 2017, Swakopmund Hotel, Swakopmund, Namibia..

Polythionate formation during uranium recovery from sulphide flotation concentrate

pH adjustment of the leach slurry was conducted either at ambient temperature or at 50°C by addition of 20% (m/m) lime (Ca(OH)₂) slurry. The pH was adjusted to either 3 or 3.5–3.8, depending on the case studied.

Resin preparation

Purolite A500/2788 RIP-grade strong-base type I resin was used for the test work. In cases 1 and 2 the resin in sulphate form was pre-fouled with silica up to approximately 15% SiO₂ by two cycles of contact with a freshly-prepared 3 g/L silica (SiO₂) solution at pH 1 for 24 hours in rolling bottles at a solution-to-resin ratio of 10 to 1. At the end of each cycle, the resin was washed with deionized water.

In case 3 the resin was used 'as is' after conversion into the sulphate form by passing four bed volumes (BVs) of 1M H₂SO₄ through the resin bed at a flow rate of 2 BV/h. After contact with the acid, the resin was washed with deionized water until the water exited the column at pH 2.

Resin-in-pulp equilibrium isotherms

Equilibrium adsorption isotherms were generated by batch contacting the pretreated resin and the pulp at different contact ratios over 24 hours at ambient temperature. The resins were separated from the pulp using a 600 µm screen. The pulp was filtered and the solids repulped (water-to-wet solids mass ratio of 2:1) and then washed (at a mass ratio of 1:1) using pH-adjusted deionized water (pH of the wash water was adjusted to 3.5).

The resin removed from each equilibrium contact was washed with deionized water to remove entrained solids and solution and was then either eluted with 30 BVs of 2M nitric acid (HNO₃) and 25 BVs of 1M sodium hydroxide (NaOH) or dried and analysed directly for uranium and other impurities.

Analysis

Depending on the focus and level of detail required, either ICP-OES/ICP-MS or XRF was used for the analysis of base metals and uranium in solution and solids.

Sample	S, %	U ₃ O ₈ , mg/kg	Fraction <38 µm, %
Sample 1	10–15	136	43
Sample 2	25–30	213	63
Sample 3	1.52	195	48
Sample 4	6.19	96	90

Sample	Mg	Al	SiO ₂	Ca	Mn	Fe	Co	Ni	Cu	Zn	S, g/L	As	U ₃ O ₈
1	928	964	3062	495	235	7410	47	169	72	90	11	104	124
2	762	868	2640	510	211	7950	62	213	81	91	10	127	140
1*	837	1160	1090	459	292	7250	25	115	57	148	9.7	74	207

*PLS generated on site with freshly produced Sample 1

Results and discussion

Four different samples of flotation concentrates were used in the study, their uranium and sulphide contents are provided in Table I.

Case 1: High sulphide content

Problem identification

Two flotation concentrates, produced during a mini-pilot plant campaign conducted by Mintek at a South African gold mine, were received and were labelled sample 1 and sample 2. The samples were air-dried prior to being prescreened and blended in preparation for the test work.

Leaching of both samples resulted in approximately 80% U₃O₈ extraction into solution. The pregnant leach solution (PLS) composition is provided in Table II. The pH was controlled between 1.5 and 1.7; no oxidant was added and the Eh ranged naturally between 414 and 422 mV (Ag/AgCl).

After 24 hours of leaching, the pH of the pulp was adjusted to 3 by the addition of lime as dry powder over 3 hours prior to the ion exchange tests, which were conducted within about 1 hour of pH adjustment.

The uranium equilibrium adsorption isotherms obtained with Purolite A500 resin at pH 3 are presented in Figure 1.

The 'displacement' shape of the equilibrium isotherms (particularly pronounced for sample 2) indicated the presence of species that adsorbed more selectively than uranium and hence displaced uranium from the resin at higher pulp-to-resin ratios. A detailed investigation of potential competing ions in the leach liquors then followed, whereby the presence of such anions as nitrates, chlorides, and phosphates was ruled out.

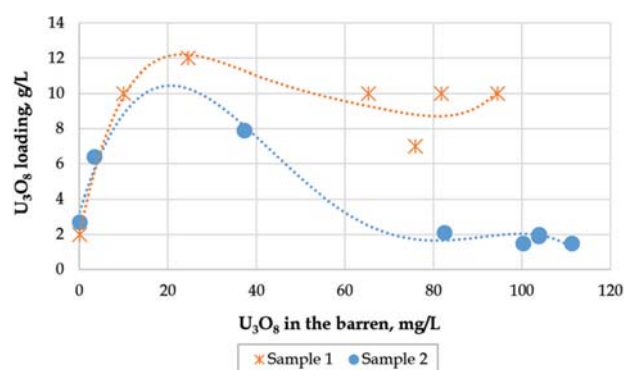


Figure 1—Uranium equilibrium adsorption isotherms: samples 1 and 2, pH 3

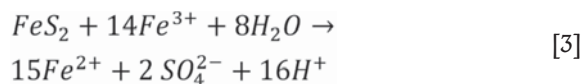
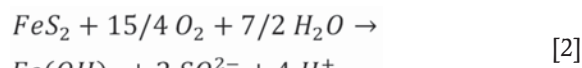
Polythionate formation during uranium recovery from sulphide flotation concentrate

The main characteristic of the samples evaluated during case 1 was the high concentration of sulphides (10–15% for sample 1 and 25–30% S²⁻ for sample 2). Unexpectedly, sulphur was detected in caustic eluates produced during silica stripping with HNO₃ after uranium elution. This suggested the presence of sulphur species like polythionates as the reason for the poor uranium adsorption of the anion exchange resin. Polythionates (S_nO₆²⁻ where n > 3) are known to be strong competitors for the exchange sites of the resin and can be eluted from the resin by treatment with caustic solution (Schmiedel, 1984).

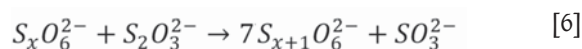
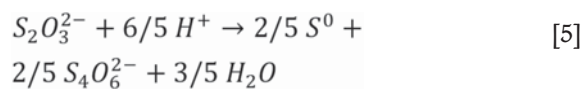
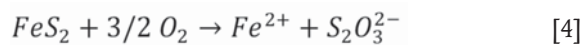
Formation of polythionates: some theory

Polythionates can be produced during leaching, milling, and flotation of materials that are rich in sulphides (Vongprom, Hawboldt, and Bottaro, 2008; Rempel and Chanda, 1986).

During oxidative leaching of uranium-containing material, dissolution/oxidation of pyrite occurs and can be described by the following equations:



The oxidation of sulphur results in the formation of sulphate, SO₄²⁻ as a final product. However, it has been shown by a number of researchers (Druschel and Borda, 2006; Descostes, Vitorge, and Beaucaire, 2004) that metastable sulphur species can be formed by FeS₂ oxidation;



The formation of polythionates depends on leaching conditions (Lowson, 1982; McKay and Halpern, 1958; Woodcock, 1961). Tetrathionate formation has been reported as a product of pyrite oxidation at pH 2.9–8.6 in the presence of molecular oxygen, at pH 8 in the presence of MnO₂, and at pH 2 in the presence of Fe(III) (Schippers, 2004). Other sources state that in order to minimize formation of polythionates during leaching, it is necessary to maintain the acid concentration at greater than 5 g/L H₂SO₄ (Nugent, 1956; Druschel and Borda, 2006). Under these conditions the polythionate concentrations were reported to be in the order of 20–30 mg/L S and not to constitute a serious problem. Should the acid concentration during leaching drop to a value ≤ 1 g/L for a period of an hour, polythionates exceeding 100 mg/L S can be formed, with serious consequences for the ion exchange process.

The degradation of polythionate strongly depends on pH and on the availability of catalysts such as pyrite and heavy metals. It has been reported that the overall rate of polythionate oxidation is markedly slower than the rate of oxidation of thiosulphate (forming polythionate) in acidic, ferric-rich solutions (Druschel, Hamers, and Banfield, 2003). In contrast, polythionate degrades at low pH in the presence of sulphide (FeS₂) (Schippers, 2004).

In summary, it is suggested that polythionates can be formed during:

- Mineral processing ahead of leaching (comminution, flotation, drying)
- Leaching at pH 1.5–1.8
- During the relatively long time intervals between leaching, neutralization, and the resin contacts, or during RIP (which was run over 24 hours).

Mitigation strategies for uranium recovery

The first mitigation strategy evaluated was polythionate destruction by Eh adjustment to 500 mV (Ag/AgCl) at pH 3.0–3.5. Hydrogen peroxide and lime were used as oxidant and neutralizing reagents respectively, and the procedure was tested on aged leach slurry of sample 2 (exhibiting the highest sulphide content). The uranium loading achieved at high pulp-to-resin ratio improved from 1.3 g/L from the slurry 'as is' (Eh 280 mV, pH 3.5) to 26.2 g/L from the pre-oxidized sample (Eh 500 mV, pH 3.5). This suggests that the species (suspected to be polythionates) competing with uranium for the ion exchange adsorption sites was destroyed by oxidation. The final barren concentrations achieved were similar, *i.e.* 119 and 100 mg/L U₃O₈ respectively. However, the oxidation of polythionates might not be attractive economically due to the increased OPEX associated with the reagent costs.

The second strategy evaluated was replacement of the strong-base resin (with high affinity for polythionates) with a chelating resin that is not selective to anionic species. RIP tests were conducted using RIP-grade iminodiacetic PuroLite S930 resin. The pulp generated during the leaching of sample 2 was used for these RIP tests, with the pH controlled at 3.5 by addition of sodium hydroxide (NaOH). The equilibrium adsorption isotherm generated is presented in Figure 2, together with the isotherm obtained for the same pulp with the strong-base PuroLite A500 resin for comparison.

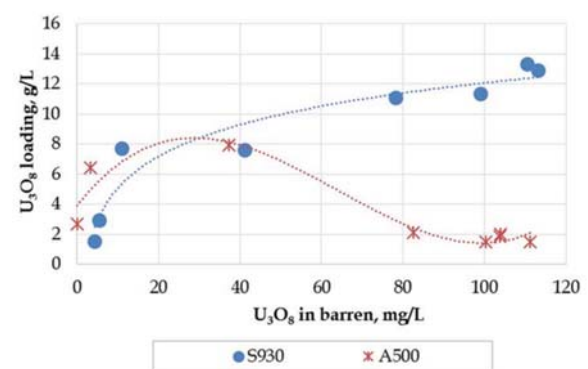


Figure 2—Uranium recovery from polythionate-bearing pulp by strong-base (A500) and chelating (S930) resins at pH 3.5

Polythionate formation during uranium recovery from sulphide flotation concentrate

The iminodiacetic resin recovered uranium more efficiently from polythionate-bearing pulp than the strong-base resin, although high co-loadings of base metals like aluminium, copper, iron, nickel, and zinc were observed. Selective elution or additional purification steps will therefore be required for downstream processing of the uranium eluate if this resin is used for uranium recovery from polythionate-bearing pulp.

The prevention of pyrite oxidation (which initiates the formation of the intermediate sulphur species appearing in Equations 4 to 7 prior to, during, and after leaching) is likely to be an economically attractive option. This concept was tested using a flotation concentrate (with 10–15% sulphide content) that had been kept 'fresh' at the mine by storage under water. The sample was leached at pH 1.8 over 8 hours with mild agitation of the slurry to minimize oxygen ingress, which could lead to sulphide oxidation. The composition of the leach liquor obtained appears in Table II; the final Eh was 422 mV (Ag/AgCl). The slurry was neutralized to pH 3.5 immediately and subjected to ion exchange test work with resin pre-fouled with approximately 12.5 % SiO₂.

The equilibrium adsorption isotherms are shown in Figure 3.

An equilibrium loading of approximately 25 g/L U₃O₈ was achieved at a barren concentration of approximately 80 mg/L U₃O₈ in solution, which is much improved compared to the loading of approximately 10 g/L obtained from the aged sample 1 at a barren concentration of 80 mg/L U₃O₈ in solution.

The strategy of minimizing sulphide oxidation and ageing of the samples was found to be successful in minimizing the presence of species competing with uranium for resin sites, yielding more typical uranium loadings.

Case 2: Low sulphide content

Problem identification

Sample 3 is a flotation concentrate blended with slimes to contain 1.52% S²⁻ and 195 mg/kg uranium. Uranium leaching was conducted at 60°C with pH and Eh controlled at 1.5 and 450 mV (Ag/AgCl) by addition of H₂SO₄ and MnO₂ respectively. The composition of the resulting leach liquor, determined immediately after the leach and after neutralization, appears in Table III.

The leach pulp was cooled and stored in a refrigerator for about one week prior to being neutralized to pH 3.0 at ambient temperature, and then used for uranium RIP test work. Uranium adsorption was evaluated using Purolite A500 resin containing approximately 15% SiO₂, with the equilibrium adsorption isotherm appearing in Figure 4.

A slight decrease in pH to 2.8 was observed upon completion of the test (after 24 hours). The resin samples were analysed for uranium and base metals using XRF.

Similar to the first results obtained under case 1 on samples 1 and 2, unexpectedly low maximum uranium loadings (approx. 16 g/L) were achieved at high pulp-to-resin ratios, and once again the presence of polythionates was suspected to be responsible.

Mitigation strategies

The following mitigating strategies were evaluated:

- ▶ Uranium leaching at 4 and 24 hours' residence time (60°C, pH 1.5, Eh > 450 mV (Ag/AgCl)), followed by neutralization to pH 3.5 (60°C) immediately upon completion of leaching), and
- ▶ RIP contacts at three pulp-to-resin ratios (due to limited amount of sample available) immediately upon completion of neutralization.

The final leach parameters and reagent consumptions appear in Table IV. The redox potential remained at 430–450 mV (Ag/AgCl) during the first 4 hours of leaching without the addition of MnO₂, and only after 7 hours was an Eh adjustment with MnO₂ required. The acid consumption during the 4-hour leach was almost 10 kg/t lower than that

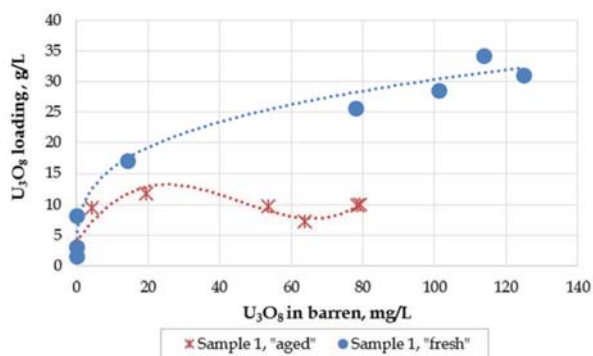


Figure 3—Uranium equilibrium isotherms from fresh and aged pulp (sample 1) by strong-base resin

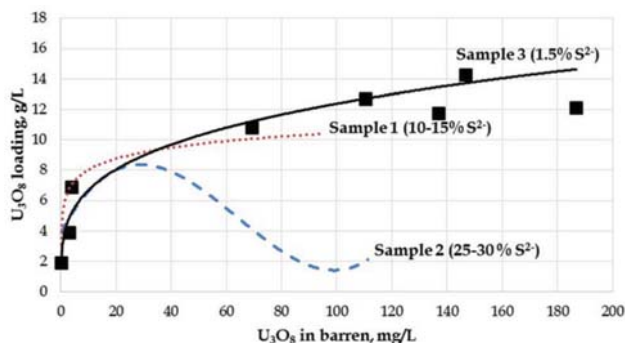


Figure 4—Uranium equilibrium isotherms from aged pulp, sample 3

Table III

PLS composition after leaching and neutralization to pH 3.0 of sample 3, mg/L

	Mg	Al	Ca	Mn	Fe	S, g/L	U ₃ O ₈
After leach	963	916	597	3145	3660	11.85	173
After neutralization	811	860	544	5200	3020	7.9	86

Polythionate formation during uranium recovery from sulphide flotation concentrate

Table IV

Leach parameters and reagent consumptions, Sample 3

Test	U ₃ O ₈ recovery, %	Consumptions	
		H ₂ SO ₄ (kg/t)	MnO ₂ (kg/t)
4 hr	90	13.3	0
24 hr	90	23	2.2
Old (24 hr)	90	21.3	3.98

of the 24-hour leach, with no compromise in uranium extraction. Moreover, as discussed for case 1, the reduced leach residence time probably minimized sulphide oxidation with the associated formation of polythionates.

The chemical composition of the leach liquors after neutralization is shown in Table V. Significant variations in Fe, Mn, and S concentrations only can be seen.

Overdosing of oxidant (MnO₂) is likely to occur during relatively small-scale laboratory experiments and most probably it resulted in additional oxidation of pyrite. Thus, difference in Fe and Mn concentrations was observed.

Similar uranium loadings were observed at all three pulp-to-resin contact ratios, irrespective of the leach residence time and ageing time. However, the iron co-loading reported after resin contact with fresh pulp was much lower than the results achieved on the aged pulp, as shown in Figure 5.

The sequential elution of the resin with HNO₃ followed by NaOH revealed that the resin samples contacted with the 4-hour leach pulp did not load sulphur as polythionates (<5 mg/L of sulphur was determined in NaOH eluate), while resin contacted with the 24-hour leach slurry contained around 1 g/L sulphur as polythionates. This confirms that an extended leach duration and/or addition of MnO₂ results in the formation of sulphur species that load onto the resin.

Unfortunately, due to limited sample, adsorption tests at higher pulp-to-resin ratios were not performed.

Case 3: Medium sulphide content

A Mintek demonstration plant was operated at the Gold Fields South Deep mine in December 2016, during which sulphide- and uranium-bearing concentrate (sample 4) was produced, bearing 6.19 % sulphides (as pyrite) and 96 mg/kg U₃O₈ (Olivera, 2016).

By this time, polythionate formation from sulphide-bearing samples was anticipated based on the prior experience described above, and the study was tailored towards a more focused research on the polythionate phenomenon.

Sample 4 was air-dried ('aged') prior to the test work and split into two portions:

- The first portion, labelled 'aged concentrate', was subjected to uranium leaching without any pretreatment
- The second portion, labelled 'washed concentrate', was washed three times by re-pulping with deionized water (1-to-3 solids to wash water) to remove any soluble products of sulphide oxidation that might have formed during its production and preparation.

The wash waters contained detectable concentrations (>2 mg/L) of Ca, Mg, Mn, and S as shown in Table VI.

Both samples were leached at 50% m/m solid content, 50°C, and pH 1.5 for 24 hours. The redox potential was controlled at 450 mV (Ag/AgCl) using MnO₂. MnO₂ addition was required for Eh control in both cases; however, in the case of the aged concentrate the Eh dropped after 1 hour of leaching, while in the case of the washed sample, addition of MnO₂ was required only after 5 hours.

After leaching the aged and washed slurries were each split into two portions. The one portion was neutralized to pH 3.5 immediately using lime at 50°C and subjected to RIP contacts, while the other was left for a week to age before neutralization and RIP.

Analyses of the PLS from the leaching of the concentrates as well as the solution analyses after the subsequent neutralization tests (prior to RIP contacts) are shown in Table VII.

Only the iron concentrations differed significantly between the aged and washed concentrates. This suggests that iron occurred in the leach slurry of the aged concentrate mainly as ferric, which was precipitated during pH adjustment, while it occurred mostly as ferrous iron in the

Table V

Leach liquor composition after neutralization

Element	Analysis versus leach residence time (mg/L)		
	4	24	Old (24 h)
Ca	493	570	661
Co	15.5	16	22
Fe ²⁺	1465	76	3250
Mg	473.5	758	812
Mn	202	1510	5020
Ni	38.5	40	63
S	980	1500	8200
Si	125	95	251
Zn	46.5	52	74

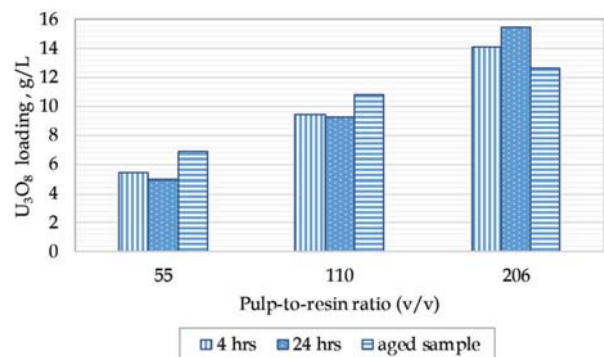


Figure 5—Uranium equilibrium loadings at similar pulp-to-resin ratios

Table VI

Wash waters analysis, mg/L

Element	Wash 1	Wash 2	Wash 3
Ca	457	214	76
Mg	31	15	6.8
Mn	8.85	<2	<2
S	404.5	178	46

Polythionate formation during uranium recovery from sulphide flotation concentrate

Table VII
Analysis of PLS before and after neutralization to pH 3.5 (mg/L)

Sample	Al	Fe	Mg	Mn	S
	After leach				
Aged concentrate PLS	1950	12100	3190	5690	24700
Washed concentrate PLS	1300	8250	2110	4280	21000
After neutralization					
Aged concentrate, fresh pulp	237	109	3390	5390	8960
Aged concentrate, aged pulp	130	550	3320	5350	9010
Washed concentrate, fresh pulp	298	2070	1880	3710	8200
Washed concentrate, aged pulp	324	1760	2020	4450	7800

case of the washed sample. Some differences in the amounts of MnO₂ addition between the two samples could also have contributed to the differences in final ferric/ferrous ratios. (At pH 3.5 all ferric present in the pulp should precipitate, hence, total Fe concentration detected after neutralization in solution was due to ferrous presence).

The equilibrium adsorption isotherms generated for uranium recovery using strong-base A500 resin from the four pre-neutralized leach slurries are shown in Figure 6.

Parameters of Langmuir isotherm ($Y_r = \frac{abX_s}{1+abX_s}$) used to fit equilibrium data are listed in Table VIII.

Ageing of the concentrate prior to uranium leaching did not have a noticeable effect on uranium recovery by RIP. This can be attributed to the relatively low sulphide grade and addition of MnO₂ during leaching (which possibly resulted in the destruction of at least part of the polythionates that might have formed during ageing).

It seems well proven that ageing of the pulp between leaching and RIP suppressed the efficiency of uranium recovery from the pulp. Sulphur was found in the caustic eluates obtained during stripping of the resin loaded from aged pulp.

Conclusions

The processing of sulphide-bearing material for uranium recovery by resin-in-pulp was found to be prone to the risk of polythionates formation by partial oxidation of sulphide minerals in the presence of oxidants such as ferric ion, manganese dioxide, and oxygen. Polythionates adversely affect uranium recovery as they are loaded more selectively than uranium by the strong-base resins that are conventionally used at uranium plants.

Polythionates could be formed during:

- Mineral processing ahead of leaching (comminution, flotation, drying)
- Acidic leaching
- Leached pulp storage and neutralization.

Possible mitigation strategies against this phenomenon include minimization of the leach duration, optimization/minimization of oxidant addition, and minimizing the ageing of pulp between the leaching, neutralization, and adsorption steps. A strategy for the destruction of polythionates will have to be developed for the

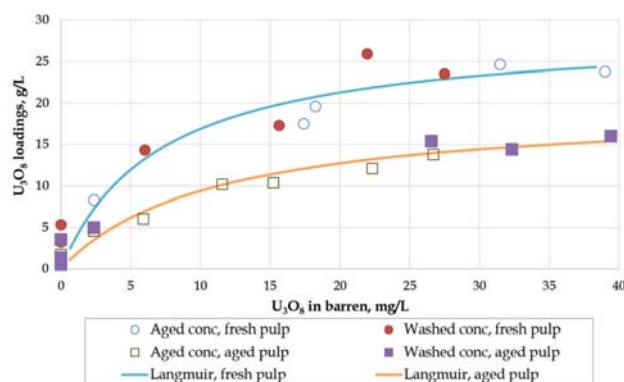


Figure 6—Uranium equilibrium data, sample 4

Table VIII
Parameters of Langmuir isotherm

Parameter	a (maximum loading)	b (selectivity coefficient)
Fresh pulp	28.87	0.14
Aged pulp	19.64	0.09

case where they do form; alternatively, resin regeneration with caustic will have to be conducted after every adsorption cycle. The topic remains under investigation at Mintek.

References

- DESCOSTES, M., VITORGE, P., and BEAUCAIRE, C. 2004. Pyrite dissolution in acidic media. *Geochimica et Cosmochimica Acta*, vol. 68, no. 22. pp. 4559–4569.
- DRUSCHEL, G. and BORDA, M. 2006. Comment on 'Pyrite dissolution in acidic media' by M. Descostes, P. Vitorge, and C. Beaucaire. *Geochimica et Cosmochimica Acta*, vol. 70. pp. 5246–5250.
- DRUSCHEL, G., HAMERS, R., and BANFIELD, J. 2003. Kinetics and mechanism of polythionate oxidation to sulfate at low pH by O₂ and Fe³⁺. *Geochimica et Cosmochimica Acta*, vol. 67, no. 23. pp. 4457–4469.
- FLEMING, C., BROWN, J., and BOTHA, M. 2010. An economic and environmental case for re-processing gold tailings in South Africa. *SGS Minerals Technical Bulletin*, March. p. 12.
- LOWSON, R. 1982. Aqueous oxidation of pyrite by molecular oxygen. *Chemical Reviews*, vol. 82. pp. 461–497.
- McKAY, D. and HALPERN, J. 1958. A kinetic study of the oxidation of pyrite in aqueous suspension. *Transactions of the Metallurgical Society of AIME*, vol. 212. pp. 301–309.
- NUGENT, E. 1956. The chemistry of the poisons associated with the ion-exchange process. *The South African Industrial Chemist*, vol. 10. pp. 282–290.
- OLIVERA, D. 2016. Mintek reveals new tailings retreatment process. http://www.miningweekly.com/article/mintek-reveals-new-tailings-retreatment-process-2016-12-07/rep_id:3650
- REMPEL, G. and CHANDA, M. 1986. Oxidation of polythionates. US patent 4582690 A.
- Schippers, A. 2004. Biogeochemistry of metal sulfide oxidation in mining environments, sediments, and soils. *Sulfur Biogeochemistry—Past and Present*. Amend, J., Edwards, K., and Lyons, T. (eds.). Geological Society of America, Boulder, Colorado. pp. 49–62.
- SCHMIEDEL, H. 1984. Reeneration of polythionate poisoned ion exchange resins used in uranium recovery. US patent 4486390.
- VAN RENSBURG, S. and MASHABA, S. 2016. Guidelines for retreatment of SA gold tailings: MINTEK's learnings. Southern African Institute of Mining and Metallurgy, Johannesburg.
- VAN TONDER, D. and KOTZE, M. 2007. Uranium recovery from acid leach liquors: IX or SX? *Proceedings of the ALTA Uranium Conference*, Perth. ALTA Metallurgical Services, Perth.
- VONGPROM, Y., HAWBOLDT, K., and BOTTARO, C. 2008. Thiosalt stability - impact on AMD. *Proceedings of the 2008 US EPA/NGWA Remediation of Abandoned Mine Lands Conference*. <http://ngwa.confex.com/ngwa/mine08/recordingredirect.cgi/id/226>
- WOODCOCK, J. 1961. Some aspects of the oxidation of sulphide minerals in aqueous suspension. *Proceedings of the Australasian Institute of Mining and Metallurgy*, vol. 198. pp. 47–48. ◆



Behaviour and fate of uranium in a high-level nuclear waste processing system

by J. Addai-Mensah*[†] and H. Musiyarira*

Synopsis

Effective control and management of high-level nuclear waste (HLNW) during its hydrothermal processing is crucial to the US Department of Energy's Savannah River tank farm operations. Approximately 130 million dm³ of this 'cold war' legacy waste liquor are stored at site. During processing, sodium aluminosilicate (SAS) polytypes (*e.g.*, amorphous, zeolite, sodalite, and cancrinite) and sodium diuranate waste products enriched in fissionable uranium (U) crystallize, invariably, leading to evaporator fouling and major criticality concern. Fissionable product fouling and its mitigation pose intractable challenges, warranting greater understanding and new knowledge of the underpinning mechanisms. In this paper, some of the tactical investigations into uranium behaviour and interactions with SAS phases in HLNW carried out are reported. It is shown that SAS-mediated co-crystallization of sodium diuranate phase from HLNW liquor at high ionic strength and pH, rather than U ion complex adsorption, largely accounts for the crystallographic destination and presence of U in the plant solid foulant.

Keywords

high-level nuclear waste, sodium diuranate, sodium aluminosilicate, evaporator fouling.

Introduction

Radioactive sodium diuranate formation and fouling in high-level nuclear waste (HLNW) processing plants presents intractable challenges to US 'cold war' legacy waste treatment plants (Hobbs and Edwards, 1994; Oji and Williams, 2002; Addai-Mensah, Li, and Zbic, 2002; Duff, 2002; Addai-Mensah *et al.*, 2005, 2004a, 2004b). Heterogeneous crystallization of sodium diuranate (Na₂U₂O₇) occurs in tandem with sodium aluminosilicate phases within the evaporators used in the waste liquor concentration in the temperature range 30–140°C. Typically, the HLNW liquor comprises high ionic strength (6–10 M) caustic solutions containing sodium hydroxide, silicate, aluminate, nitrite, and nitrate ions, trace amounts (approx. 300 mg·dm⁻³) of radionuclides (*i.e.*, uranium-235, plutonium-238) and radio-toxic species (*e.g.*, caesium-137). The supersaturation of Na ion-paired tetrahydroxo Al(III), SiO₂, and uranyl complex species in solution (the limiting reactants) created by continual water evaporation, together with the intense heating applied, synergistically act to facilitate the poly-condensation and crystallization of SAS and

fissionable uranium-based solid products (Hobbs and Edwards, 1994; Puigdomenech and Bruno, 1988; Chernorukov and Kortikov, 2001; Oji Williams, 2002; Duff, 2002; Addai-Mensah *et al.*, 2005, 2004a, 2004 b). The formation and accumulation of SAS involve an amorphous phase and three polytypes: zeolite, sodalite, and cancrinite (Addai-Mensah *et al.*, 1997, 1998, 2001a, 2001 b; Barnes *et al.*, 1999a–f). In the case of the U-based crystalline product, while sodium diuranate is believed to be formed, it is not clear whether other iso-structural U oxide compounds such as Na(UO₂)₃O₃(OH)₂ and Na₆U₇O₂₄ or the silicate soddyite ((UO₂)₂SiO₄·2H₂O), are also present. If not effectively mitigated, the accumulation of a critical mass of fissionable U in the scale deposit can (and does) proceed at an alarming rate, posing a major criticality concern and warranting an immediate plant shutdown.

Mechanistically, fouling may occur by a number of ways, including: (i) high surface energy metal substrate-mediated heterogeneous precipitation, (ii) adsorption of existing particulate matter in suspension onto a substrate, (iii) chemical reaction solid product deposition onto an 'inert' substrate, and (iv) substrate corrosion-mediated precipitation product deposition. The mechanisms and kinetics of U-free SAS crystallization and fouling have been investigated under a variety of conditions (Barnes *et al.*, 1999a–f; Addai-Mensah, Lee, and Zbic, 2002; Addai-Mensah *et al.*, 2005, 2004a, 2004b). It can be said that, depending

* Department of Mining and Process Engineering, Namibia University of Science Technology, Namibia.

† Future Industries Institute, University of South Australia, Adelaide, Australia..

© The Southern African Institute of Mining and Metallurgy, 2018. ISSN 2225-6253. This paper was first presented at the Uranium 2017 International Conference, 12–13 September 2017, Swakopmund Hotel, Swakopmund, Namibia..

Behaviour and fate of uranium in a high-level nuclear waste processing system

upon the operating conditions, all of the above modes of fouling may prevail. Furthermore, while our fundamental knowledge and understanding of SAS crystallization fouling behaviour have advanced considerably, crucial knowledge of how the actinides' solute species (*e.g.*, weapons-grade uranium and plutonium) present in the HLNW liquor are incorporated into the pervasive SAS scale is limited. This paper presents strategic basic crystallization and U sorption studies carried out to establish the crystallo-chemical characteristics and fouling behaviour of U and SAS solid products in a HLNW simulant system, thus bridging the fundamental knowledge gap.

Experimental methods

Investigations were performed using model simulant liquors and conditions reflecting the US DoE's Savannah River HLNW evaporator processing and fouling behaviour. Synthetic SiO₂-free, sodium aluminate solutions were prepared from known masses of gibbsite (99.5% γ -Al(OH)₃, Alcoa Arkansas, USA), sodium hydroxide (97.5% NaOH, 2.5% Na₂CO₃, Ajax Chemicals, Australia), anhydrous sodium carbonate (99.9% Na₂CO₃, Merck, Australia), and Milli-Q water to give a liquor of concentration 2.20–2.33 M Al(OH)₃, 5.4–6.0 M NaOH, and 0.49 M Na₂CO₃. A 0.55 dm³ aliquot of the above liquor was placed in a 1 dm³ stainless steel autoclave operating at 400 r/min agitation rate at a constant temperature. 0.05 dm³ solutions containing 0.150–1.50 g of sodium metasilicate (99.9% Na₂SiO₃, Merck, Australia), 0.05 dm³ of 6.0 M sodium nitrate, and 6.0 M sodium nitrite (99.9% NaNO₃ and NaNO₂, Merck, Australia) were added to the liquor sequentially once it had reached the required experimental temperature (80–120°C), bringing the total liquor volume to 0.65 dm³. Known masses of uranyl nitrate (UO₂(NO₃)₂) crystals (99.9% pure, Ajax Chemicals, Australia) were dissolved in the final solution to serve as a hexavalent uranium-238 source. The final liquor compositions were 0.01–0.1 M SiO₂, 6.6×10⁻³–1.2 M Al(OH)₃, 0.38 M Na₂CO₃ and 3.8–6.0 M NaOH for U-free liquor type or plus 21–3400 mg·dm⁻³ U, 1.0 NaNO₃, and 1.0 NaNO₂ for HLNW liquor type. Before use, the solutions were twice filtered through 0.45 μ m membranes to give optically clear liquors.

Self-nucleating (unseeded), isothermal crystallization/fouling tests were run over 4 hours at temperatures of 65, 85, and 120°C in a batch autoclave. A 316 stainless steel, high-pressure Parr autoclave fitted with an external heater and an interval cooling system was used. The vessel was fitted with a central four-blade, 45°-pitch, 2-tier impeller which provided constant agitation at 400 ± 2 r/min. The autoclave's temperature, heating, and agitation rates were controlled through an automatic proportional, integral, and derivative control system. To prevent boiling of solution above 100°C, the autoclave was pre-pressurized by using H₂O vapour-saturated N₂ gas to a pressure of 3200 kPa, prior to heating. This also ensured that there was no solution water loss by vapourization. Solution/slurry samples were periodically removed for solution and solid products characterization. 10 × 6 mm 316 stainless steel strips (coupons) screwed onto the shaft of the impeller were detached to routinely provide fouled substrates for standard scanning electron microscopy (SEM), powder X-ray diffraction (XRD), and time-of-flight

secondary ion mass spectrometry (ToF SIMS) analyses. The specific surface area of the crystals was determined by N₂ BET analysis (Coulter Omnisorp 100, Hiialeah Fl. USA). Solution SiO₂, Al(III), and U concentrations were analysed by ICP-MS (Spectro Analytical Instruments, Spectro SIM-SEQ ICP-OES, Kleve, Germany). The experimental runs were repeated three times for each temperature. Product particle size and size distribution were measured by laser diffraction

SEM analyses of carbon-coated samples were performed using a high-resolution field emission Cam Scan (CS44FF, Cambridge, UK) at 20 or 100 kV in imaging modes secondary electron (SE) and backscattered electron (BSE), and energy dispersive spectroscopy (EDAX) mode for elemental composition. To make BSE imaging of fouled coupons more interpretable, the scale deposit was carefully pressed to render it flat prior to analysis. The solid product/crystalline phase characterization was performed by collecting and analyzing XRD patterns on powder samples in $\theta/2\theta$ scanning mode using CuK α radiation ($\lambda = 1.5418 \text{ \AA}$). The scan speed was 1° per minute between 10° and 70° 2 θ .

Results and discussion

The kinetic behaviour of self-nucleating solutions crystallizing isothermally over 4 hours was investigated at temperatures of 65, 85, and 120°C. Typical, SEM photomicrographs and EDAX maps of pristine and fouled 316 stainless steel coupons, revealing surface topographical features and elemental composition, are shown in Figures 1–3. Well-defined grain boundaries with asperities can be clearly seen for the pristine steel coupon (Figure 1, X3). Elemental concentrations of Fe, Cr, and Ni as the principal constituents of 316 stainless steel are also indicated in Figure 1.

After heating the U-free, SAS supersaturated liquor (0.01 M SiO₂, 0.12 M Al(OH)₃, 0.38 M Na₂CO₃, 1.0 M NaNO₃, 1.0 M NaNO₂, and 4.0 M NaOH) at 85°C for 3 hours, the resulting SEM images and EDAX analyses showed the proliferation of colloidal particles and Na, Al, Si, and O atoms at the steel substrate surface (Figure 2). Common behaviour of SAS polytypes crystallization from U-free Al(III) and SiO₂ supersaturated solutions is depicted in Figure 3 via powder XRD analysis. The identities of the four distinct phases observed at 65–120°C were established as amorphous solid (Na₁₂Al₁₂Si₁₂O_{48.27}H₂O), Linde type zeolite A crystals (Na₁₂Al₁₂Si₁₂O_{48.27}H₂O) (both dominant at low temperatures <85°C), and dimorphic sodalite and cancrinite crystals (both predominant at higher temperatures > 85°C). The sodalite and cancrinite phases may both be generically described as (Na₆Al₆Si₆O₂₄Na X.nH₂O) (where 2 ≤ n < 4 and X denotes 2NO₃⁻ and 2NO₂⁻). Both the zeolite A and its amorphous solid precursor contained no detectable amounts of non-framework anionic species in solution (OH⁻, CO₃²⁻, NO₃⁻, and NO₂⁻) which are characteristic guest species in sodalite and cancrinite structures. The main influence of temperature was observed to be exerted in terms of the kinetics and thermodynamics. The crystallization and phase transformation rates of all four SAS phases increased rapidly with increasing temperature from 65 to 120°C, in the manner of chemical-reaction controlled processes. Typical results obtained in the 65–120°C range are presented herein for 85°C, for brevity. In Figure 3, the temporal, solution-

Behaviour and fate of uranium in a high-level nuclear waste processing system

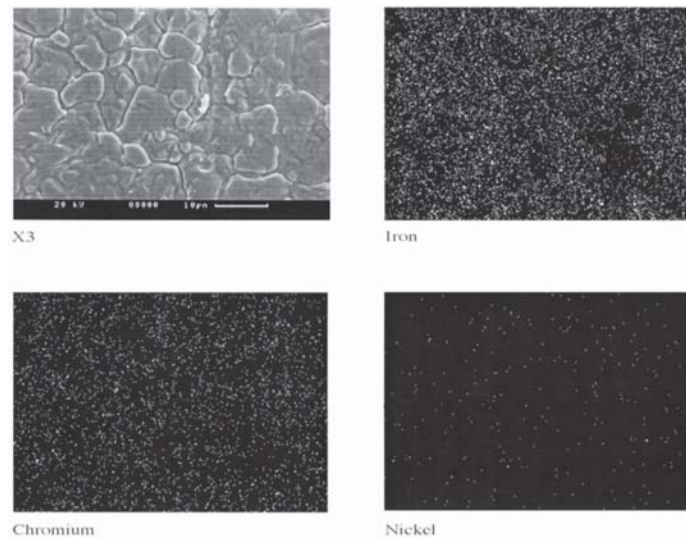


Figure 1—SEM photomicrographs (X3) and EDS maps of pristine 316 stainless steel substrate revealing surface topographical features and elemental composition, respectively

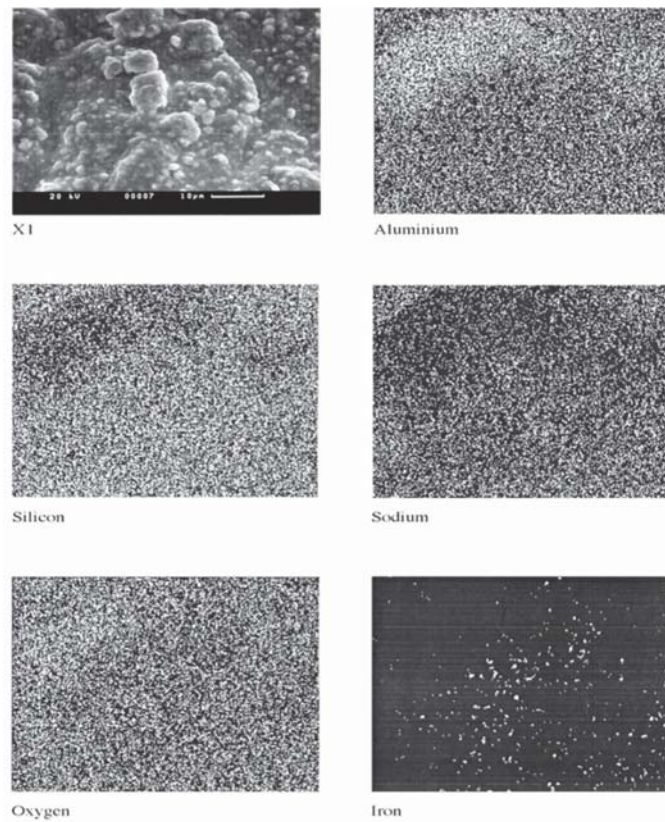


Figure 2—SEM photomicrograph and EDS maps of fouled steel substrate revealing surface topographical features and elemental composition, respectively, during fouling at 85°C from 0.01 M SiO_2 , 0.12 M $\text{Al}(\text{OH})_3$, 0.38 M Na_2CO_3 , 1.0 M NaNO_3 , 1.0 M NO_2 , and 4.0 M NaOH solution

mediated transformation of zeolite A to sodalite and then to cancrinite within 60 minutes at 85°C is exemplified.

To crystallize a U-based solid product while suppressing sodium SAS phase formation, a liquor supersaturated with 3400 $\text{mg}\cdot\text{dm}^{-3}$ U and containing dissolved Al(III) and SiO_2 at concentrations equivalent to equilibrium solubility of cancrinite, the least soluble SAS phase, was used. The U-

based product which crystallized at 65–120°C comprised massively aggregated, polycrystalline, platy and globular particles as the SEM image in Figure 4 shows. The product, crystallized without or with SAS, was established as sodium diuranate ($\text{Na}_2\text{U}_2\text{O}_7$) crystals by powder XRD analysis. The XRD analysis (based on JCPD Standard 12-0106 and data of Kovba, 1972) discounted the presence of other isostructural

Behaviour and fate of uranium in a high-level nuclear waste processing system

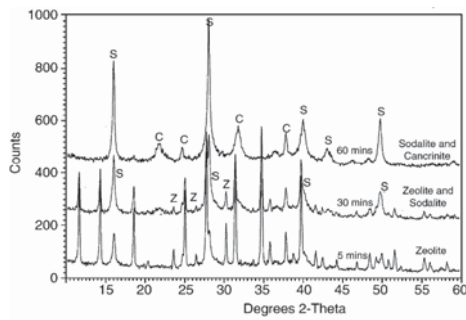


Figure 3—XRD spectra of SAS scale formed within 60 minutes at 85°C from self-nucleating, U-free solution containing 0.01 M SiO₂, 0.12 M Al(OH)₃, 0.38 M Na₂CO₃, 1.0 M NaNO₃, 1.0 M NO₂, and 4.0 M NaOH

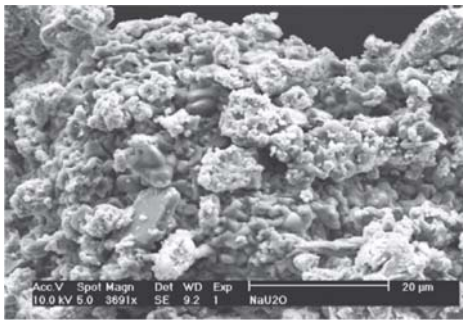


Figure 4—Typical SEM image of precipitated Na₂U₂O₇ crystals deposited onto a 316 stainless steel coupon from a self-nucleating, U-supersaturated (and SAS-saturated) liquor at 85°C

uranium oxides phases (e.g. Na(UO₂)₃O₃(OH)₂ and Na₆U₇O₂₄) (Giammar and Hering, 2002; Chernorukov and Kortikov, 2001). To understand the underpinning thermodynamics, the equilibrium solubilities of the Na₂U₂O₇ crystals and SAS solid phases in nitrated/nitric caustic aluminosilicate solutions were determined. Two types of solubility experiments were designed and used to allow the approach to equilibrium from ‘above’ (via seeded precipitation from supersaturated liquor) and from ‘below’ (via seeded dissolution in undersaturated liquor) (Addai-Mensah *et al.*, 2004).

Under the conditions used in the present investigation, the equilibrium solubility of the Na₂U₂O₇ phase was in the range 9.0–17.0 mg·dm⁻³ U, depending upon solution composition and/or temperature. The solubilities increased with increasing temperature which agreed well with the data reported for U in the literature (Duff, 2002; Hobbs and Edwards, 1994; Puigdomenech, and Bruno, 1988; Cordfunke and Loopstra, 1971) and also for SAS solid products (Zheng *et al.*, 1998; Addai-Mensah *et al.*, 2004; Barnes *et al.*, 1999d, 1999f). The equilibrium solubility (C_e) data was used together with the instantaneous U, Al(III), and SiO₂ species concentrations (C_i) to quantify the species relative supersaturations ($\sigma = C_i/C_e - 1$) with crystallization time.

For mixed SAS and sodium diuranate co-crystallization, experiments were conducted under plant-relevant solution and temperature conditions. Typical variations in U, Al(III), and SiO₂ relative supersaturations in self-nucleating solutions with time are shown in Figure 5. The data

exemplifies how rapid dissipation of SiO₂, Al(III), and U species supersaturation can proceed when the initial relative supersaturations (σ_0) of SiO₂ and Al(III) > 6 and that of U < 3 sufficiently induce SAS-U nucleation. Following rapid dissipation of supersaturation and prolonged mixed oxide co-precipitation within 2 hours, each of the three limiting reactants asymptotically approaches a plateau value.

SAS-mediated U species desupersaturation was observed, and this was dependent the of U concentration in the liquor. At very high initial U supersaturation ($\sigma_{U_i} > 10$), sodium diuranate crystallization was substantially independent of the rate of SAS co-crystallization. At low relative supersaturations ($\sigma_{U_i} < 2$ or U < 40 mg·dm⁻³, U desupersaturation was insignificant where SAS crystallization did no prevail as a precursor due to low supersaturation. Thus, at close to SAS equilibrium solubility conditions and low U supersaturation, no noticeable U crystallization occurred. Under such conditions, the uptake of U occurs largely by adsorption onto extant SAS solid phases, the extent of which is strongly dependent upon crystal surface area and charge or magma density. At low to moderate U concentration (40–70 mg·dm⁻³), SAS-U mixed-phase crystallization from supersaturated solutions prevailed. The rate of the mixed SAS and U crystallization followed the sequence: amorphous > zeolite A > sodalite > cancrinite > sodium diuranate. For liquors at low U concentration or supersaturation, SAS nucleation was a necessary precursor for the heterogeneous crystallization of sodium diuranate. The crystallization fouling reactions were observed to be distinctly temperature-dependent and dramatically enhanced at elevated temperatures (> 85°C). The nucleation and growth mechanisms and kinetics were quantified using empirical, second-, and third-order power law models, in the manner of Barnes *et al.* (1999a–d). The activation energies involved the zeolite A, sodalite, and cancrinite crystallization processes were estimated to be in the range 30–120 kJ/mol, the higher and lower values reporting to the concurrent nucleation and crystal growth mechanisms, respectively. The activation energies > 30 kJ/mol are indicative of chemical reaction-controlled crystallization processes.

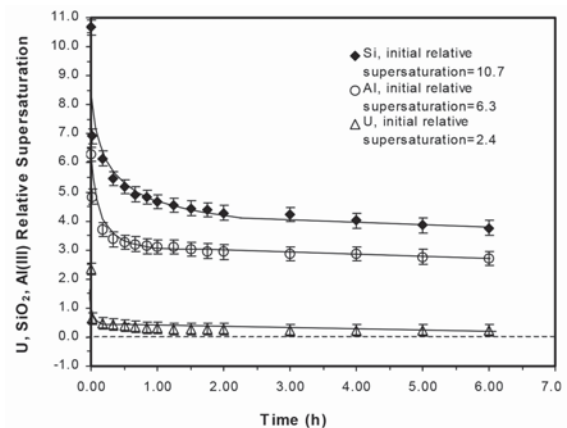


Figure 5—U, SiO₂, and Al(III) relative supersaturations as a function of time during crystallization of U-based oxide and SAS at 85°C (initial solution: NaOH = 4.0 M, NaNO₃ = 1.0 M, NaNO₂ = 1.0 M, SiO₂(♦) = 175.0 × 10⁻³ M, Al(III) (○) = 175.0 × 10⁻³ M, and U (Δ) = 30.8 mg·dm⁻³

Behaviour and fate of uranium in a high-level nuclear waste processing system

The heterogeneous scale deposits that crystallized from the U, SiO₂, and Al(III) supersaturated liquors were mixed sodium diuranate and sodium aluminosilicate (amorphous solid, zeolite, sodalite, and cancrinite) phases, as revealed by powder XRD, SEM BSE images, and EDAX analyses. Representative BSE image and EDAX data obtained for U-SAS mixed-phase fouled steel coupon is displayed in Figure 6. For the flat, mixed SAS and U oxide scale deposit prepared and analysed in the present work (*e.g.*, as in Figures 6A and 6B), the BSE images reveal grey and dark regions of high and low signals respectively, which correspond to the highest and lowest average atomic numbers, respectively. These, characteristically, translate into images of U-rich oxide appearing as grey and Al and Si-based oxide as dark areas, as in Figure 6A and EDAX bulk elemental composition analysis (Figures 6B and 6C). It is pertinent to state that the standard analytical techniques (SEM imaging, EDAX, and XRD analyses) employed provided invaluable crystallo-chemical information on the mixed U-SAS oxide scale phases identification and deconvolution.

Surface-sensitive ToF SIMS positive ion spectral analysis was also performed. The image of mixed U-SAS solid phases crystallized onto a steel coupon after 4 hours at moderate U concentration of 70 mg·dm⁻³ (ppm) and 4 M NaOH, 1 M NaNO₃, NaNO₂, 324 mM Al(III), and 324 mM SiO₂ at 85°C is displayed in Figure 7. The image clearly indicates random spatial distribution of sodium, Al and Si, and U species, which predominate on the surface as expected.

U adsorption studies

In liquors at low U species concentrations (< 40 mg·dm⁻³) and relative supersaturation ($\sigma < 2$), it was observed that sodium diuranate did not crystallize. In the presence of SAS solid phases in such liquors, adsorption processes are substantially responsible for incorporation of U species into the solid product matrix, the extent of which is dependent upon the SAS polytypes present. The results of the investigations of U adsorption onto the four different SAS solid phases revealed dependency on both substrate type and

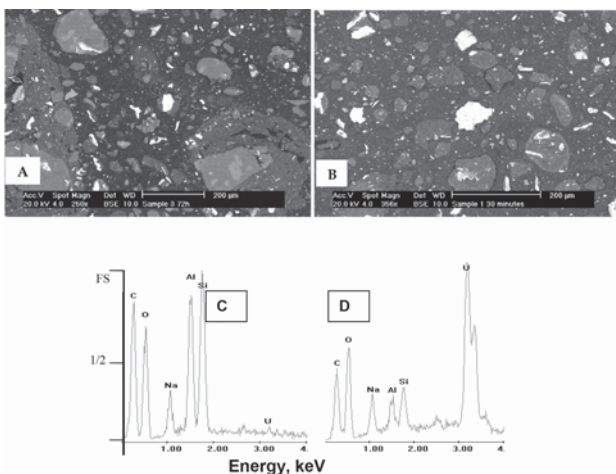


Figure 6—SEM BSE image (A and B) of fouled steel substrates due to co-precipitation of sodium aluminosilicate (dark area) and sodium diuranate (white areas) at 85°C; EDAX analysis of SAS - region (C) (dark areas in A and B), and sodium diuranate region (D) (white areas in A and B)

liquor Al (III) equilibrium concentration. Typical U species adsorption behaviour observed is demonstrated by the data in Figure 8 produced at 85°C for liquor with the following concentration: NaOH 4.0 M, NaNO₃ 1.0 M, NaNO₂ 1.0 M, SiO₂ 1.7–75.0×10⁻³ M, and U 15.0 ppm (mg·dm⁻³), and SAS seed charge 12 240 m²·dm⁻³.

The adsorption loading of U at temperatures < 85°C was highest for the amorphous SAS phase, followed by zeolite A, then sodalite, and the least for the cancrinite phase. In general, U species adsorption loading is remarkably low, accounting for < 5% of the total U species that is incorporated into the mixed SAS-U solids product formed during concentration of the HLNW liquor by the evaporation process. Thus, co-crystallization of U species with SAS solid phases is believed to be the main mechanism for the former's appearance in the HLNW evaporator solid product. These observations indicate that heterogeneous nucleation and growth of sodium aluminosilicate phases are critically important mediation processes for U oxide co-precipitation at low to moderate U supersaturations in HLNW evaporators.

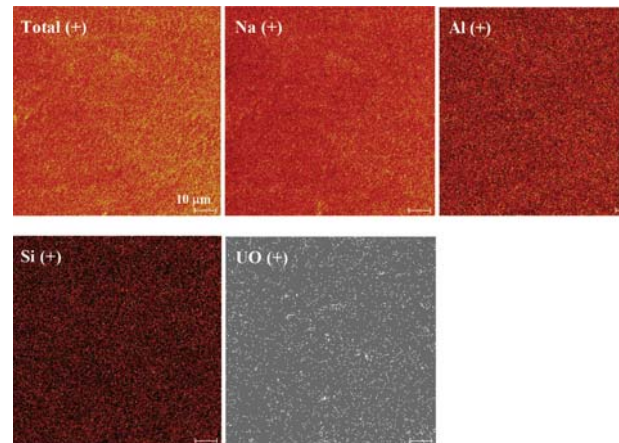


Figure 7—Selected SIMS positive ion images of mixed amorphous NAS- and U-based solid phases precipitated after 4 hours at 85°C from sodium aluminosilicate liquor initially containing 70 mg·dm⁻³ U, 324 mM Al(III), and 324 mM SiO₂. Sodium, Al, and Si (yellow spots) and U species (white points). Note the random distribution of U species at the solid deposit

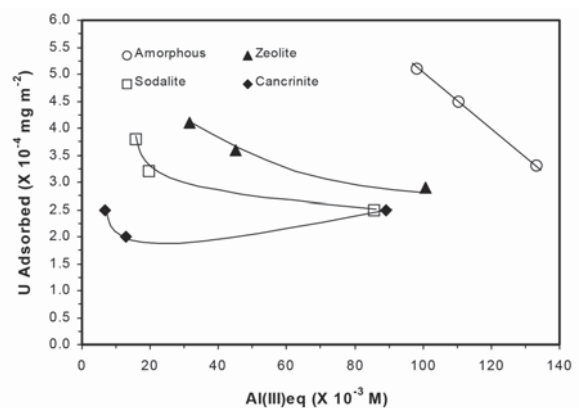


Figure 8—Adsorption loading of U species onto different SAS solid phases as a function of Al(III) equilibrium concentration at 85°C (liquor concentration: NaOH 4.0 M, NaNO₃ 1.0 M, NaNO₂ 1.0 M, SiO₂ 1.7–75.0×10⁻³ M, and U = 15.0 mg·dm⁻³. Seed charge 12240 m²·dm⁻³)

Behaviour and fate of uranium in a high-level nuclear waste processing system

Conclusions

Isothermal crystallization and fouling experiments simulating the formation and accumulation of uranium-enriched sodium aluminosilicate scale in the high-level waste evaporators at the US Department of Energy's Savannah River site, were performed. The studies aimed at providing greater understanding and new knowledge of the mechanisms and kinetic behaviour of the processes that determine the fate and crystallographic destination of uranium in the solid product. The analytical characterization of the various products observed under various conditions of liquor supersaturation, saturation, and undersaturation at 60–120°C revealed the following. Sodium diuranate was the uranium compound that crystallized in the highly caustic and high ionic strength aqueous media, regardless of the operating temperature. This U oxide product formed as both discrete and composite particles with amorphous/gel and crystalline sodium aluminosilicate polytypes (zeolite A, sodalite, and cancrinite) at moderate to high U and SAS supersaturations. The rate of sodium aluminosilicate and mixed U crystallization from supersaturated solutions increased with increasing temperature and followed the sequence of the phases: ephemeral amorphous > zeolite A > sodalite > stable cancrinite > sodium diuranate. For liquors at low U concentration or supersaturation, SAS nucleation was a necessary precursor for heterogeneous crystallization of sodium diuranate. The crystallization fouling reactions are distinctly chemical reaction-controlled, and are dramatically enhanced at elevated temperatures. The findings show that effective management and mitigation of both SAS and U oxide crystallization fouling in process heat-transfer equipment (evaporator) via an appropriate temperature control strategy are of significant importance to the HLNW industry.

Acknowledgments

Financial support for the project from Westinghouse Savannah River Company (Aiken, USA) for this work is gratefully acknowledged. Various contributions and comments made by Drs B. Wilmarth, R. Rosencrance, M. Zbik, and J. Li are also gratefully acknowledged.

References

ADDAI-MENSAH, J., LI, J. and ZBIK, M. 2002. Sodium aluminosilicate solid phases: Chemistry and crystallization behaviour. US Department of Energy-WSRS/ERDA. Report no. G008.

ADDAI-MENSAH, J., LI, J., ZBIK, M., and WILMARTH, W.R. 2005. Uranium sorption in sodium aluminosilicate phases under caustic conditions. *Separation Science and Technology*, vol. 40, no. 1-3. pp. 267-279.

ADDAI-MENSAH, J., LI, J., ZBIK, M., and ROSENCRANCE, S. 2004. Sodium aluminosilicate solid phase specific fouling behaviour. *International Journal of Transport Phenomena*, vol. 6. http://search.ror.unisa.edu.au/record/UNISA_ALMA51109601200001831/media/digital/open/9915913599601831/12143364950001831/13143363950001831/pdf

ADDAI-MENSAH, J., LI, J., ROSENCRANCE, S., and WILMARTH, W.R. 2004. Solubility of amorphous sodium aluminosilicate and zeolite A solid phases in nitrate/nitrite-rich caustic aluminate liquors. *Journal of Chemical and Engineering Data*, vol. 49, no. 6. pp. 1682-1687.

ADDAI-MENSAH, J., GERSON, A.R., JONES, R., and ZBIK, M. 2001. Reduction of sodium aluminosilicate scale in Bayer plant heat exchangers. *Light Metals*, vol. 13. pp. 13-18.

ADDAI-MENSAH, J., BARNES, M.C., and GERSON, A.R. 2001. Fouling of alumina refining heat exchangers: Effect of substrate and temperature, *Proceedings of the 6th World Congress of Chemical Engineering, Melbourne Australia*. Institution of Chemical Engineers in Australia, Melbourne. pp. 1-8.

ADDAI-MENSAH, J., GERSON, A.R., O'DEA, A., and ZHENG, K. 1997. The precipitation mechanism of sodium aluminosilicate scale in Bayer plants. *Proceedings of Light Metals 1997*, Orlando, FL. The Minerals, Metals & Materials Society, Warrendale, PA. pp. 23-28.

ADDAI-MENSAH, J., GERSON, A.R., and SMART, R.St.C. 1998. Continuous plug flow precipitation of sodalite scale on steel heat transfer surfaces, *Light Metals*, vol. 21. pp. 21-28.

BARNES, M.C., ADDAI-MENSAH, J., and GERSON, A.R. 1999a. The kinetics of desilication of synthetic spent Bayer liquor seeded with cancrinite crystals. *Journal of Crystal Growth*, vol. 200, no. 1-2. pp. 251-264.

BARNES, M.C., ADDAI-MENSAH, J., and GERSON, A.R. 1999b. The kinetics of desilication of synthetic spent Bayer liquor seeded with pure sodalite, pure cancrinite and their dimorphic mixed phase crystals. *Light Metals*, pp. 121-130.

BARNES, M.C., ADDAI-MENSAH, J., and GERSON, A.R. 1999c. The kinetics of desilication of synthetic spent Bayer liquor and sodalite crystal growth. *Journal of Colloids and Surfaces A*, vol. 147, no.3. pp. 283-295.

BARNES, M.C., ADDAI-MENSAH, J., and GERSON, A.R. 1999d. The mechanism of the sodalite-to-cancrinite phase transformation in synthetic spent Bayer liquors. *Microporous and Mesoporous Materials*, vol. 31, no. 3. pp. 287-302.

BARNES, M.C., ADDAI-MENSAH, J., and GERSON, A.R. 1999e. A methodology for quantifying sodalite and cancrinite phase mixtures and the kinetics of the sodalite to cancrinite phase transformation. *Mesoporous and Macroporous Solids*, vol. 31, no.3. pp. 303-319.

BARNES, M.C., ADDAI-MENSAH, J., GERSON, A.R., and SMART, R.St.C. 1999f. The solubility of SiO₂ in synthetic spent Bayer liquor seeded with sodalite and cancrinite. *Journal of Colloids and Surfaces A*, vol. 157, no. 1-3. pp. 101-116.

CHERNORUKOV, N.G. and KORTIKOV, V.E. 2001. Na[HSiO₆]·H₂O: synthesis, structure and properties. *Radiochemistry*, vol. 43, no. 3. pp. 229-232.

CORDFUNKE, E.G.P. and LOOPSTRA, B.O. 1971. Sodium uranates: preparation and thermochemical properties. *Journal of Inorganic and Nuclear Chemistry*, vol. 33. pp. 2427-2436.

DUFF, M.C. 2002. Uranium interactions with sodium aluminosilicates: Part 1 Sorption. US Department of Energy-WSRS. Report no. SRT-LWP-2002-00109.

GIAMMAR, D.E. and HERING, J.G. 2002. Equilibrium and kinetic aspects of soddyite dissolution and secondary phase precipitation in aqueous suspension. *Geochimica et Cosmochim. Acta*, vol. 66, no. 18. pp. 3235-3245.

HOBBS, D.T. and EDWARDS, T.B. 1994. Solubility of uranium in alkaline salt solutions. US Department of Energy-WSRC. Report TR-93-454.

KOVBA, L.M. 1972. Crystal structure of sodium diuranate. *Radiokhimiya*, vol. 14, no. 5. pp. 727-730.

OJI, L.N. and WILLIAMS, A. 2002. Incorporation of uranium into sodium aluminosilicate phase. US Department of Energy -WSRST. Report no. SRT-LWP-2002-00109.

O'CONNOR, D.J., SEXTON, B.A., and SMART, R. St.C. eds 2003. Surface Analysis Methods in Materials Science. 2nd edn. Springer, Berlin/New York/London.

PUIGDOMENECH, I. and BRUNO, J. 1988. Modeling uranium solubilities in aqueous solutions: validation of a thermodynamic database for the EQ 3/6 Geochemical Codes. SKB, Stockholm. Technical report SKB 88-21.

ZHENG, K., GERSON, A.R., ADDAI-MENSAH, J., and SMART, R. St.C. 1997. The influence of sodium carbonate on aluminosilicate crystallization and solubility in sodium aluminate solutions. *Journal of Crystal Growth*, vol. 171. pp. 197-208.

ZHENG, K., SMART, R.St.C., ADDAI-MENSAH, J., and GERSON, A.R. 1998. Solubility of sodium aluminosilicates in synthetic Bayer liquor. *Journal of Chemical and Engineering Data*, vol. 43, no. 3. pp. 312-317. ◆



3D analysis of longwall face stability in thick coal seams

by G. Song* and Y.P. Chugh†‡

Synopsis

Face falls remain the most difficult engineering problem in single-cut longwall mining. In this paper we investigated mining of two adjacent longwall faces using 3D nonlinear analysis, to obtain a better understanding of the stress distribution around excavations and development of failed zones. The gob loading behaviour was included by applying a variable force to the roof and floor behind the longwall face. The results show that:

- (1) Face failures developed in the upper portion of the face extend deeper ahead of the mined face than those in the bottom portion
- (2) Stress distribution and development of yielded zones ahead of the coal face vary along the panel width
- (3) The maximum vertical stress concentration factor (VSCF) ahead of the longwall face occurs around the middle section of the panel width
- (4) The middle section of a longwall face also experiences the most failed zones in the unmined coal
- (5) The previously mined-out face increases the VSCF and volumes of failed zones in the adjacent longwall face; however, the effect extends only a short distance along the width of the panel close to the previously mined-out panel
- (6) With increasing seam height, the stiffness of the coal face is reduced and therefore the longwall face carries less vertical load, but it deforms more and the yielded zones are larger
- (7) With decreasing GSI of the mined seam mass, the cohesion and angle of internal friction are reduced, resulting in a lower vertical stress concentration factor and larger yielded zones spatially ahead of the face.

Keywords

thick coal seam, longwall mining, numerical modelling, face stability, gob, vertical stress concentration factor, yielded zones.

Background

Thick coal seams (seam height larger than 3.5 m) account for about 44% of the proven coal reserves and about 40% of the annual coal production in China (Wang, 2009). For economic reasons, longwall mining methods are employed for mining such seams. Single-cut longwall mining offers advantages over multiple-slice top caving methods from the points of view of mining operations, mine ventilation, coal recovery, and safety. However, this mining system may result in face falls and other ground control problems. Since the height of single-cut longwall faces has increased to 7–8 m in recent years, the risk of face falls has increased considerably, resulting in safety, production, and productivity concerns (Song, 2016). Face fall

is likely to occur as illustrated in Figure 1a, but the steel plate against the face holds the coal in place and maintains the structural stability of the longwall face. In the incident shown in Figure 1b, large coal blocks fell from the longwall face and the mining operation was halted. Face falls can also result in fatalities. Therefore, face falls must be controlled scientifically to improve mine planning and safety. This paper is focused on the analysis of such falls.

Currently, the longwall face advance rate in China is about 10–15 m (or more) per day. In some coal mines face falls occur in every single cut of the longwall face, which slows the rate of face advance. In Panyi coal mine of Anhui Province, face falls and roof falls ahead of face supports were observed during a working

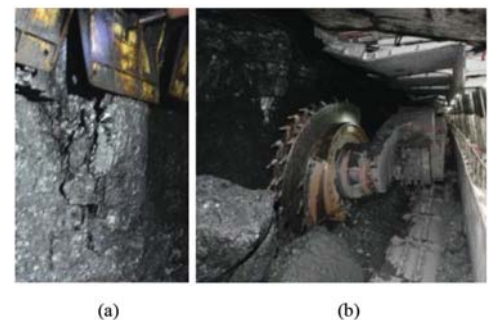


Figure 1—Face failures observed on two longwall faces. (a) Face falls may occur without protection of steel plate, (b) large coal blocks fall from the longwall face, affecting the operation of mining equipment

* School of Civil Engineering, North China University of Technology, Beijing, China.

† Department of Mining and Mineral Resources Engineering, Southern Illinois University Carbondale, United States.

‡ National Academy of Inventors, United States.

© The Southern African Institute of Mining and Metallurgy, 2018. ISSN 2225-6253. Paper received Oct. 2016; revised paper received 2017.

3D analysis of longwall face stability in thick coal seams

period of 14 days (Chen, 2012) (Figure 2). Face falls occurred every observation day, interrupting the mining operations and coal production. The middle section and tailgate side of the longwall face experienced the most face falls. Other field observations revealed that face falls typically extended less than 2 m ahead of the face, and that deeper extension of face fall was found during the periodic roof weighting and/or on longwall faces with greater mining thickness (see Figure 3).

Research hypothesis, goal, and specific objectives

Vertical stress redistribution following the excavation of a longwall panel has been discussed in depth (Whittaker, 1974; Wilson, 1983; Peng, 1984). The initial stress is redistributed around the longwall face with development of abutment loadings ahead and behind the face and development pillars on both on the headgate and tailgate sides. The vertical stress redistribution in abutment loading areas is shown in Figure 4 (Whittaker, 1974). The abutment pressures on the coal face and in the ribs of chain pillars decay to the original vertical stress level as the distance from the face line and rib edge increases. The vertical loading in the gob area is gradually re-established to the pre-mining vertical stress level behind the face upon consolidation of gob materials and their ability to sustain more load. The loading characteristics of the gob materials can have a major influence on the front abutment pressure and face stability.

A better scientific understanding of distribution of stress in and around the longwall face and failed areas is needed to effectively solve the problem. We analysed the 3D stress distribution and failed areas numerically using nonlinear analysis with FLAC 3D software. This software is based on

the finite difference approach and is extensively used globally for mining applications (Itasca, 2012). The analyses involved two adjacent longwall faces with a coal pillar left between the two panels (longwall panels 1 and 2 in Figure 5), and a consideration of gob loading behavior behind the face. Both

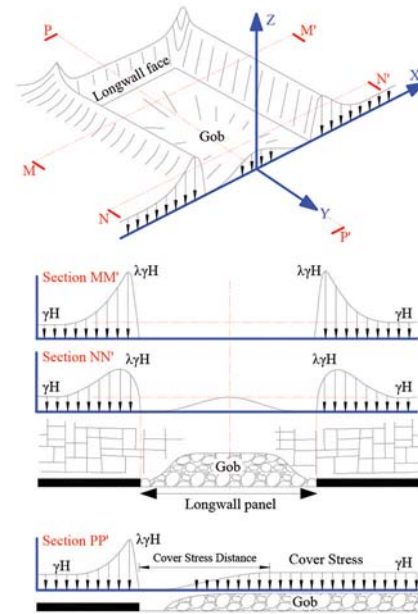


Figure 4—Vertical stress distribution at the seam level around abutments of a longwall face (after Whittaker, 1974). γ represents average overburden unit weight; H is depth of cover; and λ is vertical stress concentration factor, defined as the vertical stress at a particular point after excavation over the pre-mining applied vertical stress

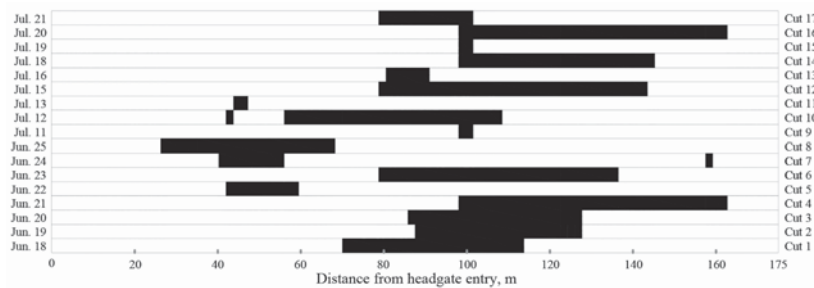


Figure 2—Distribution of face falls along the longwall face width (Chen, 2012)

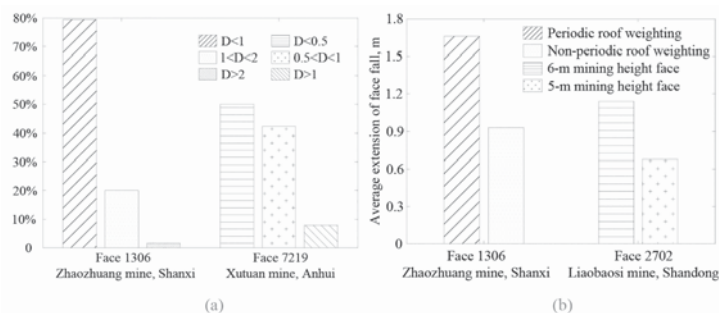


Figure 3—(a) Statistics on face fall extension observed in two coal mines; D represents depth of face fall in m. (b) Average depth of face fall extension observed during periodic and non-periodic roof weighting, and in a 6 m and 5 m mining height face

3D analysis of longwall face stability in thick coal seams

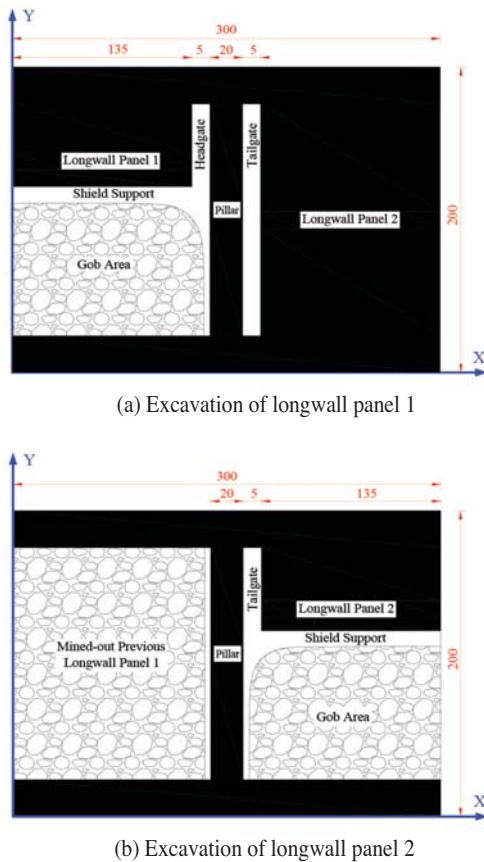


Figure 5—Schematic plan view of the geometry of two adjacent longwall faces in the numerical model

longwall panels 1 and 2 represent half of the original panel width in the studied mine site. The positive Y-direction represents the direction of face advance in the figure. The modelled mining system is similar to that practiced in China. The influence of a mined-out area of a previous longwall face (longwall panel 1) on the adjacent current longwall face (longwall panel 2) is also included (the influence of mining sequence on face failure). This investigation has two goals: (1) to develop a realistic 3D numerical model of two adjacent longwall faces with a consideration of gob loading characteristics and nonlinear rock mass properties; and (2) to perform sensitivity studies of selected variables to understand their influence on stress distribution and the development of yielded zones in unmined coal in different areas of the longwall face.

The face failure modes may be divided into structural failure and functional failure (Song, Chugh, and Wang, 2017). Stress normally exceeds peak coal strength in abutment pressure zones around the longwall face. The coal mass in some areas around abutment zones may fail (fracture or yield), while in other areas it may not fail since it is relatively confined laterally and unable to deform. When the shearer cuts into the coal face, the confinement is lost and the face may fail. The face protection plate in the front edge of the roof supports increases confinement and is therefore utilized in field practice to improve stability of the face. Upon the failure of the coal and rock mass in the abutment pressure zones, the maximum front abutment

stress would shift forward ahead of the face into the more competent rock and coal mass. The local failure of the coal mass may not, however, lead to face falls on a longwall face, and the coal may remain relatively stable and maintain its integrity for a short period of time without affecting mining operations. This is considered a ‘structural failure’ of the longwall face. ‘Functional failure’, on the other hand, refers to the state where face falls occur and production and the safety of miners is affected. The depth of structural failure ahead of the longwall face typically depends on the seam height, engineering properties of the coal and immediate roof and floor, loading characteristics of the gob, and the performance of roof supports. Structural failure may extend 0.5–2 m ahead of the longwall face and normally ceases beyond the point where abutment pressure achieves the peak value, while extension of functional failure should be less than or equal to that of the structural failure. Since structural failure increases the likelihood of functional failure, efforts to control face falls should emphasize reducing structural failure.

Previous research

3D numerical modelling of longwall face failure has been extensively pursued (Niu, Chen, and Liu, 2010; Song *et al.*, 2011; Tian *et al.*, 2012). In the previous models, the coal face is advanced through a certain distance and sensitivity studies are then performed to analyse the influence of seam height, depth of cover, seam inclination, and geological disturbance (such as a fault) on the stability of longwall faces. Therefore a broad-based observation on how these factors affect face stability has been discussed. However, these previous models did not include modelling of gob loading following the excavation of the coal seam and the creation of the mined-out void. Face stability modelling using 2D analyses has also been performed with incorporation of gob behaviour (Bai *et al.*, 2014, 2016; Song, Chugh, and Wang, 2017). The section modelled in 2D analysis is, however, located too far from the gate ends to be influenced by the previously mined-out area or the neighbouring panels. The authors believe that both the gob loading characteristics and the effects of a previously mined-out gob area on the face stability of the adjacent longwall face are important variables that must be considered. Since the total load from the overburden around the excavation is transferred to the floor through the unmined coal and the gob, ignoring the load carried by the gob around the mining area/s will result in overestimation of stresses around abutments and failed zones in the face area.

Numerical modelling of longwall mining with a consideration of gob behaviour has been documented in previous studies (Yavuz, 2004; Yasitli and Unver, 2005; Esterhuizen, Mark, and Murphy, 2010a, 2010b; Shabanimashcool and Li, 2012). In these studies, a double-yield loading model in FLAC was used for gob modelling. This approach modelled the gob as a strain-hardening material, with the stress-strain response obtained through laboratory tests on compaction of loose materials (Pappas and Mark, 1993). Shabanimashcool and Li (2014) simulated longwall mining in 3D models, and investigated the gate stability and rockbolt loading process. Esterhuizen, Mark, and Murphy (2010a) used a 3D longwall mining model to assess coal pillar performance and found that span-to-depth

3D analysis of longwall face stability in thick coal seams

ratio is an important factor affecting the ultimate deformation and loading of pillars. Yavuz (2004) developed a 2D longwall mining model to investigate the pressure distribution in the gob area and to estimate the cover pressure re-establishment distance. He concluded that cover pressure re-establishment distance is related to the mining height, depth of cover, the bulking factor for gob, and compressive strength of the waste rock materials. However, the numerical longwall models incorporating the gob behaviour have not been used for assessing the face stability of a high-seam longwall. Furthermore, gob models using double-yield elements involve a large amount of data calculation and therefore have a very large mesh. It should also be noted that such modelling has not been carried out for the Chinese mining system and geological conditions. An alternative gob loading model by Abbasi and Chugh (2014) has been included in this study. Abbasi and Chugh utilized the gob model to assess the stability of chain pillars and set-up rooms in longwall mining practice in Illinois. The gob loading behaviour was modelled in FLAC 3D by applying a variable vertical force to the immediate roof and floor. The applied vertical force in the mined-out area was estimated based on field observations of caving in headgate and tailgate entries. The applied gob load was varied along and across the face advance directions to approximate the load carried by the gob. This gob loading model not only captures the effects of load transfer around the longwall face, gob, entries, coal pillars, and adjacent face, but it also simplifies the process of calculation. In this approach the model size is reduced even with fine mesh in the areas of interest.

Generally, gob behaviour can be modelled explicitly or implicitly (Esterhuizen, Mark, and Murphy, 2010b). In the explicit approach, the gob formation process is simulated to study roof fracturing, caving, and gob development during the advance of the longwall face. The alternative or implicit approach is used to model the overall effects of gob area on the longwall faces, pillars, and entries around the excavation, so that the stress and displacement distributions surrounding the excavation are realistically captured. Both the double-yield model and the estimated gob-load model for gob modelling belong to the implicit approach. Since this paper focuses on the effect of stress redistribution on face stability, the gob-load model approach was adopted here.

Quantitative measurement of gob loading characteristic in longwall mining is a challenge because the mined-out areas are not accessible. It is widely accepted that the loading characteristics of gob vary both along and across the face advance direction in the mined-out area. The vertical stress in the gob increases longitudinally from about zero at the back of shield, and transversely from about zero at the edge of longwall face, becoming equal to or close to the pre-mining vertical stress, as shown in Figure 4. Unfortunately, gob load characteristics were not available for the studied mine site in China. Therefore, several estimated gob models were constructed to perform sensitivity analyses of the gob loading characteristics. A realistic gob behaviour was regarded as being achieved when the vertical stress concentration factors (or VSCF, defined as the vertical stress at a particular point after excavation divided by the pre-mining applied vertical stress) ahead of the longwall face had achieved reasonable values of 2.5 to 3.0. For the sake of simplification, the

applied vertical stress in the gob area behind the shields was incrementally increased until the pre-mining vertical stress was reached. Figure 6 shows the gob loading characteristics estimates after several iterations.

Song, Chugh, and Wang (2017) conducted a 2D numerical analysis of longwall face stability that included shield supports, face support plates, and gob loading behaviour. Modelling details of the shield support and face plate were included. It was found that increasing the loading capacity of the shield supports in the face area had very little effect on stress distribution on the longwall face. However, it does improve ground control in the open area, safeguarding workers and production. Also, the currently designed face support plates can hold the yielded or failed coal mass in place and prevent it from falling. However, they have very little effect on the redistribution of stresses in the face area.

Model development

Mine description

Panel 8101 of Wangzhuang coal mine was modelled in this study. The 6.3 m thick coal seam is mined using a single-pass longwall mining method at a depth of about 350 m. Figure 7 shows part of the lithological sequence used in the numerical model. The coal seam dips at about 3–7°. The longwall face is 270 m wide, but only half of the panel width was modelled in order to reduce the model size. The longwall face is oriented N-S. The maximum horizontal pre-mining

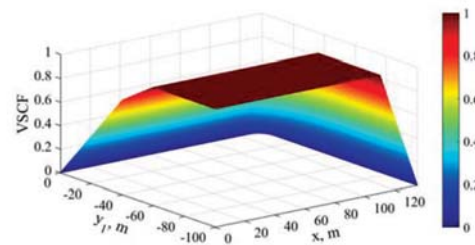


Figure 6—A 3D view of the gob loading characteristics used in this research. y is the distance from the face position in the gob area; x is the distance from panel 1 centre

Scale 1:200	LITHOLOGY	THICKNESS, m
	MUDSTONE	6.0
	FINE-GRAINED SANDSTONE	8.0
	MUDSTONE	10.5
	SANDY MUDSTONE	2.2
	COAL	6.3
	MUDSTONE	4.0
	FINE-GRAINED SANDSTONE	2.0
	MUDSTONE	6.0

Figure 7—General stratigraphy for Wangzhuang coal mine

3D analysis of longwall face stability in thick coal seams

compressive stress is about 15.75 MPa in the N55°W direction, and the other horizontal pre-mining compressive stress is oriented N35°E with a magnitude of 9.62 MPa.

Model description

One-half of each of the two adjacent longwall faces (centre to centre) was modelled. Figure 8 shows the final FLAC 3D model with the longwall panel layout and the overall geometry. The plan view of the overall model was shown in Figure 5. It is 300 m long and 200 m wide, and the model has an overall height of 63 m, with roller boundaries along the sides and at the bottom. A 20 m wide coal pillar was left between two panels, with 5 m wide entries on both sides. Solid coal barriers 30 m wide were included on both ends of the model. Longwall faces were advanced 170 m from the set-up rooms to ensure that the gob achieves the pre-mining vertical stress level. Panel 1 was advanced in 10 m increments, followed by panel 2 extraction. For improved accuracy, a fine mesh (1 m × 1 m × 0.5 m) was used for the coal and immediate roof and floor strata around the excavation. The shield (Shield ZY15000/33/72d) used in the study mine was modelled in this paper in a similar way to the earlier study (Song, Chugh, and Wang, 2017) but the face plate was not modelled.

The Hoek-Brown failure criterion (Equation [1]) was used for nonlinear analysis (Hoek, Carranza-Torres, and Corkum, 2012). Table 1 shows the rock mass engineering properties used for different lithologies in modelling. The nonlinear rock material constants (m_b , s , and a) for each lithology were calculated from estimated GSI rock mass classification values. These parameters were also used in the earlier 2D numerical modelling (Song, Chugh, and Wang, 2017).

$$\sigma_1' = \sigma_3' + \sigma_{ci}' \left(m_b \frac{\sigma_3'}{\sigma_{ci}'} + s \right)^a \quad [1]$$

where σ_1' and σ_3' are the major and minor effective principal stresses at failure, σ_{ci}' is the uniaxial compressive strength of the intact rock material, and m and s are material constants.

Matrix of models analysed

Five models were analysed in this paper. The original model has a seam height of 6.3 m, and the GSI of coal is 80. Models II and III, with seam thickness of 5 m and 7.5 m respectively, assess the influence of mining height on the stress distribution around excavations and failed zones development ahead of the face. The coal GSI was reduced to 75 in model IV and to 70 in model V to investigate the

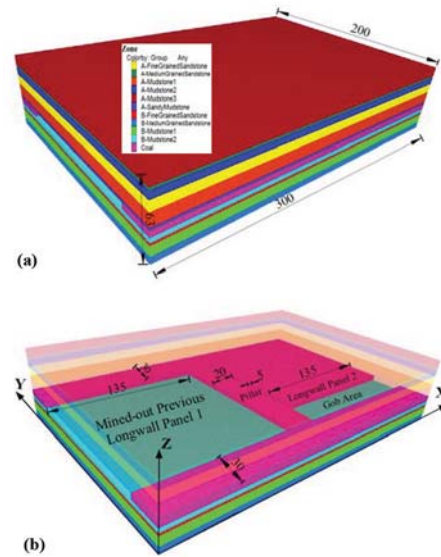


Figure 8—Numerical model used to assess the longwall face stability. (a) Final model showing the lithological sequence and overall geometry; (b) model with the general layout of the two adjacent longwall panels

influence of coal mass engineering properties on face stability. For each model, the solution stages consisted of:

- (1) Excavation of headgate and tailgate entries
- (2) Excavation of panel 1 set-up room and installation of roof support
- (3) Advance of panel 1 with shield
- (4) Incorporation of gob behind the face with changing loading behaviour
- (5) Excavation of panel 2 after panel 1 is mined.

Results and discussion

Division of panel regions

Since stress distribution around excavations and failure development on faces vary along the panel width, the half panel width was divided into different regions. Figure 9 shows that the peak VSCF values ahead of the face immediately above the coal seam continue to decrease from 3.1 at the centre of panel 1 to 1.5 at the panel edge where the face is close to the solid coal pillar and unmined panel 2. VSCF at the panel edge is only 50% of that at the middle section of the face. This would explain why most of the face falls observed in the field occur around the middle section of the longwall face rather than near the ends (see the face fall distribution along panel width in Figure 2). Based on this VSCF distribution along the panel width, panel 1 was

Lithology	ν	σ_{ci} , MPa	GSI	m_i	m_b	s	a	E_m , MPa
Fine-grained sandstone	0.15	105	92	15	11.272	0.411	0.500	7988.43
Medium-grained sandstone	0.19	90	88	15	9.772	0.264	0.500	6488.78
Mudstone	0.24	32	83	12	63539	0.151	0.500	4186.08
Sandy mudstone	0.22	35	85	12	7.023	0.1889	0.500	4493.98
Coal	0.26	28	80	11	5.385	0.1084	0.501	3697.46

3D analysis of longwall face stability in thick coal seams

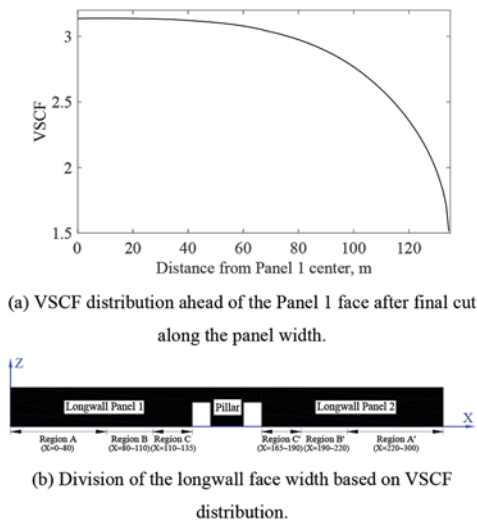


Figure 9—VSCF distribution and division of the longwall face width for analysis

subdivided into three regions: region A from $x = 0$ to $x = 80$ m, with peak VSCF values larger than 95% of the maximum VSCF; region B from $x = 80$ m to $x = 110$ m with peak VSCFs between 80 to 95% of the maximum VSCF; and region C from $x = 110$ m to $x = 135$ m with peak VSCFs less than 80% of the maximum VSCF (Figure 9(b)). Similarly, panel 2 was also subdivided into regions A, B, and C for analysis. The characteristics of stress distribution and yielded zones were analysed and compared in the three regions for both panels 1 and 2. It should be noted that ‘peak VSCF’ refers to the largest VSCF value ahead of the face in the mining direction, while ‘maximum VSCF’ refers to the largest peak value of VSCF, which occurs at the panel centre.

VSCF distribution

VSCF in the Y-direction

The VSCF is oriented in the Z-direction (vertical). The modelling analysis includes variation of the VSCF distribution along the X- and Y- directions (Figure 10). Since the VSCF values change along the panel width, three cross-sections in regions A, B, and C along the Y-direction were selected to represent the three regions of the longwall face, *i.e.* $x = 40$ m, 100 m, and 125 m shown as cross-sections AA, BB, and CC respectively in Figure 10. In Figure 11, the VSCF distributions ahead of the face and in the gob in different regions have been plotted. The peak VSCF values occur 2–3 m ahead of the longwall face. Region A has the largest peak VSCF, while region C has the lowest. From region A to region C, the distance of the peak VSCF ahead of the face decreases and becomes closer to the face location. At the same distance ahead of the face, region A has a larger VSCF and a larger area of coal ahead of the face is under the influence of higher VSCF. In the gob behind the face, VSCF distribution is almost identical for regions A and B. Pre-mining vertical stress in the gob is established about 67 m behind the longwall face. The VSCF in the gob in region C is lower.

Figure 12 documents the variation of VSCF along the cross-section DD. It shows that behind the face, the VSCF on

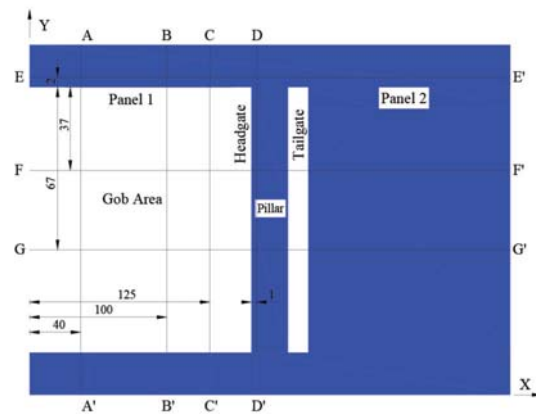


Figure 10—Locations of different cross-sections and their designations for VSCF analysis

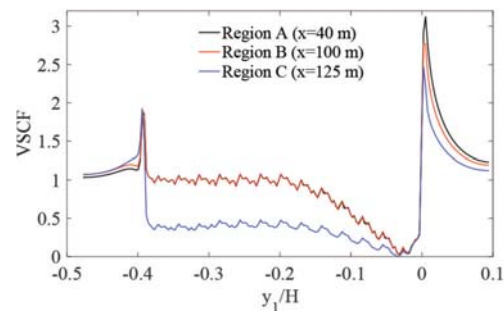


Figure 11—VSCF distribution along cross-sections AA', BB', and CC' after completion of panel 1. y_1 is the distance from face position (negative values refer to the gob area) and H represents mining depth (vertical section)

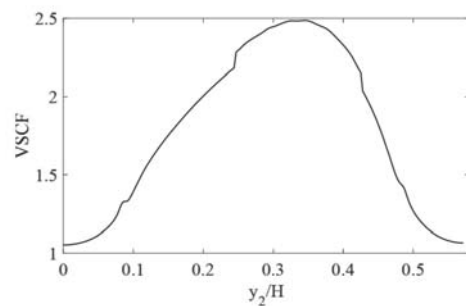


Figure 12—VSCF distribution along the vertical cross-section DD'. y_2 is the distance from point D'

the pillar first increases from unity at the face position to a maximum value of 2.49 about 50 m behind the face, and then decreases back to unity around the set-up room. This indicates the most vulnerable position of the pillar that may require additional support.

VSCF in the X-direction

VSCF distribution along the X-direction is shown in Figure 13. Figure 13a compares the VSCF distribution along cross-section EE after completion of panel 1 and panel 2. After

3D analysis of longwall face stability in thick coal seams

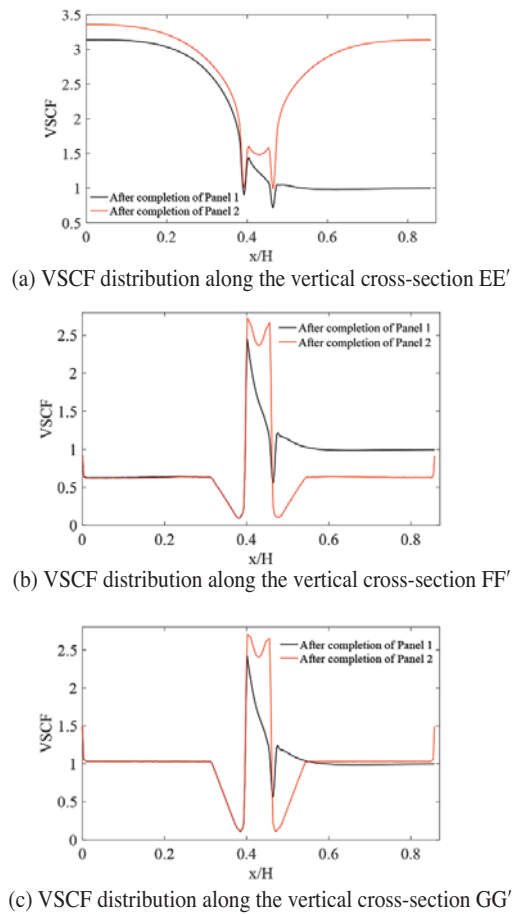


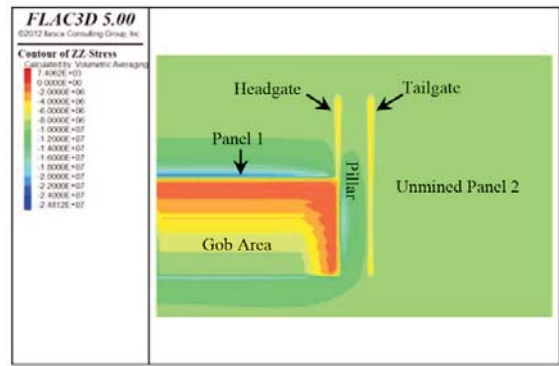
Figure 13—VSCF distributions along X- direction. x is the distance from panel 1 centre

panel 1 is mined out, the peak VSCF on the left side of the pillar is about 1.4. Unmined panel 2 is largely unaffected, with the peak side abutment VSCF only slightly larger than unity. However, after panel 2 is mined out, the VSCF on both sides of the pillar increases to about 1.58. The VSCF distribution looks symmetric about the centre line of the pillar, except that the VSCF along panel 1 is further increased. This is not a concern since panel 1 is already mined out.

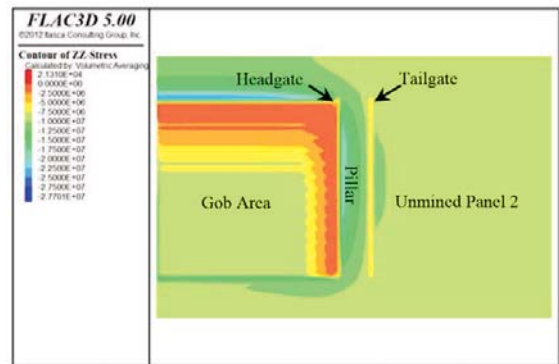
The VSCF distributions along cross-sections FF and GG are plotted in Figure 13b and 13c, respectively. After completion of panel 1, the peak VSCF on the left side of the pillar is about 2.42 in Figure 13b and 2.45 in Figure 13c, and the peak side abutment VSCF values on panel 2 are only 1.22 and 1.24, respectively. After panel 2 is mined, the VSCF values on both left and right sides of the pillar are increased. The curves also become symmetric.

Vertical stress distribution

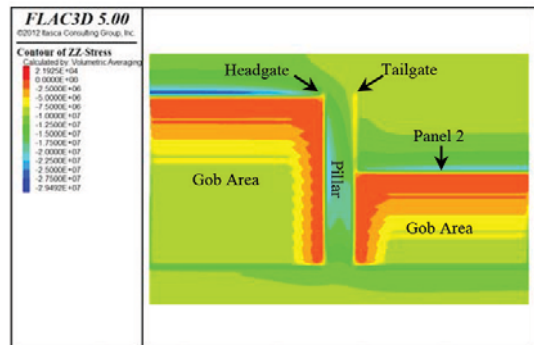
Figure 14 plots the vertical stress distribution on a horizontal plane above the coal seam at different stages of excavation. As the face advances, vertical stress in the gob area continues to change. The vertical stress is very low at the mined-out area behind the face and in the area close to the coal pillar. High vertical stress is found in the areas ahead of the face and on the pillar near entries.



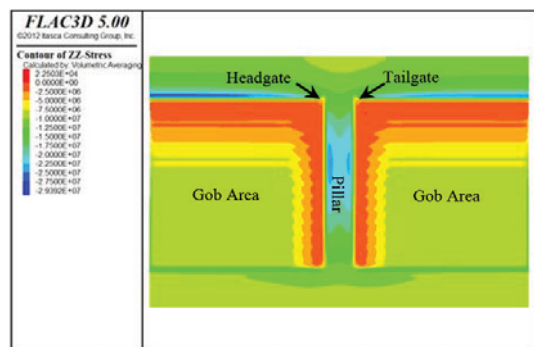
(a) Plan view of vertical stress distribution after 77 m advance of panel 1



(b) Plan view of vertical stress distribution after 137 m advance of panel 1



(c) Plan view of vertical stress distribution after 77 m advance of panel 2



(d) Plan view of vertical stress distribution after 137 m advance of panel 2

Figure 14—Vertical stress on a horizontal plane 1 m above the coal seam

3D analysis of longwall face stability in thick coal seams

Comparison of VSCF values and failure development for the two adjacent longwall faces

Peak VSCF ahead of the longwall face

Figure 15 plots the peak VSCF ahead of the face at each stage of longwall excavation as a function of face advance from the starting position. The VSCF values in different regions of the two adjacent panels are plotted. As the face advances, VSCF continues to increase until the gob assumes the full load. In regions A (A') and B (B'), the peak VSCF values at each stage are almost identical, but VSCF values in region C' of panel 2 are about 5.25% larger than those in region C of panel 1. Thus, mined-out panel 1 increases the VSCF values for the adjacent panel 2. However, this increase only extends 35–40 m (X- direction) in panel 2, *i.e.* approximately in the area of region C' of panel 2. In other words, mined-out panel 1 increases the VSCF in region C' of panel 2, which would affect face stability in this region.

Yielded zones on longwall faces

Figure 16 shows the yielded zones development ahead of the longwall face after completion of panel 1. Most of the failure in the coal face occurs in shear mode, and yielded zones typically extend 3 m ahead of the face. It is observed that further development of failed zones will progress from the centre toward the top before extending downward. Figure 17 plots the yielded zones at the different depth of the longwall face. It shows that the entire 0–1 m depth of the coal mass ahead of the face has yielded since the start of the longwall face. The next 2 m depth of the coal mass is relatively stable, but the yielded zones on longwall face in regions A, B, and C are different.

The percentage of the yielded zone volume as a function of the total volume in a specific region is used to illustrate differences between failed zones in different regions. Table II lists the percentage of failed zones in the 1–2 m depth of the coal face over the total volumes of the second row of elements in each region. It shows that as the face advances, the yielded zone percentage in each region gradually increases and then stabilizes after the gob starts to assume the full loading. Table II also compares the percentage of failure in different regions and between different panels. It is found that regions A and B of panel 1 have the same percentage of yielded zones as regions A and B of panel 2, respectively. Region A (A') sees the most failure, which peaks at about 67–70%. Yielded zone percentage in region B (B') is less, peaking at 60%. The difference in yielded zones

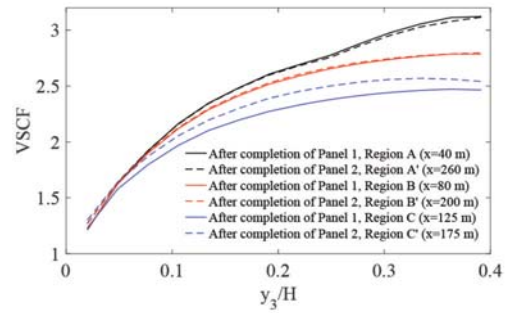


Figure 15—Peak VSCF as a function of face advance from the start position. y_3 is the distance from face start position

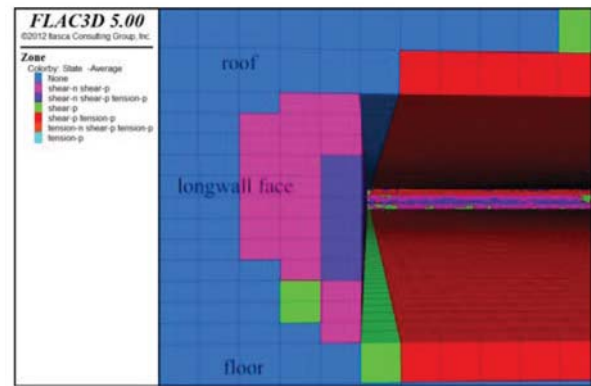


Figure 16 – Extension of the yielded zones in the face after completion of panel 1 (vertical section)

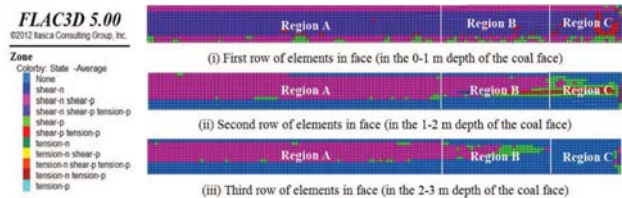


Figure 17 – Distribution of yielded zones on the longwall face after completion of panel

in regions C and C', however, is very distinct. Failure in region C of panel 1 peaks at 47%, compared to 54% in region C' of panel 2. It is once again confirmed that a previously mined-out longwall face will adversely affect face stability on the adjacent longwall face, especially in the region where it is close to the mined-out area.

Table II

Percentage of yielded zones by volume (%) in the 1–2 m ahead of the longwall face

		Cut 2	Cut 3	Cut 4	Cut 5	Cut 6	Cut 7	Cut 8	Cut 9	Cut 10	Cut 11	Cut 12	Cut 13	Cut 14
Region A/A'	Panel 1	16.67	13.85	16.98	27.71	42.50	50.00	58.33	64.38	66.67	66.67	66.67	66.67	70.83
	Panel 2	15.00	14.48	18.54	28.13	39.38	50.00	58.33	63.44	66.46	66.67	66.67	66.67	70.00
Region B/B'	Panel 1	16.67	15.00	16.67	23.61	33.33	47.50	53.88	57.22	58.61	60.56	61.11	60.56	59.17
	Panel 2	13.61	14.44	18.06	22.78	33.33	50.00	55.00	58.33	58.33	60.28	60.56	59.44	58.89
Region C/C'	Panel 1	17.71	17.71	13.19	23.26	30.90	33.33	35.76	39.93	42.36	44.79	46.18	47.22	47.22
	Panel 2	11.81	18.06	14.93	26.39	33.68	36.46	46.18	49.65	52.43	53.82	54.17	53.82	53.82

3D analysis of longwall face stability in thick coal seams

Effect of seam height on face stability

In the original model (model I) the seam height was 6.3 m. To investigate the effect of seam height on face stability, two additional models with seam heights of 5 m (model II) and 7.5 m (model III) were constructed. Figure 18 compares the peak VSCF ahead of the face in regions A, B, and C of models I, II, and III, as a function of the face advance from the start position. In each region, model II has the maximum peak VSCF while model III has the minimum. Compared to model I, the peak VSCF values in model II are higher by 4.81% in region A, 4.85% in region B, and 3.14% in region C. The peak VSCF values in model III are, however, reduced by 2.67% in region A, 2.40% in region B, and 0.70% in region C. A negative relationship is found between seam height and the peak VSCF values ahead of the face. This is because the stiffness of the coal seam decreases with increasing seam height, and the seam deforms more both laterally and vertically. Larger deformations on the face, or even face falls in the return, further destress the solid coal and decrease the VSCF values. On the other hand, thinner seams have higher stiffness and therefore can sustain more load.

It is noted that the yielded zones in model II extend only 1 m ahead of the face before the face advances 67 m from the start position (cut 7), and 2 m after completion of panel 1. Failed zones in model III, however, extend 3 m ahead of the face after 107 m advance of the longwall face (cut 11). Table III records the failed zone percentage in the 1–2 m depth of the face in each region at different stages of longwall advance. It shows a positive relationship between the seam height and volumes of yielded zones. After the gob assumes full pre-mining load from the overburden, failed zones ahead of the face become stable. Compared to model I, model II has a significantly reduced volume of yielded zones, but in model III the failed zones ahead of the face increase substantially. In the second row of elements in the face (1–2 m depth of the face), model I shows about 67–70% of the yielded zones in region A, 59–61% in region B, and only 47% in region C, compared to 56.5%, 37%, and 2–3% for model II, and 80%, 68%, and 59–63% for model III.

Effect of coal mass engineering properties on face stability

The GSI of the coal was reduced to 75 in model IV and to 70

in model V to assess the effect of coal mass engineering properties on face stability. By decreasing the GSI, other coal engineering parameters are also decreased. The percentage reductions of these parameters are listed in Table IV. Figure 19 plots the peak VSCF ahead of the longwall face in regions A, B, and C of models I, IV, and V, as a function of face advance from the start position. With the decrease in GSI, the peak VSCF immediately ahead of the face decreases for each longwall face, and in each region of the longwall face. Compared to model I, the peak VSCF of model IV is reduced

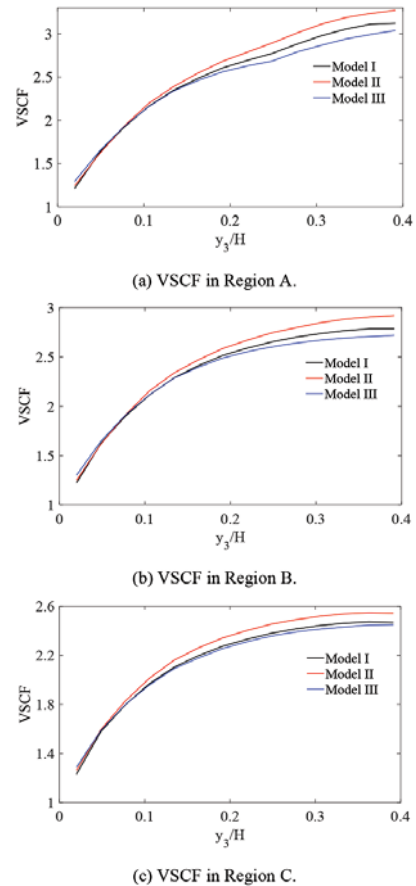


Figure 18—Peak VSCF values ahead of the face as a function of the face advance from the start position

		Cut no.												
		2	3	4	5	6	7	8	9	10	11	12	13	14
Region A	Model I	16.67	13.85	16.98	27.71	42.50	50.00	58.33	64.38	66.67	66.67	66.67	66.67	70.83
	Model II	0.00	0.00	0.00	0.00	0.00	0.00	14.88	29.75	47.38	50.00	56.38	56.75	56.50
	Model III	33.33	31.83	20.50	40.33	53.33	65.58	66.67	72.48	73.33	73.33	78.25	79.58	80.00
Region B	Model I	16.67	15.00	16.67	23.61	33.33	47.50	53.88	57.22	58.61	60.56	61.11	60.56	59.17
	Model II	0.00	0.00	0.00	0.00	0.00	0.00	0.00	8.67	18.00	27.33	34.67	36.67	37.00
	Model III	33.33	31.78	27.78	34.44	53.11	58.44	63.78	66.00	68.00	68.67	68.67	67.56	67.78
Region C	Model I	17.71	17.71	13.19	23.26	30.90	33.33	35.76	39.93	42.36	44.79	46.18	47.22	47.22
	Model II	0.83	0.83	1.25	1.25	0.83	1.25	1.25	1.25	1.25	1.25	1.25	2.08	2.92
	Model III	34.17	33.33	31.11	28.06	40.56	47.22	51.11	53.89	56.67	58.06	58.11	59.44	63.06

3D analysis of longwall face stability in thick coal seams

Table IV
Percentage changes in coal mass engineering properties for models IV and V compared to model I

Variable	Model IV	Model V
c	12.04%	21.22%
$\tan\phi$	4.59%	9.25%
E_{cm}	7.27%	16.76%
σ_{cm}	14.61%	25.84%

c is the cohesion; ϕ the internal friction angle; E_{cm} the deformation modulus of coal mass; and σ_{cm} is compressive strength of the coal mass

by about 2.79% in region A, 2.09% in region B, and 7.67% in region C, while the peak VSCF of model V is decreased by 4.55% in region A, 6.10% in region B, and 9.51% in region C. The positive relationship between VSCF and GSI implies that ‘weak coal’ with lower engineering properties can sustain less load from roof strata, while ‘hard coal’ is subjected to higher load, which is in agreement with field observations.

Failed zones extend to 3 m ahead of face after 107 m of advance in model IV (cut 11) and after 77 m of advance in model V (cut 8). Table V shows the percentage of failed zones by volume in the 1–2 m ahead of the longwall face as the face advances. With the reduction in GSI, yielded zones ahead of the face are significantly increased. As the GSI decreases from 80 to 70, the percentage of failed zones in the 1–2 m depth of the face are increased by about 25% in region A, 30% in region B, and 35% in region C. Reduction in coal strength properties has a negative effect on face stability since it increases the volumes of yielded zones ahead of the face dramatically, since the peak abutment pressure is located further away from the face.

Summary and conclusions

The face stability characteristics of two adjacent longwall along and across the panel were modelled, taking into consideration the gob loading characteristics. A total of five models (models I to V) were constructed to assess the effects of a previously mined-out longwall face, the seam height, and

coal mass engineering properties on face stability. The longwall face stability characteristics with the progressive advance of the working panel are discussed with reference to three different regions (regions A, B, and C) along the panel width based on VSCF distribution. The stress distribution around the excavation and development of failed zones on longwall faces are compared and analysed in different regions and in different models.

This study has developed scientific approaches for analysing face stability problems in different mining systems

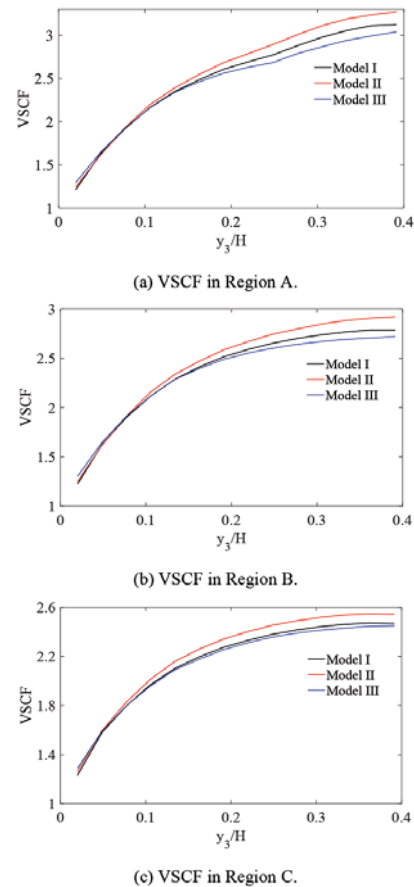


Figure 19—Peak VSCF values ahead of face as a function of face advance from start position

Table V
Percentage of yielded zones by volume (%) in the 1–2 m ahead of the longwall face

		Cut no.												
		2	3	4	5	6	7	8	9	10	11	12	13	14
Region A	Model I	16.67	13.85	16.98	27.71	42.50	50.00	58.33	64.38	66.67	66.67	66.67	66.67	70.83
	Model IV	29.69	25.42	33.33	58.3	65.10	66.67	75.00	83.33	83.33	83.33	83.33	83.33	83.33
	Model V	33.33	47.29	58.33	75.00	90.21	91.67	91.67	91.67	91.67	91.67	91.67	91.67	91.67
Region B	Model I	16.67	15.00	16.67	23.61	33.33	47.50	53.88	57.22	58.61	60.56	61.11	60.56	59.17
	Model IV	27.50	20.28	33.33	54.72	58.33	65.00	69.17	73.89	78.89	81.11	81.67	80.83	80.28
	Model V	33.33	47.22	58.33	74.17	81.94	89.17	91.67	91.67	91.67	91.67	91.67	91.67	90.83
Region C	Model I	17.71	17.71	13.19	23.26	30.90	33.33	35.76	39.93	42.36	44.79	46.18	47.22	47.22
	Model IV	26.74	25.35	27.43	39.24	49.31	53.47	56.94	60.07	61.11	61.81	62.15	61.46	61.46
	Model V	34.72	34.72	57.99	65.97	73.26	77.43	79.86	82.64	84.03	84.72	84.03	82.99	82.29

3D analysis of longwall face stability in thick coal seams

with variable geological conditions. The data provides a foundation for developing sound remedial measures for controlling face stability. Since no field measurements of observation data were available, quantitative validation of these analyses is not possible. However, the results obtained seem to conform to field observations. Furthermore, the results provide guidance to the approaches that could be researched to minimize face falls. However, each site-specific case must be analysed for design purposes.

Gob behaviour is critical for developing a physically realistic numerical model for assessing longwall face stability. The primary goal of this research was to develop a FLAC3D model of two adjacent longwall faces and observe the longwall face stability characteristics.

- (1) Thick coal seams mined in China are likely to experience face stability problems. Most of these should occur around the central part of the face and be concentrated around the upper part of the mined face near the roof-coal interface
- (2) Face falls are most likely to occur where the vertical stress is high and the horizontal confining stress is low. Therefore, yielded or failed zones on the longwall face are likely to be localized near the roof of the coal seam rather than near the bottom. This is consistent with field observations
- (3) The depth of the failed coal mass ahead of the face is 2–3 m. The 3D shape of the failed coal mass should consist of several curved surfaces
- (4) The peak vertical stress concentration factor (VSCF) ahead of the longwall face varies along the panel width. The maximum value occurs around the middle section of the panel and it continually decreases to only about 1.5 around the two ends of the face. Maximum VSCF values vary from 2.9–3.2 in different models
- (5) The distribution of failed zones on the longwall face also varies along the panel width. In region A (middle section of the panel) more failure is found, while region C (the end of the panel) has less failed zones
- (6) Regions A and B of panel 1 (first panel) have identical VSCF values and same amount of failed zones as regions A and B of panel 2 (second adjacent panel). However, peak VSCF values and failed zones in region C are 5.25% and 10% larger than those in region C. A previously mined-out panel (gob) will adversely affect the face stability of the adjacent longwall, and this influence can extend about 35–40 m toward the centre of the adjacent panel being mined
- (7) Face stability is more critical around the tailgate than around the headgate, due to the effect of low load-carrying capacity of the gob in the adjacent mined-out longwall face. This is typical of what is observed in the field.

Seam height and coal mass engineering properties are important variables affecting face stability and were selected to perform sensitivity studies.

- (8) Longwall faces with a greater seam height have larger volumes of yielded or failed zones in the unmined coal, but lower VSCF values ahead of the

face. Lower thickness seams with larger stiffness, however, deform less and sustain more load

- (9) Reduced GSI with lower cohesion and internal angle of friction will result in decreased VSCF ahead of face, but larger volumes of yielded zones on the longwall face

This paper is an extension of the 2D analyses published earlier (Song, Chugh, and Wang, 2016). Therefore, some of the conclusions here were also presented in the earlier paper.

Based on the earlier 2D study, the authors recommend that the open distance between the face and the back end of shields should be kept to a minimum to improve face stability. Therefore, all efforts must be made to ensure that the immediate roof strata behind the shields cave regularly. Furthermore, the currently designed face support plates can only hold the yielded or failed coal mass in place and control its fall so that it does not adversely affect safety and production. However, there is room for improvement in face plate design to better support the failed coal mass.

Acknowledgements

The authors are grateful for Mr S. Sinha's help in using the FLAC3D code. This research was sponsored by the Joint Funds of the National Natural Science Foundation of China (U1361209), the National Basic Research Program of China (973 Program, 2013CB227903), and the National Natural Science Foundation of General Programs (U51674264, 51574244).

References

- ABBASI, B., CHUGH, Y.P., and GURLEY, H. 2014. An analysis of the possible fault displacements associated with a retreating longwall face in Illinois. *Proceedings of the 48th US Rock Mechanics/Geomechanics Symposium*, MN, USA. American Rock Mechanics Association, Alexandria, VA.
- BAI, Q.S., TU, S.H., CHEN, M., and ZHANG, C. 2016. Numerical modeling of coal wall spall in a longwall face. *International Journal of Rock Mechanics and Mining Sciences*, vol. 88. pp. 242–253.
- BAI, Q.S., TU, S.H., ZHANG, X.G., ZHANG, C., and YUAN, Y. 2014. Numerical modeling on brittle failure of coal wall in longwall face – a case study. *Arabian Journal of Geosciences*, vol. 7, no. 12. pp. 5067–5080.
- CHEN, L. 2012. Study on the pressure behaviors of 'Three Soft' working face with large mining height and controlling technology. MS thesis, Anhui University of Science and Technology, Anhui, China (in Chinese).
- ESTERHUIZEN, E., MARK, C., and MURPHY, M.M. 2010a. The ground response curve, pillar loading and pillar failure in coal mines. *Proceedings of the 29th International Conference on Ground Control in Mining*, Morgantown, WV. University of West Virginia. pp. 19–27.
- ESTERHUIZEN, E., MARK, C., and MURPHY, M.M. 2010b. Numerical model calibration for simulating coal pillars, gob and overburden response. *Proceedings of the 29th International Conference on Ground Control in Mining*, Morgantown, WV. University of West Virginia. pp. 46–57.
- HOEK, E., CARRANZA-TORRES, C., and CORKUM, B. 2012. Hoek-Brown failure criterion - 2002 edition. *Proceedings of the NARMS-TAC Conference*, Toronto, Canada. pp. 267–273.
- ITASCA CONSULTING GROUP, INC. 2012. FLAC3D (Fast Lagrangian Analysis of Continua in 3 Dimensions), Version 5.0. Minneapolis.
- NIU, Y.Q., CHEN, S.Y., and LIU, J.F. 2010. Analysis on spalling increased mechanism of fully mechanized high cutting coal mining face and prevention measures. *Coal Science and Technology*, vol. 38, no. 7. pp. 38–41.
- PAPPAS, D. and MARK, C. 1993. Behavior of simulated longwall gob material. RI 9458. US Bureau of Mines.
- PENG, S.S. 1984. Longwall Mining. Wiley, New York.

3D analysis of longwall face stability in thick coal seams

- SHABANIMASHCOOL, M. and LI, C. 2012. Numerical modelling of longwall mining and stability analysis of the gates in a coal mine. *International Journal of Rock Mechanics and Mining Sciences*, vol. 51. pp. 24–34.
- SONG, G.F. 2016. Prediction of longwall face height and multiple regression analysis on mining height increase. *Coal Technology*, vol. 35, no. 5. pp. 31–33 (in Chinese).
- SONG, G.F., CHUGH, Y.P., and WANG, J.C. 2017. A numerical modeling study of longwall face stability in mining thick coal seams in China. *International Journal of Mining and Mineral Engineering*, vol. 8, no. 1. pp. 35–55.
- SONG, Z.Q., LIANG, S.K., TANG, J.Q., and LU, G.Z. 2011. Study on the influencing factors of coal wall rib spalling in fully mechanized working face. *Journal of Hunan University of Science and Technology (Natural Science Edition)*, vol. 26, no. 1. pp. 1–4 (in Chinese).
- TIAN, Q.Z., ZHANG, A.R., LU, Q.K., LIU, Y.F., and LI, P.X. 2012 The study on coal wall stability of thick coal seam with large-high mining face. *Journal of Taiyuan University of Technology*, vol. 43, no. 1. pp. 73–76. (in Chinese).
- WANG, J.C. 2009. Theory and Technology of Thick Seam Mining. Metallurgical Industry Press, Beijing (in Chinese).
- WILSON, A.H. 1983. The stability of underground workings in the soft rocks of the coal measures. *International Journal of Mining Engineering*, vol. 1. pp. 91–187.
- WHITTAKER, B.N. 1974. An appraisal of strata control practice. *Mining Engineering*, vol. 134. pp. 9–24.
- YAVUZ, H. 2004. An estimation method for cover pressure re-establishment distance and pressure distribution in the goaf of longwall coal mines. *International Journal of Rock Mechanics and Mining Sciences*, vol. 41. pp. 193–205.
- YASITLI, N.E. and UNVER, B. 2005. 3-D numerical modeling of stresses around a longwall panel with top coal caving. *Journal of the South African Institute of Mining and Metallurgy*, vol. 105. pp. 287–300. ◆

RECRUITMENT OF ENGINEERING PANEL OF EXPERTS MEMBERS

The Lesotho Highlands Development Authority (LHDA) is inviting Expressions of Interest from engineering specialists interested in serving on the Panel of Experts for Phase II of the Lesotho Highlands Water Project.

Specialists in the design and construction of major bridges, concrete faced rockfill dams, tunneling and tunnel structures for water and hydropower projects; geology and geotechnical engineering, mechanical and electrical engineering for water and hydropower projects, and construction and contract law for major civil engineering projects are invited to respond to the advertisement published on the LHDA Phase II website at:

<http://www.lhda.org.ls/phase2/tenderbulletin/tenderInformation.aspx?ContractNumber=5506>

Applications close on 19 March 2018.



Production of metallurgical-grade silicon from Egyptian quartz

by H.H.M. Ali*, M.H. El-Sadek*, M.B. Morsi*, K.A. El-Barawy*, and R.M. Abou-Shahba†

Synopsis

Metallurgical-grade silicon (MG-Si) was successfully produced by carbothermic reduction-smelting of Egyptian quartz using a mixture of carbonaceous materials in a locally made semi-pilot submerged arc furnace. The effects of different technical parameters such as the carbon to silica ratio, smelting time, power input, and weight ratio of carbon sources were investigated. The MG-Si product was characterized by X-ray diffraction (XRD), X-ray fluorescence (XRF), and scanning electron microscopy (SEM). A maximum silicon recovery of about 75% at a product purity of about 97% was achieved under the optimum experimental conditions of 80 minutes' smelting time, 48 kW power input, and a carbon/silica ratio of 0.39.

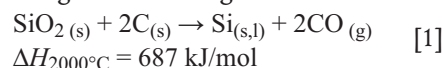
Keywords

metallurgical- grade silicon, carbothermic reduction, quartz, charcoal, coke, petroleum coke.

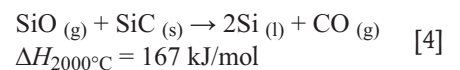
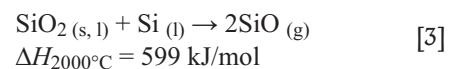
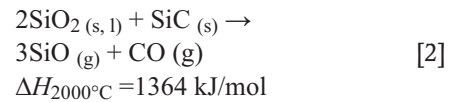
Introduction

Metallurgical-grade silicon (MG-Si) is an important metal which has a range of diverse industrial applications such as a deoxidizer in steelmaking industry, alloying element in the aluminum industry, the preparation of organosilanes, and the production of hyper-pure 'electronic grade' silicon (>99.99% Si), which is used in the electronics industry as well as solar cells (PV Education. 2013; Aasly, 2008).

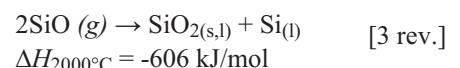
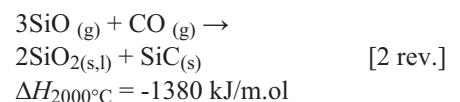
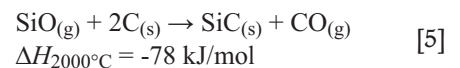
MG-silicon is produced by the carbothermic reduction-smelting process, in which silica is reduced by carbon in a submerged arc furnace at temperatures between 1300 and 2000°C under atmospheric pressure. The charge materials include a silicon source (quartz, sand, or quartzite) and a typical reductant blend comprising coke, coal, charcoal, and wood chips. The reduction process occurs according to the following reaction:



This overall reaction is the sum of different reactions inside the furnace, which can be specified according to the temperature range. The furnace environment is divided into two zones; high temperature (approx. 2000°C) and low temperature (< 1811°C) zones, in which different reactions dominate. In the high-temperature zone around the electrode tip, the following reactions occur:



The slowest of these three reactions are probably the SiO(g)-producing reactions [2] and [3], which consume a major part of the input electrical energy. Silicon can be produced through reaction [4] at temperatures above 1811°C. The SiO gas travels upwards in the furnace and is recovered either by reaction with the carbon material (Equation [5]) or by condensation where the temperature is sufficiently low (< 1800°C) (reactions [2 rev.] and [3 rev.]).



The condensate-producing reactions [2 rev.] and [3 rev.] are strongly exothermic and are the main factors that contribute to the upwards heat transport in the furnace.

The temperature at the top of the furnace can vary between 1000 and 1700°C. Typical industrial silicon yields are around 85% in a

* Central Metallurgical Research and Development Institute (CMRDI), Egypt.

† Faculty of Science, Al-Azhar University, Egypt.

© The Southern African Institute of Mining and Metallurgy, 2018. ISSN 2225-6253. Paper received Jun. 2017; revised paper received Nov. 2017.

Production of metallurgical-grade silicon from Egyptian quartz

well-operated furnace. The SiO gas will only be captured by reactions [2 rev.] and [3 rev.]. The temperature has a major effect on the equilibrium conditions for these two reactions. Much work has been done in recent years to define the reaction zones inside the silicon furnace (Myrhaug, 2003; Tangstad *et al.*, 2010; Ringdalen and Tangstad, 2012; Asen 2012; Tangstad, 2012; Schei, Tuset, and Tvei, 1998).

In Egypt, tremendous resources of high-quality sands and quartz (the average content of SiO₂ is 99%) exist in Sinai and in the Eastern Desert. Despite the huge silica resources and the availability of reductants, there is no silicon industry in Egypt. In this paper we investigate the possibility of utilizing the local quartz resource for the production of MG-Si by studying the factors affecting the production process, such as carbon/silica ratio, reduction time, power input, and weight ratio of carbon sources.

Experimental

Materials

One ton of quartz from the Al Faleg area, Marsa Alam, Eastern Desert was subjected to a series of crushing cycles using a pilot jaw crusher. The particle size between 16 mm and 2 mm was used for the production of MG-Si. XRF analysis showed that quartz consists mainly of SiO₂ (99.94%), with minor amounts of Fe₂O₃ (0.02%), Al₂O₃ (0.02%), and MgO (0.02%). Trace amounts of other oxides such as CaO (0.002%), K₂O (0.003%), and TiO₂ (0.0002%) were detected. XRD analysis was conducted to determine the phase composition of the quartz. Figure 1 shows that all the peak positions match the standard quartz phase.

Different carbon sources such as charcoal, coal, petroleum coke, and wood chips (with a fixed carbon content of 45%) were used as reductants. Table I shows the approximate chemical analysis of the carbonaceous materials.

Reduction technique

Reduction-smelting tests were performed in a locally-made electric arc furnace (EAF). The furnace is a submerged single-electrode (125 kW) furnace powered by five transformers. Smelting tests were conducted in a graphite hearth of 35 cm diameter which acts as the earth conductor, with a graphite rod 10 cm in diameter and 120 cm in length, located in the center of the graphite hearth, acting as the live electrode. The graphite electrode is connected to the terminal of the power transformer through a pure copper tube cooled

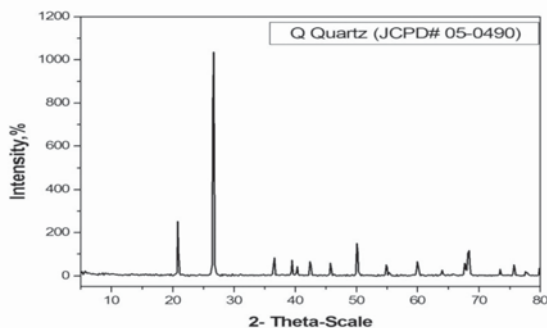


Figure 1—XRD spectrum of the quartz

by a flowing current of water. The furnace is tilted on its horizontal axis to pour the molten silicon metal at the end of each experiment. The quartz sample was mixed thoroughly with predetermined amounts of carbonaceous materials according to the following relationship.

The reduction experiments were carried out by introducing about 10 kg of the mixture through the feeder into the furnace. After smelting, the extent of the reduction process was calculated according to the following formula:

$$\text{Extent of reduction \%} = \left[\frac{Si_p}{Si_0} \right] \times 100$$

where Si₀ is the initial silicon content in quartz and Si_p is the produced Si metal

Results and discussion

The data obtained and technical parameters affecting the carbothermic reduction smelting of quartz to produce MG-silicon metal are discussed in the following sections

Charge composition

Effect of carbon/silica weight ratio

To ensure a high silicon recovery, it is necessary to maintain the carbon/silica weight ratio of the charge at the required stoichiometric value. A series of experiments was carried out using mixtures of the pure crushed quartz sample with different proportions of coal, petroleum coke, charcoal, and wood chips. Different ratios of fixed carbon to silica (C/SiO₂) ranging from 0.30 to 0.45 (*i.e.* from 1.5 to 2.25 molar ratio of fixed carbon to silicon dioxide) were used in this study. The charges were smelted in the EAF at constant conditions of current (about 0.8 kA), voltage (about 45 V), and power input (about 36 kW) for a constant smelting time of 60 minutes. The extent of reduction of silica as a function of the carbon/silica ratio is depicted in Figure 2. It is clear that the reduction extent increases from 15% to about 30% as the carbon/silica ratio increases from 0.3 to 0.39 (*i.e.* from 1.5 to 1.95 molar ratio of fixed carbon to silicon dioxide). The maximum recovery of MG-Si was about 30%. Increasing the C/SiO₂ ratio above 0.39 was accompanied by a decrease in reduction extent. It can be concluded that the optimum C/SiO₂ weight ratio is about 0.39 (1.95 molar ratio of C/SiO₂), which is in good agreement with the published results (Dosaj *et al.*, 1992; Arvidson, Dosaj, and May, 1991).

XRD characterization of the product metal was conducted to ascertain the reasons for these trends. Figure 3 shows the presence of the silicon carbide phase behind silicon metal in the product from a charge containing a C/SiO₂ weight ratio of

Table I

Chemical analysis (%) of the different types of carbon used as reductants

	Carbon type		
	Coal	Pet. coke	Charcoal
Moisture	0.5	0.43	3.6
Volatile matter	19.8	14.6	12.9
Ash	8.4	0.38	2.86
Fixed carbon	71.3	84.6	80.6

Production of metallurgical-grade silicon from Egyptian quartz

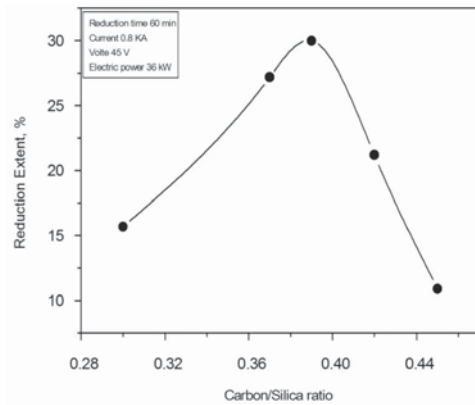


Figure 2—Effect of carbon/silica ratio on the extent of SiO₂ reduction

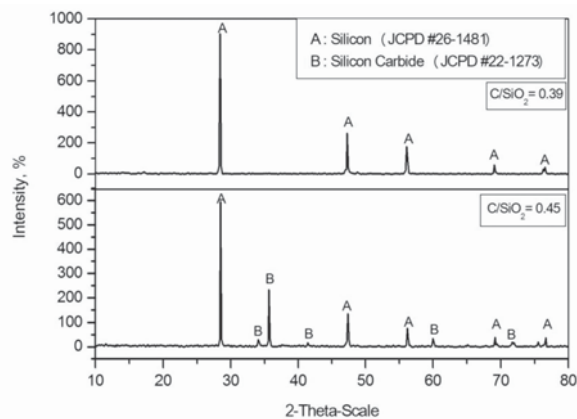


Figure 3—XRD patterns of product from charge containing carbon/SiO₂ ratios of 0.39 and 0.45

0.45, which indicates that the reaction is not complete. However, with the charge containing a C/SiO₂ weight ratio of 0.39 (1.95 molar ratio of C/SiO₂), only the silicon metal phase was detected. Smelting with an excess of carbon promoted the formation of an excess of silicon carbide, which lowered the amount of silicon produced. Subsequently, silicon carbide accumulated and filled the hearth of the furnace, which made it necessary to raise the electrode, which increased the temperature in the outer zone of the furnace. This will lead to an increase in the electrode consumption. Therefore, it is important for efficient furnace operation that the furnace is kept in carbon balance (Dosaj *et al.*, 1992).

Effect of carbon types on MG-Si production at constant carbon/silica weight ratio

There is no doubt that the carbonaceous reductant in the mix should have a minimum ash content, large reactive surface, low volatile matter content, high electrical resistance, and sufficient mechanical strength for achieving a good silicon yield with acceptable purity. A primary factor affecting the efficiency of the silica reduction process is the reactivity of the carbon reductants. Based on reactivity, purity, and the cost of the reductant, we investigated mixtures of different types of carbonaceous materials (coal, petroleum coke,

charcoal, and wood chips). In order to estimate the optimum reductant recipe, we varied the mass of each type of carbonaceous materials while keeping the masses of the other types constant. The mass ratio of fixed carbon to silica was kept constant (0.39) in all the experiments.

Effect of varying charcoal additions

Charcoal was found to be the best reductant due to its high reactivity, low ash content, and high electrical resistivity, which has a positive influence on the furnace electrical efficiency and process chemistry. A series of experiments was carried out using charges of quartz mixed with constant weights of coal, petroleum coke, and wood chips with different weights of charcoal. The carbon/silica ratio was maintained at 0.39, and the applied electrical power was about 36 kW with a smelting time of 60 minutes. Figure 4 shows the variation of the extent of silica reduction as a function of the ratio of charcoal to silica in the charge. The extent of reduction increased with increasing charcoal content in the charge up to 30% by mass, and then decreased. The initial increase in the extent of reduction is due to the high reactivity of charcoal, which enhances the reduction process and leads to the formation of excess silicon carbide. However, further charcoal additions accelerate the formation of silicon monoxide gas in the outer zone of the furnace, which escapes from the surface of reaction and leads to a decrease in the extent of reduction and lower recovery of silicon metal (Vaish, 2012; Kuhlmann, 1965)

Effect of varying petroleum coke additions

A series of experiments was performed in which the ratio of petroleum.coke to quartz was varied while keeping the carbon/silica ratio constant at 0.39. The applied electrical power was about 36 kW and the smelting time 60 minutes. Figure 5 shows the variation in the extent of reduction as a function of the petroleum coke/quartz ratio.

The extent of reduction increased with increasing petroleum coke additions up to about 28% by mass, after which further increases in petroleum coke decreased the extent of reduction and the yield of silicon metal. Although petroleum coke plays an important role in the reduction process, it contains ash with a low iron content and much finer material. The introduction of these fines into the

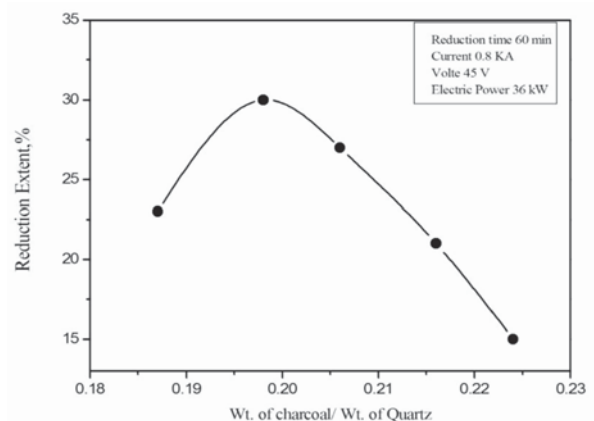


Figure 4—Effect of charcoal to quartz ratio at constant carbon/silica ratio on the extent of reduction

Production of metallurgical-grade silicon from Egyptian quartz

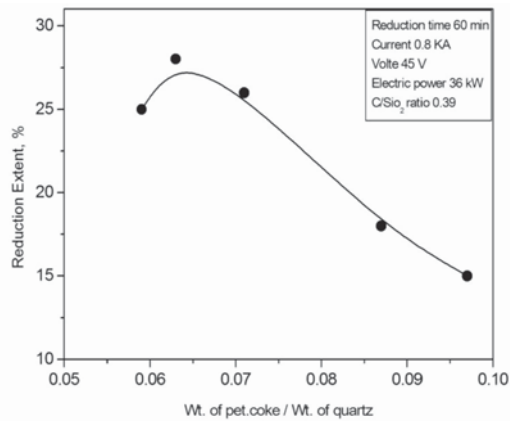


Figure 5—Effect of petroleum coke to quartz ratio at constant carbon/silica ratio on the extent of reduction

furnace results in poor furnace efficiency because it reduces the porosity of the charge, leading to the entrainment and subsequent blowing out of the fines with the furnace off-gas (Kuhlmann, 1965).

Effect of varying coal additions

Coal has a high electrical resistance and negligible quantities of volatile matter, but contains undesirable impurities such as iron. Figure 6 shows the extent of reduction as a function of the coal/quartz ratio. The extent of reduction increases with increasing coal additions until about 28% yield, beyond which the yield decreases with further coal additions. This may be due to the coal containing from about 5 to 15% ash (25% of which is iron oxide). The iron partitions into the silicon metal and affects the purity of the product (Kuhlmann, 1965).

From these results, the optimum charge composition was determined to be 64.63 wt.% quartz, 4.08 wt.% coal, 12.6 wt.% charcoal, 11.77 wt.% petroleum coke, and 6.92 wt.% wood chips.

Effect of smelting time

A series of smelting experiments was conducted on charges containing 64.63 wt.% quartz, 4.08 wt.% coal, 12.6 wt.% charcoal, 11.77 wt.% petroleum coke, and 6.92 wt.% wood chips at a C/SiO₂ ratio of 0.39 and power input of 36 kW, while varying the smelting time from 60 to 90 minutes. It was found (Figure 7) that the recovery of silicon metal increased from 28 to 40% as the smelting time was increased from 60 to 80 minutes. Further increases in smelting time up to 90 minutes decreased the silicon recovery to about 20%. This sharp decrease is due to the evaporation of the silicon metal product in the form of silica fumes as a result of the long smelting time. The optimum smelting time of 80 minutes yielded a silicon recovery of about 40%.

Effect of furnace power input

The smelting process was investigated at different power inputs ranging from 30 to 60 kW using charges having a C/SiO₂ ratio of 0.39 and a constant smelting time of 80 minutes. Figure 8 illustrates the variation in silicon recovery with power input. Silicon recovery was increased from about

20% to 75% as the power input was increased from 30 to 48 kW. With further increases in power, silicon recovery decreased, falling to about 30% at 60 kW power input.

The optimum recovery of about 75% of MG-Si was obtained at a power input of 48 kW. This may be due to the power input being sufficient to increase the furnace temperature to a level that enhances the reaction between SiO gas and SiC to form silicon metal. Higher power inputs, and higher temperatures, lead to the formation of excess SiO gas

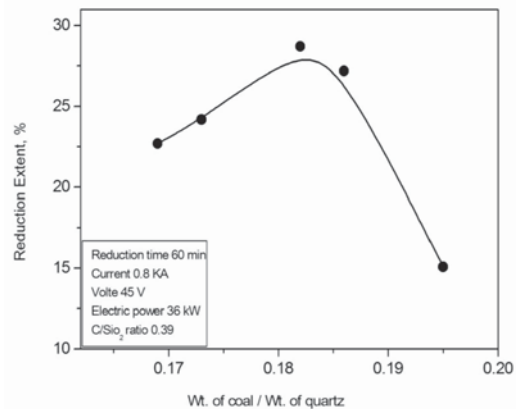


Figure 6—Effect of coal to quartz ratio at constant fixed carbon/silica ratio on the extent of reduction

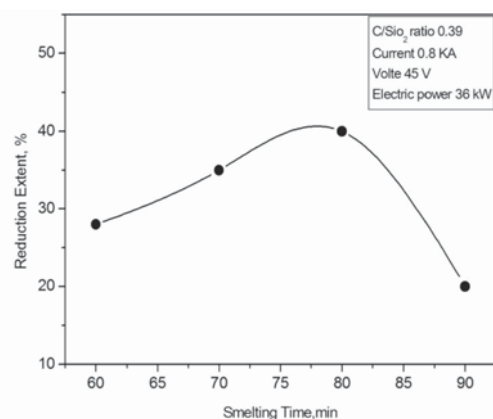


Figure 7—Effect of smelting time on the extent of reduction

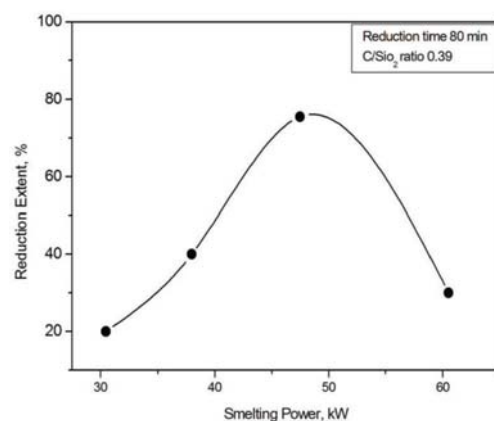


Figure 8—Effect of smelting power on the extent of reduction

Production of metallurgical-grade silicon from Egyptian quartz

and consequently increase the silica loss (Mitsuhiro and Hirasawa, 2000).

Evaluation of the MG-silicon product

Figure 9 displays photographs of the MG-silicon product obtained at the optimum reduction-smelting conditions (carbon/silica mass ratio 0.39, smelting time 80 minutes, and power input 48 kW). The microstructure and chemical composition were investigated using XRD, SEM, and XRF.

X-ray diffraction (XRD)

Figure 10 shows the XRD spectrum of the MG-Si produced under optimum conditions, which indicates the presence of silicon metal only.

X-ray fluorescence (XRF)

The MG-silicon was chemically analysed by XRF to determine its purity. The results are summarized in Table II. The MG-silicon product contained about 97% Si and 1.15% Fe, with traces of other elements. It is clear that the MG-Si product had low traces of P, and it is noteworthy that no boron was detected. It is known that most impurities such as Fe, Al, and Ti, contained in the raw materials are transferred to the MG-silicon product.

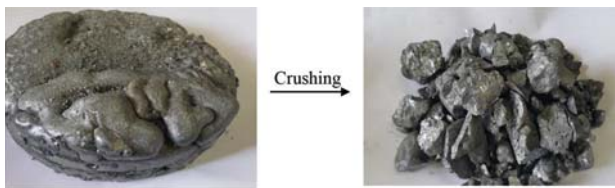


Figure 9—Photographs of MG-Si product

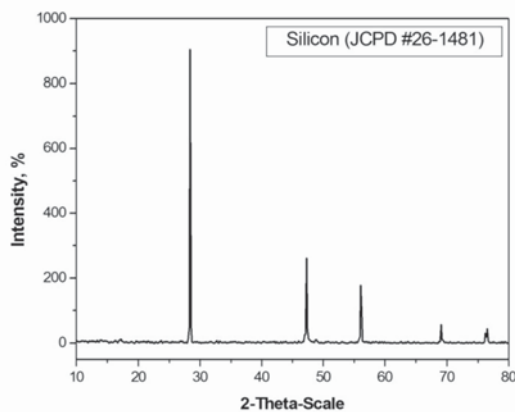


Figure 10—XRD spectrum of MG-silicon produced at optimum conditions

Morphology

Scanning electron microscopy (SEM) images of the MG-silicon product are shown in Figure 11. A general distribution of silicon metal grains with traces of iron at the grain boundaries is evident.

Conclusions

MG-Si was produced from Egyptian quartz using a locally made submerged arc furnace, with a recovery of about 75% and product purity of about 97% silicon.

The optimum conditions for production of MG-Si are summarized as follows:

- Carbon/silica weight ratio (C/SiO_2) 0.39
- Charge composition quartz 64.63 wt.%, coal 4.08 wt.%, charcoal 12.6 wt.%, petroleum coke 11.77 wt.%, and wood chips 6.92 wt.%
- Smelting time 80 minutes
- Power input 48 kWh
- Electrical energy consumption approx. 19 kWh/kg of silicon metal produced
- Electrode consumption 0.11 kg/kg of silicon metal produced
- Silicon metal purity about 97%.

References

AASLY, K. 2008. Properties and behavior of quartz for the silicon process PhD dissertation, Norwegian University of Science and Technology, Trondheim.

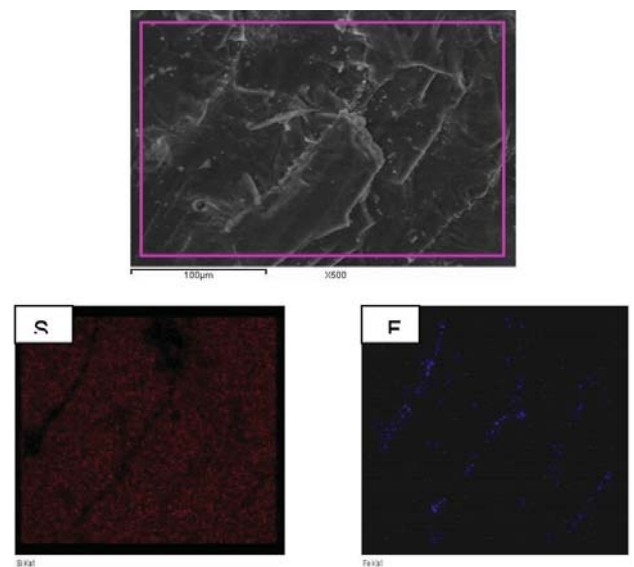


Figure 11—SEM micrographs of the MG-silicon product

Table II

XRF analysis of MG-Si product (wt.%)

Si	Al	Fe	Ca	Na	Ni	P	Mn	Cu	S	Ti
96.94	0.393	1.153	1.085	0.013	0.035	0.028	0.028	0.102	0.012	0.186

Production of metallurgical-grade silicon from Egyptian quartz

- ARVIDSON, A.N., DOSAJ, V.D., and MAY, J.B. 1991. Silicon smelting process in direct current furnace. US patent 5009703. Dow Corning Corporation.
- ASEN, J.V. 2012. Metal-producing mechanisms in the carbothermic silicon process. Master's thesis, NTNU, Norway.
- DOSAJ, V.D., HAINES, C.M., MAY, J.B., and OLESON, J.D. 1992. Control of carbon balance in a silicon smelting furnace. US patent 5174982. Dow Corning Corporation
- KUHLMANN, A.M. 1965. Silicon metal production. US patent 3215522. Union Carbide Corp.
- MITSUHIRO, T. and HIRASAWA, M. 2000. A two-stage reduction process for silicon production. *High Temperature Materials and Processes*, vol. 19. pp. 281-297.
- MYRHAUG, E.H. 2003. Non-fossil reduction materials in the silicon process – properties and behavior. PhD thesis, Norwegian University of Science and Technology, Trondheim.
- PV EDUCATION. 2013. Refining silicon. <http://pvcfrom.pveducation.org/ MANUFACT/REFINE.HTM>
- RINGDALEN, E. and TANGSTAD, M. 2012. Reaction mechanisms in carbothermic

- production of silicon, study of selected reactions. *Proceedings of the TMS International Smelting Technology Symposium: Incorporating the 6th Advances in Sulfide Smelting Symposium*. Downey, J.P., Battle, T.P., and White, J.F. (eds.). <http://onlinelibrary.wiley.com/doi/10.1002/9781118364765.ch24/pdf>
- Schei, A., Tuset, J.K., and Tvei, H. 1998. Production of high silicon alloys. Tapir Forlag, Trondheim, Norway.
- TANGSTAD, M., KSIAZEK, M., ANDERSEN, V., and RINGDALEN, E. 2010. Small scale laboratory experiments simulating an industrial silicon furnace. *Infacon 12. Proceedings of the Twelfth International Ferroalloys Congress: 'Sustainable Future'*, Helsinki, Finland, 6-9 June 2010. Vartiainen, A. (ed.). Outotec Oyj, Oslo. pp.661-669.
- TANGSTAD, M. 2012. Staged heat and mass balance of the Si process. Unpublished report, SINTEF, Trondheim, Norway.
- VAISH, A.K. 2012. Production of ferro-silicon and calcium silicon alloys. National Metallurgical Laboratory, Jamshedpur, India. <http://eprints.nmlindia.org/5785/1/6.01-6.17.PDF> ◆

SAIMM: Diamonds — Source to Use 2018 Conference *'Thriving in Changing Times'*

11 June 2018 — Workshop: SAMREC/SAMVAL Reporting – Diamond Projects
12–13 June 2018 — Conference • 14 June 2018 — Technical Visits

Birchwood Conference Centre (Jet Park, Johannesburg)

BACKGROUND

Being the seventh conference in the series, the *Diamonds – Source to Use* conferences target the full spectrum of the diamond pipeline from exploration through to sales and marketing. The last conference in this series (*Diamonds – Still Sparkling*) was held in Botswana in 2016 and it is now returning to Johannesburg, where it was last held in 2013

Keynote Speakers

The State of the Diamond Market

E. Blom, *Blom Diamonds (Pty) Ltd*

Financing Diamond Projects

J. Campbell, *Botswana Diamonds PLC*



For further information contact:

Camielah Jardine • Head of Conferencing - SAIMM
Tel: (011) 834-1273/7 • Fax: (011) 833-8156 or (011) 838-5923
E-mail: camielah@saimm.co.za • Website: <http://www.saimm.co.za>



Prevention of spontaneous combustion in coal drifts using a lining material: a case study of the Tuncbilek Omerler underground mine, Turkey

by M.V. Ozdogan, G. Turan, D. Karakus, A.H. Onur G. Konak, and E. Yalcin

Synopsis

The spontaneous combustion of coal in underground mines is a vital subject for miners. Every year, many coal fire incidents are caused by spontaneous combustion.

In this study, a lining material for coating the coal surface to prevent coal fires was designed in laboratory conditions. Three kinds of gypsum as well as plaster, satin plaster, moulding plaster, hydrated lime, cement, and fly ash were used to prepare different types of mixtures.

Sixteen different mixtures were prepared and tested. Only plaster plus water and cement plus fly ash plus water gave satisfactory results in the laboratory tests, and these mixtures were then applied on a small scale in an underground coal mine. Observations showed that plaster reacted with pyrite, increasing the porosity of the lining material upon exposure to water, which is ubiquitous in underground mines. However, a 7–8 mm thick application of the cement plus fly ash plus water mixture proved impermeable to air and maintained its structure in underground mine conditions. The cement and fly ash mixture was then applied to some hazardous areas on a larger scale. When the investigations were completed, the lining material was applied in new development drifts that had been driven into the coal at the Omerler underground mine.

Keywords

spontaneous combustion, coal fire, lining material, coating.

Introduction

Spontaneous combustion is an oxidation reaction that occurs without an external heat source (Philips, Uludağ, and Chabedi, 2011). All coals have the potential to combust spontaneously, thereby constituting a potential coal fire risk caused by the auto-oxidation of coal. Spontaneous combustion has been one of the major hazards in underground coal mines for very many years. It causes safety problems and economic losses as a result of inaccessible underground areas. Many methods exist for the detection, prevention, and management of spontaneous combustion in surface mining operations, but in underground mines most of the methods developed for detecting and preventing fires have been unsuccessful. Although the ignition of coal can be detected at the coal surface, the combustion of coal occurs quickly, and it may often be too late to take precautions before a fire begins. So, unexpected mine accidents may take place, and many miners may lose their lives.

Underground coal fires occur in many countries worldwide. One of the most recent

significant mine accidents caused by coal fire happened in the Soma underground coal mine in Turkey on 13 May 2014. Unfortunately, 301 miners died in that accident.

Coal fires require three basic elements: oxygen, heat, and fuel. If one of these elements is removed from the environment or contact between them is interrupted, the fire mechanism tends to be suppressed. In coal mines, coal is the main source of fuel, oxygen is needed for the workers, and heat is generated by the exothermic reaction of coal and oxygen, so none of these elements can be removed from the environment. However, the contact between coal and oxygen can be obstructed.

Several theoretical and experimental studies have been carried out on the theory, susceptibility, and detection of spontaneous coal combustion (Handa *et al.*, 1985; Sarac and Soyturk, 1992; Grever, 1994; Wang, Dlugogorski, and Kennedy, 1999; Kaymakçı and Didari, 2000; Guřanová, 2008; Zubíček, 2008; Zeng-hua *et al.*, 2009; Li, Beamish, and Jiang, 2009; Singh, 2013; Liang and Wang, 2017). However, fewer studies exist on preventing the spontaneous combustion of coal, and most of the prevention methods are based on chemical agents. Goodson & Associates Inc. has developed a new cellular (foam-containing) grout fire control technology called Thermocell. The basic grout is composed of sand, cement, and water and requires a high proportion of fly ash (a byproduct of coal combustion), to which a quantity of air-entraining foam is added (much like shaving cream) (Colaizzi, 2004). Tibbs *et al.* (2013) suggest a 'thin spray-on liner' for replacing steel mesh and they claim that this polymer-based coating material is an effective fire retardant.

* Department of Mining Engineering, Dokuz Eylul University, Izmir, Turkey.

© The Southern African Institute of Mining and Metallurgy, 2018. ISSN 2225-6253. Paper received Apr. 2017; revised paper received Oct. 2017.

Prevention of spontaneous combustion in coal drifts using a lining material



Figure 1—Location of Tuncbilek lignite district

Also, Li *et al.* (2016) reported the potential of a thin spray-on liner for controlling spontaneous combustion and various gas emissions. Wang *et al.* (2014) studied some chemical inhibitors to prevent the spontaneous combustion of coal due to its structure.

Many other commercial chemical agents have been used for coating the coal surface to prevent air contact, but their cost is quite high. Therefore, a coating application with chemical agents is generally used only for locations that have a high combustion risk. In this research, a cheap, airtight coating material was developed to prevent the contact between coal and oxygen.

Study area

The Tuncbilek lignite district is located in the north-east Aegean region of Turkey and is about 60 km away from Kutahya. The site location map is given in Figure 1. Turkish Coal Enterprise (TKI) is the owner of the lignite licences in the region and accounts for 7.5% of all Turkish lignite production in this licence area. According to statistics obtained from TKI for 2014, 80% of lignite production came from open pits, whereas the remaining 20% was mined from an underground mine in the Omerler district (<http://www.gli.gov.tr/faaliyet.html>).

The Omerler underground coal mine was faced with fire problems in the years between 2009 and 2011. The development galleries, which were driven into the coal seam, became inaccessible because of the frequent ignition of coal. This caused serious economic losses and threatened the lives of workers. Chemical agents had been used for coating the coal surface, but only some risky areas were coated due to the high cost of lining material. This restricted application was not successful in preventing fires in the mine.

The first serious coal fire occurred on 8 November 2009 in 185 m of the tailgate of panel B2. The concentration of CO was measured at 200 ppm in that part of the tailgate. The CO level reached 1000 ppm in a very short time, and smoke was

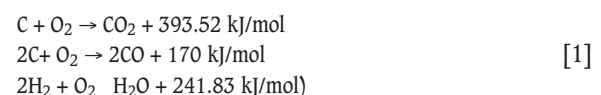
observed in the drift. Finally, open flame occurred in the tailgate, and the drift was closed with a fire dam. The second coal fire occurred on 30 May 2010 between 510 and 525 m of the bottom gate of panel B2. A CO concentration of 284 ppm was detected initially and reached 400 ppm within one hour. It then increased to 1000 ppm in a short period of time, and smoke was observed. After open flame was seen at the bottom gate, the drift was also closed with a fire dam. The third coal fire occurred on 22 December in haulage road K2, and the haulage way was also closed with a fire dam. The locations of the fires and panels are provided in Figure 2.

In this study, some types of materials with the potential to be used as economical linings for coal surfaces were tested for their ability to prevent spontaneous combustion in the Omerler underground coal mine. First, laboratory studies were carried out to determine the proper mixture. Then, an *in-situ* study and an industrial-scale application were carried out at the Omerler mine

Mechanism of spontaneous combustion

The complete oxidation of carbon to carbon dioxide is an exothermic reaction that emits between 21 and 42 kJ per gram of coal, taking into account that coal is not composed of pure carbon (Grewer, 1994).

The chemical and heat balances involved in the low-temperature oxidation of coal, spontaneous combustion, and final combustion are illustrated by a few fundamental process equations, demonstrating the exothermic nature of the reaction (Grewer, 1994):



Because of its structure, as the coal comes into contact with oxygen, it adsorbs the oxygen. At temperatures above 40°C, the adsorption leads to an exothermic reaction and causes the ambient temperature to increase (Sarac and

Prevention of spontaneous combustion in coal drifts using a lining material

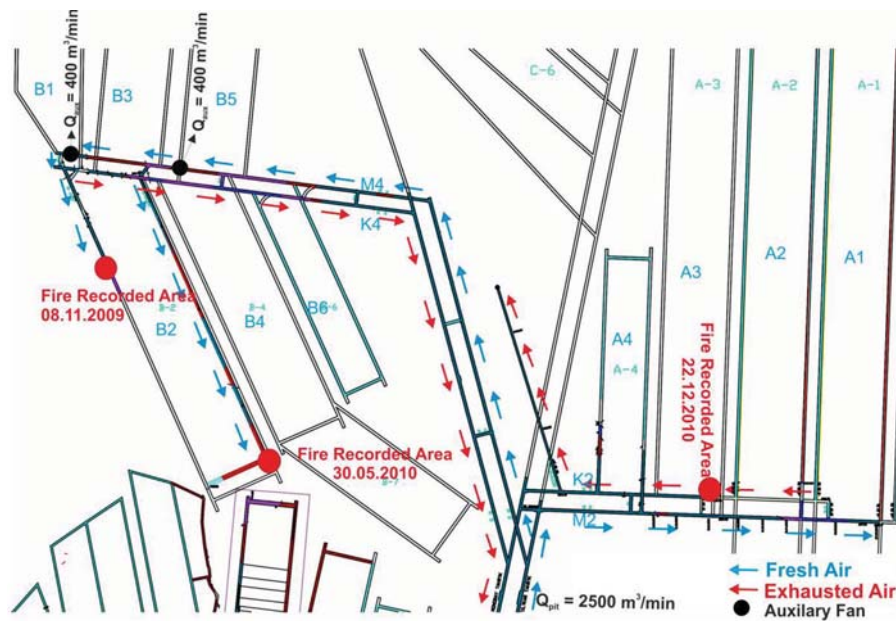


Figure 2—Location of fires in Omerler underground coal mine

Seam factors	Mining factors	Geological factors
Rank	Mining methods	Seam thickness
Petrographic composition	Rate of advance	Seam gradient
Temperature	Pillar conditions	Caving characteristics
Available air	Roof condition	Faults/dykes
Particle size	Crushing	Coal outbursts
Moisture	Packing	Friability
Sulphur	Effect of timber	Depth of cover
Effect of previous oxidation	Leakage	
Physical properties	Multi-seam working	
Heating due to earth movement	Coal losses	
Bacteria	Main roads	
Other minerals	Worked-out areas	
	Stowing	
	Ventilating pressure	
	Humidity	

Soyturk, 1992). If this heat cannot be removed from the environment, the CO and CO₂ concentrations increase at temperatures above 70°C, and water vapour is given off at 125°C. As the increasing temperature of the medium reaches the ignition temperature of coal, underground fires start (Sarac and Soyturk, 1992; Kural, 1998; Jones and Townend, 1949).

Factors affecting spontaneous combustion

A number of factors are significant when determining the risk of spontaneous combustion in coal. One of the earliest classifications of these factors was revealed by Davis and Reynolds (1928) (Philips, Uludağ, and Chabedi, 2011). The factors are grouped by chemical and physical properties. In order of importance, the chemical factors to be considered are the rank of the coal and the presence of pyrite, weathering, moisture, organic sulphur, chemical retardants (calcium chloride and sodium bicarbonate), ozone, and bacteria. The

physical factors are particle size, moisture, oxygen supply, temperature, 'occluded' gases, and ventilation (Davis and Reynolds, 1928). Later, the Davis and Reynolds classification of factors was extended by various researchers. One of the latest classifications was mooted by Singh (2013), as shown in Table 1.

The susceptibility of lignites in the Kutahya region to spontaneous combustion was examined by Oren and Sensogut (2010). The ignition temperatures, average heating rates, and liability indices of Kutahya region lignites vary in the ranges 141–188°C, 0.894–2.619°C/min, and 5.78–17.34 min⁻¹, respectively. Therefore, the lignites from the Kutahya region are in the 'medium-high' risk group (Oren and Sensogut, 2010) based on the classification developed by Feng (1973) and assuming an average heating rate between 110 and 220°C. The proximate analysis and liability classification (Yildirim *et al.*, 2006) for the study area are given in Table II.

Prevention of spontaneous combustion in coal drifts using a lining material

Table II
Proximate analysis and liability classification for Omerler coal seam (Yildirim, Sensogut, and Gokay, 2006)

Coal seam	Moisture (%)	Ash (wt%)	Volatile matter (wt%)	Fixed carbon (wt%)	Total sulphur (wt%)	Liability index (m ⁻¹)	Risk group 0–5 Low 5–10 Medium >10 High
Omerler A	14.80	18.01	35.74	31.40	1.22	15.20	High
Omerler B	16.20	16.76	28.36	38.68	4.27	8.50	Medium
Omerler C	12.10	32.35	27.77	27.79	1.65	9.60	Medium–high

Experimental investigations

The lining material to be applied to prevent coal fires must be impermeable to air, inexpensive, resistant to water and heat, easy to obtain and apply, and have sufficient strength and a low rebound ratio during application. Also, it should not be harmful to human health and must be resistant to environmental effects. Although the main function of the lining material is not to support the roof load, it must be solid enough to form one unified piece across the applied surface. Otherwise, the lining may break or fall down and allow the reaction between coal and oxygen to proceed, resulting in the ignition of coal. For this purpose, three kinds of gypsum (plaster, satin plaster, and moulding plaster) as well as lime, cement, and fly ash were considered. Different mixtures of these materials were tested as a lining material in laboratory conditions. Then, the mixtures were subjected to laboratory tests to determine if they could meet the above-listed specifications. Subsequently, the mixtures were applied on a testing wall by means of a Mono pump to determine the applicability and rebound ratios of the mixtures. After all of tests were completed, the lining materials were applied at the Omerler underground coal mine on an industrial scale.

Laboratory studies

Sixteen mixtures were prepared in laboratory conditions. The contents and proportions of materials in the mixtures are shown in Table III.

The mixtures were prepared in cylindrical moulds to facilitate testing of their uniaxial compressive strength (UCS). They were cured under atmospheric conditions for 14 days, and the cured samples were tested in a compression machine to determine their UCS. The setting times of the mixtures were also determined. A short setting time would block the pump, whereas a long setting time would increase the rebound ratio of the mixture. The setting times of the mixtures were tested using a pin penetrating method: a pin was used to puncture samples repeatedly until it could not penetrate, and the corresponding time was recorded as the setting time for each mixture. A setting time of 15 minutes and less is considered to be risky.

One of the most important constraints for a lining material is air permeability. Only the samples that passed all of the other tests were subjected to the air permeability test. The samples were placed in a tube, which was then placed in a burette filled with water to an exact level (Figure 3).

The thickness 't' that completely blocked air flow under certain air pressures was tested in the permeability test. Air pressure in the test device was obtained using a water column with a height of 10 cm, which gave 100 kg/m² of air pressure (980 Pa). Specimens of different thicknesses were tested and those that did not cause any change in water level were accepted as airproof.

Table III
Proportions of materials in mixtures (wt%)

Mixture	Plaster	Satin plaster	Moulding plaster	Hydrated lime	Cement	Fly ash	Water
1		55		4.5	4.5		36
2		65					35
3		31.5	31.5				37
4		12.8	51.2				36
5	64						36
6		36	36				28
7	29.5	29.5			5		36
8	32		32				36
9		62			3		35
10*	30.75	30.75					37.5
11	23.5	23.5					33
12					20	20	26
13	35					35	30
14	20			10		40	30
15				10	20	40	30
16	50			12.5			37.5

* Plus 1% wood binder

Prevention of spontaneous combustion in coal drifts using a lining material

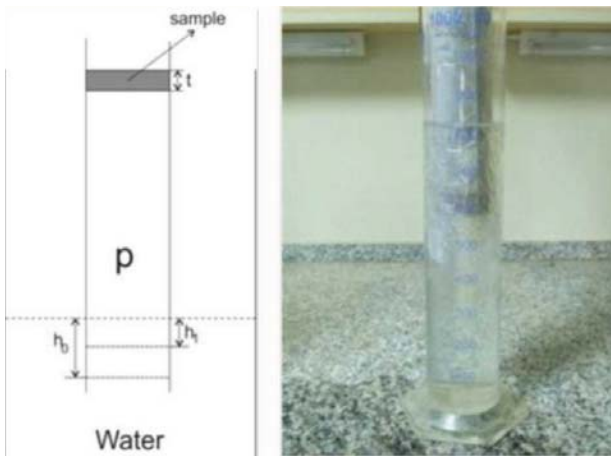


Figure 3—Test device for determining air permeability

Studies on test wall

After the laboratory tests, the mixtures were sprayed on a relatively large-scale, rough retaining wall using a Mono pump (2.5 kW, 380 V) and compressor at 5 bar to conduct some observational tests (Figure 4).

The pumpability and rebound of the mixtures were evaluated by observation during the application studies on the test wall. These studies yielded a methodology for finding the best applicable thicknesses for the mixtures. After the spraying process, the coatings on the wall were watered every day to determine their water resistance.

Results of experimental investigations

The UCS, setting time, pumpability, rebound ratio, air permeability, and water resistance of the mixtures are given in Table IV.



Figure 4—Mixtures sprayed on wall

Table IV

Results of experimental investigations

Mixture no.	Unit weight (kN/m ³)	UCS* (14 days) (MPa)	Setting time (min)	Resistance to water (Empirical)	Rebound (Empirical)	Comment
1	10.10	2.95	>60	Washed	High	Low water resistance (failed)
2	11.18	3.76	>180	Unwashed	Low	Long setting time (failed)
3	11.18	3.61	>60	Unwashed	Low	Acceptable
4	11.67	8.52	80	Washed	Low	Low water resistance (failed)
5	11.77	14.05	26	Unwashed	Low	Acceptable
6	14.13	9.84	90	Washed	Low	Low water resistance (failed)
7	11.48	8.95	75	Washed	High	High rebound and low water resistance (failed)
8	11.87	11.71	20	Unwashed	High	Acceptable
9	11.48	5.11	>60	Washed	High	Low water resistance (failed)
10	10.89	5.84	>60	Unwashed	Low	Highly fractured (failed)
11	11.77	9.07	>60	Washed	Low	Low water resistance (failed)
12	13.44	7.78	>60	Unwashed	Low	Acceptable
13	12.26	12.45	10	Unwashed	Low	Short setting time (failed)
14	10.69	4.91	15	Unwashed	Low	Acceptable
15	11.58	3.91	40	Unwashed	High	High rebound (failed)
16	9.91	9.02	20	Unwashed	High	High rebound (failed)

* UCS: Uniaxial compression strength over 14 days

Prevention of spontaneous combustion in coal drifts using a lining material

The mixtures that passed all of the tests (mixtures 3, 5, 8, 12, and 14) were subjected to the air permeability test. Only mixtures 5 and 12 tested as impermeable at a 5 mm thickness and were accepted as airtight.

Site application

After all of the laboratory tests and observations were completed, mixtures 5 and 12 were considered as suitable mixtures. The first small-scale test applications of mixture 5 (plaster plus water) and mixture 12 (cement plus fly ash plus water) were carried out at the Omerler underground coal mine in a small part of a drift that was opened in the coal (Figures 5a and 5b).

Both mixtures were applied successfully and both demonstrated strong adhesion to coal. After 10 days of observation, cracks and splitting were apparent in mixture 5. The plaster (CaSO_4 plus $0.5 \text{ H}_2\text{O}$) also interacted with pyrite

in the coal to form FeSO_4 . This reaction occurred rapidly, and the FeSO_4 was visible on the lining material as a yellow colour (Figure 6).

One piece of the lining material containing FeSO_4 was taken from the test area and exposed to water. This lining material dissolved in water and became porous, which showed that the plaster and water mixture could not provide air tightness. So mixture 5 failed in underground conditions.

Mixture 12 was undisturbed and kept its original shape. During the two-month observation period, the cement plus fly ash and water mixture did not undergo any reaction. Subsequently, a second application was tested in the coal drift. The wedges between two supports were removed, mixture 12 was applied between the two support elements, and the wedges were replaced (Figure 7). Three coatings of the mixture were applied to increase the lining thickness to 7–8 mm.



Figure 5—(a) Application of mixture 12; (b) application of mixture 5



Figure 6—Effect of pyrite on plaster



Figure 7—Application of cement, fly ash, and water mixture between two supports

Prevention of spontaneous combustion in coal drifts using a lining material

Table V

Composition of lining material (mixture 12)

Material	Vol. %
Fly ash	75
Portland cement	25
Water/cement	2

Table VI

Chemical composition of Tuncbilek fly ash (%)

SiO ₂	58.25	K ₂ O	1.37
Al ₂ O ₃	16.66	Na ₂ O	0.33
Fe ₂ O ₃	12.91	Ignition loss	2.09
S+A+F	87.82	Cl ⁻	0.002
CaO	1.95	Free CaO	0.16
MgO	5.08	Reactive SiO ₂	40.05
SO ₃	0.76	Reactive Cao	1.03

After the laboratory and *in-situ* studies, the drifts which had a high combustion risk were coated with mixture 12. The proportions of the mixture used in the pilot studies are given in Table V. An accelerating admixture was added to the mixture at the spray nozzle to lower its rebound. The ratio of accelerating admixture to cement was 0.01.

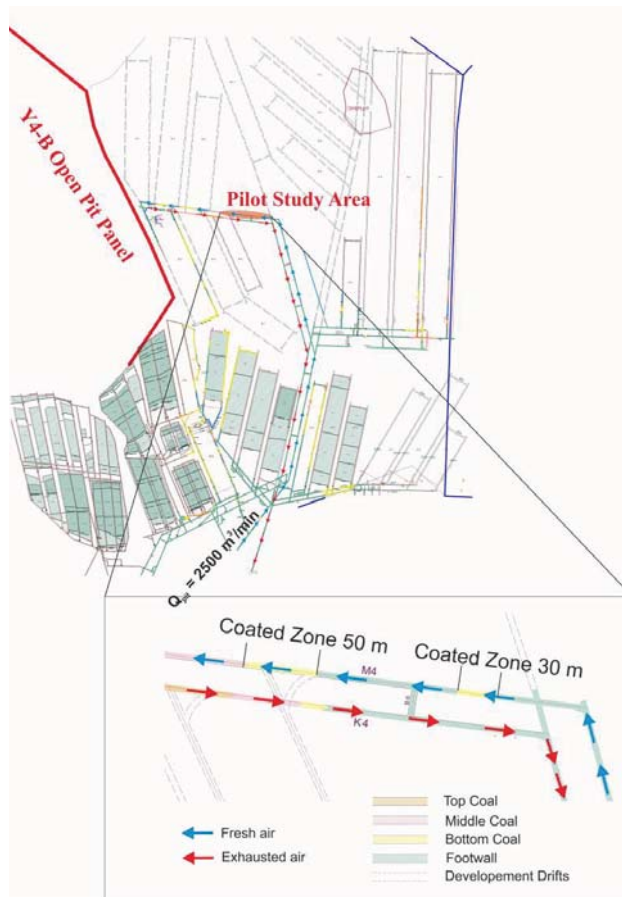


Figure 8—Location of the pilot study

Table VII

Technical specifications of spraying machine

Specifications	
Power	AC 380 / 1000 V / 50 Hz
Pump motor	7.5 kW
Mixer motor	3 kW
Flow rate	0–120 l/min
Pumping distance (horizontal)	1000 m
Pumping distance (vertical)	100 m
Maximum pressure	40 bar
Maximum particle size	10 mm
Volume of mixer tank	150 l

The fly ash used in this study was supplied from the Tuncbilek power plant. The chemical composition of the fly ash is given in Table VI. Ordinary Portland cement was also used in the mixtures.

A fly-ash silo was established outside the main access to the mine, and a special spray machine was purchased for the pilot study. The spray machine had two tanks: the upper tank was used for mixing dry cement and fly ash, and the lower tank for mixing the blend with water and then pumping it. The technical specifications of the spray machine used in the pilot study are given in Table VII.

The first pilot study was carried out in March 2011. The lining material was applied on the haulage way of panel B, which partly intersected the coal seam (Figure 8). This haulage way was too close to the open pit panels, so the coal around it had a high ignition potential due to air leakage from the cracks connected to the open pit benches. Also, the haulage way was cut by a fault and this increased the ignition potential. The first and second application areas were about 50 and 30 m in length, respectively.

The wire mesh between the Toussaint-Heintzmann (TH) type supports was ripped out before the spraying process. An 80 m length of the haulage way of panel B was successfully coated in one shift, and the mesh was replaced after spraying (Figure 9). The behaviour and performance of the lining material was then inspected each month, and no ignition was recorded. After the successful coating application, all new development drifts that were driven into the coal were coated with the cement and fly ash blend immediately after supporting the galleries with TH supports. Since the coating application, no coal fires have been recorded in the Omerler underground coal mine.

The unit cost of the lining material was calculated from the application of the coating between two supports as \$0.42 per m² for a 1 cm thickness, excluding labour. The fire retardant chemical previously used by the mine authorities cost about \$70 per m² for a 1 cm thickness.

Conclusion

The spontaneous combustion of coal is a serious hazard in underground coal mines. Every year, many underground mineworkers are injured or killed by this kind of disaster, which also causes economic losses for the companies involved.

The easiest way to prevent coal fires is to avoid contact between the coal and air, and an airproof lining material is

Prevention of spontaneous combustion in coal drifts using a lining material



Figure 9—Coated drifts in Omerler underground coal mine

suitable for this purpose. In this study, various airproof lining materials were designed and tested. Given that the first constraint for materials in mixtures is to provide an impermeable barrier to air, the laboratory studies and *in-situ* applications showed that coating the drifts driven into the coal with a cement plus fly ash and water mixture could prevent coal fires. Furthermore, the cost of materials was shown to be acceptable, as the cement proportion in the mixture was low and the cost of fly ash was almost negligible. However, some procedures have to be considered before and after spraying application.

- The spraying process has to be done before ignition starts
- Large gaps in a drift section have to be filled before the spraying application
- The coating has to be applied between the main supports, just after the main support elements are set up. Then other support elements like wire mesh, wedges, or canopy can be placed between the supports
- The thickness of cement plus fly ash blend has to be a minimum 7–8 mm to provide air impermeability
- To prevent breakage of the lining material, high deformation rates caused by the roof load cannot be tolerated in the drift section
- The coated surfaces must be checked regularly, and failed surfaces must be repaired immediately.

Using this method, coal fires can be prevented effectively and economically.

Acknowledgements

The authors would like to thank the technical staff of GLI of Turkish Coal Enterprises for their motivation and help in the application of tested materials on drift surfaces. The laboratory studies for this investigation were presented at the 23rd World Mining Congress 2013, Canada (Onur *et al.*, 2013).

References

- COLAIZZI, G.J. 2004. Prevention, control and/or extinguishment of coal seam fires using cellular grout. *International Journal of Coal Geology*, vol. 59. pp. 75–81.
- DAVIS, J.D. and REYNOLDS, D.A. 1928. Spontaneous heating of coal. TP 409. US Bureau of Mines. pp. 74.
- GU ANOVÁ, P. 2008. Spontaneous combustion of coal and its early detection in Okr mines. *GeoScience Engineering*, vol. 4. pp. 23–28.
- GARP LIGNITE. 2017. <http://www.gli.gov.tr/faaliyet.html> [accessed 22 November 2016].
- GREWER, T. 1994. *Thermal Hazards of Chemical Reactions*. Elsevier, Amsterdam.
- HANDA, T., NISHIMOTO, T., MORITA, M., and KOMADA, J. 1985. Spontaneous combustion of coal. *Fire Science and Technology*, vol. 5. pp. 21–30.
- JONES, R.E. and TOWNEND, D.T.A. 1949. Oxidation of coal. *Journal of the Society of Chemical Industry*, vol. 68. pp. 197.
- KAYMAKÇI, E. and DIDARI, V. 2000. Relations between coal properties and spontaneous combustion parameters. *Turkish Journal of Engineering and Environmental Sciences*, vol. 26. pp. 59–64.
- KURAL, O. 1998. *Coal Specifications, Technology and Environmental Correlations*. Ozgun Printing House, Istanbul.
- LI, L., BEAMISH, B.B., and JIANG D.Y. 2009. Self-activation theory of spontaneous combustion of coal. *Journal of China Coal Society*, vol. 34, no. 4. pp. 505–508.
- LI, Z., SAYDAM, S., MITRA, R., and CHALMERS, D. 2016. Potential use of thin spray-on liners for gas management in underground coal mines. *Journal of the Southern African Institute of Mining and Metallurgy*, vol. 116. pp. 1091–1100. <http://dx.doi.org/10.17159/2411-9717/2016/v116n12a1>
- LIANG, Y. and WANG, S. 2017. Prediction of coal mine goaf self-heating with fluid dynamics in porous media. *Fire Safety Journal*, vol. 87. pp. 49–56.
- ONUR, A.H., KARAKUS, D., OZDOGAN, M.V., KONAK, G., and YALCIN, E. 2013. Design of an optimal lining material to prevent coal fires at underground coal mines. *Proceedings of the 23rd World Mining Congress*, Montreal, Canada, 11–15 August. CIM, Montreal.
- OREN, O. and SENSOGUT, C. 2010. Spontaneous combustion liability of Kutahya (Turkey) region lignites. *Energy Sources, Part A*, vol. 32. pp. 877–885.
- PHILIPS, H., ULUDAĞ, S., and CHABEDI, K. 2011. Prevention and control of spontaneous combustion. Coaltech Research Association, Johannesburg, South Africa.
- SARAÇ, S. and SOYTURK, T. 1992. An investigation on the liability of Tuncbilek lignites to spontaneous combustion. *Proceedings of the 8th Coal Congress of Turkey*, Zonguldak, 6–8 June 2012. pp. 141–152. <https://doi.org/10.1080/15567031003587605>
- SINGH, R.V.K. 2013. Spontaneous heating and fire in coal mine. *Procedia Engineering*, vol. 62. pp. 78–90.
- TIBBS, M.P., TYLER, O.K., DUIN, S.V., and BAAFI, E. 2013. Autonomous thin spray-on liner application in irregular tunnel and mine roadway surfaces. *Proceedings of the 30th International Symposium on Automation and Robotics in Construction, Mining & Petroleum Industries*. CIM, Montreal. pp. 1456–1463.
- WANG, H., DLUGOGORSKI, B.Z., and KENNEDY, E.M. 1999. Theoretical analysis of reaction regimes in low-temperature oxidation of coal. *Fuel*, vol. 78. pp. 1073–1081.
- WANG, D., DOU, G., ZHONG, X., XIN, H., and QIN, B. 2014. An experimental approach to selecting chemical inhibitors to retard the spontaneous combustion of coal. *Fuel*, vol. 117. pp. 218–223.
- YILDIRIM, O.S., SENSOGUT, C., and GOKAY, M.K. 2006. Effects of electrical resistance on spontaneous combustion tendency of coal and interaction matrix concept. *Journal of University of Science and Technology Beijing*, vol. 13. pp. 1–7.
- ZENG-HUA, L., YA-LI, W., NA, S., YONG-LIANG, Y., and YU-JING, Y. 2009. Experiment study of model compound oxidation on spontaneous combustion of coal. *Procedia Earth and Planetary Science*. pp. 123–129.
- ZUBIČEK, V. 2008. Assessment of susceptibility of coal to spontaneous combustion in Okr. *GeoScience Engineering*, vol. 4. pp. 1–9. ◆



Modelling coal pillar stability from mine survey plans in a geographic information system

by M. Mathey

Synopsis

A practical method for analysing the individual stability of large numbers of pillars in bord-and-pillar workings based on mine survey plans is outlined. The procedure aims at modelling pillar safety factors and failure probabilities under tributary area loading assumption in a geographic information system.

The mining dimensions and geometries, as available from mine survey plans, are processed in a quasi-3D mine model. Analytical solutions are implemented in the model so as to predict the stability of each individual pillar and its time-dependent deterioration due to scaling. Thus a dynamic analysis is achieved, which gives a good estimate of the risk associated with abandoned mine sites over time. The results can be projected back onto mine survey plans in order to provide an overview of the areal distribution of stability and instability in the underground panels. The limitations and accuracy of the model are discussed.

The proposed pillar stability model is applied to real mining situations, including a case of pillar collapse, so as to verify the validity of the technique.

Keywords

pillar stability, safety factor, GIS, modelling.

Introduction

An underground bord-and-pillar coal mine can, over a lifetime of a few decades, result in several tens of thousands of pillars being left behind in its abandoned workings. For South Africa, the total number of coal pillars in abandoned workings is estimated to be in the region of 6 million (van der Merwe and Mathey, 2013a).

Currently, there are 98 cases known in which isolated but large groups of pillars have collapsed (van der Merwe and Mathey, 2013b). Consequently, large subsidence troughs occur on surface, potentially endangering infrastructure, housing, and ultimately lives. The prediction of long-term instabilities in underground workings therefore becomes imperative for regional development planning, and is also compulsory for mining companies in order to obtain mine closure certificates.

The challenge in assessing pillar stability-related risk is to take into account the great number of pillars, their individual dimensions, geometries, and deterioration over time. One can imagine that an unfavourable combination of these factors may cause localized areas of

weakness in the underground panels. Those areas can eventually trigger a collapse, which subsequently may spread towards stronger regions within the same panel. Such examples have been discussed in the literature (Mathey, 2010, 2013; Mathey and Schulte, 2011).

It is apparent that an extensive risk assessment for abandoned mine sites is required that allows fast and detailed access to spatial information. Furthermore, the long-term stability of underground panels needs to be analysed in high resolution, *i.e.* on an individual pillar-by-pillar basis. In this paper the use of a geographic information system to address issue is proposed.

Methodology

The principal methodology underlying the pillar stability analysis is to pick up mining dimensions, geometries, and dates from the original survey plans and process the data in a quasi-3D digital mine model, making use of a geographic information system (GIS). Within this model, individual safety factors are determined for each pillar in the underground workings.

Empirical equations are implemented to predict pillar scaling, giving the expected deterioration of pillar size over time. Thus a dynamic risk assessment for pillar-related stability problems is obtained. All static and dynamic, measured and inferred information related to a pillar is stored in a relational database.

Finally, the analytical results are projected back onto maps in order to facilitate the use of stability-related information by mine personnel. Surface structures can be included on these maps, so as to provide a comprehensive and detailed basis for assessing the risk involved with abandoned

* Associate to the Wits Mining Institute, University of the Witwatersrand, South Africa.

© The Southern African Institute of Mining and Metallurgy, 2018. ISSN 2225-6253. Paper received Nov. 2015; revised paper received Apr. 2016.

Modelling coal pillar stability from mine survey plans in a geographic information system

mine sites over time. The modelling methodology is schematically shown in Figure 1.

Pillar stability modelling

The GIS pillar stability model

The analytical procedure aims at modelling pillar safety factors under tributary area loading conditions. All relevant geometrical and time-related mining information is derived from the original underground survey plans. The work flow and data types used in the modelling exercise are diagrammatically shown in Figure 2.

A prerequisite for the modelling exercise is therefore that the relevant information is available in digital format, *i.e.* that elevation contours of the land surface, the outline of coal pillars, panel boundaries, survey points, and quarterly boundaries of the mining advance are digitized precisely in the GIS. Furthermore, any digitized feature needs to be attributed with relevant information (*e.g.* surface contour lines with elevation values, survey points with mining height and roof elevation values, *etc.*).

Once all data is available in digital format, a quasi-3D model of the underground workings can be created in the GIS. Geostatistical modelling techniques are adopted in order to create digital elevation models for the land surface and the coal seams. They are also used to interpolate a model for the mined height in the underground workings from available survey points.

The GIS software is then programmed to assign the essential pillar design parameters, *i.e.* the individual mining depth below surface H , the pillar height h , and effective square width w_e , to each individual pillar in the database. The latter parameter may be calculated from the pillar base area A_p and circumference C according to the equation provided by Wagner (1980):

$$w_e = \frac{4A_p}{C} \quad [1]$$

At this stage, the database only suffices for modelling the individual pillar strength from the pillar's effective square width and height and the assumption of an empirical pillar

strength equation. Pillar stability, however, is commonly judged based on the concept of a safety factor, the ratio of strength *versus* load.

Pillar loading

It is good engineering practice to estimate the load on pillars in a bord-and-pillar coal mining based on the so-called tributary area theory (TAT). Here, each individual pillar in a panel is assumed to support the full overburden weight immediately above it, plus a share of the rock mass above its unsupported surrounding roadways. It should be noted that this loading assumption is a worst-case scenario, which makes it safe to use in risk assessment, even though it may overestimate actual pillar loads to some extent.

Nevertheless the validity of the TAT is generally accepted for mining layouts in horizontal or near-horizontal seams with a regular pattern of fairly square pillars, and where the panel span is greater than the depth of mining (Salamon and Oravecz, 1973; Abel, 1988). These conditions are usually fulfilled in South African coal mining.

Roberts *et al.* (2002) investigated loading conditions in bord-and-pillar coal mines by means of parametric numerical modelling. They concluded that the loading of pillars is relatively insensitive to the overburden stiffness (in ranges of 1.5–15 GPa), but that the TAT becomes increasingly

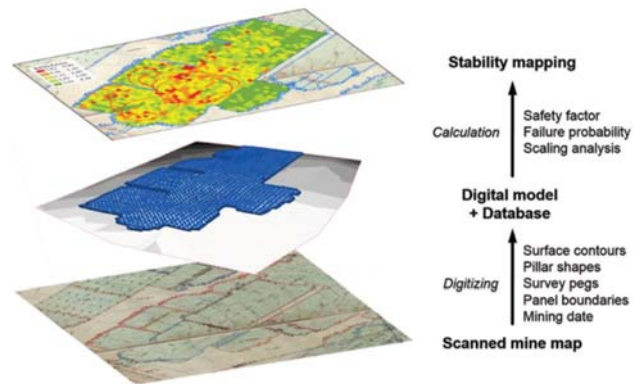


Figure 1—Pillar stability modelling process in the GIS

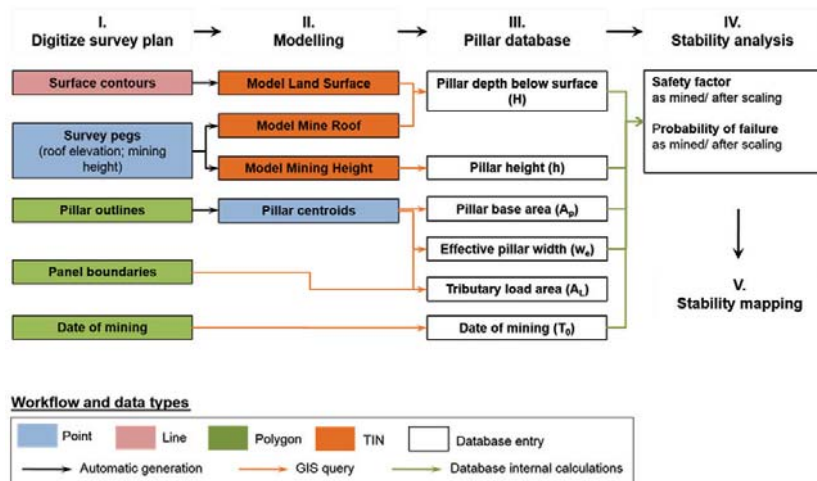


Figure 2—Work flow and data types used in the GIS

Modelling coal pillar stability from mine survey plans in a geographic information system

inaccurate as the span-to-depth ratio drops below 1.25 and the panel extraction rate exceeds 65%. Beyond those limits, the error in pillar load estimation becomes greater than 5%. At extraction ratios exceeding 75%, the error is greater than 10% and increases rapidly (Roberts *et al.*, 2002).

Based on the database for South African coal mining (van der Merwe and Mathey, 2013b), it is estimated that about 85% of all panels ever mined in the country fall into a range of less than 75% extraction, and therefore it can be expected that using the TAT for pillar load estimation is reasonably accurate in most cases. In cases of higher extraction, it will err on the safe side.

The tributary pillar loading can be modelled in GIS as follows. First, the pillar centre points are computed for each individual pillar shape. Then a centroidal Voronoi tessellation based on the distribution of all pillar centre points in a mining panel determines the individual tributary pillar loading areas A_L . A graphic of the result of this procedure is shown in Figure 3.

It should be noted that the TAT and the determined Voronoi polygons give the correct estimate of the tributary loading areas only when the arrays of pillars in a panel are set out in a regular, checkerboard-type pattern and the pillars are of more or less uniform size, as seen in Figure 3.

The TAT is therefore likely to be inaccurate in panels where geological weaknesses in the coal or the overburden were approached during the mining activities and the panel layout became irregular. For such situations it can also be anticipated that not only the loading, but also the strength conditions of the pillars, is disturbed and cannot be taken into appropriate consideration by the simple means employed in this analysis; or, in fact, by commonly used methods in the mining industry.

In situations where pillars are located adjacent to the abutment or large boundary pillars, the TAT is again not applicable. This is due to the circumstance that a great portion of the load is transferred away from these relatively small pillars to the overall larger abutment or boundary pillars nearby. Consequently, the TAT overestimates the load on those pillars. A more probable loading condition can be estimated only by a numerical analysis of the situation, where the relative pillar dimensions and distances, the thickness of the overburden strata, and the stiffness of the overburden and pillars are taken into account. In the GIS model, it might be justified to omit all pillars that are immediately adjacent to boundaries from the calculation to avoid a misinterpretation of the results (Figure 4).

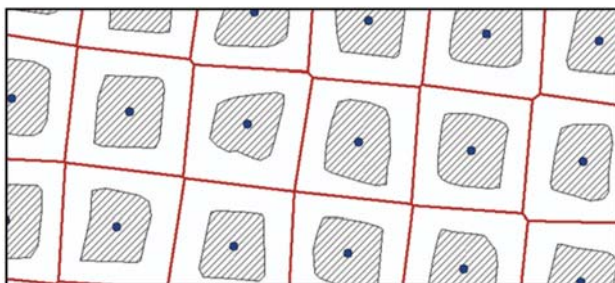


Figure 3—Coal pillars (shaded) with individual centre-points and the tributary pillar loading areas (red polygons) as modelled by Voronoi tessellation for a regular system of pillars

However, other minor irregularities such as small offsets between rows of pillars, which cause a localized disturbance in the regularity of pillar arrays, can be taken into account in the loading prediction made in the GIS model. The loading conditions modelled in GIS may agree with the real loading conditions satisfactorily, as shown in Figure 5.

Pillar scaling analysis

The strength of coal pillars deteriorates over time, owing mainly to scaling on the pillar sidewalls. This phenomenon is due to the formation of fractures in the pillar 'skin' that migrate progressively inwards as soon as the fractured coal fragments detach from the sidewalls. Consequently, pillars decrease in width and may fail after some time at a smaller safety factor than the original 'as-built' safety factor. For a dynamic risk assessment, it is imperative to implement different pillar scaling scenarios in the GIS model.

A method to predict the amount of scaling and the related weakening of pillars in South African coal mines was proposed by van der Merwe (2003, 2004). He derived scaling prediction formulae for different South African coalfields based on observations on the age and initial dimensions of failed pillars, and verified the formulae by on-site measurements of scaling pillars.

It is important to note from van der Merwe's (2004) work that measurements of scaling pillars did not show any preferential direction for scaling. Neither have pillar corners been observed to spall significantly more than pillar mid-areas.

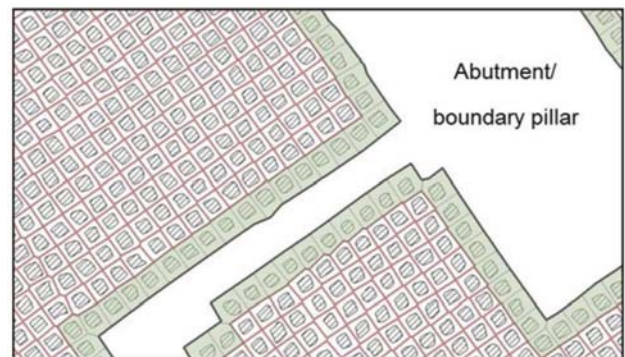


Figure 4—Pillars adjacent to boundaries are taken out of the calculation (shaded in grey colour)

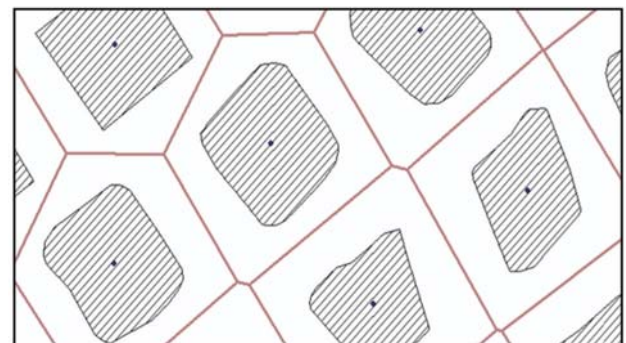


Figure 5—Tributary area loading for adjacent rows of pillars with offset in the pillar centre distance

Modelling coal pillar stability from mine survey plans in a geographic information system

Van der Merwe's scaling equations are implemented into the GIS model to predict the individual amount of pillar scaling for a number of desired time stages after mining. The original 'as-built' pillar shape is then buffered by the calculated amount of scaling in order to reduce the pillar in size, as it is demonstrated in Figure 6. For each scaling step, a new effective pillar square width and safety factor is calculated.

Pillar strength and stability analysis

The safety factor calculation follows the conventional concept of strength-to-load ratio, $SF = \sigma_s / \sigma_L$. For the calculation of the individual pillar strength an appropriate equation must be chosen, e.g. the formula from Salamon and Munro (1967):

$$\sigma_s = 7.2 w^{0.46} / h^{0.66} [\text{MPa}] \quad [2]$$

or, for improved accuracy, the recently updated version by van der Merwe and Mathey (2013c):

$$\sigma_s = 6.6 w^{0.50} / h^{0.70} [\text{MPa}] \quad [3]$$

When using any of the empirical formulae, one should remember that a correction applies for pillars that have been mined with continuous miners instead of drilling and blasting (van der Merwe and Madden, 2010).

The pillar's tributary area load σ_L is given by Equation [4]:

$$\sigma_L = 0.025 H A_L / A_p [\text{MPa}] \quad [4]$$

where the coefficient 0.025 is the unit weight of sedimentary strata in MN/m³.

For South African collieries, a link between the pillar safety factor and the probability of failure in practice was established (van der Merwe and Mathey, 2013). If pillar safety factors are calculated with the updated maximum likelihood strength formula as shown in Equation [3], the link with the failure probability PoF [%] is as follows:

$$PoF_{ML} = 100 \text{Exp} [-2.7 SF_{ML}^{1.9}] \quad [5]$$

The implementation of a failure probability model in GIS assists in quantifying the likelihood of a pillar collapse and improves the risk assessment exercise. Therefore, it should be incorporated in the GIS pillar model as well.

GIS pillar database

All information related to the stability of the underground pillars is stored in a relational database in the GIS. The database is structured in six blocks as follows (Figure 7).

- *Pillar identification*—Each pillar in the database is identified through its centre-point coordinates and a uniquely assigned pillar ID.
- *Mining dimensions*—The essential geometrical features of pillars, i.e. the base area, circumference, effective square width, and height are stored in the database. Linked to this information is the predicted individual tributary loading area. The pillars depth below surface is the distance between the surface and mine roof elevation at the position of the pillar. The age of the

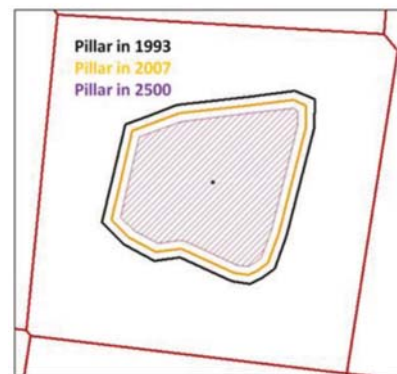


Figure 6—Pillar scaling scenarios in the GIS model

Identification			Initial dimensions & time of mining from model								
Pill ID	Coord_X	Coord_Y	P_AREA	P_CIRCU	P_WIDTH	P_TA	M_SURF	M_ROOF	M_HEIGHT	M_YEAR	M_MONTH
594422498	22	-29	55.951	28.791	7.702	101.378	1562.32	1534.96	3.59	1992	
593722508	22	-29	79.9	34.088	9.376	198.304	1562.1	1534.79	3.64	1992	
593222459	22	-29	66.471	29.905	8.891	225.411	1563.34	1535.39	3.65	1992	
592922520	22	-29	75.643	32.907	9.195	216.738	1562.03	1534.71	3.71	1992	
592622500	22	-29	83.855	34.536	9.715	185.586	1563.12	1535.27	3.56	1992	
592222481	22	-29	66.19	30.829	8.588	221.995	1564.33	1535.77	3.69	1992	

Scaling (predicted)					Dimensions after scaling (predicted)				
Sc2007	Sc2012	Sc2025	Sc2100	Sc2500	P.W. 2007	P.W. 2012	P.W. 2025	P.W. 2100	P.W. 2500
-0.42	-0.43	-0.45	-0.56	-0.74	6.849	6.827	6.76	6.534	6.126
-0.42	-0.44	-0.47	-0.57	-0.75	8.451	8.406	8.339	8.116	7.712
-0.42	-0.44	-0.47	-0.57	-0.75	8.01	7.967	7.904	7.693	7.311
-0.43	-0.44	-0.45	-0.57	-0.76	8.265	8.243	8.156	7.959	7.542
-0.42	-0.43	-0.46	-0.56	-0.75	8.799	8.777	8.711	8.491	8.114
-0.43	-0.44	-0.47	-0.57	-0.75	7.665	7.643	7.578	7.361	6.969

Safety factors (initial & predicted)					Failure probability (initial & predicted)					
SF_98	SF_2007	SF_2012	SF_2025	SF_2100	SF_2500	PoF_98	PoF_2007	PoF_2012	PoF_2025	PoF_2100
1.9	1.7	1.54	1.2	0.7	0.4	0	1.01	2.22	3.66	12.4
1.48	1.34	1.05	1.02	0.92	0.8	0	0	2.05	1.7	12.4
1.88	1.64	1.33	1.3	1.19	1.07	0	1.22	1.29	1.5	13.4
2.52	1.92	1.9	1.86	1.74	1.5	0	0	0	0	0.66
2.51	1.98	1.92	1.86	1.73	1.5	0	0	0	0	0.67
0.96	0.96	0.66	0.64	0.56	0.4	9.7	21.34	21.34	21.86	23.42

Figure 7—Overview of the pillar stability database created in the GIS

Modelling coal pillar stability from mine survey plans in a geographic information system

pillar is determined from the year and quarter in which the panel was mined.

- *Amount of pillar scaling*—The amount of pillar scaling is determined individually from the pillar age and height.
- *Pillar dimensions after scaling*—Pillar scaling is modelled according to the individually predicted amount of scaling, as previously shown in Figure 6. From the resulting outlines of pillars after scaling, the new effective pillar square width is calculated and stored in the database.
- *Pillar safety factors*—Pillar safety factors are calculated for the initial ‘as-mapped’ pillar dimensions and for each scaling step in time.
- *Pillar failure probability*—If available, the failure probability (%) of the individual pillars can be linked to the calculated safety factors for any step in time.

The pillar database is the core of the GIS model and can be subjected to a wide range of queries; for example, on the safety factors or failure probabilities of selected pillars or for the statistical distribution characteristics of the same within a mining panel. All relevant information can be mapped back onto the original survey data in order to get an impression of the distribution of regional stabilities and instabilities. In conjunction with existing or planned surface infrastructure, this provides the basis for a comprehensive risk assessment. Some practical examples of the modelling procedure are presented at the end of this paper.

Accuracy of safety factor calculations based on survey plans

Some considerations must be given to the general accuracy of safety factor predictions based on survey plans, which are the basis of the GIS model.

Possible sources of error in the safety factor prediction may arise from the underground measurements of the mining dimensions and the quality of mapping. The typical scale of survey plans for South African collieries is 1:1500, which is rather unsuitable for an accurate mapping and reading of pillar sizes. It must be borne in mind that 1 mm of inaccuracy in mapping or reading would reduce or increase the interpreted pillar size by 1.5 m. Further sources of inaccuracies may be found in the GIS model, where digitized, and therefore to some extent modified, data is used. An unavoidable source of error is introduced through the interpolation and extrapolation of point-type information such as underground mining heights and elevations from singular survey points.

The magnitude of *possible* inaccuracy that results in the predicted pillar safety factor calculation from all these factors can be determined only if the error in all the input data is known. This is rarely the case. For example, assume a scenario where a mining depth below surface of $H = 80$ m and pillars of width $w = 10$ m, $h = 4$ m, and centre distance of $D = 16$ m are measured from the survey plan. Further assume that each parameter is accompanied by a *possible* (not definite) inaccuracy of $e(w) = e(D) = 1$ m and $e(H) = e(h) = 0.3$ m. The pillar safety factor formula based on the updated maximum likelihood strength equation presented is:

$$SF_{ML} = 264 \frac{w^{2.5}}{H D^2 h^{0.7}} \quad [6]$$

For the given scenario a value of $SF = 1.54$ is determined. The possible inaccuracy of the determined safety factor, $e(SF)$, can then be estimated based on the law of error propagation:

$$e^2(SF) = \left(\frac{\partial SF}{\partial w} e(w) \right)^2 + \left(\frac{\partial SF}{\partial H} e(H) \right)^2 + \left(\frac{\partial SF}{\partial h} e(h) \right)^2 + \left(\frac{\partial SF}{\partial D} e(D) \right)^2 \quad [7]$$

$$e(SF) = \sqrt{e^2(SF)} \quad [8]$$

where $(\partial SF/\partial w)$, $(\partial SF/\partial H)$, $(\partial SF/\partial h)$, and $(\partial SF/\partial D)$ are the partial derivatives of the safety factor equation.

In the given scenario, the estimated possible inaccuracy is $e(SF) = 0.44$ or 28% of the safety factor (the same result is obtained when Equation [2] is used to calculate the safety factor). This is unfavourable for a risk assessment, although it is believed to be unavoidable for any pillar stability analysis that is based on survey plans only. The magnitude of *possible* error must be kept in mind when any risk-related judgements and decisions are made.

Nevertheless, the possible error should remain practically the same for all underground pillars in a panel or region with similar mining dimensions. The predicted safety factors will therefore serve well for locating groups of comparatively weak pillars in the panel. Hence, trigger areas for a possible pillar collapse can be predetermined, which in return allows for prioritizing of preventative steps in risk management.

Application to case studies

The proposed GIS-based pillar stability analysis method has been applied to mine survey data from a bord-and-pillar coal mine in South Africa. This exercise also provided the opportunity to back-analyse a case of pillar collapse in high resolution, *i.e.* on a pillar-by-pillar basis, and to check the validity of the stability predictions made in the model. For safety factor calculations, the updated van der Merwe and Mathey coal pillar strength formula (Equation [3]) was used.

In the following sections, the results from the modelling exercise are presented in the form of maps, displaying the predicted pillar safety factors according to a traffic-light colour scheme. The assumption is made that a pillar safety factor of 1.4 or higher is desirable in a pillar stability risk assessment (green), while any safety factor less than unity indicates an increased risk for instabilities (red). Intermediate values are displayed in shades of yellow.

It should be understood that the stability of pillars is assessed on an individual basis, but that the performance of many adjacent pillars in a panel depends on its stability or instability. For instance, it is very unlikely that a single weak (yellow/red) pillar situated within an overall competent (green) pillar environment will cause the panel to collapse. This is because relatively weak pillars can shed excess load which is taken up by adjacent, stronger pillars. Experiences of surface subsidence due to bord-and-pillar mining show

Modelling coal pillar stability from mine survey plans in a geographic information system

that it takes a relatively large number of adjacent weak pillars to trigger a pillar collapse.

One example of an overall stable panel is shown in Figure 8. One observes that the pillar safety factors are very favourable, with values well above 1.6. Only in isolated cases does the predicted pillar safety factor drop below 1.4.

The available mine survey data also provides an opportunity to back-analyse a pillar collapse event. This assisted in verifying the reliability of the predicted safety factors and gaining insight into the mechanism responsible for pillar failure in the case study.

The collapsed panel under consideration was mined in the 1980s through drilling and blasting at a shallow depth of 35–55 m below surface. Pillars were intended to be designed with a safety factor of 1.6, but the mapped pillar dimensions were found to deviate significantly from this design guideline.

On the event of the initial collapse, about 30 years after mining the panel, a near-circular subsidence trough with a diameter of 200 m was observed on surface. The pillar collapse spread in the subsequent three years for a further 200 m into neighbouring panels. Figure 9 shows the calculated distribution of pillar safety factors at the time of mining and the outline of the subsidence trough at various development stages (blue lines).

Analysis of the *as-mapped* stability situation in the relevant panels on a pillar-by-pillar basis reveals a large group of distinctly weak pillars in the centre of the collapsed panel. Pillars inside the area of the initial collapse are predicted to have an average safety factor of 1.35. Some pillars are indicated with safety factors of less than 0.8. The neighbouring panels in the north- and southeast exhibit more favourable stability conditions. It can thus be concluded that the trigger area for the original collapse was already predestined at the time of mining.

The scaling analysis was then applied to approximate the stability situation at the time of collapse (Figure 10). The average amount of scaling that acted on the pillars until the collapse occurred was predicted to be about 0.4 m along the pillar circumference.

After scaling, those pillars in the area of initial collapse exhibit a safety factor range of 0.4–1.6, with an average safety factor of 0.9. This prediction can be regarded as being remarkably accurate, considering that the nominal safety factor of pillars at failure should be just below unity. The reason why some individual pillars could maintain an extraordinary low safety factor up to the time of collapse can probably be attributed to the phenomenon of load-shedding, since enough pillars with relatively larger safety factors were existent in this area.

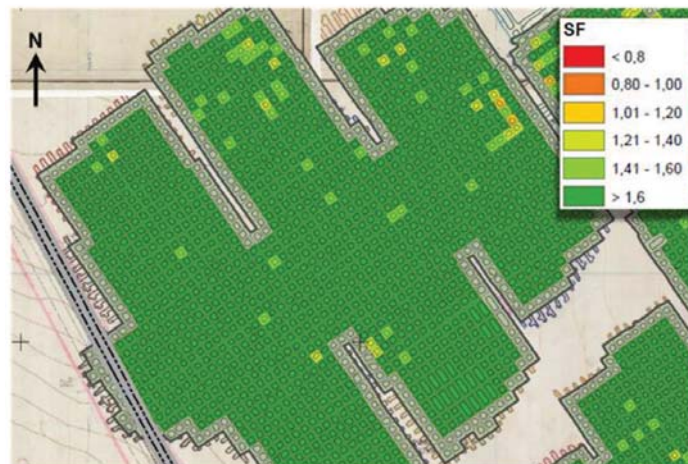


Figure 8—Panels with favourable stability conditions, as modelled in the GIS

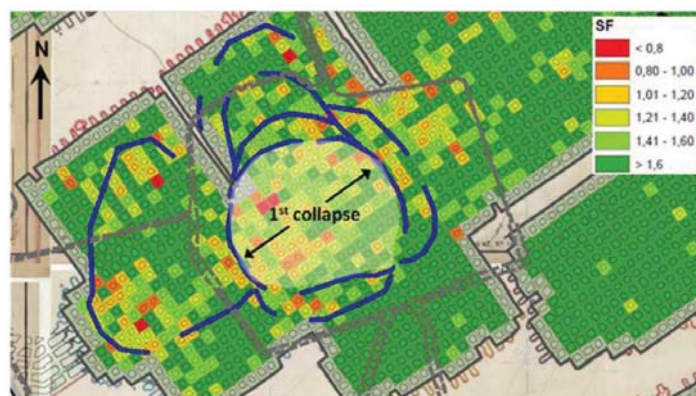


Figure 9—Distribution of 'as-mapped' safety factors in the area of collapse

Modelling coal pillar stability from mine survey plans in a geographic information system

Figure 10 also explains why the collapse spread mainly towards the north and west, where larger groups of relatively weak pillars were situated. It can also be seen why the failure did not extend to the small panel in the southeast, as still enough pillars with safety factors of about SF 2.0 and higher can be found there.

It is also useful to look at the situation from a risk point of view. The link between the pillar safety factor and the failure probability, as given in Equation [5], can be applied to quantify the risk involved. Figure 11 plots the areal distribution of predicted pillar failure probabilities (*PoF*) in the collapsed zone at the time of pillar failure. It is observed that the bulk of pillars in the collapsed area exhibit values of *PoF* > 5 %, and frequently even in excess of 10%. The uncollapsed panel in the southwest, however, is predicted to be in favourable stability conditions with *PoF* < 1 %.

Conclusions

A practical method for analysing the stability of large numbers of pillars based on mine survey data has been demonstrated. A geographic information system (GIS) was devised for processing the spatial and physical parameters of

mining with the aim of calculating individual pillar safety factors and to predict the impact of pillar scaling over time.

The main advantage of the method is that each pillar in a mine is evaluated individually, quickly, and easily, as opposed to using an average number for a panel as a whole. This provides the ability to identify zones of suspect stability in a panel. This is further facilitated by visualizing the predicted stability parameters, *e.g.* safety factors or failure probabilities, in the GIS on the digital survey plans. In conjunction with spatial information on surface infrastructures, these plans provide the basis for a comprehensive risk assessment.

It has been shown that any pillar stability analysis based on mine survey plans is subject to some level of uncertainty. The application of the proposed modelling procedure to the back-analysis of a pillar collapse, however, established confidence that both the time-dependent weakening of pillars and their related safety factors can be determined with reasonable accuracy in the GIS model. The average factor of safety of the group of collapsed pillars was predicted as just below unity, where pillar failure would normally occur. Also, the risk maps created by the software gave a satisfying



Figure 10—Pillar safety factors at the time of collapse

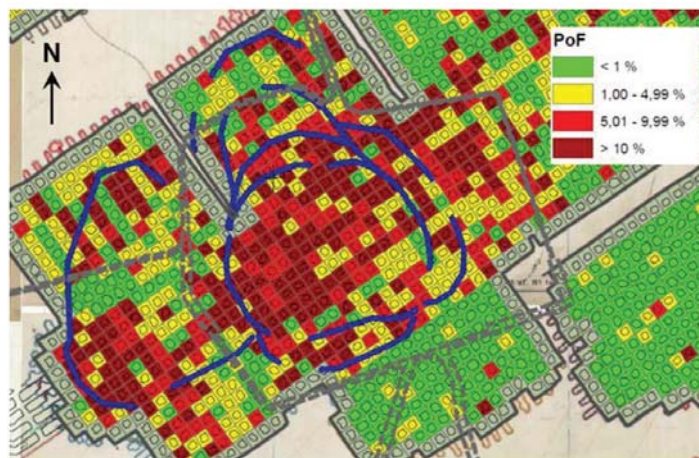


Figure 11—Failure probabilities at the time of collapse

Modelling coal pillar stability from mine survey plans in a geographic information system

prediction of the location of pillar failure and the extent of its subsequent spread.

References

- ABEL, J.F. 1988. Soft rock pillars. *International Journal of Mining and Geological Engineering*, vol. 8. pp. 215–248.
- MATHEY, M. 2010. A contribution to risk assessment for abandoned bord and pillar mining in shallow depth. *Proceedings of the 14th International Congress of the Society for Mine Surveying*, Sun City, South Africa, 24–27 September 2010.
- MATHEY, M. 2013. Addressing the challenges involved with abandoned underground coal mines in South Africa. *Proceedings of the 15th International Congress of the Society for Mine Surveying*, Aachen, Germany.
- MATHEY, M. and SCHULTE, R. 2011. GIS-based risk management for abandoned bord and pillar mining in South Africa. *Proceedings of the Energy & Resources Conference*, Freiberg, Germany. (in German).
- ROBERTS, D.P., VAN DER MERWE, J.N., CANBULAT, I., SELLERS, E.J., and COETZER, S. 2002. Development of a method to estimate coal pillar loading. SIMRAC COL 709 research report. Safety in Mines Research Advisory Committee, Johannesburg.
- SALAMON, M.D.G. AND ORAVECZ, K.I. 1973. Rock mechanics in coal mining. *Research Report no. 26/73*, Collieries Research Laboratory. Chamber of Mines of South Africa, Johannesburg.
- SALAMON, M.D.G. and MUNRO, A.H. 1967. A study of strength of coal pillars. *Journal of the South African Institute of Mining and Metallurgy*, vol. 67 pp. 55–67.
- VAN DER MERWE, J.N. 2003. Predicting coal pillar life in South Africa. *Journal of the South African Institute of Mining and Metallurgy*, vol. 103, no 5. pp. 293–301.
- VAN DER MERWE, J.N. 2004. Verification of pillar life prediction method. *Journal of the South African Institute of Mining and Metallurgy*, vol. 104, no 11. pp. 667–675.
- VAN DER MERWE, J.N. and MADDEN, B.J. 2010. Rock engineering for underground coal mining. *Special publication no. 8* (2nd edn). Southern African Institute of Mining and Metallurgy, Johannesburg.
- VAN DER MERWE, J.N. and MATHEY, M. 2013a. Probability of failure of South African coal pillars. *Journal of the Southern African Institute of Mining and Metallurgy*, vol. 113, no. 11. pp. 825–840.
- VAN DER MERWE, J. N. and MATHEY, M. 2013b. Update of coal pillar database for South African coal mining. *Journal of the Southern African Institute of Mining and Metallurgy*, vol. 113, no. 11. pp. 825–840.
- VAN DER MERWE, J.N. and MATHEY, M. 2013c. Update of coal pillar strength formulae for South African coal using two methods of analysis. *Journal of the Southern African Institute of Mining and Metallurgy*, vol. 113, no. 11. pp. 841–847.
- WAGNER, H. 1980. Pillar design in coal mines. *Journal of the South African Institute of Mining and Metallurgy*, vol. 80. pp. 37–45. ♦



SAIMM
THE SOUTHERN AFRICAN INSTITUTE
OF MINING AND METALLURGY

Geometallurgy Conference 2018

BACK TO THE FUTURE

Supported by



SAIMM
THE SOUTHERN AFRICAN INSTITUTE
OF MINING AND METALLURGY

6th August 2018—Technical Workshop • 7–8th August 2018—Conference
Lagoon Beach Conference Venue, Cape Town, South Africa

BACKGROUND

The theme of this first geometallurgy conference 'Back to the future' is inspired by looking both into the past and the future: the concept of Geometallurgy goes back to some of the earliest mining activities when mineral recognition, mining, separation and concentration were undertaken simultaneously. Over time, changes in operational structures, product expansion and specialisation ultimately led to the diminishment and breakdown of this holistic approach.

In the last two decades 'Geometallurgy' has become a sophisticated yet entirely logical return to this integrated approach to mine planning. In a world of exponentially increasing ore heterogeneity and economic complexity, Geometallurgy is effectively a highly structured, integrated multi-disciplinary collaboration for optimising the value of an ore deposit. The approach is premised on acquiring multi-dimensional, spatially constrained (blocked) ore body knowledge that quantifies and qualifies all aspects of ore body variability. This data must include each element's response to blasting, excavation, crushing, grinding, separability and the environment and of course, its economic factors. These discrete elemental data sets are modelled to optimise a mine plan which takes into account the respective threshold criteria for each of the dataset components. Looking into the future, we need to visualise what our 'ideal' mining operation in Southern Africa should look like, how it will function, and be equipped to articulate what we need to do to achieve this. Geometallurgy is a critical tool in achieving this.

For further information contact:

Camielah Jardine, Head of Conferencing, Saimm, P O Box 61127, Marshalltown 2107, Tel: +27 (0) 11 834-1273/7, E-mail: camielah@saimm.co.za, Website: <http://www.saimm.co.za>



Integration of commodity price uncertainty in long-term open pit mine production planning by using an imperialist competitive algorithm

by M. Mokhtarian Asl* and J. Sattarvand†

Synopsis

Production planning for an open pit mine is a procedure in which the ore blocks are assigned to different production periods in a way that leads to the highest net present value (NPV) subject to some operational and technical constraints. Incorporation of uncertainty in the input parameters makes this process much more complicated. In this paper we describe a new stochastic optimization procedure, based on the imperialist competitive algorithm (ICA), for long-term production planning of open pit mines under conditions of commodity price or market uncertainty. The procedure involves generating simulated realizations of commodity price values and finding the solution by ICA. The proposed approach has been tested on a real-world copper mine and the results show that ICA could be efficiently applied to stochastic production planning of a real mine.

Keywords

imperialist competitive algorithm, stochastic programming, open pit mining, production planning, commodity price uncertainty.

Introduction

Production planning for open pit mines is a complex and significant problem that has been investigated by many researchers. The planning process usually starts with the construction of a geological block model, which comprises the set of imaginary regular blocks that covers the ore deposit and surrounding host rock. A set of attributes such as grade, specific gravity, and coordinate is then assigned to or estimated for each of these blocks using drill-hole sample data. Geological attributes are combined with technical and economic parameters in the next stage to determine the monetary value of each block and construct the economic block model, which provides the basic input for the production planning problem.

Generally, production planning for an open pit mine entails finding the sequence of blocks for the optimal annual schedules in a way that leads to the highest net present value (NPV) of the project cash flows, while meeting the technical constraints such as mining capacity, processing capacity, sequencing, and pit slope (Dagdelen, 2001).

Long-term production planning could be categorized into two major classes, of deterministic and stochastic-based approaches. Deterministic open pit production planning has

been studied since 1968 (Johnson, 1968) and, conventionally, several methodologies have been developed, such as integer programming (Caccetta and Hill, 2003; Dagdelen and Johnson, 1986), mixed integer programming (Boland *et al.*, 2009; Elkington and Durham, 2011), dynamic programming (Wang and Sevim, 1992), and meta-heuristic approaches such as the genetic algorithm (Denby and Schofield, 1994), particle swarm algorithm (Khan and Niemann-Delius, 2014), and ant colony algorithm (Sattarvand and Niemann-Delius, 2009; Shishvan and Sattarvand, 2015). The fundamental and significant drawback of these approaches is the assumptions about input parameters. Assuming exactly known (deterministic) parameters, unlike reality in which a significant degree of uncertainty is associated with these parameters, may lead to unrealistic and incorrect production planning (Abdel Sabour and Poulin, 2010; Dimitrakopoulos, Farrelly, and Godoy, 2002; Marcotte and Caron, 2013).

Unlike the conventional deterministic mine design process, which is usually implemented based on deterministic input parameters, stochastic planning of open pit mines considers uncertainty in input parameters. This approach has attracted research during the last decade and several methods have been developed, which can be divided into three main categories: mathematical-based, heuristic, and meta-heuristic approaches. Mathematical formulations using linear programming (Dimitrakopoulos, Farrelly, and Godoy, 2002), integer linear programming (Dimitrakopoulos and Ramazan, 2008; Kumral, 2010; Marcotte and Caron, 2013; Moosavi *et al.*, 2014) or maximum flow (Asad

* Faculty of Mining and Metallurgical Engineering, Urmia University of Technology, Urmia, Iran.

† Department of Mining and Metallurgical Engineering, University of Nevada Reno, Nevada, USA.

© The Southern African Institute of Mining and Metallurgy, 2018. ISSN 2225-6253. Paper received Sept. 2016; revised paper received Jan. 2018.



Integration of commodity price uncertainty in long-term open pit mine production planning

and Dimitrakopoulos, 2012; Asad, Dimitrakopoulos, and van Eldert, 2014; Chatterjee *et al.*, 2016) have been developed to solve stochastic problems. The maximum upside potential / minimum downside risk method (Dimitrakopoulos, Martinez, and Ramazan, 2007) is predominant among the heuristic techniques. Genetic algorithms (Denby and Schofield, 1995), simulated annealing (Albor Consuegra and Dimitrakopoulos, 2009), Tabu search (Lamghari and Dimitrakopoulos, 2012), and ant colony algorithm (Gilani and Sattarvand, 2016) meta-heuristic approaches have also been reported to be successfully applied. The majority of research has been focused on incorporation of metal grade uncertainty. Investigation into commodity price uncertainty seems to be in need of further development.

In this paper we propose an efficient solution methodology based on the imperialist competitive algorithm (ICA) to solve real-scale planning problems that are present due to commodity price uncertainty. The procedure has the capability to simultaneously optimize the ultimate pit limit (UPL) and production scheduling.

Commodity price simulation

A review of price fluctuations of raw minerals shows that the prices of mining products are highly volatile. For example, as illustrated in Figure 1, the price of copper has been highly volatile during the past 30 years (Indexmundi, 2018), with variations of approximately 200% from 2004 to 2011. Commodity price uncertainty clearly plays an important role in production planning, as constant-price-based planning would lead to an unrealistic answer, increasing the investment risk and the risk due to economic downturns.

Uncertainty in metal prices in future arises because of two main factors:

1. The lack of exact knowledge of factors leading to the increase/decrease in metal supply and demand
2. The practices of producers or consumers in the face of powerful speculative and political motives (Macavoy, 1988).

Forecasting is the process of making statements about events whose actual outcomes have not yet been observed. It is the prediction of future events and is often based on past experiences. The accuracy of predictions of input assumptions is a key factor for success of the procedure.

Several forecasting approaches have been developed to date that could be utilized to simulate future price

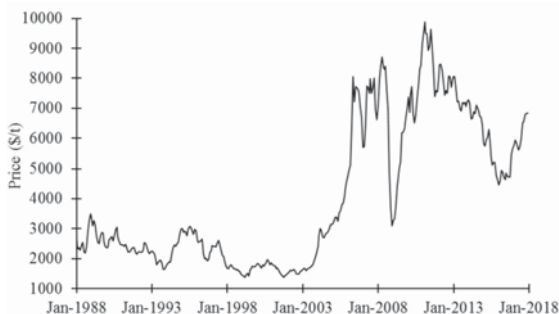


Figure 1—Fluctuation in the copper price during last 30 years (Indexmundi, 2018)

fluctuations. Using stochastic processes is a popular commodity price forecasting method. A stochastic process changes a variable over time in a random way, such as in a Wiener process. A Wiener process is a continuous-time stochastic process with three important properties. Firstly, it is a Markov process. This means that the probability distribution of all future values of the process depends only on its current value and is unaffected by past values of the process or by any other current information. Secondly, a Wiener process has independent increments. This means that the probability distribution for the change in the process over any time interval is independent of any other time interval. Finally, changes in the process over any finite interval of time are normally distributed, with a variance that increases linearly with the time interval. The most commonly used stochastic processes are the geometric Brownian motion (GBM) and the mean reverting process (MRP) (Dixit and Pindyck, 1994). Generally, the MRP is appropriate for modelling variables that have a long-term equilibrium level, such as metal prices (Schwartz, 1997). The logic behind a MRP derives from microeconomics: when prices are depressed (or below their long-term mean level), the demand for the product tends to increase while production tends to decrease. The opposite will occur if prices are high (or above the long-term mean) (Pindyck and Rubinfeld, 1998). The simplest form of MRP is the one-factor Ornstein-Uhlenbeck process, which is defined by:

$$dx_t = \eta(\bar{x} - x_t)dt + \sigma dz_t \quad [1]$$

where x_t is the variable, η the mean reversion speed, \bar{x} is the long-term average to which x_t reverts, σ the volatility of process, and dz_t is the standard Wiener process (Dixit and Pindyck, 1994). The natural logarithm of the variable is used since in the case of commodities it is generally assumed that these prices have a lognormal distribution. Under this condition, Schwartz (1997) proposed the commodity price (S) follows the mean reversion process, as:

$$dS = \eta[\ln \bar{S} - \ln S]S \cdot dt + \sigma \cdot S \cdot dz \quad [2]$$

where \bar{S} is the long-term mean price.

Formulation of mine production planning under uncertainty

The uncertainties in input parameters could be divided into those that arise from the nature of the variables and those that are too expensive to be defined. For example, metal grade of the orebody is a variable whose uncertainty would be diminished by extension of the exploratory studies, which requires time and money (Abdel Sabour, Dimitrakopoulos, and Kumral, 2008). In contrast, commodity price is a variable where uncertainty arises from a number of factors and exact forecasting is not possible for future years. From an economic point of view, uncertain future commodity prices have a critical influence on mine project evaluation (Asad and Dimitrakopoulos, 2013; Haque, Topal, and Lilford, 2014).

Open pit production planning under commodity price uncertainty may be effectively modelled as a stochastic integer programming (SIP) formulation with the objective of NPV maximization subject to a set of technical and operational constraints. It can be expressed as follows:

Integration of commodity price uncertainty in long-term open pit mine production planning

$$\text{Maximize } \sum_{r=1}^R p_r \sum_{t=1}^T \sum_{n=1}^N \frac{v_{rm}}{(1+d)^{t-1}} x_m \quad [3]$$

where:

- T : Number of time periods
- N : Number of mine blocks
- R : total number of price realizations for each year of the mine life
- p_r : Probability of realization r
- v_{rm} : Economic value of a block n in period t and realization r
- x_{tm} : Binary decision variables of the model ($x_{tm}=1$ if block n is mined in time period t , otherwise $x_{tm}=0$)
- d : Annual discount rate.

The economic value of a block equals the difference between revenue earned from selling the commodity (mineral) content of that block and the total costs involved in its mining and processing. For example, for a copper mine, the economic value of block n is calculated as follows:

$$\text{Return}_m = \left(\frac{[(\text{Copper price} - \text{Sales costs}) \times \text{Recovery} \times \text{Tonnage}_m \times \text{grade}_m]}{-(\text{Mining cost} + \text{Milling cost} + \text{Smelting cost} + \text{Refining cost} + \text{Transport cost})} \right) \quad [4]$$

$$v_m = \max[\text{Return}_m, (-\text{Mining cost}_m)] \quad [5]$$

The described objective function is subject to the following constraints.

Mining capacity constraints: Total tonnage of extracted material should be between a pre-determined upper and lower limit for each scheduling period.

$$MC_{min}^t \leq \sum_{n=1}^N W_n x_m \leq MC_{max}^t \quad \text{for } \forall t \quad [6]$$

where

- W_n : Tonnage of block n
- MC_{max}^t, MC_{min}^t : Maximum and minimum acceptable mining capacity for period t .

Processing capacity constraints: Quantity of ore production should satisfy processing capacity limitations:

$$PC_{min}^t \leq \sum_{n=1}^N O_{rn} x_m \leq PC_{max}^t \quad \text{for } \forall t \text{ and } \forall r \quad [7]$$

where

- O_{rn} : Tonnage of ore block n in realization r . If the block economic value is greater than zero ($v_n > 0$), it will be considered as ore
- PC_{max}^t, PC_{min}^t : Maximum and minimum tolerable processing capacity for period t .

Reserve constraint: This constraint is mathematically necessary to ensure that a block is mined only once in the model.

$$\sum_{t=1}^T x_m \leq 1 \quad \text{for } \forall n \quad [8]$$

Sequencing constraints: The sequencing constraints ensure that a block can be removed only if all overlying blocks have been removed earlier periods or are considered for the same period, t .

$$\sum_{i=1}^t (x_{ij} - x_n) \geq 0, \quad t = 1, \dots, T, \text{ for } \forall (i, j) \in A \quad [9]$$

where A is the set of pairs (i, j) of blocks such that block j is

a key block to block i and must be removed before block i can be mined.

The fundamental and significant drawback of this approach is the high computational cost when applied to real-world problems. In most cases, the block model contains thousands to millions of blocks that make up a SIP model with millions of integer variables and constraints, which can be extremely difficult or expensive to solve. Investigation using a higher class of heuristics, called meta-heuristics, has been of interest recently. A meta-heuristic is a set of algorithmic concepts that can enhance the applicability of heuristic methods to difficult problems. These concepts are usually inspired by biology and nature. The use of meta-heuristic methods has significantly increased the ability to find very high-quality solutions for hard combinatorial problems in a reasonable computation time (Dorigo, Birattari, and Stützle, 2006).

Imperialist competitive algorithm (ICA)

Imperialism is the strategy of expanding the power and scope of rule of government beyond its own boundaries through any type of domination, such as direct rule or by less obvious instruments such as cultural influence, market control, or control of energy and other important commodities. The imperialist competitive algorithm (ICA) is a novel population-based meta-heuristic algorithm proposed by Atashpaz-Gargari and Lucas (2007), mimicking the socio-political process of imperialism and imperialistic competition as a source of inspiration (Khabbazi, Atashpaz-Gargari, and Lucas, 2009). The algorithm's capability in dealing with different types of optimization problems has been proven by the authors (Atashpaz-Gargari and Lucas, 2007). Similar to any evolutionary algorithm, ICA also starts with an initial population of solutions, called countries, representing the concept of nations. Based on the quality of the objective function in each solution, some of the best countries in the population are chosen to be the 'imperialists' and the rest are assumed to be the 'colonies' of those imperialists. A set of one imperialist and its colonies is called an 'empire' (Shokrollahpour, Zandieh, and Dorri, 2011). Over time, imperialists try to extend their own characteristics to the governing colonies; however, it is not a tightly controlled procedure and 'revolutions' may happen in each country. Countries can also leave an empire and migrate to another if they see a better chance of promotion there. Within each empire the position of imperialist could be altered too. Iteratively, the algorithm evolves towards better countries and empires. ICA has been used extensively to solve different kinds of optimization problems. For example, this method is used for stock market forecasting (Sadai *et al.*, 2016), digital filter design (Sharifi and Mojallali, 2015), travelling salesman problems (Ardalan *et al.*, 2015), multi-objective optimization (Maroufmashat, Sayedin, and Khavas, 2014), integrated product mix-outsourcing problems (Nazari-Shirkouhi *et al.*, 2010), and scheduling problems (Behnamian and Zandieh, 2011, Lian *et al.*, 2012).

The following sections describe the practical implementation of ICA in open pit mine production planning. The flow chart of the proposed procedure is illustrated in Figure 2.

Integration of commodity price uncertainty in long-term open pit mine production planning

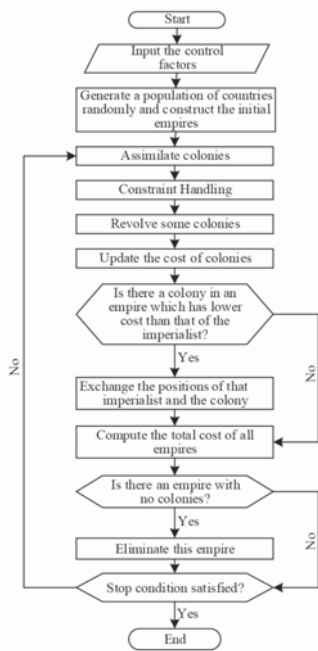


Figure 2—Flow chart of imperialist competitive algorithm

Generating initial empires

The main purpose of optimization is to find an optimal solution; each solution in this algorithm is called a ‘country’. In an n -dimensional optimization problem, a country is an $n \times 1$ array as follows:

$$\text{country} = [p_1, p_2, p_3, \dots, p_n] \quad [10]$$

where p_i s are decision variables whose values need to be determined in order to maximize or minimize the objective function. The decision variables of an open pit mine production planning problem are the extraction time of the blocks in the economic block model, and the objective is to maximize the NPV of the project.

To start the optimization algorithm, an initial population is generated containing N_{pop} solutions (mine schedules), among which N_{imp} of the most powerful solutions (according to their NPVs) are selected as ‘imperialists’. The rest of the population members ($N_{col} = N_{pop} - N_{imp}$) will be the colonies of the chosen empires. To form the primary empires, colonies are randomly divided among the imperialists based on their power as the higher the power of an empire, the more colonies belong it. To proportionally distribute the colonies among imperialists, the normalized cost of the n^{th} imperialist is defined as:

$$C_n = \frac{\max\{c_i\} - c_n}{\sum_{i=1}^{N_{imp}} (\max\{c_i\} - c_i)} \quad [11]$$

where c_n and C_n are the cost and the normalized cost of n^{th} imperialist respectively. The objective of ICA is set to minimize the sum of the cost function value of all countries.

To convert the production planning problem from maximization to minimization, the negative value of the NPV is used as the cost function.

$$\text{Cost}(\text{country}) = - \sum_{r=1}^R p_r \sum_{t=1}^T \sum_{n=1}^N \frac{v_{rtn}}{(1+d)^{t-1}} x_m \quad [12]$$

Hence the normalized power of each imperialist can be determined as below:

$$pow_n = \left| C_n / \sum_{i=1}^{N_{imp}} C_i \right| \quad [13]$$

The normalized power of an imperialist indicates the number of colonies that should be probably controlled by that imperialist. Thus, the initial number of colonies of an empire will be as follows:

$$ColEmp_n = \text{round}(pow_n \times N_{col}) \quad [14]$$

where $ColEmp_n$ is the initial number of the colonies of the n^{th} empire; those are chosen randomly from the whole colony population. Each imperialist together with its colonies will form an empire.

Modified assimilation process

The goal of an assimilation policy is to improve the properties of the colonies. This policy is implemented by moving all the colonies toward their corresponding imperialist. The colonies will approach the imperialist along different socio-political axes such as culture, language, etc. As shown in Figure 3, the assimilating operator for the open pit mine production planning problem follows the steps below:

- Create the country array with the size equal to the number of blocks in the block model of the mine. The value of the cell n in array is equal to unity if block n is mined (the coloured blocks in Figure 3), and equal to zero otherwise
- Select a sub-array randomly in the imperialist array (for example, cells 5 to 11)
- Copy the imperialist sub-array to the colony array.

Constraint handling

There is not an explicit mechanism for constraint handling in ICA. Considering the special structure of constraints involved in the production scheduling of an open pit mine, the following two constraint handling techniques may be used.

Sequencing constraint

Usually, the assimilated colony (Figure 3) does not result in a feasible pit shape with acceptable slope angles and block precedence. A feasible pit generation procedure is called

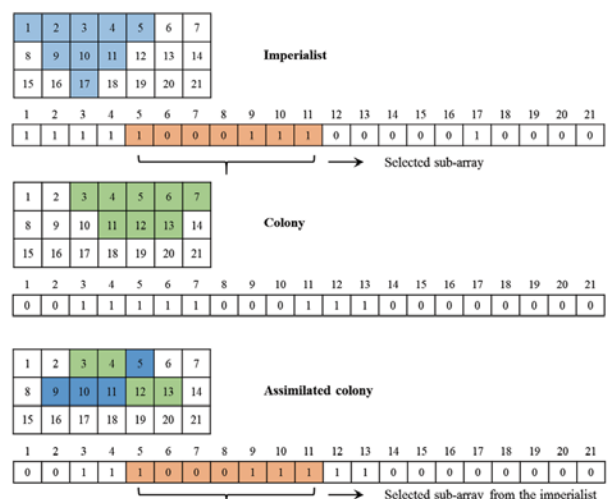


Figure 3—Assimilation operator for a production planning problem

Integration of commodity price uncertainty in long-term open pit mine production planning

normalization. Consequently, normalization is required to satisfy any sequencing constraints (Equation [9]), as shown in Figure 4.

Capacity constraint

To deal with violations of mining and processing capacity constraints a constant penalty method has been used. The objective function (Equation [5]) can be written as follows:

$$\text{Maximize } \sum_{r=1}^R p_r \sum_{t=1}^T \sum_{n=1}^N \frac{v_{rm}}{(1+d)^{t-1}} x_m - \quad [15]$$

$$P_t^{M^-} M_{rt}^- - P_t^{M^+} M_{rt}^+ - P_t^{O^-} O_{rt}^- - P_t^{O^+} O_{rt}^+$$

where

$P_t^{M^-}, P_t^{M^+}$: Represent the discounted unit costs (penalty) for a shortage or surplus in the total weight of rock mined in period t , respectively

M_{rt}^-, M_{rt}^+ : Denote the shortage or surplus in the amount of rock mined during period t if scenario r occurs, respectively

$P_t^{O^-}, P_t^{O^+}$: Represent the discounted unit costs (penalty) for a shortage or surplus in the ore produced in period t , respectively

O_{rt}^-, O_{rt}^+ : Represent the shortage or excess amount of ore produced in period t if scenario r occurs, respectively.

Revolution

While the assimilation process is responsible for intensification, a revolution mechanism diversifies ICA to explore new regions. The revolution mechanism prevents the algorithm from being trapped in local optima. It is only applied to colonies, and imperialists remain untouched (Mortazavi, Khamseh, and Naderi, 2015). For this purpose, the weakest colony (production plans with the lowest NPV) in each iteration is selected and replaced with a new one, randomly.

Exchanging positions of the imperialist and a colony

When moving toward the imperialist, a colony might reach a position with a lower cost function than that of its imperialist. In this condition, the positions of the imperialist and colony are swapped. Afterwards, the algorithm continues using the new imperialist, and colonies move towards the new leader of the empire.

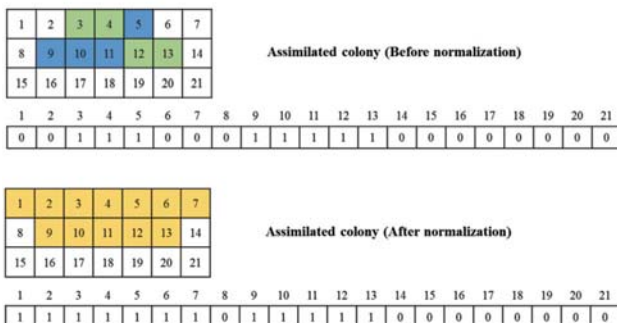


Figure 4—Normalization process for the assimilated colony

Total power of an empire

The total power of an empire is mainly based on the power of its imperialist country; however, the powers of its individual colonies have also an effect, albeit relatively insignificant. Therefore, the total cost of an empire is described as:

$$TC = \text{cost}(\text{imperialist}_n) + \xi \text{mean}(\text{cost}(\text{colonies of empire}_n)) \quad [16]$$

where TC is the total cost of the n th empire and ξ is a positive number which is considered to be less than unity. A small value of ξ causes the total power of the empire to be determined by mainly the imperialist, and a larger value will increase the role of the colonies in determining the total power of the empire.

Imperialistic competition

In general, empires try to take possession of colonies of the other empires and control them. Through this process, the power of weaker empires will decrease and that of the more powerful ones will increase. This competition is modelled by choosing one of the weakest colonies of the weakest empire and creating competition among all empires to possess this colony. Each of the empires (based on its total power) will have a chance to taking ownership of the mentioned colony. In other words, a colony has no certainty of belonging to the most powerful empire; however, the more powerful empires will be more likely to possess it. The possession probability of each empire is proportional to its total power. The normalized total cost of each empire is determined as:

$$NTC_n = \max \{TC_i\} - TC_n \quad i = 1, 2, \dots, N_{imp} \quad [17]$$

where TC_n and NTC_n are respectively the total cost and normalized total cost of the n th empire. Now the possession probability of each empire can be given by:

$$P_n = \left| \frac{NTC_n}{\sum_{i=1}^{N_{imp}} NTC_i} \right| \quad [18]$$

To divide the mentioned colonies among empires based on the possession probability of them, vector P , is formed as follows:

$$P = [p_1, p_2, p_3, \dots, p_{N_{imp}}] \quad [19]$$

Then, the vector R with the same size as P whose elements are uniformly distributed random numbers between 0 and 1, is created.

$$r = [r_1, r_2, r_3, \dots, r_{N_{imp}}], \quad r_1, r_2, r_3, \dots, r_{N_{imp}} \sim U(0, 1) \quad [20]$$

Then, vector D is formed by subtracting R from P .

$$D = P - R = [d_1, d_2, d_3, \dots, d_{N_{imp}}] = [p_1 - r_1, p_2 - r_2, p_3 - r_3, \dots, p_{N_{imp}} - r_{N_{imp}}] \quad [21]$$

Referring to vector D , the mentioned colonies in an empire whose corresponding index in D is maximum will win the possession competition (Atashpaz-Gargari and Lucas, 2007).

Integration of commodity price uncertainty in long-term open pit mine production planning

Eliminating powerless empires

Powerless empires will collapse in imperialistic competition and their colonies will be distributed among other empires. In modelling the collapse mechanism, different factors can be defined to consider an empire as powerless. In the current study, an empire collapses when it loses all of its colonies.

Stopping criteria

The algorithm continues until no iteration is remaining or just one empire exists in the world.

Numerical results and discussion

A three-dimensional numerical example was used for examination of the proposed methodology. It consists of a copper deposit with geological block model containing 36 720 blocks that are 15×15×15 m and with a pit slope angle of 45° along all azimuths. Mining will be operated for 5 years and the maximum and minimum mining capacities are 21.04 and 16.82 Mt/a respectively. The maximum and minimum processing capacities are considered to be 16.05 and 9.63 Mt/a respectively and the discount rate is assumed to be 10%. Table I displays the technical and economic parameters required for the construction of the economic block model. Equation [2] was used for forecasting of future copper price, which was simulated for the next 5 years in 20 realizations (Figure 5). The proposed procedure for applying ICA to a production planning problem in open pit mines has been implemented using the C++ programming language.

The most common performance measure of algorithms that is used in the literature is the relative percentage deviation (RPD). The performance measure for this study has been calculated as follows:

$$RPD = \frac{Math - ICA_{best}}{ICA_{best}} \times 100 \quad [22]$$

where ICA_{best} and Math are respectively the best solutions generated by ICA and the optimal mathematical solution.

A hypothetical examination was conducted to test the performance of ICA in an open pit mine production planning

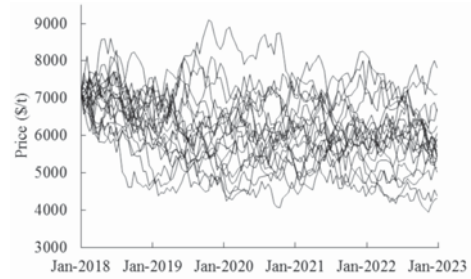


Figure 5—Copper price realizations for the next 5 years

Table I

Technical and economic parameters required for the construction of the economic block model

Parameter	Value
Mill recovery rate	80%
Mill concentrate grade	28%
Smelting loss (kg/t)	10
Refining loss (kg/t)	5
Mining cost (\$/t)	1.5
Milling cost (\$/t)	5.5
General and administration cost (\$/t)	0.5
Amortization and depreciation cost (\$/t)	0.8
Transport cost of mill concentrate to the smelter (\$/t)	30
Smelting cost (\$/t)	92
Transport cost of the blister copper to the refinery (\$/t)	2
Refining cost (\$/t)	184
Selling and delivery cost (\$/t)	0.01
General plant cost (\$/kg)	0.01

problem. Different levels for various control factors (ξ , number of countries, and number of imperialists) were used in the optimization and are shown in Figure 6. The small RPD show the effectiveness of ICA in mine production planning. Hence, ICA was used for long-term production planning of a real-world copper mine, based on copper price realizations for the next 5 years. Figure 7 shows north-south and east-west sections of the production planning using the ICA approach.

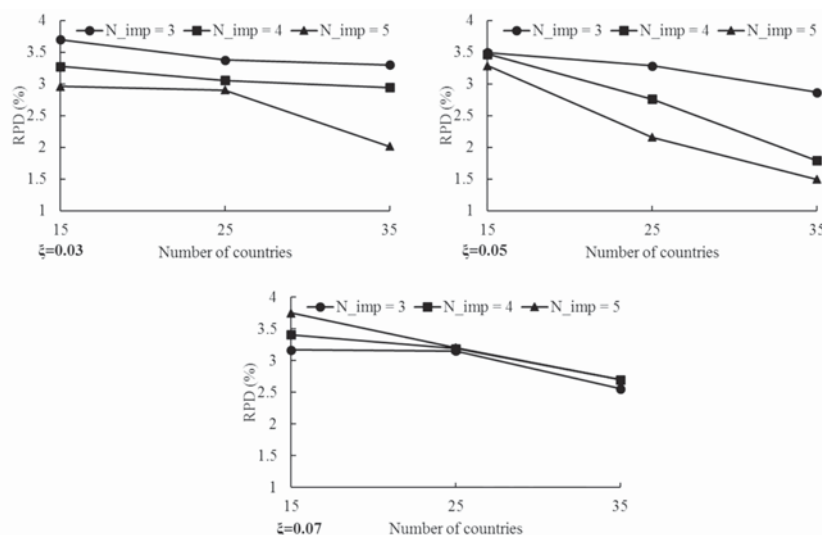


Figure 6—RPD for different values of N_{pop} and N_{imp} in $\xi = 0.03$, $\xi = 0.05$, and $\xi = 0.07$

Integration of commodity price uncertainty in long-term open pit mine production planning

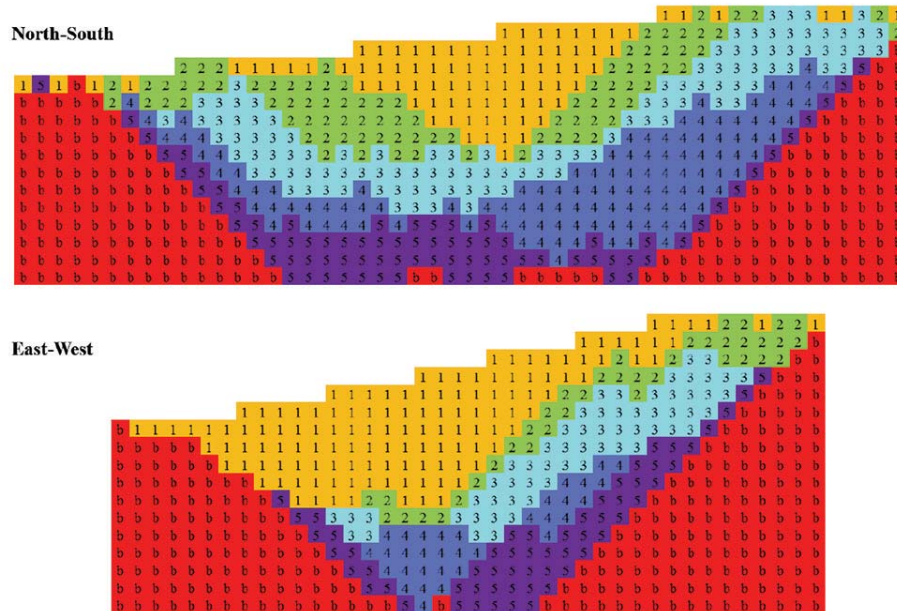


Figure 7—Sections of the copper mine production plan by ICA (the numbers are indicative of block extraction year)

Method	NPV (million \$)	RPD (%)	Number of blocks inside the UPL	Average grade of UPL (%)	CPU time (s)
ICA	622.465	5.1	12 205	0.304	8446
SIP	654.212		12 323	0.306	19 550

In order to compare the new ICA approach with stochastic integer programming methods (SIP), production planning was also performed by SIP. Table II compares the SIP and ICA approaches. It shows the CPU time of the ICA approach equals 8446 seconds, which is less than for the SIP method, and the small RPD shows the effectiveness of ICA in stochastic production planning of a real-world mine. All the numerical experiments were completed on an AMD Athlon (2.01 GHz) and 2.5 GB RAM running Windows 7.

Conclusion

Open pit mine production scheduling is difficult as there are a large number of blocks, with the future economic value of the blocks unknown at the time decisions are made. This results in a large-scale stochastic optimization problem. In this work, we proposed a meta-heuristic method based on an imperialist competitive algorithm to solve an important real-world problem that arises in surface mine planning, namely open pit mine production planning with commodity price uncertainty. The approach has been tested on a copper mine. By comparing ICA with the more commonly used stochastic integer programming method, it was shown that the proposed ICA method can produce good quality robust solutions with low RPD and CPU time for mine stochastic production planning.

References

- ABDEL SABOUR, S.A., DIMITRAKOPOULOS, R.G., and KUMRAL, M. 2008. Mine design selection under uncertainty. *Mining Technology*, vol. 117, no. 2. pp. 53–64.
- ABDEL SABOUR, S.A. and POULIN, R. 2010. Mine expansion decisions under uncertainty. *International Journal of Mining, Reclamation and Environment*, vol. 24, no. 4. pp. 340–349.
- ALBOR CONSUEGRA, F.R. and DIMITRAKOPOULOS, R. 2009. Stochastic mine design optimisation based on simulated annealing: pit limits, production schedules, multiple orebody scenarios and sensitivity analysis. *Mining Technology*, vol. 118, no. 2. pp. 79–90.
- ARDALAN, ZANIAR, KARIMI, SAJAD, POURSABZI, Omid, and NADERI, B., 2015. A novel imperialist competitive algorithm for generalized traveling salesman problems. *Applied Soft Computing*, vol. 26. pp. 546–555.
- ASAD, M.W.A. and DIMITRAKOPOULOS, R. 2012. Implementing a parametric maximum flow algorithm for optimal open pit mine design under uncertain supply and demand. *Journal of the Operational Research Society*, vol. 64, no. 2. pp. 185–197.
- ASAD, M.W.A., DIMITRAKOPOULOS, R., and VAN ELDERT, J. 2014. Stochastic production phase design for an open pit mining complex with multiple processing streams. *Engineering Optimization*, vol. 46, no. 8. pp. 1139–1152.
- ASAD, M.W.A. and DIMITRAKOPOULOS, R. 2013. Implementing a parametric maximum flow algorithm for optimal open pit mine design under uncertain supply and demand. *Journal of the Operational Research Society*, vol. 64, no. 2. pp. 185–197.

Integration of commodity price uncertainty in long-term open pit mine production planning

- ATASHPAZ-GARGARI, E. and LUCAS, C. 2007. Imperialist competitive algorithm: an algorithm for optimization inspired by imperialistic competition. *Proceedings of the IEEE Congress on Evolutionary Computation (CEC 2007)*, Singapore, 25–28 September. IEEE, New York.
- BEHNAMIAN, J. and ZANDIEH, M. 2011. A discrete colonial competitive algorithm for hybrid flowshop scheduling to minimize earliness and quadratic tardiness penalties. *Expert Systems with Applications*, vol. 38, no. 12. pp. 14490–14498.
- BOLAND, N., DUMITRESCU, I., FROYLAND, G., and GLEIXNER, A.M. 2009. LP-based disaggregation approaches to solving the open pit mining production scheduling problem with block processing selectivity. *Computers & Operations Research*, vol. 36, no. 4. pp. 1064–1089.
- CACCETTA, L. and HILL, S.P. 2003. An application of branch and cut to open pit mine scheduling. *Journal of Global Optimization*, vol. 27, no. 2-3. pp. 349–365.
- CHATTERJEE, S., SETHI, M.R., and ASAD, M.W.A. 2016. Production phase and ultimate pit limit design under commodity price uncertainty. *European Journal of Operational Research*, vol. 248, no. 2. pp. 658–667.
- DAGDELEN, K. 2001. Open pit optimization-strategies for improving economics of mining projects through mine planning. *Proceedings of the 17th International Mining Congress and Exhibition of Turkey (IMCET2001)*, Ankara, Turkey, 19–22 June 2001. Chamber of Mining Engineers of Turkey. https://s3.amazonaws.com/academia.edu.documents/30191663/1259a0cb2431834_ek.pdf?AWSAccessKeyId=AKIAIWOWYYGZ2Y53UL3A&Expires=1519570263&Signature=1Fys8Kk4TjhehXNqZsaiOE6eNY%3D&response-content-disposition=inline%3B%20filename%3DOpen_pit_optimization_strategies_for_imp.pdf
- DAGDELEN, K. and JOHNSON, T.B. 1986. Optimum open pit mine production scheduling by Lagrangian parameterization. *Proceedings of the 19th International Symposium on Application of Computers and Operations Research in the Mineral Industry (APCOM '86)*. SME, Littleton, CO. pp. 127–142. USA.
- DENBY, B. and SCHOFIELD, D. 1995. Inclusion of risk assessment in open pit design and scheduling. *Transactions of the Institution of Mining and Metallurgy. Section A. Mining Industry*, vol. 104. pp. A67–A71.
- DENBY, B. and SCHOFIELD, D. 1994. Open-pit design and scheduling by use of genetic algorithms. *Transactions of the Institution of Mining and Metallurgy. Section A. Mining Industry*, vol. 103. pp. A21–A26.
- DIMITRAKOPOULOS, R., MARTINEZ, L., and RAMAZAN, S. 2007. A maximum upside / minimum downside approach to the traditional optimization of open pit mine design. *Journal of Mining Science*, vol. 43, no. 1. pp. 73–82.
- DIMITRAKOPOULOS, R. and RAMAZAN, S. 2008. Stochastic integer programming for optimising long term production schedules of open pit mines: methods, application and value of stochastic solutions. *Mining Technology*, vol. 117, no. 4. pp. 155–160.
- DIMITRAKOPOULOS, R., FARRELLY, C., and GODOY, M. 2002. Moving forward from traditional optimization: grade uncertainty and risk effects in open-pit design. *Mining Technology*, vol. 111, no. 1. pp. 82–88.
- DIXIT, V.K. and PINDYCK, R.S. 1994. *Investment under Uncertainty*. Princeton University Press.
- DORIGO, M., BIRATTARI, M., and STÜTZLE, T. 2006. Ant colony optimization. *Computational Intelligence Magazine*, vol. 1, no. 4. pp. 28–39.
- ELKINGTON, T. and DURHAM, R. 2011. Integrated open pit pushback selection and production capacity optimization. *Journal of Mining Science*, vol. 47, no. 2. pp.177–190.
- GILANI, S-O. and SATTARVAND, J. 2016. Integrating geological uncertainty in long-term open pit mine production planning by ant colony optimization. *Computers & Geosciences*, vol. 87. pp. 31–40.
- HAQUE, MD.A., TOPAL, E., and LILFORD, E. 2014. A numerical study for a mining project using real options valuation under commodity price uncertainty. *Resource Policy*, vol. 39. pp. 115–123.
- INDEXMUNDI. 2018. Copper, grade A cathode, LME spot price. World Bank. <http://www.indexmundi.com/commodities/?commodity=copper&months=300>
- JOHNSON, T.B.1968. Optimum open-pit mine production scheduling. PhD thesis, Berkeley University.
- KHABBAZI, A., ATASHPAZ-GARGARI, E., and LUCAS, C. 2009. Imperialist competitive algorithm for minimum bit error rate beamforming. *International Journal of Bio-Inspired Computation*, vol. 1, no. 1-2. pp. 125–133.
- KHAN, A. and NIEMANN-DELIUS, C. 2014. Production scheduling of open pit mines using particle swarm optimization algorithm. *Advances in Operations Research*, 2014, no. 1. pp. 1–9.
- KUMRAL, M. 2010. Robust stochastic mine production scheduling. *Engineering Optimization*, vol. 42, no. 6. pp. 567–579.
- LAMGHARI, A. and DIMITRAKOPOULOS, R. 2012. A diversified Tabu search approach for the open-pit mine production scheduling problem with metal uncertainty. *European Journal of Operational Research*, vol. 222, no. 3. pp. 642–652.
- LIAN, K., ZHANG, C., GAO, L., and SHAO, X. 2012. A modified colonial competitive algorithm for the mixed-model U-line balancing and sequencing problem. *International Journal of Production Research*, vol. 50, no. 18. pp. 5117–5131.
- MACAVOY, P.W. 1988. Explaining metals prices: economic analysis of metals markets in the 1980s and 1990s. *Rochester Studies in Managerial Economics and Policy*. Brunner, K. (ed.). Kluwer Academic, Boston.
- MARCOTTE, D. and CARON, J. 2013. Ultimate open pit stochastic optimization. *Computers & Geosciences*, vol. 51. pp. 238–246.
- MAROUFMASHAT, A., SAYEDIN, F., and KHAVAS, S.S. 2014. An imperialist competitive algorithm approach for multi-objective optimization of direct coupling photovoltaic-electrolyzer systems. *International Journal of Hydrogen Energy*, vol. 39, no. 33. pp. 18743–18757.
- MOOSAVI, E., GHOLAMNEJAD, J., ATAEE-POUR, M., and KHORRAM, E. 2014. Improvement of Lagrangian relaxation performance for open pit mines constrained long-term production scheduling problem. *Journal of Central South University*, vol. 21, no. 7. pp. 2848–2856.
- MORTAZAVI, A., KHAMSEH, A.A., and NADERI, B. 2015. A novel chaotic imperialist competitive algorithm for production and air transportation scheduling problems. *Neural Computing and Applications*, vol. 26, no. 7. pp. 1709–1723.
- NAZARI-SHIRKOUHI, S., EIVAZY, H., GHODSI, R., REZAEI, K., and ATASHPAZ-GARGARI, E. 2010. Solving the integrated product mix-outsourcing problem using the imperialist competitive algorithm. *Expert Systems with Applications*, vol. 37, no. 12. pp. 7615–7626.
- PINDYCK, R.S. and RUBINFELD, D.L. 1998. *Econometric Models and Economic Forecasts*. vol. 4. Irwin/McGraw-Hill, Boston.
- SADAEI, H.J., ENAYATIFAR, R., LEE, M.H., and MAHMUD, M. 2016. A hybrid model based on differential fuzzy logic relationships and imperialist competitive algorithm for stock market forecasting. *Applied Soft Computing*, vol. 40. pp. 132–149.
- SATTARVAND, J. and NIEMANN-DELIUS, C. 2009. Long-term open-pit planning by ant colony optimization. PhD thesis, Institut für Bergbaukunde III, RWTH Aachen University.
- SCHWARTZ, E.S. 1997. The stochastic behavior of commodity prices: Implications for valuation and hedging. *Journal of Finance*, vol. 52, no. 3. pp. 923–973.
- SHARIFI, M.A. AND MOJALLALI, H. 2015. A modified imperialist competitive algorithm for digital IIR filter design. *Optik - International Journal for Light and Electron Optics*, vol. 126, no. 21. pp. 2979–2984.
- SHISHVAN, M.S. and SATTARVAND, J. 2015. Long term production planning of open pit mines by ant colony optimization. *European Journal of Operational Research*, vol. 240, no. 3. pp. 825–836.
- SHOKROLLAHPUR, E., ZANDIEH, M., and DORRI, B. 2011. A novel imperialist competitive algorithm for bi-criteria scheduling of the assembly flowshop problem. *International Journal of Production Research*, vol. 49, no. 11. pp. 3087–3103.
- WANG, Q. and SEVIM, H. 1992. Enhanced production planning in open pit mining through intelligent dynamic search. *Proceedings of the 23rd International Symposium on Application of Computers and Operations Research in the Mineral Industry*, Tucson, AZ. Society for Mining, Metallurgy and Exploration, Littleton, CO. pp. 461–471. ◆



Accounting for a spatial trend in fine-scale ground-penetrating radar data: a comparative case study

by Y. Dagasana*, O. Erten*, and E. Topal†

Synopsis

In geostatistics, one of the challenges is to account for the spatial trend that is evident in a data-set. Two well-known kriging algorithms, namely universal kriging (UK) and intrinsic random function of order k (IRF- k), are mainly used to deal with the trend apparent in the data-set. These two algorithms differ in the way they account for the trend and they both have different advantages and drawbacks. In this study, the performances of UK, IRF- k , and ordinary kriging (OK) methods are compared on densely sampled ground-penetrating radar (GPR) data acquired to assist in delineation of the ore and waste contact within a laterite-type bauxite deposit. The original GPR data was first pre-processed to generate prediction and validation data-sets in order to compare the estimation performance of each kriging algorithm. The structural analysis required for each algorithm was carried out and the resulting variograms and generalized covariance models were verified through cross-validation. The variable representing the elevation of the ore unit base was then estimated at the unknown locations using the prediction data-set. The estimated values were compared against the validation data using mean absolute error (MAE) and mean squared error (MSE) criteria. The results show although IRF- k slightly outperformed OK and UK, all the algorithms produced satisfactory and similar results. MSE values obtained from the comparison with the validation data were 0.1267, 0.1322, and 0.1349 for IRF- k , OK, and UK algorithms respectively. The similarity in the results generated by these algorithms is explained by the existence of a large data-set and the chosen neighbourhood parameters for the kriging technique.

Keywords

ground-penetrating radar, geostatistics, nonstationarity, universal kriging, ordinary kriging, intrinsic random function of order k .

Introduction

In the geological modelling of the laterite-type deposits, the exploration boreholes may be sparsely spaced for two major reasons: (1) the attributed grades do not tend to vary significantly across the deposit; (2) the overall exploration costs must be minimized. However, since the geological contact between the ore and underlying waste unit fluctuates in a rather complex manner, one should not rely solely on the interpolation of the sparsely-spaced borehole data, as the estimates would not reflect the actual variability in the surface. Therefore, it is imperative that the sparsely-spaced borehole data be supplemented with appropriate geophysical information for more accurate resource estimations (Erten *et al.*, 2015, 2013). Ground-penetrating radar (GPR) has widely been used to acquire a

complementary dense data-set to better delineate the interface between two geological units (bauxite/ferricrete) (Francke and Nobes 2000; Francke and Parkinson 2000; Watts 1997). Due to the tropical weathering and leaching mechanisms that generate laterite-type deposits, the geological interface measured through GPR appears to be well correlated with the easting (X) and northing (Y) coordinates of the surface, which indicates the presence of a spatial trend (McLennan, Ortiz, and Deutch, 2006; Leuangthong, Lyall, and Deutsch, 2002). Geostatistical techniques are the main tools which are used to estimate the elevation of the interface at non-sampled locations, and there are different approaches used to account for the trend in a data-set. In this paper, we estimate the elevation of the geological interface through ordinary kriging (OK), universal kriging (UK), intrinsic random function of order k (RF- k) methods and compare the estimation performances.

Geostatistical techniques are based on the theory of regionalized variables (RVs) and are used to estimate an attribute of interest at non-sampled locations (Goovaerts, 1997; Journel and Huijbregts, 1978). The idea behind the theory is that a RV $Z(\mathbf{u}_\alpha), \{\alpha=1, \dots, n\}$ is considered to be the realization of an order-two random function (RF) $Z(\mathbf{u})$ and is assumed to have been generated according to a probability density function (Matheron, 1971; Olea, 1974). Due to this characteristic of the RV, there is a spatial correlation between the samples, which allows the prediction of $Z^*(\mathbf{u})$ at each non-sampled location \mathbf{u} . The prediction of $Z^*(\mathbf{u})$ requires the covariance function $C(\mathbf{h})$ of $Z(\mathbf{u})$ to be known, and this statistical inference can practically be made from an available realization if the realization

* Mining and Metallurgical Engineering Department, WA School of Mines, Curtin University, Kalgoorlie, WA, Australia.

† School of Mining and Geosciences, Nazarbayev University, Astana, Kazakhstan.

© The Southern African Institute of Mining and Metallurgy, 2018. ISSN 2225-6253. Paper received Apr. 2016; revised paper received Aug. 2017.

Accounting for a special trend in fine-scale ground-penetrating radar data

exhibits stationary characteristics. If there is a trend in the realization/data-set and the realization exhibits nonstationary characteristics, the change in the value of RV is no longer dependent on the lag distance \mathbf{h} , but is also dependent on the location of the RV. In the case of a nonstationarity, there are basically two geostatistical methods to account for the trend in the data-set: universal kriging and intrinsic random function of order k (IRF- k). These two methods differ in the way they detect the trend and the type of structural function used to describe the spatial relationship.

In order to estimate the value of an attribute at a non-sampled location, the kriging algorithm requires the computation of a system of equations with a known variogram $\gamma(\mathbf{h})$. The problem with UK arises when the underlying variogram or covariance function is not known. In UK, the RF $Z(\mathbf{u})$ is comprised of a trend $m(\mathbf{u})$ and a residual $R(\mathbf{u})$ component. The variogram of residuals can be used to calculate the underlying variogram, but this requires the determination of the trend component $m^*(\mathbf{u})$. Calculation of $m^*(\mathbf{u})$, on the other hand, requires the variogram to be known. One solution to this circular problem is refining both the variogram and the trend estimates iteratively, as mentioned in Neuman and Jacobson (1984). However, it has some associated drawbacks, such as underestimation of the underlying variogram and extreme difficulties in determining the degree of trend or the underlying variogram from the residuals (Armstrong, 1984; Cressie, 1993). Another solution to these problems exists if there is a particular direction or subzone where there is a sub-stationary zone in a nonstationary data-set. Journel and Rossi (1989) proposed that experimental variograms inferred in these directions or subzones can be used to estimate the trend optimally. Chilès (1976) gives an example of such practice assuming an isotropic variogram model computed from the sample variogram in stationary directions or subzones.

IRF- k was introduced by Matheron (1973) due to the practical difficulties in the application of the UK approach. It basically decomposes the trend and covariance structure through increments of a sufficient order to filter out the trend and to achieve stationarity (Chiles and Delfiner, 2012). The kriging system of the IRF- k method is identical to the UK method except that the variogram employed in UK is replaced by the generalized covariance (GC) in the IRF- k method. Contrary to UK, where the trend is required to be estimated beforehand as a linear combination of known, linearly independent functions to obtain the stationary residuals, nonstationarity in IRF- k is accounted for through the calculation of the GC. The advantage of using GC is that it has wider class of admissible functions compared to the variogram and the automatic detection of the parameters of GC makes the application easier (Delhomme, 1978). On the other hand, the use of GC creates some hurdles in practical modelling since the method requires identification of the order k and it is difficult to interpret the GC (Cressie, 1993). Both UK and IRF- k methods have advantages and disadvantages and as a result, the choice between the two methods is based heavily on the practical difficulties of fitting functions (Buttafuoco and Castrignano, 2005). Christensen (1990) states that the IRF- k and UK are identical provided that the GC is identified correctly.

UK, IRF- k , and OK have been compared in several publications. Journel and Rossi (1989) compared OK and UK in a case study in which they regionalized seam thickness and coal quality variables. The results indicated that the OK and UK methods gave similar results. It was also concluded that any kriging algorithm with moving data windows is equal to considering a nonstationary random function model with a mean re-estimated at each new location. Similarly, Zimmerman *et al.* (1999) compared the performances of four interpolation algorithms, two of which were OK and UK. They stated that although UK was expected to outperform OK in situations where trends exist, OK performed slightly better than UK. Odeh, McBratney, and Chittleborough (1994) modelled soil variables by using different interpolation methods, and stated that OK was the most inferior of all the methods implemented, including UK. Odeh, McBratney, and Slater (1997) compared the performance of several prediction models, including OK and IRF- k , in prediction of soil parameters. The IRF- k method performed slightly better than OK. It is therefore apparent that the performance ranking of UK, IRF- k , and OK algorithms varies between different investigations.

The objective of this study is to predict the variability in elevation of the base of the ore unit and compare the performance of different kriging estimators using densely sampled GPR data. The contribution of this paper is the implementation of, and comparison of, the performance of, different kriging algorithms in the case of a bauxite laterite deposit. This was mainly done in order to ascertain which kriging algorithm is more suitable for bauxite base elevation data with a spatial trend. Since GPR data represents the elevation of an interface surface, nonstationarity was intuitively expected. This was also confirmed by the omnidirectional variograms computed in the initial data analysis. The omnidirectional variograms revealed the existence of nonstationarity in the prediction data-set, requiring handling of the trend by UK and IRF- k methods. Therefore, these methods were employed to account for the spatial trend in the data-set along with the OK algorithm, which considers the spatial trend to be constant. In order to evaluate the performances of each kriging algorithm, GPR data representing the elevation was resampled to form validation and prediction data-sets. The validation data-set was used to assess the performance of the UK, IRF- k , and OK estimators.

General review of methods

Geostatistical theory

The RF can be represented by the following model:

$$Z(\mathbf{u}) = m(\mathbf{u}) + R(\mathbf{u}) \quad [1]$$

where $m(\mathbf{u})$ represents the trend component and $R(\mathbf{u})$ represents the random part having a covariance function in two-dimensional space $\mathbf{u}=(x,y)$. The covariance $C(\mathbf{h})$ is defined as the following:

$$C(\mathbf{h}) = E[R(\mathbf{u})R(\mathbf{u} + \mathbf{h})] \quad [2]$$

where \mathbf{h} is the lag distance. Considering the second-order

Accounting for a special trend in fine-scale ground-penetrating radar data

stationarity assumption, $R(\mathbf{u})$ is assumed to have a zero mean value and the trend $m(\mathbf{u})$ is assumed to be constant (Oliver and Webster, 2015). Hence, $C(\mathbf{h})$ is equal to:

$$C(\mathbf{h}) = E [Z(\mathbf{u})Z(\mathbf{u}+\mathbf{h}) - m(\mathbf{u})^2] \quad [3]$$

In situations where the mean is not constant, the covariance cannot exist. In these cases, the assumption of stationarity is weakened to the one called *intrinsic stationarity* (Matheron, 1963), where the expected differences $E[Z(\mathbf{u}+\mathbf{h})-Z(\mathbf{u})]$ are equal to zero and the covariance of the random part, which is used to measure the spatial relations of the residuals, is replaced by the variance of the differences:

$$Var[Z(\mathbf{u}+\mathbf{h})-Z(\mathbf{u})] = E[\{Z(\mathbf{u}+\mathbf{h})-Z(\mathbf{u})\}^2] = 2\gamma(\mathbf{h}) \quad [4]$$

where $\gamma(\mathbf{h})$ represents the variogram at lag \mathbf{h} . The following relationship between the variogram $\gamma(\mathbf{h})$ and covariance $C(\mathbf{h})$ function exists for a RF which is second-order stationary:

$$\gamma(\mathbf{h}) = C(\mathbf{0}) - C(\mathbf{h}) \quad [5]$$

where $C(\mathbf{0})$ represents the variance σ^2 of the RF.

Ordinary kriging (OK)

In OK, the RV is estimated at an unsampled location \mathbf{u} as a linear combination of available neighbouring data $\{Z(\mathbf{u}_\alpha), \alpha=1, \dots, n\}$ (Goovaerts, 2000).

$$Z^*_{OK}(\mathbf{u}) = \sum_{\alpha=1}^n \lambda_{\alpha}^{OK} Z(\mathbf{u}_\alpha) \quad [6]$$

As with all kriging algorithms, the objective of OK is to minimize the estimation variance as well as ensure the unbiasedness of the estimator. OK weights $\lambda_{\beta}(\mathbf{u})$ are determined to satisfy this unbiasedness and minimized variance goals. The following OK system is used to obtain the kriging weights:

$$\begin{cases} \sum_{\beta=1}^n \lambda_{\beta}^{OK} \gamma(\mathbf{u}_\alpha - \mathbf{u}_\beta) - \mu_{OK}(\mathbf{u}) = \gamma(\mathbf{u}_\alpha - \mathbf{u}) & \alpha = 1, \dots, n \\ \sum_{\beta=1}^n \lambda_{\beta}^{OK}(\mathbf{u}) = 1 \end{cases} \quad [7]$$

where $\mu(\mathbf{u})$ represents the Lagrange parameter used to minimize the variance. The only information needed for the OK system is the variogram value corresponding to every lag distance \mathbf{h} . The kriging variance of OK is calculated by:

$$\sigma_{OK}^2(\mathbf{u}) = C_R(\mathbf{0}) - \sum_{\alpha=1}^n \lambda_{\alpha}^{OK}(\mathbf{u}) C(\mathbf{u}_\alpha - \mathbf{u}) - \mu_{OK}(\mathbf{u}) \quad [8]$$

Universal kriging (UK)

In UK, the trend component is modelled as a smoothly varying deterministic function of \mathbf{u} and is expressed as:

$$m(\mathbf{u}) = \sum_{l=0}^L a_l f_l(\mathbf{u}) \quad \text{for } l = 0, \dots, L \quad [9]$$

where $m(\mathbf{u})$ represents the local mean, a_l , the unknown coefficients of the trend function, and $f_l(\mathbf{u})$ represent the known functions of the coordinates \mathbf{u} and are called *trial* or

base functions (Kitanidis, 1997; Rossi and Deutsch, 2014). The residual component $R(\mathbf{u})$ is modelled as a second-order stationary RF with a zero-mean, $E[Z(\mathbf{u})]=0$. Combining the trend and the residual, the RV is represented by the following equation:

$$Z(\mathbf{u}) = \sum_{l=0}^L a_l f_l(\mathbf{u}_\alpha) + R(\mathbf{u}) \quad [10]$$

The trend can be modelled as a low-order polynomial function of the spatial coordinates \mathbf{u} . Previous studies have indicated that increasing the number of order of trend functions does not lead to better modelling of the trend (Journel and Rossi, 1989).

To satisfy the unbiasedness condition $E[Z^*(\mathbf{u})-Z(\mathbf{u})]=0$, Equation [9] can be rewritten as:

$$\sum_{\alpha=1}^n \lambda_{\alpha}^{UK} f_l(\mathbf{u}_\alpha) = f_l(\mathbf{u}) \quad \text{for } l = 0, \dots, L \quad [11]$$

where the set of L constraints is termed the *universality* or *unbiasedness conditions*. The kriging system satisfying these requirements is then defined by:

$$\begin{cases} \sum_{\beta=1}^n \lambda_{\beta}^{UK} C(\mathbf{u}_\alpha - \mathbf{u}_\beta) + \sum_{l=0}^L \mu_l^{UK} f_l(\mathbf{u}_\alpha) = C(\mathbf{u}_\alpha - \mathbf{u}) & \alpha = 1, \dots, n \\ \sum_{\beta=1}^n \lambda_{\beta}^{UK} = 1 \\ \sum_{\beta=1}^n \lambda_{\beta}^{UK} f_l(\mathbf{u}_\beta) = f_l(\mathbf{u}) & l = 0, \dots, L \end{cases} \quad [12]$$

where λ_{β} are the UK weights and μ_l are the Lagrange parameters used to determine the coefficients λ_{β} minimizing the error variance.

The UK estimate variance is defined as:

$$\sigma_{UK}^2(\mathbf{u}) = C_R(\mathbf{0}) - \sum_{\alpha=1}^n \lambda_{\alpha}^{UK}(\mathbf{u}) C_R(\mathbf{u}_\alpha - \mathbf{u}) - \sum_{k=0}^K \mu_k^{UK}(\mathbf{u}) f_k(\mathbf{u}) \quad [13]$$

The inference of the residual variogram $\gamma_R(\mathbf{h})$ is, however, not straightforward, as the only available data is in fact Z values, not R values. The experimental variogram of Z values is defined by:

$$\begin{aligned} 2\gamma(\mathbf{h}) &= E\{[Z(\mathbf{u}) - Z(\mathbf{u}+\mathbf{h})]^2\} \\ &= E\{[R(\mathbf{u}) + m(\mathbf{u}) - R(\mathbf{u}+\mathbf{h}) - m(\mathbf{u}+\mathbf{h})]^2\} \\ &= 2\gamma_R(\mathbf{h}) + [m(\mathbf{u}) - m(\mathbf{u}+\mathbf{h})]^2 \end{aligned} \quad [14]$$

For UK, the underlying (trend-free) variogram is assumed to be known (Armstrong, 1984). To predict this variogram, the form of the trend should be known. However, to estimate the form of the trend, the variogram must be known. Various approaches have been developed to resolve this circular problem. The most common approach is to select a direction or a subzone in which the trend $m(\mathbf{u})$ can be negligible and calculating the experimental covariance along these selected directions or within this subzone (Atkinson and Lloyd, 2007; Chihi *et al.*, 2000; Journel and Rossi, 1989; Myers, 1989).

Intrinsic random function of order k (IRF- k)

Intrinsic random function of order k was developed by Matheron (1973) and later refined by Delfiner (1976). It is an alternative tool used in nonstationary data to remove the trend by filtering out the low-order polynomials and is commonly used when it is difficult to infer the underlying

Accounting for a special trend in fine-scale ground-penetrating radar data

variogram of the variable of interest (Wackernagel, 2002). In the IRF- k method, the deterministic functions $f_l(\mathbf{u})$ used to represent the trend model $m(\mathbf{u})$ in Equation [9] are restricted to those which are only translation-invariant and pairwise orthogonal (Wackernagel, 2002).

Considering a set of weights λ_{α} applied to particular points \mathbf{u}_{α} , a discrete measure \mathbf{u}_{α} is defined as:

$$\lambda = \sum_{\alpha=1}^n \lambda_{\alpha} \delta_{\mathbf{u}_{\alpha}} \quad [15]$$

where $\delta_{\mathbf{u}_{\alpha}}$ represents the Dirac measure at point \mathbf{u}_{α} . Any linear combinations of the weights with RV at locations \mathbf{u}_{α} are defined as:

$$Z(\lambda) = \sum_{\alpha=0}^n \lambda_{\alpha} Z(\mathbf{u}_{\alpha}) \quad [16]$$

The expression shown in Equation [16] is called the allowable linear combination of order k (ALC- k) in Equation [17]

$$\sum_{\alpha=0}^n \lambda_{\alpha} f_l(\mathbf{u}_{\alpha}) = 0 \text{ for } l = 0, \dots, L \quad [17]$$

holds true for all monomials of order $\leq k$. Considering a nonstationary $Z(\mathbf{u})$, if the expression given in Equation [16] is second-order stationary regardless of any translation \mathbf{h} and whatever the ALC- k λ , the RV $Z(\mathbf{u})$ is called as IRF- k .

The variogram in IRF- k is replaced by a new function called the GC function (Chiles and Delfiner, 2012). GC is denoted by $K(\mathbf{h})$ and is used to describe the correlation structure of the random part $R(\mathbf{u})$. The GC function of an IRF- k is a symmetric function, $K(\mathbf{h})=K(-\mathbf{h})$, and satisfies the condition:

$$C(\mathbf{u}_{\alpha} - \mathbf{u}_{\beta}) = \sum_{\alpha=1}^n \sum_{\beta=1}^n \lambda_{\alpha} \lambda_{\beta} K(\mathbf{u}_{\alpha} - \mathbf{u}_{\beta}) \quad [18]$$

An example to GC function is known the as *polynomial generalized covariance function*. The equation of the polynomial generalized covariance function is given as:

$$K(\mathbf{h}) = \sum_{p=0}^k (-1)^{p+1} b_p |\mathbf{h}|^{2p+1} \quad [19]$$

The conditions on b_p are satisfied if $b_p \leq 0 \forall p$.

The intrinsic kriging system minimizing the variance is expressed in terms of the GC and shown in the following:

$$\begin{cases} \sum_{\beta=1}^n \lambda_{\beta} K(\mathbf{u}_{\alpha} - \mathbf{u}_{\beta}) - \sum_{l=0}^k \mu_l f_l(\mathbf{u}_{\alpha}) = K(\mathbf{u}_{\alpha} - \mathbf{u}) & \alpha = 1, \dots, n \\ \sum_{\beta=1}^n \lambda_{\beta} f_l(\mathbf{u}_{\beta}) = f_l(\mathbf{u}) & l = 0, \dots, L \end{cases} \quad [20]$$

The estimation variance is defined by:

$$\sigma^2(\mathbf{u}) = K(\mathbf{0}) - \sum_{\alpha=1}^n \lambda_{\alpha} K(\mathbf{u}_{\alpha} - \mathbf{u}) + \sum_{k=0}^K \mu_k (\mathbf{u}) f_k(\mathbf{u}) \quad [21]$$

Case study

Geological setting

The region where the mine site is located is composed of Proterozoic and Palaeozoic basement in the eastern part. This basement comprises acid intrusives, extrusives, and metamorphics. Overlying the basement to the west, Mesozoic and Cenozoic sediments dominate. The sediments were

intensively weathered, which played a crucial role in the formation of laterites rich in alumina and bauxites. The bauxite sits above an almost entirely kaolinized pallid zone (Morgan, 1992).

The bauxite deposit in the mine area is thought to have formed from *in-situ* chemical weathering of kaolinite, quartz, and iron oxide minerals (Loughnan and Bayliss, 1961). The occurrence of the alumina-rich was horizon controlled by climate, vegetation cover, chemical conditions, bedrock composition and texture, groundwater circulation, relief, time, and tectonic conditions (Gow and Lozej, 1993). There is a regolith zone in the mine area comprising, from top to bottom, post-weathering sediments (red soil), bauxitic cement, pisolitic bauxite, nodular ferricrete, the kaolinite zone, and the saprolitic zone (Bardossy and Aleva 1990).

The GPR survey

An electromagnetic (EM) wave that travels through shallow ground shows different responses to subsurface structures with varying electromagnetic properties such as dielectric permittivity, conductivity, and electromagnetic permeability. GPR utilizes the dielectric permittivity contrast that exists between the geological structures (ASTM D 6432-99 2005). The EM wave emitted into the ground from the transmitting antenna at the surface is reflected back when there is a difference in the electrical properties of the subsurface structures. This reflected wave is then received by a receiving antenna and recorded as a function of time (Davis and Annan, 1989). Being a function of depth, antenna spacing, and average radar-wave velocity, the time taken for the wave to travel to the interface and back up to the surface is called the *two-way travel time*. Knowing the radar wave velocities, this two-way travel time is then converted into depth.

Selection of GPR method to map the lateral variability at the mine site

The main aim of the survey was to map the lateral variability at the bauxite/ferricrete interface. As the area to be surveyed was large (360 × 800 m), the method chosen needed to be easy to implement as well as provide fast data acquisition so that the surveying results could be checked immediately. Other considerations in selecting a suitable geophysical method were spatial resolution capability, cost-effectiveness, and data processing requirements (Erten, 2012).

In order to be sure about the applicability of the method selected, the petrophysical properties established in previous work on samples collected from another location within the mine site were considered. The laboratory results revealed that the conductivities of the bauxite and ferricrete are rather low and there is a dielectric permittivity contrast between the bauxite and the ferricrete. This indicated that the emitted waves would reflect from the bauxite interface, favouring the use of the GPR method.

The data

The mine area chosen in this case study is approximately 360 × 800 m in size. The data-set comprises the GPR pick-points acquired from the surface of the mine area using a radar device. The specifications of the radar device are given by Francke and Utsi (2009). The total areal coverage of the GPR survey at the mine area was 142 300 m² with GPR profiles

Accounting for a special trend in fine-scale ground-penetrating radar data

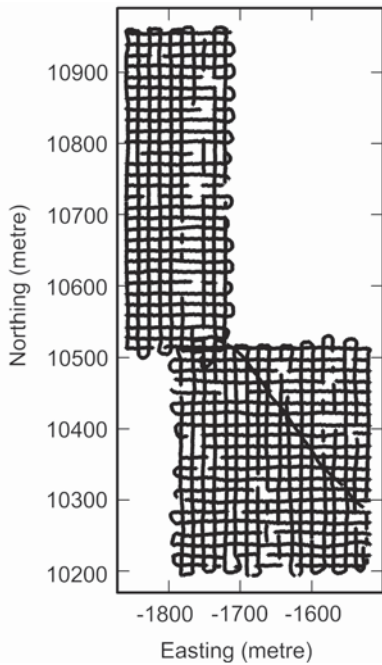


Figure 1—GPR pick-points collected from the mine area

17 940 m in length, which provided 64 670 GPR pick-points distributed along the GPR profiles at 0.25 m interval (Figure 1). The GPR profiles were arranged in a square grid with a line spacing of about 15 × 15 m (Erten, 2012).

Due to the nature of GPR data acquisition, it is expected that there might be multiple points that have the same coordinates. Therefore, the data-set was first pre-processed to mask the potential duplicates in order to avoid any kriging matrix instability in the estimation process. This was carried out by masking all the sample points that were within 0.25 m of the other data-points. The number of raw GPR pick-points, after processing, reduced to 30 630. In order to compare the performance of each kriging method, the data was split into two parts: prediction and validation data-sets. The prediction data-set was generated by re-sampling the GPR pick-points randomly on a regular 15 × 15 m grid. This process yielded 735 pick-points as a prediction/training data-set to be used in the estimation. The remaining 29 895 pick-points were kept for the validation. The flow chart of the data processing and the methodology are presented in Figure 2.

Exploratory data analysis

The target variable to be regionalized in this study is the

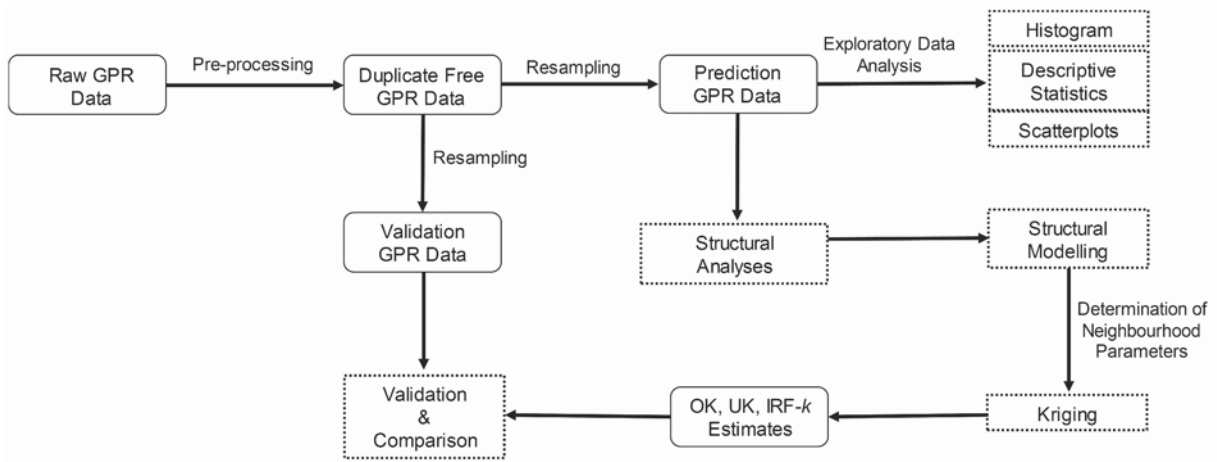


Figure 2—Pre-processing of the GPR data and the methodology

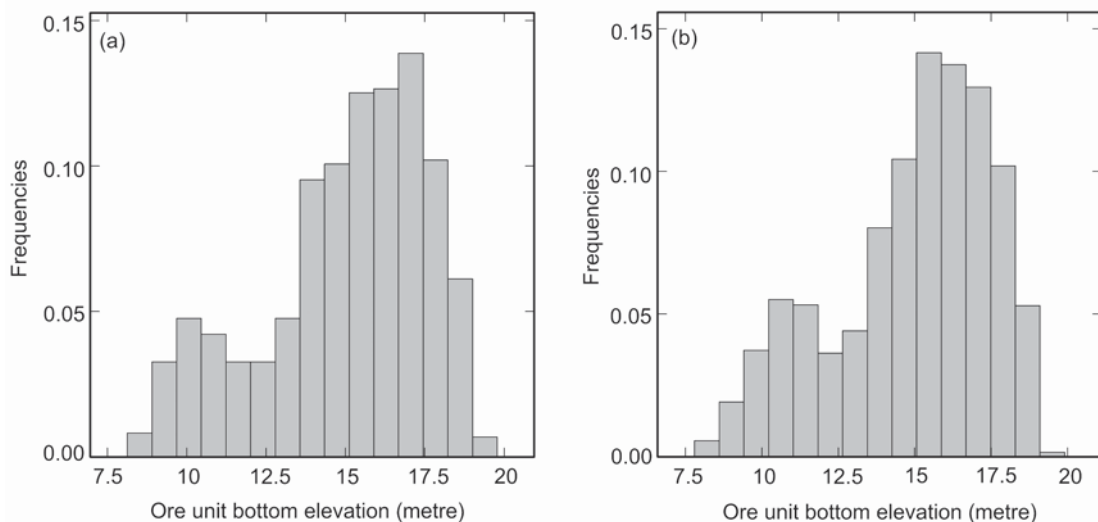


Figure 3—(a) Histograms of prediction GPR data-set and (b) the original raw GPR data

Accounting for a special trend in fine-scale ground-penetrating radar data

Table 1

Descriptive statistics of the GPR data for elevation of the ore unit base

Variable	Unit	Count	Mean	SD	Min.	Max.	CV
Ore unit base elevation prediction data	m	735	15.01	2.60	8.14	19.77	0.17
Ore unit base elevation original data	m	30,630	14.92	2.57	7.81	19.90	0.17

elevation of the bauxite/ferricrete interface. This variable was obtained through the GPR survey, the depth to the interface being calculated from the two-way travel time. This depth was then subtracted from the ground surface elevation to obtain the elevation of the bauxite/ferricrete interface. The unit of the variable is metres (m).

The histograms of both prediction and validation data corresponding to the elevations of the base of the ore unit are shown in Figure 3.

As it can be seen in Figure 3, the histograms of the prediction and validation data are closely similar. This resemblance is also revealed in the descriptive statistics of these two data-sets given in Table 1.

The calculated coefficients of skewness of the prediction/training and validation data-sets are -0.70 and -0.64 , respectively.

Scattergrams plotted against X and Y coordinates in Figure 4 reveals that the elevation variable decreases towards the east and increases towards the north, which suggests a possible trend dipping in southeasterly direction.

Structural analysis

The raw omnidirectional variograms of the ore unit base elevation were computed from the prediction data with 50 lags, having a lag distance of 15 m and a lag tolerance of 7.5 m. This lag distance was the average distance between the samples in the prediction data-set. The experimental omnidirectional variogram is shown in Figure 5.

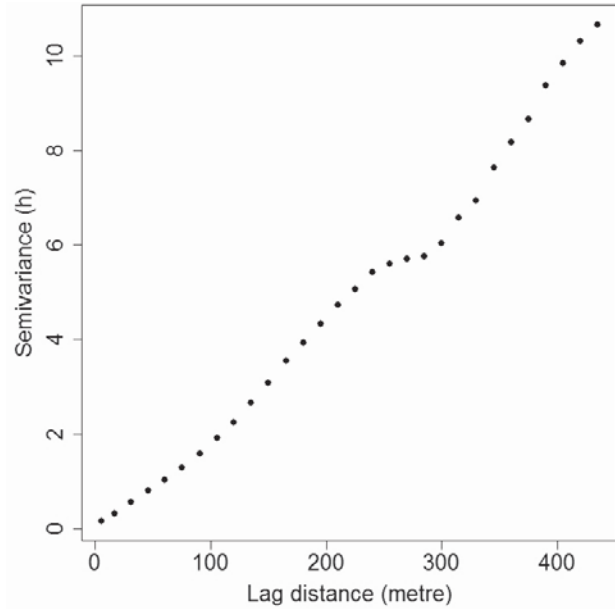


Figure 5—Omnidirectional variogram of prediction data

The apparent increase in the variogram parallel to the increasing lag distance also confirms the existence of a trend or nonstationarity of the elevation variable. This conclusion is supported by the scattergrams shown in Figure 4.

A variogram map was computed to detect the maximum and minimum spatial continuity directions as well as any possible anisotropies. The variogram map and experimental variograms in these directions are shown in Figure 6.

The maximum spatial continuity in the variogram map is seen in the $N20^\circ$ direction as the variogram values do not change significantly along this direction. On the other hand, perpendicular to this direction, which is $N110^\circ$, the elevation varies more rapidly, indicating the minimum spatial continuity direction. In the $N70^\circ$ direction, there are relatively high variogram values. As seen in Figure 6b, the variogram values in the $N70^\circ$ direction are higher only for the lag values

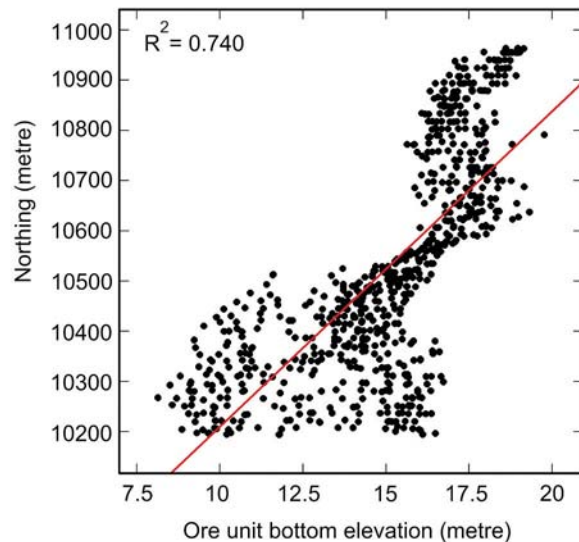
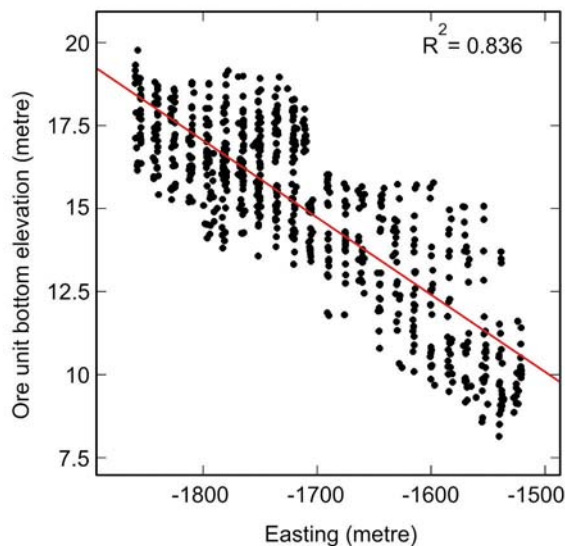


Figure 4—Elevation changes along X and Y coordinates

Accounting for a special trend in fine-scale ground-penetrating radar data

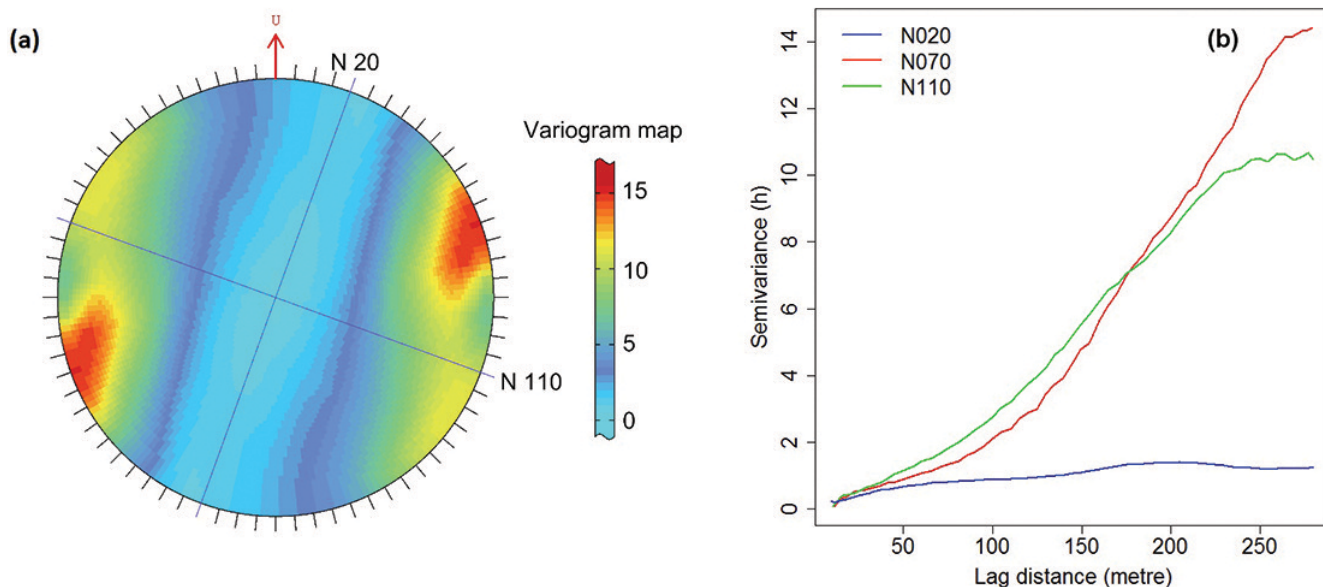


Figure 6—(a) Variogram map of the elevation variable (prediction-training data-set) and (b) experimental variograms in N20°, N70°, and N110° directions

greater than 180. Since the GPR data is densely sampled, only samples that are around 80–100 m apart from the estimation grid node are considered for the estimation and are of greatest importance. This fact confirms the selection of the N110° direction as the minimum spatial continuity direction, since the experimental variogram values in the N110° direction are higher in the 0–100 lag distance range.

Structural modelling for UK

UK was the first approach used in this study to account for the nonstationarity seen in the data. UK requires a prior determination of the L trend functions $F_L(\mathbf{u})$ and the covariance $C_R(\mathbf{h})$ of the residual component $R(\mathbf{u})$ inferred from the residual variogram $\gamma_R(\mathbf{h})$ (Goovaerts, 1997). The L trend functions were identified by testing low-order polynomial functions, $k \leq 2$, by locally fitting the polynomial functions through the ordinary least-squares method. The trend component identification of the elevation variable is summarized in Table II.

In order to identify the order k of the trend component, the degree of trend, a number of varying orders of polynomials were selected and fitted to the data-points. In this process, errors obtained from the fitting of different orders of k polynomials are calculated at each point and ranked by order of absolute magnitude. The ranks obtained from each point are then averaged and the order k having the lowest average rank selected as true k . In this case study,

polynomials of order 0, 1, and 2 were tried. As is seen from Table II, the smallest mean rank value was 1.850, and it was yielded by the first-order polynomial, $k=1$. Therefore, the first-order trend function, which is comprised of $1, x, y$ monomials, was selected as the best-fit trend. It would, therefore, be expected that the OK, UK, and IRF- k estimates would be similar due to the linear model fitted to the trend.

The first step in determining the underlying variogram for UK was to estimate the coefficients of the drift function with a least-squares based estimator. Once the coefficients of the drift function are determined, the residuals are computed by subtracting the drift from the data. An experimental variogram of the residuals is then calculated and a model is fitted to the residuals experimental variogram. The bias associated with the experimental variogram is computed and an iteration is applied to compute the corrected experimental

Table II

Trend component identification summary

Trend	Mean error	Mean squared error	Mean rank
1 x y	0.0025	0.6008	1.850
No trend	-0.0006	0.8851	2.149
1 x y x ² xy y ²	0.0082	1.221	2.001

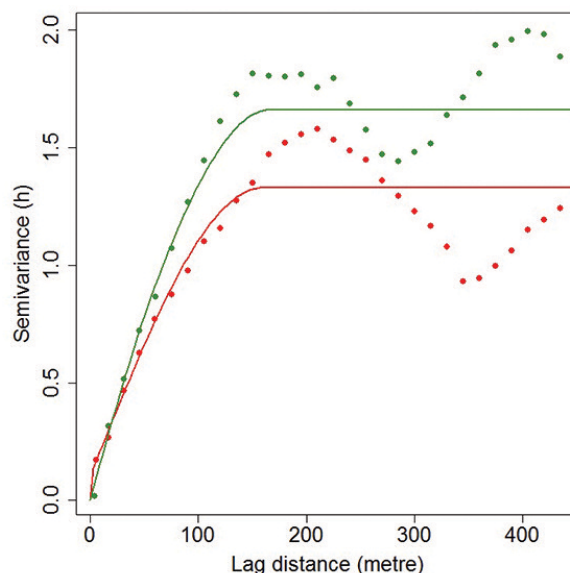


Figure 7—Experimental and theoretical variogram of inferred residuals

Accounting for a special trend in fine-scale ground-penetrating radar data

variogram. This iteration is carried out n times, n being a user-defined maximum iteration number. Variogram fitting for UK was carried out by using ISATIS software. The mathematical expression of the model fitted to the underlying variogram model is as follows:

$$\gamma_R(\mathbf{h}) = 0.34Sp_{h_{b_1}}\left(\frac{20^\circ}{48}\right) + 1.06Sp_{h_{b_2}}\left(\frac{20^\circ}{256}\right)$$

The mathematical model fitted to the underlying variogram is given in Figure 7.

Structural modelling for IRF- k

The second approach used to account for the nonstationarity was the IRF- k method. Nonstationary modelling with the IRF- k method involves three steps: (1) determination of order k , (2) inference of the optimal GC model, and (3) kriging the elevation variable based on the inferred GC. The GC model is readjusted (if necessary) based on the comparison of the obtained error with the theoretical standard deviations (Delfiner, 1976). Trend analysis has already been carried out for the UK case and the results were summarized in Table II. It was found that the best fit trend for the variable was the order 1 trend ($k=1$).

In order to infer the optimal GC, several arbitrary models of GCs were proposed and tested. The optimality of a GC model was determined on the basis of the ratio called 'Jackknife' which is basically the number indicating the ratio of the theoretical variance to the experimental one (Farkhutdinov *et al.*, 2016). The calculated Jackknife numbers were ranked in ascending order and the GC model corresponding to the Jackknife number closest to unity was selected as the optimal GC. The tested GC models and their scores can be seen in Table III.

It can be seen in Table III that the order 1 GC function yielded the Jackknife score closest to unity. Hence, order 1 type of the GC function was selected with a sill value of 3.148 and a range value of 170 m. Any possible anisotropy that may exist in the data-set is accounted for by the polynomial function which filters out the trend (Delfiner, 1976).

Structural modelling for OK

In the OK case, the residual variogram $\gamma_R(\mathbf{h})$ was inferred by calculating the experimental variogram of $Z(\mathbf{u})$ along the direction in which the trend $m(\mathbf{u})$ was deemed negligible. The deemed trend-free direction was detected as N20° from the variogram map shown in Figure 6, and the experimental variogram and the model fitted are shown in Figure 8.

However, since the GPR data is densely sampled, only the samples that are 80–100 m away from any estimation grid

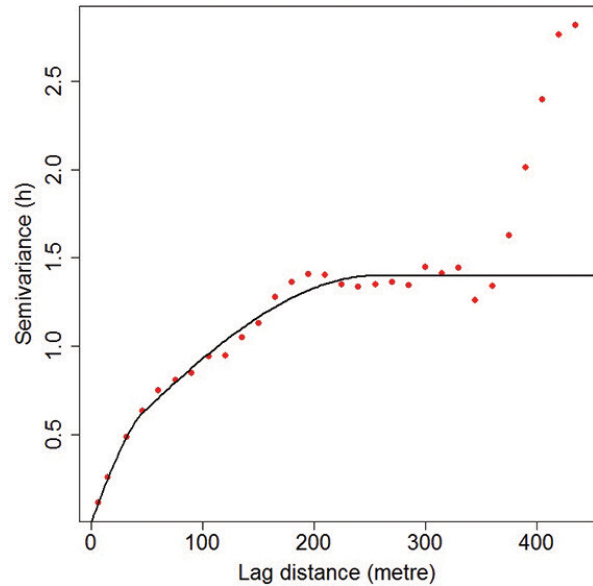


Figure 8—Experimental variogram and the fitted variogram model of the elevation variable in-trend-free direction

are considered and are of greater importance. Therefore, the variogram model reaching the sill value at range value of 256 is considered as robust.

Two spherical models without a nugget variance provided the best fit to the experimental variogram computed by using 15 m as the lag distance and 0.5 h as the lag tolerance. The mathematical representation of the fitted model is shown in the following:

$$\gamma_R(\mathbf{h}) = 0.34Sp_{h_{b_1}}\left(\frac{20^\circ}{48}\right) + 1.06Sp_{h_{b_2}}\left(\frac{20^\circ}{256}\right)$$

Cross-validation

The cross-validation technique was used to assess the accuracy of the variogram models fitted to the experimental variograms. It utilizes diagnostic statistics and the accuracy of the prediction is evaluated through various tools (Webster and Oliver, 2001). The criteria used to estimate the accuracy in this study are the mean absolute error (MAE) and mean squared deviation ratio (MSDR). The MAE should ideally be zero, which satisfies the unbiasedness condition. The MSDR is basically the ratio of the computed squared errors to the kriging variances, and the closer the MSDR is to unity, the better the model for kriging (Oliver 2010). These two criteria are calculated as follows:

$$MAE = \frac{1}{N} \sum_{i=1}^N |Z^*(u_{\alpha_i}) - Z(u_{\alpha_i})|$$

$$MSDR = \frac{1}{N} \sum_{i=1}^N \frac{(Z^*(u_{\alpha_i}) - Z(u_{\alpha_i}))^2}{\sigma^2(\mathbf{u})}$$

where N is the number of data values (which is 735 for this study), $Z(u_{\alpha_i})$ is the true value, $Z^*(u_{\alpha_i})$ is the predicted value, and $\sigma^2(\mathbf{u})$ is the kriging variance. The results of the cross-validation technique that was implemented to assess the accuracy of the variograms used for UK, IRF- k , and OK are given in Table IV.

Table III

Tested GC function models and their Jackknife scores

Order 1 GC	Spline	Spherical	Cubic	Jackknife score
3.148	0.000	0.000	0.000	0.902
0.000	1.469	0.000	0.000	0.733
0.000	0.000	2.062	0.000	0.892
0.000	0.000	0.000	8.087	0.624

Accounting for a special trend in fine-scale ground-penetrating radar data

Table IV

Results of cross-validation for UK, IRF-*k*, and OK

Variograms of algorithms	MAE	MSDR
OK	0.00047	1.02941
IRF- <i>k</i>	0.00153	0.97807
UK	0.00145	1.21735

The results of the diagnostic statistics show that, although the variogram modelled for OK has the minimum MAE and the closest MSDR value to unity, all of the computed MAE values are small, indicating that there is no significant difference among the error statistics. Based on these results, all of the modelled variograms are considered to be appropriate for spatial prediction.

Prediction of ore unit base elevation

The first step of the prediction of the elevation of the ore unit base is to define an estimation grid that is capable of covering the whole area containing the data-points as well as minimizing the extrapolation. In this case study, a two-dimensional grid having the following properties was created: the origin is $X_0 = -1872.00$ m, $\gamma_0 = 10181.00$ m, the dimensions of the mesh are $dx = 5.00$ m, $dy = 5.00$ m, the number of meshes is 75 along the x direction and 163 along the y direction, resulting in 12 225 meshes in total. This was then followed by constructing a polygon delineating the boundaries of the data, which defines the resource estimation area. The number of meshes within the polygon boundary is 7 089.

Neighbourhood parameters

A moving type of neighbourhood was used in all the aforementioned algorithms to estimate the ore unit base elevations. In order to make the data around the estimation grid evenly distributed, eight angular sectors around the estimation grid were defined with a minimum of four samples in each sector. Delfiner (1976) states that the number of

angular sectors should at least be twice the number of unbiasedness conditions, and considering the linear trend, there should at least be six angular sectors around the data. Hence, the number of angular sectors selected satisfies the given rule of thumb. Based on the parameters selected, a minimum of 32 samples around the estimation grid were used in each search neighbourhood. The radius of the search window circle was determined to be 170 m. However, since GPR pick-points were densely sampled, 32 samples around any estimation grid node do not fall further than 80 m radius. In another words, points that are 80 m away from any estimation grid node are not taken into account for estimations through kriging techniques due to this neighbourhood selection. This selected neighbourhood was used for all the kriging methods.

Predictions with UK, IRF-*k*, and OK techniques

UK was used to estimate the ore unit base elevation variable by making use of the inferred underlying variogram of the residuals and the trend function, which describe the spatial relationships between the sample data. The spatial maps of the ore unit base elevation obtained from the UK estimation are given in Figure 9.

Contrary to UK, IRF-*k* does not require the trend and the underlying variogram of the residuals to be determined beforehand, since it has its own automatic structure identification algorithm allowing it to pick up the best set of parameters within a preselected set of models (Chiles and Delfiner, 2012). Hence, parameters describing the spatial relationship for IRF-*k* algorithm in this study were automatically detected. These parameters are the trend and the chosen optimal GC model. The spatial maps of the estimates from IRF-*k* method are given in Figure 10.

In addition to these nonstationary methods, OK was implemented by neglecting the nonstationarity present in the data. In this method, the variogram model obtained along the trend-free direction was used as a structural input describing the spatial relationship. The maps of the results produced by OK are given in Figure 11.

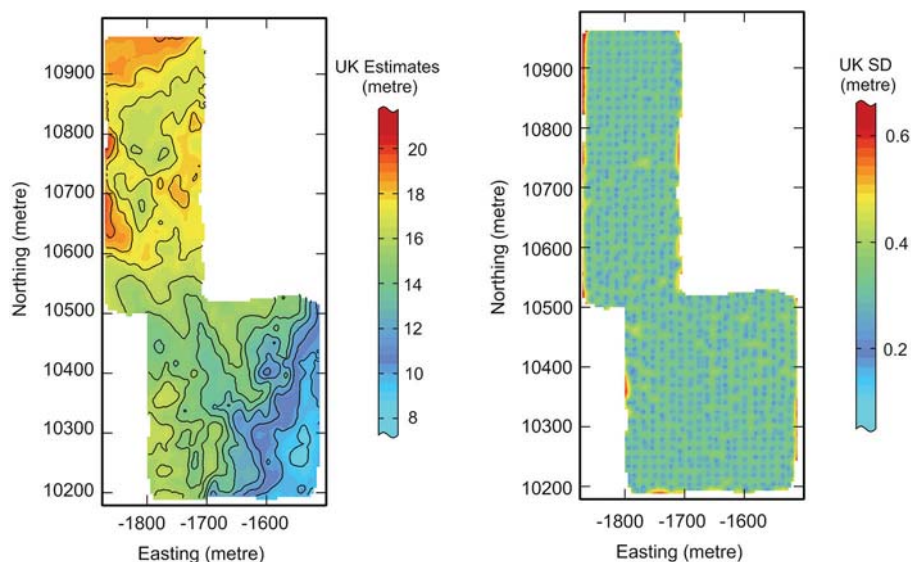


Figure 9—Maps of ore unit base elevation estimates and the associated standard deviation (SD) map calculated by the UK method

Accounting for a special trend in fine-scale ground-penetrating radar data

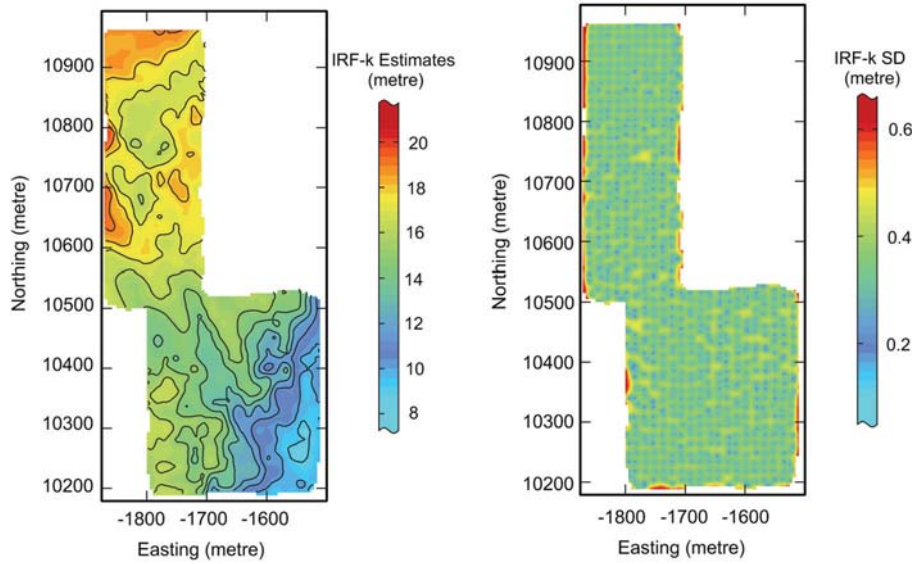


Figure 10—Maps of ore unit base elevation estimates and the associated standard deviation (SD) map calculated by the IRF-*k* method

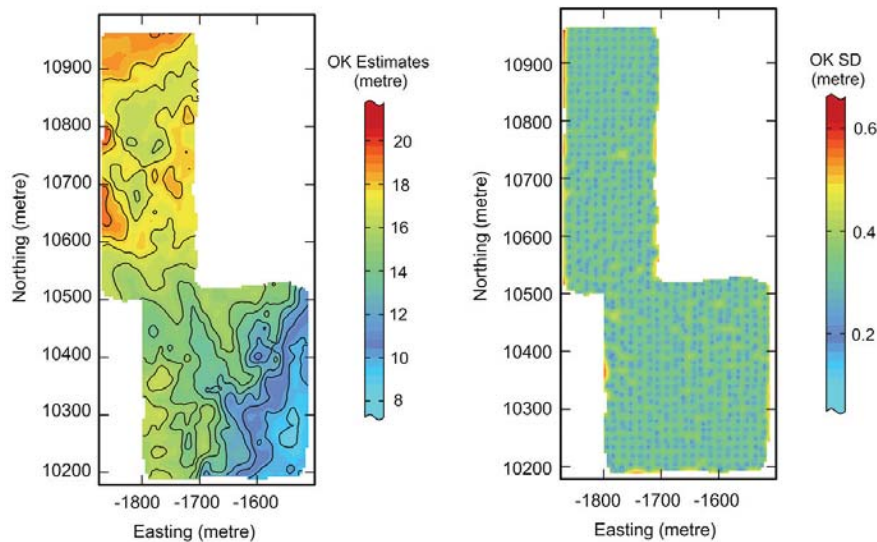


Figure 11—Maps of ore unit base elevation estimates and the associated standard deviation (SD) map calculated by the OK method

Results and discussion

The performance of the kriging estimators was tested by comparing the validation data with the kriged data. This was done by comparing the mean squared error (MSE) and MAE values. In order to compute these errors, kriged data, which was collocated with the validation data, was copied from each of the UK, IRF-*k*, and OK maps and used to calculate the error associated with each estimation algorithm. The results of MSE and MAE are shown in Table V.

Table V

MAE associated with validation of the predicted data

Variable	GPR elevation		
	IRF- <i>k</i>	OK	UK
MAE	0.2445	0.2506	0.2535
MSE	0.1267	0.1322	0.1349

The differences between the errors calculated from the different kriging algorithms are similar and the errors are not significant, considering the mean 15.01 m of the prediction data-set.

Scattergrams generated by plotting the kriged values obtained from the three kriged algorithms against the validation data yielded almost identical results. The coefficients of correlations were 0.990, 0.990, and 0.991 for UK, OK, and IRF-*k*, respectively.

Although IRF-*k* slightly outperformed the other predictor algorithms, the estimation errors were not significant enough to conclude that the more sophisticated IRF-*k* algorithm outperformed OK in this particular case study. The similarity in the results yielded by these techniques is thought to be due to factors such as the densely sampled GPR elevation variable and the selected neighbourhood parameters.

The elevation variables were densely sampled and a maximum of 32 samples were used in the estimation of the

Accounting for a special trend in fine-scale ground-penetrating radar data

variable at an unknown grid node due to the neighbourhood definition. Since 32 samples were almost always within a 80–100 m radius, the trend was probably not apparent within such a radius. Therefore, the effect of the trend was not experienced to any significant degree, since all the samples used in the estimation were from the immediate vicinity of the estimation grid.

Conclusions

The focus of this case study was to implement and compare the performances of different geostatistical estimators in the case of a trend apparent in a densely sampled GPR data-set. The UK and IRF- k methods were implemented to account for the trend seen in the data-set and OK was implemented by considering the spatial trend to be constant.

The performances were assessed by comparing the kriged values with the preselected validation data for each kriging algorithm. The results of the comparisons with the validation data have shown that IRF- k outperformed the other algorithms considering MAE and MSE criteria. However, the differences between the results were not sufficiently significant for one kriging algorithm to stand out among the others. For example, the MSE values obtained from the comparison with the validation data were 0.1267, 0.1322, and 0.1349 for the IRF- k , OK, and UK algorithms, respectively. Similarly, the plotted scattergrams demonstrated a similar outcome; the coefficient of correlations obtained from plotting the kriged values against the validation data were 0.990, 0.990, and 0.991 for UK, OK, and IRF- k , respectively. This similarity was mainly due to the large data-set and neighbourhood parameters chosen.

References

- ARMSTRONG, M. 1984. Problems with universal kriging. *Journal of the International Association for Mathematical Geology*, vol. 16. pp. 101–108. doi:10.1007/Bf01036241
- ASTM D 6432-99. 2005. Standard guide for using the surface ground penetrating radar method for subsurface investigation. ASTM International, West Conshohocken, PA.
- ATKINSON, P.M. and LLOYD, C.D. 2007. Non-stationary variogram models for geostatistical sampling optimisation: An empirical investigation using elevation data. *Computers and Geosciences*, vol. 33. pp. 1285–1300.
- BARDOSSY, G. and ALEVA, G.J.J. 1990. Lateritic Bauxites. Elsevier, Amsterdam.
- Buttafuoco, G. and Castrignano, A. 2005. Study of the spatio-temporal variation of soil moisture under forest using intrinsic random functions of order k . *Geoderma*, vol. 128. pp. 208–220. doi:10.1016/j.geoderma.2005.04.004
- CHIH, H., GALLI, A., RAVENNE, C., TESSON, M., and DE MARSILY, G. 2000. Estimating the depth of stratigraphic units from marine seismic profiles using nonstationary geostatistics. *Natural Resources Research*, vol. 9. pp. 77–95.
- CHILÈS, J.-P. 1976. How to adapt kriging to non-classical problems: three case studies. *Advanced Geostatistics in the Mining Industry: Proceedings of the NATO Advanced Study Institute*, Istituto di Geologia Applicata of the University of Rome, Italy, 13–25 October 1975. Springer. pp. 69–89.
- CHILÈS, J.P. and DELFINER, P. 2012. *Geostatistics: Modeling Spatial Uncertainty*. Wiley.
- CHRISTENSEN, R. 1990. The equivalence of predictions from universal kriging and intrinsic random-function kriging. *Mathematical Geology*, vol. 22. pp. 655–664. doi:10.1007/Bf00890514
- CRESSIE, N. 1993. *Statistics for Spatial Data*. Wiley-Interscience, New York.
- DAVIS, J.L. and ANNAN, A.P. 1989. Ground-penetrating radar for high-resolution mapping of soil and rock stratigraphy. *Geological Prospecting*, vol. 37. pp. 531–551.
- DELFINER, P. 1976. Linear estimation of non stationary spatial phenomena. *Advanced Geostatistics in the Mining Industry*. Springer. pp. 49–68.
- DELHOMME, J.P. 1978. Kriging in the hydrosocieties. *Advances in Water Resources*, vol. 1. pp. 251–266. doi:10.1016/0309-1708(78)90039-8
- ERTEN, O. 2012. Profiling and mining control to mitigate dilution effect from SiO₂ at the base of a bauxite deposit. PhD thesis, University of Queensland.
- ERTEN, O., KIZIL, M.S., TOPAL, E., and McANDREW, L. 2013. Spatial prediction of lateral variability of a laterite-type bauxite horizon using ancillary ground-penetrating radar data. *Natural Resources Research*, vol. 22. pp. 207–227.
- ERTEN, O., McANDREW, L., KIZIL, M.S., and TOPAL, E. 2015. Incorporating fine-scale ground-penetrating radar data into the mapping of lateral variability of a laterite-type bauxite horizon. *Mining Technology*, vol. 124. pp. 1–15.
- FALLON, G.N., FULLAGAR, P.K., and SHEARD, S.N. 1997. Application of geophysics in metalliferous mines. *Australian Journal of Earth Sciences*, vol. 44. pp. 391–409.
- FARKHUTDINOV, A., GOBLET, P., DE FOUQUET, C., and CHERKASOV, S. 2016. A case study of the modeling of a hydrothermal reservoir: Khankala deposit of geothermal waters. *Geothermics*, vol. 59, Part A. pp. 56–66. <http://dx.doi.org/10.1016/j.geothermics.2015.10.005>
- FRANCKE, J. and UTSI, V. 2009. Advances in long-range GPR systems and their applications to mineral exploration, geotechnical and static correction problems. *First Break*, vol. 27. pp. 85–93.
- FRANCKE, J.C. and NOBES, D.C. 2000. A preliminary evaluation of GPR for nickel laterite exploration. *Proceedings of the Eighth International Conference on Ground Penetrating Radar*, Gold Coast, Queensland. Noon, D.A., Stickley, G.F., and Longstaff, D. (eds). SPIE, Bellingham, WA. pp. 7–12.
- FRANCKE, J.C. and PARKINSON, G. 2000. The new role of geophysics in nickel laterite exploitation and development. *Proceedings of the Mining Millennium/PDAC Convention*, Toronto, Canada. Prospectores and Developers Association of Canada.
- GOOVAERTS, P. 1997. *Geostatistics for Natural Resource Evaluation*. Oxford University Press, New York.
- GOOVAERTS, P. 2000. Geostatistical approaches for incorporating elevation into the spatial interpolation of rainfall. *Journal of Hydrology*, vol. 228. pp. 113–129. doi: 10.1016/S0022-1694(00)00144-X
- GOW, N.N. and LOZEJ, G.P. 1993. Bauxite. *Geoscience Canada*, vol. 20. pp. 9–16.
- ISATIS. 2016. Software manual, 9.0 edn. Avon Cedex, France.
- JOURNEL, A.G. and HUIJBREGTS, C.J. 1978. *Mining Geostatistics*. Academic Press, London.
- JOURNEL, A.G. and ROSSI, M.E. 1989. When do we need a trend model in kriging? *Mathematical Geology*, vol. 21. pp. 715–739.
- KITANIDIS, P.K. 1997. *Introduction to Geostatistics: Applications to Hydrogeology*. Cambridge University Press.
- LEUANGTHONG, O., LYALL, G., and DEUTSCH, C. 2002. Multivariate geostatistical simulation of a nickel laterite deposit. *APCOM 2002: Proceedings of the 30th International Symposium on the Application of Computers and Operations Research in the Mineral Industry*, University of Alaska. Bandopadhyay, S. (ed.). Society for Mining, Metallurgy, and Exploration, Littleton, CO. pp. 261–273.
- LOUGHNAN, F.C. and BAYLISS, P. 1961. The mineralogy of the bauxite deposits near Weipa, Queensland. *American Mineralogist*, vol. 46. pp. 209–217.
- MATHERON, G. 1963. Principles of geostatistics. *Economic Geology*, vol. 58. pp. 1246–1266.
- MATHERON, G. 1971. The theory of regionalised variables and its applications. *Ecole des Mines, Cahiers du Centre de Morphologie Mathématique*, Paris. Vol. 5. pp. 211.

Accounting for a special trend in fine-scale ground-penetrating radar data

- MATHERON, G. 1973. The intrinsic random functions and their applications *Advances in Applied Probability*, pp. 439–468.
- McLENNAN, J.A., ORTIZ, J.M., and DEUTCH, C.V. 2006. Geostatistical simulation of optimum mining elevations for nickel laterite deposits. *CIM Bulletin*, vol. 1, no. 6. pp. 1–9.
- MORGAN, C.M. 1992. Geology of the spheres at Weipa. *Travaux de Comité Internationale pour l'Etude des Bauxites, de Alumine et de l'Aluminium*, vol. 22. p. 61–74.
- MYERS, D.E. 1989. To be or not to be...stationary? That is the question. *Mathematical Geology*, vol. 21. pp. 343–362.
- NEUMAN, S.P. and JACOBSON, E.A. 1984. Analysis of nonintrinsic spatial variability by residual kriging with application to regional groundwater levels. *Journal of the International Association for Mathematical Geology*, vol. 16. pp. 499–521. doi: 10.1007/Bf01886329
- ODEH, I., McBRATNEY, A., and SLATER, B. 1997. Predicting soil properties from ancillary information: non-spatial models compared with geostatistical and combined methods. *Proceedings of Geostatistics Wollongong 96*. Vol. 1. Baafi, E.Y. and Scofield, N.A. (eds). Kluwer. pp. 1008–1019.
- ODEH, I.O.A., McBRATNEY, A.B., and CHITTLEBOROUGH, D.J. 1994. Spatial prediction of soil properties from landform attributes derived from a digital elevation model. *Geoderma*, vol. 63. pp. 197–214.
- OLEA, R.A. 1974. Optimal contour mapping using universal kriging. *Journal of Geophysical Research*, vol. 79. pp. 695–702. doi: 10.1029/JB079i005p00695
- OLIVER, M.A. 2010. *Geostatistical Applications for Precision Agriculture*. Springer.
- OLIVER, M.A. and WEBSTER, R. 2015. *Basic Steps in Geostatistics : the Variogram and Kriging*. Springer.
- ROSSI, M.E. and DEUTSCH, C.V. 2014. *Mineral Resource Estimation*. Springer.
- SINGH, N.K. 2007. Ground penetrating radar (GPR) 'mineral base profiling and orebody optimisation'. *Proceedings of the 6th International Heavy Minerals Conference 'Back to Basics'*, Hluhluwe, South Africa. Southern African Institute of Mining and Metallurgy, Johannesburg. pp. 179–182.
- WACKERNAGEL, H. 2002. *Multivariate Geostatistics*. Springer, Berlin.
- WATTS, A. 1997. Exploring for nickel in the 90s, or 'Til depth us do part! Geophysics and Geochemistry at the Millenium. *Proceedings of Exploration 97: Fourth Decennial International Conference on Mineral Exploration*, Toronto, Canada. Gubins, A.G. (ed.) Prospector and Developers Association of Canada. pp. 1003–1013.
- WEBSTER, R. and OLIVER, M.A. 2001. *Geostatistics for environmental scientists. Statistics in Practice*. Wiley, Chichester, UK.
- ZIMMERMAN, D., PAVLIK, C., RUGGLES, A., and ARMSTRONG, M.P. 1999. An experimental comparison of ordinary and universal kriging and inverse distance weighting. *Mathematical Geology*, vol. 31. pp. 375–390. ♦

4th YOUNG PROFESSIONALS CONFERENCE

CREATING A SUSTAINABLE AFRICA MINERALS INDUSTRY THROUGH APPLIED INNOVATION

**18–19 September 2018, Focus Rooms
The Core, Sunninghill, Sandton**

BACKGROUND

The minerals industry is a backbone for most of the economies in the African continent, thus, it is vital that the exploitation of the mineral resources is conducted profitably. However, without any paradigm shift in the tactics we employ to mine these resources, the mineral wealth we possess will not be of any benefit to the current and future generations. There need to be a shift in the way we exploit the resources in order to ensure longevity of current operations and enable mining of deep-level complex orebodies in a safe, healthy and profitable manner. This can be achieved through integration of 1st, 2nd, 3rd and 4th revolutions to create a sustainable minerals industry

FOR FURTHER INFORMATION CONTACT:

Conference Co-ordinator: Camielah Jardine • E-mail: camielah@saimm.co.za
Tel: +27 11 834 1273/7 • www.saimm.co.za





Towards safer mining: scientific measurement approaches that could be applied for imaging and locating the buried container lamp-room at Lily mine

by I. Hussain*, F.T. Cawood*, and S. Ali†

Synopsis

When the crown pillar at Lily mine collapsed on 5 February 2016, a lamp-room in a container on surface was engulfed in the sinkhole that formed, trapping three miners who were in the lamp-room at the time. In situations like this, it is imperative to locate and rescue the missing miners before the window of opportunity to find them alive closes. The Wits Mining Institute (WMI) at the University of the Witwatersrand was requested to assist with suggestions, and a conceptual study was undertaken to identify techniques that were likely to be successful. Several techniques that have the potential to locate the position of the container were identified, but the typical noise in the form of steel objects, mine cavities, and a combination of broken and solid rock in a complex geographical and geomechanical environment will pose significant challenges.

Keywords

safety, leadership, human factors, human error, human behaviour, safety culture.

Introduction

The purpose of the study is to apply science and technology to determine the likely location of a lamp-room housed in a shipping container, in which three miners were trapped after the Lily mine disaster. The container was engulfed in a sinkhole and descended into the underground workings, along with backfill debris, broken rock, and other (mostly metallic) pieces of surface infrastructure. The objective of this article is solely to investigate which technologies and techniques are likely to be successful in locating the container. This study is of interest to mineworkers, their families, the mining industry, government, and mine rescue teams. Technologies for physical testing are expensive and mostly unproven in complex and harsh mining environments with many different scenarios. As a result, the study is mostly conceptual with minimal testing, but the methodology followed resulted in the identification, evaluation, and systematic exclusion of technologies to arrive at a point where costs could be minimized through targeting technologies with a high probability of success. It is hoped that this study will contribute to firstly, a better understanding of what happened at Lily mine; secondly, the national imperative of achieving zero harm in mining; and thirdly, the development of a pool

of knowledge that can be consulted during mine disaster and rescue management.

Overview of the mine, the event, and the broad technology approaches

Lily Mine is about 38 km southeast of Nelspruit and 25 km northeast of Barberton in the Mpumalanga Province of South Africa. The study area is shown in Figure 1.

Underground mining remains a high-risk activity prone to accidents and sometimes mine disasters. The costs associated with an accident can be so substantial that mining operations may be infeasible following the event. One such accident occurred at the Lily Mine on 5 February 2016, when the crown pillar protecting the underground and surface workings collapsed. The lamp-room, which was housed in a steel shipping container, fell into the sinkhole that formed, with three miners trapped inside. Two metallic water tanks, one 550 kVA generator, and many other metallic objects went down the sinkhole due to the abrupt and unexpected nature of the accident. The reasons for the collapse are still under investigation. The collapsed area was declared unsafe and unstable by the mine and the Chief Inspector of Mines, South Africa.

On 25 February 2016 the Mine Health and Safety Council (MHSC) of South Africa requested the Wits Mining Institute (WMI) at the University of the Witwatersrand to suggest methods that could be used to locate the lost container. A quick and promising response was received from all over the University. The ideas suggested included using an unmanned aerial vehicle (UAV) equipped with a magnetometer and digital camera, detecting the underground cavity with ground penetrating radar (GPR), using acoustic equipment like geophones to detect sound, electrical resistivity tomography, thermal

* University of the Witwatersrand, South Africa.

† NUST College of Civil Engineering, Risalpur Campus, Pakistan.

© The Southern African Institute of Mining and Metallurgy, 2018. ISSN 2225-6253. Paper received Jan. 2017; revised paper received Dec. 2017.

Towards safer mining: scientific measurement approaches that could be applied

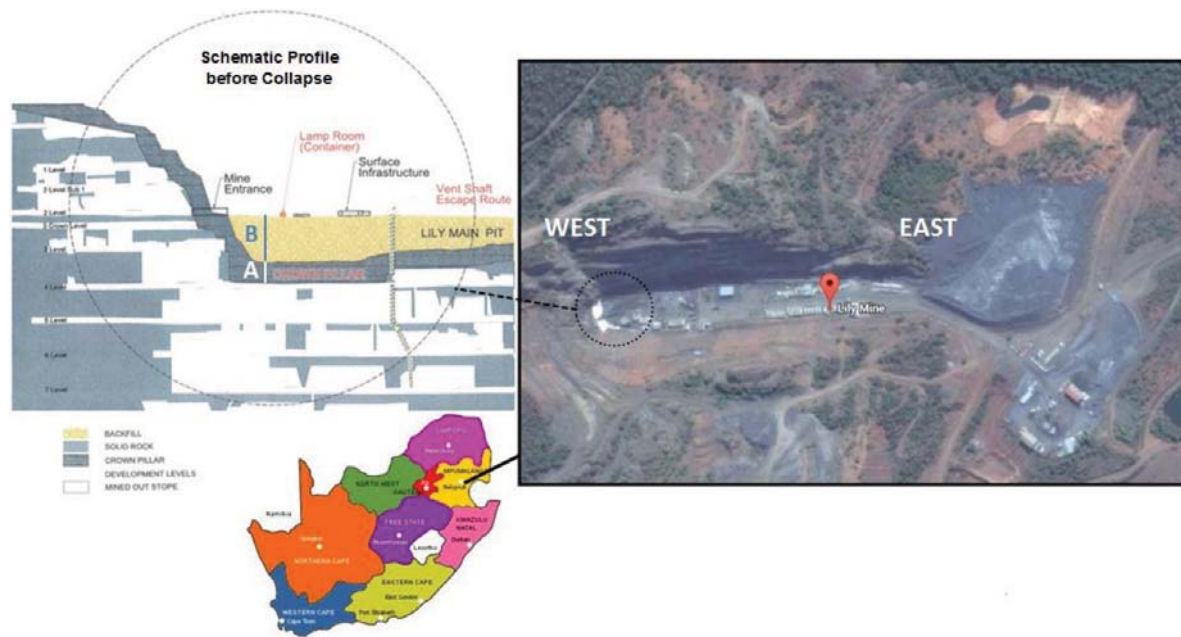


Figure 1—Location map of the study area. The height of the crown pillar (A) and backfill (B) is approximately 35 m

imaging, through-the-earth communication systems, electrical resistivity metering, and simulating the movement of the container using 3D geographical and numerical simulation software. These solution-based ideas were then divided into two distinct groups—those used to locate the container and those used to simulate the movement of the container through 3D fluid flow and advanced numerical modelling software, as used to find trapped persons after an avalanche in mountainous areas. At a visit to Lily mine on 9 March 2016, the WMI team suggested a two-way strategy going forward:

- First, a temporal 3D modelling approach using software technology
- Second, a scientific measurement and testing approach, which is the topic of this paper.

The role of technology for imaging and locating buried objects in underground mine disasters

Despite the availability of modern rescue equipment and technologies for tracking and monitoring, the harsh underground environment causes most technologies to give questionable results during mine-related rescue operations (Mine Safety and Health Administration, 2010). This study identifies technologies for imaging and locating buried objects. It also evaluates some suitable technologies for finding steel objects, underground voids, and communication devices. The compiled record of suitable technologies would be useful for future mine search-and-rescue operations.

Conceptual approach followed for detecting the lamp-room container

Fundamentally, the objective of the study is to apply science and technology to determine the likely locations of the container, the communicating devices of the miners inside the container, and of course the missing miners. The following specific objectives were set:

- Identify potential technologies that can locate the lamp-room container
- Apply a combination of science and technology to determine the location of the lamp-room container
- Test certain technologies in a mining environment and record the findings
- Compile a record of suitable technologies for future mine search-and-rescue purposes
- Collect information that will assist a research project to understand what happened at Lily Mine.

Potential technologies for imaging and locating subsurface objects

The fundamental principle behind such imaging technologies is to input energy into the earth and to then analyse the reflected energy. Interpretation of the reflected energy can indicate the horizontal position of the object of the search. The following sections discuss electromagnetic (EM), magnetic, infrared thermography, resistivity, seismic, ground penetrating radar (GPR), micro-gravitational, and communications approaches, which are based on different geophysical principles.

Magnetic/electromagnetic (EM) approach

The magnetic approach utilizes variations in the intensity of the Earth's magnetic field. The local geology at Lily mine includes highly magnetic rock units, and the magnetic noise from the two water tanks, one 550 kVA generator, and many other metallic objects that were engulfed by the sinkhole would pose additional challenges in interpreting the results.

Pipe and cable locator

The pipe and cable locator works on the principle of a conductive or inductive mode transmitter emitting an EM wave (generally 50 Hz to 480 kHz) and a receiver that detects the reflected waves from underground objects (American Society of Civil Engineers, 2002). If the

Towards safer mining: scientific measurement approaches that could be applied

transmitted EM wave comes in contact with a metallic object, an electromagnetic current is induced in that object and the receiver detects and processes the induced magnetic field, indicating the presence of the object by means of an audible or visual signal. The available pipe and cable locator in the market can detect underground utilities up to 6 m depth (Amprobe, n.d.). This method cannot image nonmetallic objects, unless they are marked with metallic tape or wire. Considering the conditions at Lily mine, where the container is likely to be deeper than 6 m, and the surface area directly above the container is too unstable to access, pipe and cable locators are unlikely to be successful.

Electronic marker system (EMS)

In this technology, a transmitter emits radio frequency signals to an electronic marker that was fitted to the facility at the time of construction or installation. Different frequencies can be used to assign to and locate different buried objects. The specially designed markers can be detected even in the presence of power lines, metallic conductors, and fences. The available EMS system in the market can detect underground utilities up to 3 m depth (3M Infrastructure Protection Division, 2012). The short range and the fact that the Lily mine lamp-room container was not equipped with an EMS marker eliminate this technology. It has, however, wider applications than the pipe and cable locator because the receiver can also work from underground.

Metal detector

The metal detector works by transmitting an AC (alternating current) magnetic field into the ground and then the receiver analyses the corresponding field (American Society of Civil Engineers, 2002). The search coil senses the change in the magnetic field caused by a conductive metal object. The reflected magnetic field from the magnetic objects is slightly different to that of the surrounding soil. The available metal detectors in the market have a range of up to 6 m depth (Benson, Glaccum, and Noel, 1984). Considering its longer range and the fact that it can be operated underground, a good quality metal detector could be sourced to alert the rescue team when they come in close proximity to metal objects.

Magnetometer

This is an instrument that records the Earth's magnetic field. It uses two methods for imaging and locating underground utilities (American Society of Civil Engineers, 2002). The first method is total field measurement, which is useful for searching for metallic objects over large distances in the absence of power lines, vehicles, railroads, or other sources

of interference. The second method is gradiometric measurement, which is useful for detecting shallow metallic objects. The depth of penetration greatly depends on the field strength and the average detection depth is 3–6 m (Dodge and Anspach, 1995). It can detect larger metallic objects up to 20 m deep (Benson, Glaccum, and Noel, 1984). Although a magnetometer has potential, the simplicity of a metal detector makes it a more flexible option.

Ground penetrating radar (GPR)

GPR works on a reflection technique that uses high-frequency electromagnetic waves (typically 10–1000 MHz) to acquire subsurface information. It responds to changes in electrical properties (*i.e.*, conductivity and dielectric constant), which are a function of soil, rock material, and moisture content (SubSurface Surveys & Associates Inc., n.d.). The technology can also be mounted on a moving vehicle or a drone. GPR waves can reach 30–40 m in low-conductivity materials such as dry sand or massive, dry concrete or granite (Jeong *et al.*, 2003).

Ground Penetrating Analyzer GPA 3000

This image analyser gives a visual indication of size, shape, and even the type of metal detected (KTS-Electronic, 2016). It also gives an exact distance from the detector to the top of target metal down to a depth of 25 m.

This technology has potential for imaging and locating the buried container lamp-room (and other objects) at Lily mine, but its effectiveness when used underground needs to be established.

Electrical resistivity tomography

Electrical resistivity tomography using intrinsic properties, *i.e.*, electric resistance and stiffness contrast of the subsurface materials, has been successfully used to detect leachates, groundwater, bedrock, stratigraphic layers, buried objects, cavities, and utilities (Jusoh, 2010). Besides being nondestructive, electrical resistivity geophysical techniques can be implemented quickly, are relatively inexpensive, and have larger coverage in both the horizontal and vertical extents (Khatri, Shrivastava, and Chandak, 2011). A 2D illustration of the resistivity results at a project site is shown in Figure 2. A 3D manifestation of an archeological investigation carried out to locate a grave is shown in Figure 3. With a suitable number, spacing, and arrangement of arrays, the electrical resistivity method can be used to locate buried objects up to great depths (the depth of penetration equals a third to a quarter of the horizontal separation of the electrodes at ground surface).

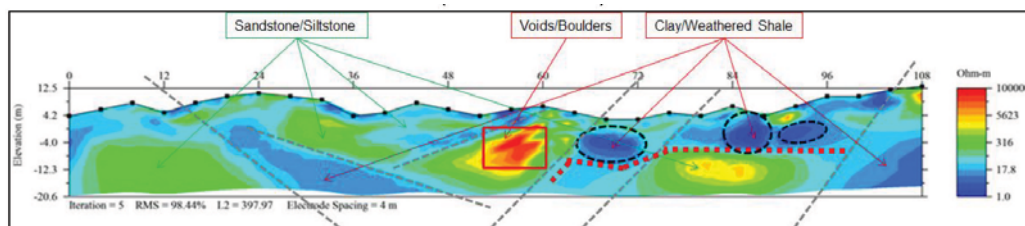


Figure 2—A 2D subsurface characterization of materials on the basis of difference in electrical resistivity

Towards safer mining: scientific measurement approaches that could be applied

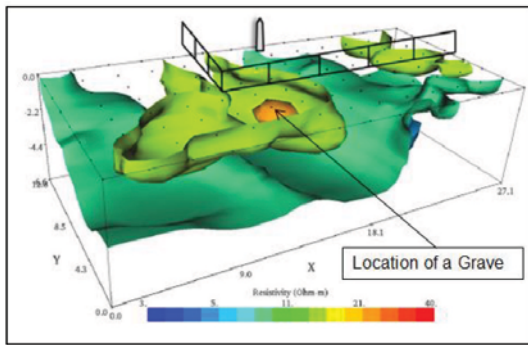


Figure 3—3D illustration of a grave located using electrical resistivity method (Advanced Geosciences, Inc., 2016)

Infrared (IR) thermography

IR thermography detects infrared radiation emitted from an object and converts the signal to visible wavelengths on the electromagnetic spectrum. Each object has different thermal characteristics. This method is effective for finding buried utilities that have different thermal characteristics from the surrounding ground. It cannot measure the dimensions, but relative sizes of objects can be deduced (Jeong *et al.*, 2003). This method does not require ground contact, making it suitable as a remote sensing technology. Figure 4 shows an example of a thermal image of underground pipes as observed from a drone.

Satellite IR imagery

Satellite images are of benefit to Earth scientists due to the sensor responding to multiple spectral bands, which allows scientists to interpret wavelengths that cannot be seen by the human eye, such as near infrared, short-wave infrared, and thermal infrared, to identify anomalies (Satellite Imaging Corporation, 2013). Multispectral imaging and thematic mapping allows researchers to collect data on the reflection and absorption properties of soils, rock, and vegetation. This data could be utilized to interpret actual surface lithology to identify clays, oxides, and soils from satellite images. This method could be useful for imaging and locating the buried container lamp-room at Lily mine.

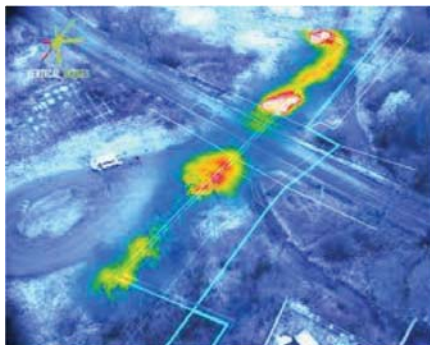


Figure 4—Thermal image for inspecting underground pipes (Workswell, 2016); The maximum measurement distance depends on the distance-to-spot ratio of the camera and the target size, i.e. D/S ratio \times Target size = maximum measurement distance

IR camera

Handheld infrared cameras can also be used for obtaining IR imagery. Although a camera is also an option at Lily mine, satellite imagery is considered better because of the area coverage, availability, and affordability.

Microgravity

Microgravity techniques measure variations in the Earth's gravitational field for locating areas of contrasting densities (Mariita, 2007). This technique is useful for imaging and locating large utilities (or cavities) that are predominantly empty. A cavity represents a mass deficiency, thus a small reduction in the gravitational field, or negative gravity anomaly, is observed. Gravity anomalies are due to the differences in density of underlying material. This technique can detect and image anomalies up to a depth of 33 m (Jeong *et al.*, 2003).

SCINTREX CG5M gravimeter

This gravimeter can detect gravity anomalies at depths up to about 30–40 m (Innogeo, 2013). The size of the measurement mesh depends on the depth and size of the anomaly. This technology has some potential for imaging and locating the buried container lamp-room at Lily mine.

Seismic techniques

Seismic techniques work on the principle that the seismic waves travel with different velocities in different materials, *i.e.* rocks, soils, and underground objects. Seismic waves penetrate the ground and the travel time of reflected/refracted seismic waves is observed by geophones (SubSurface Surveys & Associates Inc., n.d.). A seismic wave is generated by an explosive shot, hammer, weight drop, or some other shock that induces vibration. The detectors are placed at regular intervals and measure reflected energy and time of arrival. The data is plotted on a time-distance graph from which the velocities and depth of different subsurface layers can be obtained. Figure 5 shows a seismic refraction tomography of a salt diapir in central Utah. The maximum depth of interest is usually about 12 km (Stark, 2008).

Trapped person locator (TPL)

The trapped person locator (TPL) instrument can detect and pinpoint the location of trapped persons. It amplifies the faint sounds made by the trapped victims (Elpam Electronics Ltd., 2014). It uses seismic sensors to convert ground motion into a voltage. Geophones can also amplify sound and can be used to listen to sounds generated by missing persons.

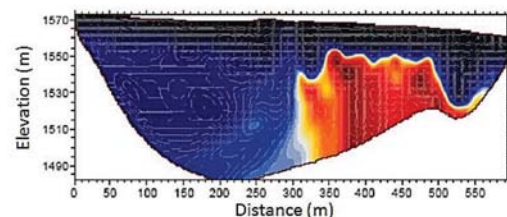


Figure 5—Seismic refraction tomography of a salt diapir in central Utah (Subsurface Surveys & Associates, Inc., n.d.)

Towards safer mining: scientific measurement approaches that could be applied

Communications

Mines and mineworkers have become highly connected over the last 30 years. This connectivity was accelerated by the take-off of the cellular phone industry. The increased upgrade of mine telecommunications systems and (personal) cellular phone use caused a decrease in the use of portable hand-held systems (hand-held transceiver or HT—commonly known as ‘walkie-talkies’). Communications technology is by far the most practical way of establishing location, through either dialling-and-asking or tracking transponder signals.

Cell phone calling and tracking

The first step is to call on either HT or cell phone, and in the event that there is no response, the cell phone can be tracked through its unique International Mobile Subscriber Identity (IMSI) or International Mobile Equipment Identity (IMEI) number. It does not matter if the phone has a different SIM card or is switched off. This is the quickest and most efficient way of tracking the person carrying the phone if there is no answer. It is highly likely that the trapped miners at Lily mine had their cell phones with them at the time of the accident, as the lamp-room was located on surface. So determining the position of the lamp-room using the workers’ cell phones becomes possible. The capability of this technology or how effective it will be under these circumstances is unknown because this technology is not publicly available.

Through-the-earth (TTE) communication system

TTE communication systems use significant transmitting power and large antennae to transfer low-frequency signals that can penetrate several hundreds of metres through solid rock (Bandyopadhyay, Chaulya, and Mishra, 2010). These systems are designed for use in mine emergencies when no other form of communication is possible. Therefore, TTE communication can be used in case of disaster recovery to

locate trapped miners (Michael *et al.*, 2012; Hussain *et al.*, 2017). These systems support real-time voice, voice messages, data messages, and beacon signals but there are limitations on transmission rates due to the low operating frequency bands (Michael *et al.*, 2012). This technology is not suitable as the Lily mine lamp-room was not ‘intelligent’, *i.e.* it was not equipped with a TTE communication system for mine emergencies.

Communication systems are the most likely method identified thus far, but the probability of success diminishes significantly over time. During the first few hours or perhaps days following the incident, it was critical to explore this option first before the window of opportunity of finding the trapped miners alive closed.

Exploring some of the technologies identified

Some of the technologies described in the previous sections were tested for locating and imaging the missing Lily mine lamp-room. The findings summarized in Table I. Although none yielded unambiguous results that led to finding the missing miners, the lessons learnt are documented here for future eventualities.

EM approach: metal detector

GyroLAG conducted an EM survey shortly after the collapse in the hope of locating the buried container. The metal detector was mounted on an unmanned aerial vehicle (UAV) that flew the area at a height of 20 m above the rubble because of difficult flying conditions. The survey identified eight possible positions after taking account of the ‘noise’ from the magnetic host rock (Figure 6). The initial results (left image) were of little use, but after the maps were georectified with the help of six ground-control points, the positions of the points correlated with the terrain. Although the approach worked and gave good results, these were of

Table I

Technology approaches that require follow-up

Approach	Technology	Comment	Test/measurement
EM	Geophysical: metal detector	Will notify rescue team when they come within a 6 m range of buried steel objects	None required, but a good quality device needs to accompany the rescue team
GPR	Geophysical: Ground Penetrating Analyzer GPR 3000	Its 25 m range for detecting metal and imaging shapes makes it a good option for Lily mine	Testing is required at a suitable site, e.g. Sterkfontein Caves (test both surface and underground)
Electrical resistivity	Geophysical	This technique is useful for investigation at relatively greater depths and provides diverse data for stratigraphic, hydrological, and geostructural information	Testing is required at a site such as Sterkfontein Caves for calibration / validation
IR thermography	Satellite images or IR camera	Considering that satellite data is affordable and available, it should be considered. The IR camera has potential, but is unlikely to be a better option than satellite imagery	Ordering of IR imagery for incorporation into a GIS system. Satellite images preferred over the IR camera
Microgravity	Geophysical: gravimeter	Has potential, but unlikely to be a better option than GPR	GPR preferred
Seismic	Geophysical: TPL	If the missing miners were still alive, this method would have ranked highly. Under the circumstances, however, GPR is a better option	GPR preferred, considering the fact that the trapped miners are no longer alive
Communications	HT or cell phone	If the missing miners were still alive, calling them would have been the best option. Under the circumstances, however, tracking the phones is the next best option	The technology to track cell phones is not available to the public

Towards safer mining: scientific measurement approaches that could be applied



Figure 6—UAV surveyed points

little use, primarily because of the significant ‘noise’ as a result of the many buried steel objects and other surface infrastructure. In addition to the noise problem, the surface was considered too unsafe to allow detailed inspection of the target areas. The lessons for future rescue attempts are as follows.

- EM surveys are appropriate technologies for rescue operators and can be quickly deployed. Metal detectors are versatile technologies that can be operated through hand-held devices (both on surface and underground) and mounting on moving platforms like UAVs
- After the results have been processed and target areas identified, the EM surveys should be followed by either a visual inspection or using a camera mounted on the UAV. If ground conditions are unstable, such inspections should be done from a UAV platform
- A good quality hand-held metal detector should accompany the rescue team underground to investigate target areas defined by software modelling (Ashraf and Cawood, 2016) and to warn rescue teams withdrawing loose rock containing steel objects (which could include the missing container in which the miners are) gravitating to withdrawal points.

Seismic approach: TPL

Mine Rescue Services used a TPL 310D (Mini TPL) in an effort to establish if anyone survived the disaster. This instrument can detect and pinpoint the location of trapped persons below and above the ground if they are alive and respond to knocking. It has two modes of operation, *i.e.* SURVEY and LOCATE. SURVEY is used on rescue sites to establish communication with trapped persons using acoustic sensors, if any living and conscious survivors are under the rubble. The system also provides a means to communicate with trapped persons. The acoustic sensor functions as a loudspeaker/microphone, which can be inserted into crevices and allows two-way communication to be established with the trapped persons. The LOCATE mode provides information about the location of the person, in or below the rescue site, so as to guide the rescue team. By moving the sensors around, trapped persons can be traced to within 5 m (Elpam Electronics Ltd., 2014). In the case of Lily mine, it was assumed that some trapped persons survived the initial disaster and were alive to provide a minimal response to calls or knockings from the rescue team. The TPL was used underground at level 5 and established a location in an ‘East 1’ direction of the sensor, but could not indicate inclination or

distance. The technology has significant potential, and had it been used in conjunction with the communication devices of the missing miners, the position of the container could have been established with more certainty. The lessons for future rescue attempts are as follows.

- TPLs are very effective technologies for rescue operators and can be quickly deployed. As is the case with metal detectors, TPLs are versatile technologies that can be operated through hand-held devices (both on surface and underground)
- Attention should be given to the correct (full) use and (accurate) location of the device. This will help with plotting target areas on the mine plan
- A good quality TPL should accompany any rescue effort. More importantly, the operators must be trained in the correct and full use of the device and must have some knowledge of surveying principles so that readings can be projected onto the mine plans.

Communications approach: HT or cell phone tracking

This approach was not tested in the days after the Lily mine disaster, but has significant potential while the batteries are still charged. The chances of success would be enhanced if communication technology is combined with other technologies like a TPL. Although no inventory of items in the Lily Mine lamp-room was available, it was established that there was a HT, but batteries were dead because of the time lapse since the disaster.

The next option was to track the cell phones. The cell phone numbers and the names of the trapped workers were provided by the mine to MHSC on 10 March 2016. The cell phone numbers of the trapped workers were dialled, just to establish that the numbers were the correct ones. As an additional measure, the numbers were passed on to the service provider so that they could establish if tracking the location of the three phones was possible. They indicated that it would not be possible to establish the location of the phone if the batteries were run down, and some of the numbers provided were not linked to the trapped individuals. In addition to contacting the cell phone service provider, the SAPS (South African Police Service) was contacted for assistance. In their letter of response, dated 18 March 2016, they indicated that cell phones can be traced only when reported missing within 24 hours, and that in their opinion, it is not possible to trace a cell phone underground. This response requires further testing in preparation for future

Towards safer mining: scientific measurement approaches that could be applied

mine disasters. The lessons for future rescue attempts are:

- In a connected world, it is highly likely that there will be some communicating device with trapped miners, especially if they were on surface at the time of the disaster. The likelihood of a successful outcome is greater early after the disaster, when the batteries of the devices still have power and when the communications approach is used in tandem with other devices, *e.g.* a TPL
- It is important to keep inventory records for all facilities, along with personal and work phone information – and have these available for rescue efforts
- The technology to track cell phones is not available to the public and cannot be tested. Lily mine will not be the last to have a disaster at the time when mine workers carry cell phones on them. Future rescue efforts will be assisted if the SAPS allows the technology to be tested for accuracy and the maximum depth it can record signals from persons trapped below the surface or rubble .

Summary

Underground mining is prone to accidents, sometimes even disasters. These accidents may cause fatalities, injuries, and also result in significant economic losses. Such an accident occurred at the Lily mine on 5 February 2016 when the crown pillar supporting the surface workings collapsed. The lamp-room container on surface, with three miners inside, subsided and was lost in the sinkhole along with two 550 kVA transformers, one generator, and two steel water tanks. This study discusses the role of technology for imaging and locating the buried objects in underground mine disasters, following a conceptual approach for detecting the lamp-room container at Lily mine. The technical aspects of potential technologies for imaging and locating subsurface utilities have been discussed, along with observations made during the testing of some of the technologies. Although the rescue efforts could not establish the location of the trapped miners, many lessons were learned. The purpose of this article is to record the lessons and advise on further testing and image modelling. This will not only assist with finding the Lily miners, but could be considered for future rescue operations.

Recommendations

In addition to what has been tested at Lily mine to date, it is important to also establish the application of IR data and GPR to mine disaster scenes. Its longer range (up to about 30 m) for detecting metal and imaging shapes makes GPR a good option for Lily mine, but the effectiveness should be tested at a suitable site elsewhere, *e.g.* Sterkfontein Caves, where tests could be conducted both on surface and underground. The combination of IR and GPR technologies can possibly establish the depth, location, and shape of the target.

The following aspects should be considered by the authorities in order to speed up future mine rescue operations.

- The communications approach has significant potential for a successful outcome, but speed is important and

the options will run out quickly when the batteries of the devices lose their power

- Obtain permission from the SAPS to conduct scientific tests on the technology for tracking cell phones in the event of a mine disaster. Tests are required to establish the accuracy and the maximum depth to which the technology can receive signals from below the surface or rubble
- A TPL should accompany any rescue effort, but it is essential that the operator is trained in the correct use of the device and has some knowledge of surveying principles so that readings can be projected onto the mine plans
- A good quality hand-held metal detector should accompany the rescue team and the team should be trained in its operational principles, functionality and limitations, and the correct use of the device
- Inventory records should be kept for all facilities, along with personal and work phone information – and these should be available for rescue efforts
- It is recommended that, where surface infrastructure is established over undermined ground, a risk assessment should be conducted and such infrastructure be made 'intelligent' through the installation of either an EMS or a basic TTE communication system. The electronic marker consists of passive radio frequency identification (RFID) system for locating both metallic and nonmetallic objects, whereas the TTE communication system is useful in disasters for locating miners trapped underground.

References

- 3M INFRASTRUCTURE PROTECTION DIVISION. 2012. 3M™ Electronic Marker System (EMS) Full-Range Markers. http://solutions.3m.com/3MContentRetrievalAPI/BlobServlet?lmd=1352220294000&locale=en_WW&assetType=MMM_Image&assetId=1319241427287&blobAttribute=ImageFile [accessed 22 July 2016].
- ADVANCED GEOSCIENCES, INC. 2016. Historic cemetery, Texas; Archeological grave site location. <http://www.agiusa.com/historic-cemetery-texas> [accessed 29 September 2016].
- AMERICAN SOCIETY OF CIVIL ENGINEERS. 2002. Standard guidelines for the collection and depiction of existing subsurface utility data. *Report no. CI/ASCE 38-02*. ASCE Codes and Standards Activity Committee (CSAC), New York.
- AMPROBE. n.d. Underground pipe and cable locator. <http://www.amprobe.com/amprobe/usen/wire-tracers-underground-cable-and-cable-locators/underground-cable-and-pipe-locators-/amp-at-5000.htm?pid=73171> [accessed 25 July 2016].
- ASHRAF H. and CAWOOD F.T. 2018. Towards safer mining: the role of modelling software to detect the container in which the Lily miners were trapped. *Mining of Mineral Deposits*. (Accepted for publication).
- BANDYOPADHYAY, L.K., CHAULYA, S.K., and MISHRA, P.K. 2010. *Wireless Communication in Underground Mines: RFID-based Sensor Networking*. Springer, New York, Dordrecht, Heidelberg, London.
- BENSON, R., GLACCUM, R.A., and NOEL, M.R. 1984. Geophysical techniques for sensing buried wastes and waste migration. *Report no. EPA-600/7-84-064*. US Environmental Protection Agency, Environmental Monitoring Systems Laboratory, Las Vegas, NV.
- DODGE, L.J. and ANSPACH, J.H. 1995. Case study of an environmental assessment combining historical practices and subsurface utility engineering. *Proceedings of the 57th American Power Conference*, Chicago, IL, 18-20 April 1995. *International Nuclear Information System*, IAEA, vol. 57, no. II. pp. 870-873.

Towards safer mining: scientific measurement approaches that could be applied

- ELPAM ELECTRONICS LTD. 2014. TPL 310D-Mini Trapped Person Locator. <http://www.elpam.com/products/search-rescue/tpl-310d-mini-trapped-person-locator/> [accessed 15 June 2016]
- HUSSAIN I., CAWOOD F., AND OLST R.V. 2017. Effect of tunnel geometry and antenna parameters on through-the-air communication systems in underground mines: Survey and open research areas. *Physical Communication (Elsevier)*, vol. 23. pp. 84–94. ISSN 1874-4907.
- INNOGEO. 2013. Microgravimetry to search for underground cavities, subsidence, galleries, decompressed zones. <http://www.inngeo.fr/english/wp-content/uploads/sites/7/2014/01/TD-microgravimetry.pdf> [accessed 21 March 2016].
- JEONG, H.S., ARBOLEDA, C.A., ABRAHAM, D.M., HALPIN, D.W., and BERNOLD, L.E. 2003. Imaging and locating buried utilities. *Technical Report* no. FHWA/IN/JTRP-2003/12. National Technical Information Service, Springfield, VA.
- JUSOH, Z. 2010. Application of 2-D resistivity imaging and seismic refraction technique in subsurface investigation for civil engineering. MS thesis, School of Physics, Science University, Penang, Malaysia.
- KHATRI,R., SHRIVASTAVA, V.K., and CHANDAK, R. 2011. Correlation between vertical electric sounding and conventional methods of geotechnical site investigation. *International Journal of Advanced Engineering Sciences and Technologies*, vol. 4, no. 2. pp. 42–53
- KTS-ELECTRONIC. 2016. Ground Penetrating Analyzer: GPA 3000. <http://kts-electronic.com/en/ground-penetrating-analyzer-gpa-3000.html> [accessed 21 March 2016].
- LOKE, M.H. 1999. Electrical imaging surveys for environmental and engineering studies: A practical guide to 2-D and 3-D surveys. <http://www.geo.mtu.edu/~ctyoung/LOKENOTE.PDF> [accessed 2 June 2016].
- MARITA, N.O. 2007. The gravity method. Short Course II on Surface Exploration for Geothermal Resources, organized by UNU-GTP and KenGen, Lake Naivasha, Kenya, 2–17 November 2007.
- MICHAEL, R.Y., GERALD, T.H., NICHOLAS, W.D., and JUSTIN, R.S. 2012. NIOSH-sponsored research in through-the-earth communications for mines: a status report. *IEEE Transactions on Industry Applications*, vol. 48, no. 5. pp. 1700–1707.
- MINE SAFETY AND HEALTH ADMINISTRATION. 2010. "Are You Prepared?" Mine emergency preparedness and response initiative. <http://arweb.msha.gov/focuson/areyouprepared/MineEmergency.asp> [accessed 5 April 2016].
- SATELLITE IMAGING CORPORATION. 2013. Mineral exploration and mining. <http://satimagingcorp.tw.cn/svc/mining.html> [accessed 10 June 2016].
- STARK, A. 2008. Seismic Methods and Applications: A Guide for the Detection of Geologic Structures, Earthquake Zones and Hazards, Resource Exploration, and Geotechnical Engineering. BrownWalker Press, Boca Raton, FL.
- SUBSURFACE SURVEYS & ASSOCIATES, Inc. n.d. Geophysical methods & applications. <http://www.subsurfacesurveys.com/pdf/Methods.pdf> [accessed 19 March 2016].
- WORKSWELL. 2016. Thermal Vision Pro. <http://www.drone-thermal-camera.com/thermal-vision-pro/> [accessed 26 March 2016]. ◆

Discussion on the paper: ‘Effect of frother and depressant interaction on flotation of Great Dyke PGM ore’

by T. Mberi, L.L. Mguni, and F. Ntuli

which was published in the January 2018 issue of the *Journal*

This is a well-conducted and useful investigation of the often confusing and sometimes controversial effect of what can at times be two antagonistic reagents in the flotation of sulphide minerals where naturally floatable gangue minerals are present in the ore. Some of the older readers of the *SAIMM Journal* may recall that the writer was an enthusiastic developer and marketer of gangue depressant for the flotation of both Merensky Reef and Great Dyke platinum ores.

During the 1970–1990 period the writer suggested, based on laboratory flotation experiments, that optimum grade and recovery results could be obtained by operating at the minimum frother addition needed for good recovery combined with the maximum depressant addition that could be used without reducing recovery. The authors' results appear to support this.

The concept that the writer operated on was that excessive frother addition promoted the reporting of floatable gangue to the concentrate. This may have been due to actual frother adsorption on the floatable gangue mineral surface or to gangue mineral entrainment in the increased mass pull of froth into the concentrate. High frother additions can promote both these phenomena.

At the same time, insufficient depressant addition has two adverse effects. Firstly it allows gangue minerals to adsorb on the bubble surface and therefore reduces collection of sulphide minerals on the bubble. Secondly it results in too much gangue being sent to the cleaner stages.

In the flotation of ores from the Great Dyke and the Merensky Reef, commercial plants employ circuits that usually contain rougher, scavenger, cleaner, and recleaner stages. For this reason a rougher flotation test alone may not indicate the optimum addition of frother and depressant to the rougher or other stages. Cleaner tests and possibly scavenger and recleaner tests should also be carried out.

The relative additions of frother and depressant in each of these stages are often varied in order to obtain the optimum results. For example, in the writer's opinion sufficient depressant should be added to the rougher stages to keep the bubble surface clear of attached gangue mineral and therefore provide the best conditions for sulphide recovery. In addition, the rougher stage should not produce a concentrate that is of such a low grade that the cleaner cells cannot cope with a high concentration of floatable gangue in their feed. But at the same time, sufficient frother and collector should be added to the rougher stage to ensure optimum sulphide mineral recovery. There is always competition between the depressant addition and the frother/collector addition.

In the cleaner stages there will probably be sufficient frother present in the feed pulp, and a minimum of depressant should be added in order to maximize grade.

J.M.W. (Murdoch) Mackenzie

NATIONAL & INTERNATIONAL ACTIVITIES

2018

12–14 March 2018— Society of Mining Professors 6th Regional Conference 2018

'Overcoming challenges in the Mining Industry through sustainable mining practices'

Birchwood Hotel and Conference Centre, Johannesburg, South Africa

Contact: Camielah Jardine

Tel: +27 11 834-1273/7, Fax: +27 11 838-5923/833-8156

E-mail: camielah@saimm.co.za, Website: <http://www.saimm.co.za>

23–26 April 2018—Application of Multiple Point Statistics to Mineral Resource Estimation—School

School of Mining Engineering at the University of the Witwatersrand

Contact: Yolanda Ndimande

Tel: +27 11 834-1273/7, Fax: +27 11 838-5923/833-8156

E-mail: yolanda@saimm.co.za, Website: <http://www.saimm.co.za>

May 2018 — Micro TBM Tunneling coming to the fore in South Africa Conference 2018

Gauteng

Contact: Camielah Jardine

Tel: +27 11 834-1273/7, Fax: +27 11 838-5923/833-8156

E-mail: camielah@saimm.co.za, Website: <http://www.saimm.co.za>

6–7 June 2018— Digitalization in Mining Conference

'Mining business make-over –Exploiting the digital resolution'

Johannesburg, South Africa

Contact: Yolanda Ndimande

Tel: +27 11 834-1273/7, Fax: +27 11 838-5923/833-8156

E-mail: yolanda@saimm.co.za, Website: <http://www.saimm.co.za>

11–14 June 2018— SAIMM: Diamonds — Source to Use 2018 Conference 'Thriving in Changing Times'

Birchwood Conference Centre (Jet Park)

Contact: Camielah Jardine

Tel: +27 11 834-1273/7, Fax: +27 11 838-5923/833-8156

E-mail: camielah@saimm.co.za, Website: <http://www.saimm.co.za>

9–12 July 2018— Copper Cobalt African association with The 9th Southern African Base Metals Conference

Avani Victoria Falls Resort, Livingstone, Zambia

Contact: Camielah Jardine

Tel: +27 11 834-1273/7, Fax: +27 11 838-5923/833-8156

E-mail: camielah@saimm.co.za, Website: <http://www.saimm.co.za>

30–31 July 2018 —Introduction to Process Engineering School 2018 Volume 1

Birchwood Hotel & OR Tambo Conference Centre

Contact: Yolanda Ndimande

Tel: +27 11 834-1273/7, Fax: +27 11 838-5923/833-8156

E-mail: yolanda@saimm.co.za, Website: <http://www.saimm.co.za>

6–8 August 2018—Geometallurgy Conference 2018

Lagoon Beach Conference Venue, Cape Town, South Africa
Contact: Camielah Jardine

Tel: +27 11 834-1273/7, Fax: +27 11 838-5923/833-8156

E-mail: camielah@saimm.co.za, Website: <http://www.saimm.co.za>

13–14 August 2018 — The SAMREC and SAMVAL CODES

'Advanced Workshop: Can you face your peers?'

Birchwood Hotel and Conference Centre, Johannesburg, South Africa

Contact: Camielah Jardine

Tel: +27 11 834-1273/7, Fax: +27 11 838-5923/833-8156

E-mail: camielah@saimm.co.za, Website: <http://www.saimm.co.za>

10–11 September 2018 — ASM Conference 2018

'Fostering a regional approach to ASM transformation in sub-Saharan Africa'

Nasrec, Johannesburg (Electra Mining)

Contact: Yolanda Ndimande

Tel: +27 11 834-1273/7, Fax: +27 11 838-5923/833-8156

E-mail: yolanda@saimm.co.za, Website: <http://www.saimm.co.za>

12–14 September 2018 — MineSafe 2018 Technical Conference and Industry day

Emperors Palace, Hotel Casino Convention Resort, Johannesburg

Contact: Camielah Jardine

Tel: +27 11 834-1273/7, Fax: +27 11 838-5923/833-8156

E-mail: camielah@saimm.co.za, Website: <http://www.saimm.co.za>

18–19 September 2018 — 4th Young Professionals Conference

'Creating a sustainable African minerals industry through applied innovation'

Focus Rooms, The Core, Sunninghill, Sandton

Contact: Camielah Jardine

Tel: +27 11 834-1273/7, Fax: +27 11 838-5923/833-8156

E-mail: camielah@saimm.co.za, Website: <http://www.saimm.co.za>

14–17 October 2018 — Furnace Tapping 2018 Conference

Nombolo Mdhuli Conference Centre, Kruger National Park, South Africa

Contact: Gugu Charlie

Tel: +27 11 834-1273/7, Fax: +27 11 838-5923/833-8156

E-mail: gugu@saimm.co.za, Website: <http://www.saimm.co.za>

25–26 October 2018 — Across-the-board training needs and requirements for the South African Mining Industry Workshop

Johannesburg

Contact: Camielah Jardine

Tel: +27 11 834-1273/7, Fax: +27 11 838-5923/833-8156

E-mail: camielah@saimm.co.za, Website: <http://www.saimm.co.za>

2019

13–15 November 2019 — XIX International Coal Preparation Congress & Expo 2019

New Delhi, India

Contact: Coal Preparation Society of India

Tel/Fax: +91-11-26136416, 4166 1820

E-mail: cpsideli.india@gmail.com, president@cpsi.org, inrksachdev01@gmail.com, hi.sapru@monnetgroup.com

Company Affiliates

The following organizations have been admitted to the Institute as Company Affiliates

3M South Africa (Pty) Limited	Duraset	Murray and Roberts Cementation
AECOM SA (Pty) Ltd	Elbroc Mining Products (Pty) Ltd	Nalco Africa (Pty) Ltd
AEL Mining Services Limited	eThekweni Municipality	Namakwa Sands(Pty) Ltd
Air Liquide (PTY) Ltd	Expectra 2004 (Pty) Ltd	Ncamiso Trading (Pty) Ltd
Alexander Proudfoot Africa (Pty) Ltd	Exxaro Coal (Pty) Ltd	New Concept Mining (Pty) Limited
AMEC Foster Wheeler	Exxaro Resources Limited	Northam Platinum Ltd - Zondereinde
AMIRA International Africa (Pty) Ltd	Filtaquip (Pty) Ltd	PANalytical (Pty) Ltd
ANDRITZ Delkor(pty) Ltd	FLSmith Minerals (Pty) Ltd (FFE001)	Paterson & Cooke Consulting Engineers (Pty) Ltd
Anglo Operations Proprietary Limited	Fluor Daniel SA (Pty) Ltd	Perkinelmer
Anglogold Ashanti Ltd	Franki Africa (Pty) Ltd-JHB	Polysius A Division Of Thyssenkrupp Industrial Sol
Arcus Gibb (Pty) Ltd	Fraser Alexander (Pty) Ltd	Precious Metals Refiners
Atlas Copco Holdings South Africa (Pty) Limited	G H H Mining Machines (Pty) Ltd	Rand Refinery Limited
Aurecon South Africa (Pty) Ltd	Geobrug Southern Africa (Pty) Ltd	Redpath Mining (South Africa) (Pty) Ltd
Aveng Engineering	Glencore	Rocbolt Technologies
Aveng Mining Shafts and Underground	Hall Core Drilling (Pty) Ltd	Rosond (Pty) Ltd
Axis House Pty Ltd	Hatch (Pty) Ltd	Royal Bafokeng Platinum
Bafokeng Rasimone Platinum Mine	Herrenknecht AG	Roytec Global (Pty) Ltd
Barloworld Equipment -Mining	HPE Hydro Power Equipment (Pty) Ltd	RungePincockMinarco Limited
BASF Holdings SA (Pty) Ltd	IMS Engineering (Pty) Ltd	Rustenburg Platinum Mines Limited
BCL Limited (BCL001)	Ivanhoe Mines SA	Salene Mining (Pty) Ltd
Becker Mining (Pty) Ltd	Joy Global Inc.(Africa)	Sandvik Mining and Construction Delmas (Pty) Ltd
BedRock Mining Support Pty Ltd	Kudumane Manganese Resources	Sandvik Mining and Construction RSA(Pty) Ltd
BHP Billiton Energy Coal SA Ltd	Leco Africa (Pty) Limited	SANIRE
Blue Cube Systems (Pty) Ltd	Longyear South Africa (Pty) Ltd	Sebilo Resources (Pty) Ltd
Bluhm Burton Engineering Pty Ltd(BLU003)	Lonmin Plc	SENET (Pty) Ltd
Bouygues Travaux Publics	Lull Storm Trading (Pty) Ltd	Senmin International (Pty) Ltd
CDM Group	Magnetech (Pty) Ltd	Smec South Africa
CGG Services SA	MAGOTTEAUX (PTY) LTD	Sound Mining Solution (Pty) Ltd
Chamber of Mines of South Africa	MBE Minerals SA Pty Ltd	SRK Consulting SA (Pty) Ltd
Coalmin Process Technologies CC	MCC Contracts (Pty) Ltd	Technology Innovation Agency
Concor Opencast Mining	MCC Contracts (Pty) Ltd	Time Mining and Processing (Pty) Ltd
Concor Technicrete	MD Mineral Technologies SA (Pty) Ltd	Timrite Pty Ltd
Council for Geoscience Library	MDM Technical Africa (Pty) Ltd	Tomra (Pty) Ltd
CRONIMET Mining Processing SA Pty Ltd	Metalock Engineering RSA (Pty)Ltd	Ukwazi Mining Solutions (Pty) Ltd
CSIR Natural Resources and the Environment (NRE)	Metorex Limited	Umgeni Water
Data Mine SA	Metso Minerals (South Africa) Pty Ltd	Webber Wentzel
Department of Water Affairs and Forestry	Minerals Operations Executive (Pty) Ltd	Weir Minerals Africa
Digby Wells and Associates	MineRP Holding (Pty) Ltd	Worley Parsons RSA (Pty) Ltd
DMS Powders	Mintek	
DRA Mineral Projects (Pty) Ltd	MIP Process Technologies (Pty) Limited	
	Modular Mining Systems Africa (Pty) Ltd	
	MSA Group (Pty) Ltd	
	Multotec (Pty) Ltd	



BM

BASE METALS
2018

Copper Cobalt Africa

In Association with

The 9TH Southern African Base Metals Conference

9–12 July 2018

Avani Victoria Falls Resort, Livingstone, Zambia



SAIMM is proud to host the Second Copper Cobalt Africa Conference in the heart of Africa

To be held in Livingstone, Zambia, this anticipated and prestigious event provides a unique forum for discussion, sharing of experience and knowledge, and networking for all those interested in the processing of copper and cobalt in an African context, in one of the world's most spectacular settings - the Victoria Falls.



The African Copper Belt is again experiencing a resurgence of activity following the commodity downturn of recent years. A significant proportion of capital spending, project development, operational expansions, and metal value production in the Southern African mining industry take place in this region. The geology and mineralogy of the ores are significantly different to those in other major copper-producing regions of the world, often having very high grades as well as the presence of cobalt. Both mining and metallurgy present some unique challenges, not only in the technical arena, but also with respect to logistics and supply chain, human capital, community engagement, and legislative issues. This conference provides a platform for discussion of a range of topics, spanning the value chain from exploration, projects, through mining and processing, to recycling and secondary value addition.

For international participants, this conference offers an ideal opportunity to gain in-depth knowledge of and exposure to the African copper and cobalt industries, and to better understand the various facets of mining and processing in this part of the world.

Jointly hosted by the Mining and Metallurgy Technical Programme Committees of the Southern African Institute of Mining and Metallurgy (SAIMM), this conference aims to:



- Promote dialogue between the mining and metallurgical disciplines on common challenges facing the industry
- Enhance understanding of new and existing technologies that can lead to safe and optimal resource utilization

- Encourage participation and build capacity amongst young and emerging professionals from the Copper Belt region. The organizing committee looks forward to your participation.

Conference Topics

- Mineralogy
- Exploration and new projects
- Open-cast mining
- Underground mining
- Rock engineering
- Mine planning
- Mineral resource management
- Geometallurgy
- Minerals processing
- Pyrometallurgy
- Hydrometallurgy
- Current operational practices and improvements
- Project development and execution
- Novel technologies for this industry
- Socio-economic challenges
- Recycling
- Waste treatment and minimization
- Environmental issues



Sponsors

To add your name to the mailing list and to receive further information, please e-mail your contact details to: Camielah Jardine: Head of Conferencing SAIMM, P O Box 61127, Marshalltown 2107, Tel: +27 (0) 11 834-1273/7 E-mail: camielah@saimm.co.za, Website: <http://www.saimm.co.za>



SAIMM
THE SOUTHERN AFRICAN INSTITUTE
OF MINING AND METALLURGY



Programme in Project Management (PPM)

20 years of developing practical project managers. Thousands of people have benefitted from this programme since 1997.

- Taught by a variety of subject matter experts from the University of Pretoria – to a large extent the same lecturers that teach Africa's only master's degree internationally accredited by the Global Accreditation Centre of the PMI.
- Skills are developed during contact sessions and practised on workplace assignments.

This multi-disciplinary programme is presented over eight modules by a variety of experts in the different disciplines:

- Project Management Principles, Practices and Scheduling
- Project Procurement and Contract Management
- Project Risk Management
- Legal Aspects for Project Managers (Law of Contract, Labour Law, OSH Act)
- Financial Aspects and Project Cost Management
- The People-Side of Project Management
- Project Quality Management
- Project Management in the Business Context


**The first module
of PPM is also
available online**

5 CPD points (ECSA)

Book your seat today on one of the most renowned and respected training interventions in the industry.
For further information, frequently asked questions and to enrol, please visit

www.ppm.up.ac.za

Shifting knowledge to insight

